Universidad de Huelva

Departamento de Ciencias Integradas

Propiedades interfaciales y equilibrio de fase de promotores/inhibidores de hidratos mediante dinámica molecular

Memoria para optar al grado de doctor
presentada por:

Jesús Algaba Fernández

Fecha de lectura: 26 de septiembre de 2019

Bajo la dirección de los doctores:

Felipe Jiménez Blas

José Manuel Míguez Díaz

Huelva, 2019

Universidad de Huelva

Facultad de Ciencias Experimentales
Departamento de Ciencias Integradas (Física Aplicada)
Centro de Investigación en Química Sostenible (CIQSO)

Propiedades interfaciales y equilibrio de fase de promotores/inhibidores de hidratos mediante dinámica molecular

Memoria para optar al grado de Doctor

Jesús Algaba Fernández

Directores: Dr. Felipe Jiménez Blas y Dr. José Manuel Míguez Díaz

Huelva, Septiembre 2019

Del Colegio a la Aventura...

Seymour Skinner

Agradecimientos

Con la finalización de esta tesis doctoral se cierra un capítulo en mi vida, no solo puramente académico o profesional, sino también personal. Mirando hacia atrás y pensando en el camino recorrido durante estos cuatro años hasta aquí, me resulta difícil imaginar que una tesis doctoral pueda ser desarrollada por completo por una única persona sin ningún tipo de ayuda. Por suerte, durante todo el desarrollo de este trabajo me he encontrado rodeado por grandes personas y profesionales sin las cuales este trabajo no habría sido el mismo. Espero no olvidarme de nadie.

Primero, y ante todo, quisiera agradecer a mi director de tesis, Felipe Jiménez Blas, quién hizo que me interesara en el mundo de la investigación y de la simulación molecular desde el primer año de licenciatura. Fuiste claro, como has sido siempre, me dijiste que hacer una tesis es duro, que sería difícil conseguir financiación, pero que haríamos todo lo que pudiéramos. Aún sin la certeza de como resultaría todo, comenzaste a formarme en programación, Mecánica Estadística, Monte Carlo,.... tú apostate por mí y yo cada día tenía más claro que o hacía la tesis contigo o no la haría. Tú me has ayudado a crecer como investigador, y como persona. Más que un director has sido un maestro, un sensei, un guía. Gracias por todas las palabras de ánimo y por todos los consejos.

También quisiera agradecer especialmente a mi codirector de tesis José Manuel Míguez, quién se incorporó al grupo durante mi primer año de tesis y con quién desde entonces he estado trabajando mano a mano, intercambiando ideas y aprendiendo de su experiencia. Siempre hiciste un hueco para mí, para discutir sobre el trabajo, para resolverme dudas, para todo. Gracias por todo José Manuel.

Gracias a todo el grupo de FILICO de la Universidad de Huelva. Gracias a Iñaqui, a Paula y a Curro, por vuestros consejos y por tener siempre unas palabras de ánimo. También quiero dar las gracias mis compañeros María, Ismael y Esther. A tí María, amiga y compañera de laboratorio, de alegrías y de penas, solo decirte que las tardes se habrían hecho muy largas sin tu compañia.

También quisiera agradecer a todas aquellas personas con las que he tenido el placer de conocer y/o trabajar a lo largo del desarrollo de este trabajo. Gracias a Antonio Padilla (Universidad de Huelva), a José Matías Garrido y Andrés Mejía (ambos de la Universidad de Concepción-Chile), a Bruno Mendiboure (Universidad de Pau) y a Manuel Martínez Piñeiro (Universidad de Vigo).

También me gustaría agradecer a todas las personas a las que conocí durante mi estancia en Imperial College. A Erich, que me dió la oportunidad de trabajar tres meses con él y que siempre tuvo un rato que dedicarme. A Doris, que hizo de su casa también la mía. A Mac, Andrés y Miguel por todas las charlas en la cafetería de Imperial y fuera de ella. También me gustaría agradecer a todas las personas a las que conocí durante mi estancia en Madrid. A Mac, que me abrió las puertas de su casa. A todo el equipo del CSIC de Madrid, a Enrique Lomba, Itziar, Pablo, Antonio, Ariel, Leandro y sobre todo a Eva, quien me aventuró en el vasto mundo del cálculo de energías libres. A todos ustedes, gracias.

Por supuesto, fuera del plano profesional hay muchas otras personas a las que quisiera darles las gracias. Quisiera agradecer a mi familia, a mis padres, a mi hermana, a Javier, a Elizabeth, a Toñi y a Vicente, gracias por todo vuestro apoyo incondicional, por los ánimos, por todo. También quisiera agradecer a mis amigos Samuel, Cesar, Moises y Gaby, mis hermanos sin lazos de sangre, mi otra familia. Gracias por las risas y por los buenos momentos.

Cada parte de este trabajo, es de todos ustedes, de los que estáis y de los que estuvisteis.

Resumen

Existe un creciente interés en el estudio de los hidratos de gases debido a sus aplicaciones, no solo energéticas sino también medioambientales. Las condiciones de estabilidad de estos hidratos pueden ser ampliamente modificadas mediante aditivos que pueden promover o inhibir la formación de estos. El tetrahidrofurano (THF) es uno de los promotores de hidratos más ampliamente conocido y usado. Sin embargo, muy pocos estudios han sido dedicados a la determinación de sus propiedades termodinámicas, y al estudio de los equilibrios de fases de sus mezclas con el resto de compuestos que forman el hidrato de gas (agua, H_2O, metano, CH_4, dióxido de carbono, CO_2,...). En este aspecto, la simulación molecular y los formalismos teóricos pueden proporcionar información no solo macroscópica sino también microscópica acerca de los equilibrio de fases y las propiedades interfaciales de las mezclas binarias de THF con H_2O, CH_4 y CO_2.

Como primera aproximación para comprender las propiedades termodinámicas de las mezclas binarias de THF + CO_2 (2), CH_4 (2) y + H_2O (2), los diagramas de fases a altas presiones de estos sistemas fueron obtenidos usando la ecuación de estado SAFT-VR (del inglés, *Statistical Associating Fluid Theory-Variable Range*). En este trabajo, se estudió el comportamiento termodinámico de estos sistemas mezcla desde un punto de vista teórico. Las predicciones teóricas obtenidas fueron usadas como punto de partida en los siguientes trabajos.

También se ha estudiado la capacidad de diferentes modelos de THF, tomados de la literatura, para determinar sus propiedades interfaciales a través de la simulación directa de la interfase líquido-vapor. El THF fue modelado utilizando seis modelos moleculares diferentes, tres de ellos basados en la aproximación de átomos-unidos y los otros tres basados en la aproximación de *coarse grained*. Uno de los modelos de átomos-unidos se propuso en este estudio y es una versión rígida y plana del modelo original TraPPE-UA (del inglés, *Transferable Potentials for Phase Equilibria-United Atoms*) de THF propuesto por Keasler *et al.* [J. Phys. Chem. B 115, 11234 (2012)]. Para los seis modelos de THF estudiados, se examinaron los perfiles de densidad, las densidades de coexistencia, la anchura interfacial y la tensión interfacial. Esta versión rígida pudo proporcionar resultados similares al modelo flexible original al mismo tiempo que proporciona simulaciones más rápidas.

Para validar las predicciones teóricas obtenidas para la mezcla binaria THF+CO_2, se ha medido experimentalmente la tensión interfacial, las densidades de coexistencia y la adsorción de Gibbs relativa a dos temperaturas (298.15 y 353.15 K) y a varias presiones. Además, se calcularon los perfiles de densidad aplicando la Teoría del Gradiente Cuadrado. Los resultados experimentales se utilizaron, junto con las predicciones teóricas obtenidas utilizando SAFT-VR, como punto de partida en el estudio de la mezcla binaria THF+CO_2 utilizando simulación en dinámica molecular. Estas simulaciones se llevaron a cabo en las mismas condiciones termodinámicas en las que se llevaron a cabo los experimentos. El THF fue modelado usando la versión original y la versión rígida del modelo TraPPE-UA de THF. El acuerdo entre los resultados de simulación, utilizando ambos modelos, con los datos experimentales

y las predicciones teóricas fue excelente en la mayoría de los casos.

Siguiendo los pasos de los trabajos anteriores, se ha estudiado, de forma experimental y mediante simulación en dinámica molecular, las propiedades interfaciales y los equilibrios de fases de la mezcla binaria THF+CH_4 a 300 y 370 K a varias presiones. En este estudio, el THF solo se modeló utilizando el modelo rígido TraPPE-UA, ya que este proporciona resultados igualmente aceptables que el modelo flexible original de Keasler, pero necesita tiempos menores de simulación. Nuevamente, el acuerdo entre resultados obtenidos mediante simulación, teoría y experimentos fue excelente en la mayoría de las condiciones termodinámicas estudiadas. En este punto, es importante mencionar, que antes de este trabajo, no existían datos experimentales o de simulación para la mezcla binaria THF+CH_4.

Por otro lado, la familia de los 1−alcanoles ha sido ampliamente utilizada como inhibidor de hidratos. Para la mezcla binaria de H_2O + 1−alcanol (desde el 1−butanol al 1−heptanol), hemos estudiado las propiedades interfaciales (perfiles de densidad, densidades de coexistencia y tensiones interfaciales) y los equilibrios de las fases. Los resultados obtenidos de simulación en dinámica molecular se compararon con resultados experimentales tomados de la literatura.

Palabras claves: Hidratos de gas, promotores de hidratos, inhibidores de hidratos, dinámica molecular, SAFT-VR, 1-alcanol, tetrahidrofurano, metano, dióxido de carbono, simulación molecular.

Summary

There is an increasing interest in the gas hydrates study due to their energetic and environmental applications. The thermodynamic stability conditions of these hydrates can be widely modified using additives which can promote or inhibit their formation. Tetrahydrofuran (THF) is one of the most known and used hydrate promoters. However, a very limited number of studies have been devoted to the determination of its thermodynamic properties, and to the study of the phases equilibria of their mixtures with the rest of the compounds which form the gas hydrate (water, H_2O, methane, CH_4, carbon dioxide, CO_2,...). In this aspect, the molecular simulation and the theoretical formalisms are able to proportionate not only macroscopic information, but also microscopic information, about the phases equilibria, and the interfacial properties of the binary mixtures of THF with H_2O, CH_4, and CO_2.

As a first approximation to understand the thermodynamic properties of the THF+CO_2(2), CH_4(2), and + H_2O(2) binary mixtures, the high pressures phases diagrams of these systems were obtained using the equation of state SAFT-VR (Statistical Associating Fluid Theory-Variable Range). In this work, the thermodynamic behaviour of these mixture systems was studied from a theoretical point of view. The theoretical predictions obtained were used as a start point in the following works.

We have also studied the ability of different THF models, taken from the literature, to determine their interfacial properties through the direct simulation of the vapor-liquid interface. The THF was modeled using six different molecular models, three of them based on the united-atoms approach and the other three based on a coarse-grained approach. One of the united-atoms models was proposed in this study and it is an approximate rigid and planar version of the original TraPPE-UA THF model (*Transferable Potentials for Phase Equilibria-United Atoms*) proposed by Keasler *et al.* [J. Phys. Chem. B 115, 11234 (2012)]. For the six studied THF model, we examined the density profiles, the coexistence densities, interfacial thickness and the surface tension in terms of temperature. This rigid version was able to provide similar results as the original flexible model at the same time that it provides faster simulations.

In order to validate the theoretical predictions obtained to the THF+CO_2 binary mixture, we have measured experimentally the interfacial tension, the coexistence densities and the relative Gibbs adsorption at two temperatures (298.15 and 353.15 K) and at several pressures. In addition, density profiles were calculated applying the Square Gradient Theory. The experimental results were used, together with the theoretical predictions obtained using SAFT-VR, as a start point in the study of the THF+CO_2 binary mixture using molecular dynamic simulation. These simulations were carried out at the same thermodynamic conditions at which the experiments were performed. THF was modeled using the original and the rigid version of the TraPPE-UA THF model. The agreement between molecular dynamic simulation results, using both models, with the experimental results and the theoretical predictions were excellent in the majority of the cases.

Following the steps of the previous works, we have studied experimentally, and using molecular dynamic simulation, the interfacial properties and the phase equilibria of the binary mixture of THF+CH_4 at 300 and 370 K at several pressures. In this study, the THF was only modeled using the rigid TraPPE-UA THF model due to this one provides equally acceptable results than the original flexible Keasler's model, but it needs lesser simulation times. Again, the agreement between simulation, theoretical and experiment results was excellent in the majority of the thermodynamic studied conditions. At this point, it is important to mention that before this work there were not experimental or simulation results for the THF+CH_4 binary mixture.

On the other hand, the family of the 1−alkanols has been widely used as hydrate inhibitors. For the H_2O+1−alkanol binary mixture (from 1−butanol to 1−heptanol), we have studied the interfacial properties (density profiles, coexistence densities, and interfacial tensions) and the phases equilibria. The results obtained from molecular dynamics simulation were compared with experimental results taken from the literature.

Key Words: Gas hydrate, hydrate promoter, hydrate inhibitor, molecular dynamic, SAFT-VR, 1-alkanol, tetrahydrofuran, methane, carbon dioxide, molecular simulation.

Índice de contenidos

Parte I

Introducción y Objetivos

Capítulo 1

Introducción

1.1 Motivaciones

Un hidrato es un sólido cristalino de inclusión no estequiométrico constituido por una red de moléculas de agua (H_2O) enlazadas mediante puentes de hidrógeno que forman cavidades en cuyo interior, moléculas de pequeño tamaño y bajo peso molecular como pueden ser el metano (CH_4), el dióxido de carbono (CO_2) o el hidrógeno (H_2), pueden ser encapsuladas bajo determinadas condiciones termodinámicas [1]. La naturaleza de la molécula huésped determinará las propiedades termodinámicas y la estructura cristalográfica del hidrato [1, 2], siendo las estructuras más comunes en la naturaleza la *s*I [3], la *s*II [4] y la *s*H [5]. Es precisamente esta capacidad que tienen los hidratos de encapsular a otros compuestos lo que los ha puesto en el punto de mira como una futura reserva de gas natural y como un posible material para el almacenamiento y captura de gases. Los hidratos de metano constituyen una reserva de energía fósil de gran valor debido a su alto contenido en metano ($1m^3$ de hidrato contiene unos $160m^3$ de metano en condiciones estándar). Se estima que la cantidad de gas natural atrapado en forma de hidrato supera con creces la cantidad de gas natural disponible en yacimientos convencionales, convirtiendo a los hidratos de gas en una importante fuente de energía fósil. Pese a que el hidrato de gas es conocido desde hace décadas (debido a su formación en gaseoductos), ha sido recientemente cuando se ha comenzado a usar como fuente de energía. La obtención de metano a partir de sus hidratos plantea una serie de problemas técnicos, siendo el problema principal la extracción de este. Entre las técnicas más prometedoras para extraer este metano atrapado en los hidratos, se encuentran la despresurización del hidrato y la captura selectiva de CO_2 al sustituir este al metano como molécula huésped. La captura de CO_2 a través de la cristalización de hidratos es un método novedoso y prometedor, no solo por su alta y segura capacidad de almacenamiento de gas [6–9], sino también por el reducido consumo de energía involucrado en los procesos de formación y disociación del hidrato [10–13]. Para ayudar a comprender y optimizar el proceso de extracción de metano, numerosos estudios experimentales, teóricos y computacionales están siendo desarrollados en la actualidad con el propósito de ampliar el conocimiento sobre el comportamiento termodinámico de estos hidratos, que dependerá del tipo de estructura de hidrato que sea, así como de las interacciones intermoleculares entre las moléculas encapsuladas dentro del hidrato y las interacciones entre estas moléculas huésped con el agua. A su vez, también se están desarrollando y estudiando el comportamiento de estos hidratos en

presencia de aditivos que pueden ayudar tanto a la estabilización del hidrato y fomentar su formación, como a la inhibición de estos mismos.

Estos aditivos pueden modificar ampliamente las condiciones termodinámicas de equilibrio de los hidratos, y pese a que tanto promotores como inhibidores de hidratos han sido ampliamente utilizados con el fin de modificar estas condiciones, se desconoce exactamente como intervienen a nivel molecular. Frente al elevado coste económico y a la necesidad de disponer de un laboratorio con el equipo necesario para el estudio experimental de las propiedades termodinámicas de estos aditivos, los métodos de simulación por ordenador y algunos formalismos teóricos han demostrado ser una alternativa económica, segura y precisa para llevar acabo estos estudios, aportando un punto de vista único y diferente al que ofrece la experimentación acerca de como estos aditivos pueden alterar las propiedades termodinámicas de los hidratos. Desafortunadamente, existen pocos modelos moleculares disponibles en la literatura acerca de estos promotores e inhibidores de hidratos y, en los casos en los que si existe un modelo molecular, se desconoce si estos son capaces de describir de forma adecuada las propiedades termodinámicas y los equilibrios de fases del compuesto real.

El tetrahidrofurano, o simplemente THF, es un éter cíclico ampliamente utilizado como promotor termodinámico de hidratos [2, 14–16]. Una mezcla de THF y agua forman una fase hidrato del tipo *s*II (constituido por 17 moléculas de agua por cada molécula de THF) [15, 16]. Cuando el THF es añadido como aditivo a una fase hidrato, se produce un pronunciado cambio en la curva de coexistencia, disminuyendo drásticamente la presión de equilibrio al formarse el hidrato de THF. La celdilla unidad del hidrato de THF (*s*II) consiste en 16 cavidades pequeñas formadas por dodecaedros pentagonales (5^{12}) y 8 cavidades grandes formadas por hexadecaedros ($5^{12}6^4$) donde las moléculas de THF quedan encapsuladas. Este hidrato se forma fácilmente y se disocian alrededor de 277K a presión atmosférica, condiciones mucho más suaves que las que normalmente son necesarias para mantener estable una fase hidrato. Dado que el THF solo ocupa las cavidades grandes del hidrato, las pequeñas pueden ser ocupadas por otro tipo de molécula huésped de menor tamaño. Esta habilidad, junto a las condiciones relativamente suaves de presión y temperatura en las que se forman los hidratos de THF, les confiere importantes aplicaciones. Por ejemplo, existen varios estudios [17–20] en los que el THF es usado para reducir significativamente la presión de equilibrio de los hidratos de H_2, obteniendo así una forma estable y segura de almacenar H_2 gas. Otro importante ejemplo de las aplicaciones de los hidratos de THF es la captura de CO_2. Las emisiones de CO_2 procedentes de la combustión de combustibles fósiles son el principal motivo del calentamiento global [21]. Esto ha promovido el esfuerzo de la comunidad científica por encontrar nuevos métodos y técnicas para la captura de CO_2. La captura de CO_2 mediante la formación de hidratos es un método alternativo a las técnicas convencionales [22–24] que está siendo ampliamente estudiado debido a la gran capacidad de almacenaje que presentan los hidratos de CO_2 [6–9], a la capacidad de alterar las condiciones termodinámicas del proceso de formación/disociación del hidrato mediante aditivos [10–13] y por tratarse de un método respetuoso con el medioambiente. Pese a que el THF es ampliamente utilizado, no solo como promotor de hidratos, sino como disolvente en gran variedad de procesos industriales, existen pocos modelos moleculares de este compuesto en la literatura.

Por otro lado, en ocasiones se desea evitar la formación de hidratos. Cuando se forma un hidrato de forma indeseada durante un proceso industrial, se pueden bloquear las tuberías, conexiones instrumentales, válvulas y otros equipos, causando alteraciones en el proceso que pueden ser peligrosas, además de suponer un elevado coste económico si se dañan los equipos. Por ello, en algunas ocasiones es necesaria la inhibición de hidratos. Se pueden agregar muchos compuestos al agua para reducir la temperatura de hidratación y de congelación. Sin embargo, pocos son tan eficaces y baratos como

los alcanoles (cadenas alquílicas con un grupo funcional −OH). El metanol ha sido ampliamente utilizado como inhibidor termodinámico de hidratos [25–32]. Sin embargo, al aumentar el tamaño de la cadena alquílica, van disminuyendo los trabajos que pueden ser encontrados en la literatura sobre otros alcanoles lineales como el etanol [32–36] o el 1-propanol [37, 38], siendo prácticamente inexistentes para tamaños de cadena mayores (1-butanol, 1-pentanol, ...). Lo mismo ocurre con los estudios disponibles en la literatura acerca de las propiedades interfaciales y los equilibrios de fases de la mezcla binaria agua + 1-alcanoles, aunque existen algunos estudios para 1-alcanoles de cadena corta (metanol, etanol y propanol) [39], escasean los estudios, tanto teóricos y computacionales como experimentales, de la mezcla de agua con alcanoles lineales de cadenas más largas.

Debido a la necesidad de obtener una descripción teórica precisa de las propiedades termodinámicas (entre ellas, las propiedades interfaciales y los equilibrios de fases) de un elevado número de mezclas complejas de interés industrial, en los último años se han desarrollado diversos procedimientos teóricos para la obtención de una predicción precisa del comportamiento termodinámico de sistemas reales. Pese a que la obtención de resultados experimentales sigue siendo uno de los métodos actuales más empleados para el estudio de sistemas reales, en ocasiones es necesario el uso de métodos teóricos o computacionales para una mayor comprensión de los fenómenos que ocurren durante el experimento. Entre los numerosos formalismos teóricos que pueden ser encontrados en la literatura, destaca entre ellos el basado en la ecuación de estado SAFT (Statistical Asociation Fluid Theory). SAFT es uno de los formalismos más exitosos para la predicción de las propiedades termodinámicas, y particularmente los equilibrios en fase fluida [40, 41]. La expresión general de la ecuación de estado SAFT se basa en la teoría de perturbaciones de primer orden, mediante la cual, la energía libre de Helmholtz del sistema viene dada por la suma de diferentes contribuciones que toman en cuenta la energía libre total del sistema desde el riguroso punto de vista de la Mecánica Estadística [42–45]. Existen varias expresiones de esta ecuación basadas en distintas aproximaciones [46–50]. Entre ellas se encuentra la versión SAFT-VR [51, 52]. En las diferentes versiones de SAFT-VR, las moléculas se consideran formadas por segmentos tangencialmente unidos, y la energía libre de Helmholzt que aporta cada segmento viene expresada por la contribución a la energía libre de Helmholtz de un potencial de referencia (el potencial de esfera dura) y una serie de términos adicionales obtenidos a partir de la teoría de perturbaciones aplicada sobre un potencial de interacción de rango variable (potencial de Yukawa, de pozo cuadrado, de Mie, de Lennard-Jones, etc). Además, cada segmento puede contar con sitios de interacción adicionales para tener en cuenta las interacciones asociantes. Estas versiones han demostrado obtener unas predicciones excelentes del comportamiento termodinámico de mezclas complejas [53–57] y ser capaces de predecir las propiedades termodinámicas y los equilibrios en fase fluida de sistemas puros y sistemas mezclas con alta precisión.

En un punto intermedio entre la teoría y la experimentación se encuentra la simulación molecular por ordenador [58–62]. La simulación molecular nos permite reproducir los procesos físicos y químicos que sufre un sistema complejo a nivel molecular y es considerada, junto a la teoría y a los experimentos, la tercera forma de hacer ciencia. Tradicionalmente, la simulación molecular ha necesitado el apoyo de los resultados experimentales a la hora de parametrizar modelos de sustancias reales para reproducir, mediante simulación, los resultados obtenidos experimentalmente. Sin embargo, debido a la rápida evolución de los ordenadores, a la mejora de los algoritmos matemáticos y computacionales empleados, y al desarrollo de nuevas técnicas avanzadas de simulación, cada vez es más frecuente el estudio de sistemas complejos utilizando la simulación molecular, para así obtener información fiable del comportamiento termodinámico del sistema que ayude a un mejor diseño y realización de los experimentos. Las dos técnicas de simulación molecular más ampliamente utilizadas son la dinámica molecular y el método

de Monte Carlo. En el método de Monte Carlo se genera un conjunto de configuraciones microscópicas, todas compatibles con el estado macroscópico del sistema bajo estudio, de acuerdo a una función de distribución. Esto da lugar a una cadena de Markov que permitirá determinar las propiedades macroscópicas del sistema [62]. Por otro lado, la dinámica molecular estudia la evolución temporal del sistema mediante la resolución de las ecuaciones del movimiento de Newton, bajo el supuesto de que el movimiento de las partículas obedece las leyes de la Mecánica Clásica, como se verá en mayor detalle en el próximo capítulo.

El éxito de estos métodos, tanto teóricos como de simulación molecular, para determinar el comportamiento termodinámico de sistemas complejos, depende en gran medida de cómo de preciso es el modelo matemático utilizado para describir las moléculas que conforman el sistema y sus interacciones, es decir, como de exacta es la descripción de la estructura química de los modelos utilizados, así como sus interacciones intramoleculares e intermoleculares. La necesidad de tener un modelo capaz de describir de forma precisa las moléculas bajo estudio, se incrementa en el caso de que el sistema no se trate de un sistema puro, sino de un sistema mezcla, en donde ya no solo existen interacciones entre moléculas de una misma especie, sino entre moléculas de especies distintas. Esta necesidad también se ve incrementada cuando se trata de obtener las propiedades interfaciales del sistema bajo estudio. Estas propiedades y, en particular, la tensión interfacial, son extremadamente sensibles a los detalles moleculares de los modelos, lo que permite, siempre que haya resultados experimentales disponibles, que sean usadas para comprobar la capacidad de predicción de los modelos moleculares utilizados. Determinar el grado de detalle de un modelo molecular para obtener resultados precisos y una representación físicamente realista del sistema bajo estudio, mientras se mantiene un compromiso con la potencia de cálculo necesaria, es el primer paso tanto para la simulación molecular como para los formalismos teóricos.

Resumiendo, y como ya hemos dicho anteriormente, existe un creciente interés en las propiedades termodinámicas de los hidratos de gas por sus posibles aplicaciones, tanto desde un punto de vista energético como medioambiental. Estas propiedades pueden ser ampliamente modificadas al añadir aditivos que pueden actuar como promotores de hidratos, ayudando a la formación de estos, o como inhibidores, evitando su formación. El THF y la familia de 1-alcanoles, en concreto los 1-alcanoles lineales, han demostrado ser unos excelentes aditivos para alterar las propiedades termodinámicas y el equilibrio de fases de los hidratos. Pese a ser compuestos comunes y ampliamente utilizados desde un punto de vista industrial, existen pocos trabajos acerca de las propiedades y del modelado de estos compuestos. El objetivo de esta tesis doctoral ha sido el estudio de las propiedades interfaciales y de los equilibrios de fases de estos compuestos y de algunas de sus mezclas mediante simulación molecular, teoría y experimentos, como se verá en mayor detalle en el siguiente apartado.

1.2 Organización de la Tesis y Objetivos

Esta tesis doctoral ha sido organizada en un total de 10 capítulos. En este capítulo, se realiza una introducción para contextualizar las motivaciones que han llevado a realizar este trabajo, así como de la bibliografía principal de apoyo y una descripción de la estructura de la tesis. En los **Capítulo 2-4** se hace una pequeña introducción a los conceptos básicos de la Mecánica Estadística (**Capítulo 2**), una breve descripción de los fundamentos básicos de la dinámica molecular y de alguna de las técnicas básicas empleadas en simulación (**Capítulo 3**) y una breve explicación de los orígenes y los conceptos básicos de la ecuación de estado SAFT (**Capítulo 4**). En los **Capítulo 5-10** se expondrán

los resultados obtenidos y publicados durante la realización de esta tesis doctoral. Cada capítulo consistirá en un artículo ya publicado, como se explica a continuación:

Capítulo 5: Understanding the phase behaviour of tetrahydrofuran + carbon dioxide, + methane, and + water binary mixtures from the SAFT-VR approach. J. M. Míguez, M. M. Piñeiro, J. Algaba, B. Mendiboure, J.-P. Torré y F. J. Blas *Journal of Physical Chemistry B*, **119**, 14288-14302 (2015).

En este primer trabajo, se estudió el diagrama de fases a altas presiones de las mezclas binarias de THF(1) + CO_2(2), CH_4(2), y + H_2O(2) usando la ecuación de estado SAFT-VR. Con este trabajo se consiguió una primera aproximación en la obtención de los diagramas de fases de las mezclas binarias del promotor de hidratos THF con H_2O (que constituye la estructura cristalina del hidrato) y con CH_4 y CO_2 (dos moléculas huésped del hidrato de gran interés). Las presiones, temperaturas, densidades y composiciones de equilibrio de estas mezclas binarias obtenidas de forma teórica mediante la ecuación de estado SAFT-VR serán utilizadas en varios trabajos posteriores como punto de partida de las simulaciones realizadas y de los experimentos.

Capítulo 6: On interfacial properties of tetrahydrofuran: atomistic and coarse-grained models from molecular dynamic simulations. J. M. Garrido, J. Algaba, J. M. Míguez, B. Mendiboure, A. I. Moreno-Ventas Bravo, M. M. Piñeiro y F. J. Blas *Journal of Chemical Physics*, **144**, 144702-10 (2016).

Como hemos dicho anteriormente, pese a que el THF ha sido ampliamente utilizado tanto como promotor de hidratos como disolvente en un gran número de procesos industriales, no existen muchos modelos moleculares en la literatura. En este trabajo se comprobó la habilidad de distintos modelos de THF presentes en la literatura para determinar sus propiedades interfaciales mediante simulación directa de la interfase líquido-vapor. El THF fue modelado usando seis modelos diferentes, tres de ellos basados en la aproximación de átomos-unidos (uno de ellos propuesto por nosotros) y los otros tres se basaron en la aproximación de coarse-grained (CG), siendo en este último caso modelado como una esfera, un dímero y un anillo de tres miembros. Los resultados obtenidos fueron comparados con resultados experimentales tomados de la literatura.

Capítulo 7: Measurement and modeling of high pressure density and interfacial tension of carbon dioxide plus tetrahydrofuran mixture. J. Matías Garrido, M. Cartes, A. Mejía, J. Algaba, J. M. Míguez, F. J. Blas, I. Moreno-Ventas Bravo y M. M. Piñeiro *Journal of Supercritical Fluids*, **128**, 359-369 (2017).

En este trabajo se estudió, de forma experimental, el equilibrio de fases líquido-vapor de la mezcla binaria THF+CO_2 a dos temperaturas (298.15 y 353.15 K) y elevadas presiones. De forma experimental se obtuvieron los valores de la tensión interfacial y las densidades de coexistencia, a partir de los cuales se obtuvieron las isotermas de adsorción relativa de Gibbs. Además, se aplicó la Teoría del Gradiante Cuadrado o SGT (del inglés *Square Gradient Theory*) para calcular los perfiles de la densidad y las tensiones interfaciales mediante el modelado del comportamiento interfacial de la mezcla binaria.

Capítulo 8: Interfacial Properties of Tetrahydrofuran and Carbon Dioxide Mixture from Computer Simulation. J. Algaba, J. Matías Garrido, J. M. Míguez, A. Mejía, A. I. Moreno-Ventas Bravo y F. J. Blas *Journal of Physical Chemistry C*, **122**, 16142-16153 (2018).

Usando los resultados previos adquiridos, teórica y experimentalmente, acerca del equilibrio de

fases y de las propiedades interfaciales de la mezcla binaria de THF+CO_2, se realizaron simulaciones en dinámica molecular utilizando un modelo rígido y un modelo flexible de THF TraPPE-UA (del inglés *Transferable Potentials for Phase Equilibria-United Atom*) estudiados previamente en el trabajo expuesto en el **Capítulo 6**. Se evaluó la habilidad de estos dos modelos para describir las propiedades interfaciales de la mezcla binaria al comparar los resultados obtenidos mediante simulación molecular con los resultados experimentales y las previsiones teóricas obtenidas con anterioridad.

Capítulo 9: Phase Equilibria and Interfacial Properties of the Tetrahydrofuran + Methane Binary Mixture from Experiment and Computer Simulation. J. Algaba, M. Cartes, A. Mejía, J. M. Míguez y F. J. Blas *Journal of Physical Chemistry C*, Enviado.

Continuando con el estudio de las mezclas binarias de THF, se determinó el diagrama presión-densidad y la tensión interfacial de la mezcla binaria de THF+CH_4 mediante experimentos a dos temperaturas (300.15 y 370.15K) y a varias presiones (desde 0.1 a 20 MPa). Además, se obtuvo el equilibrio de fases y las propiedades interfaciales de este sistema mediante simulación directa de la interfase líquido-vapor a las mismas condiciones termodinámicas a las que se realizaron los experimentos. Las simulaciones fueron realizadas con el modelo rígido de THF TraPPE-UA, el cual ha demostrado, en los trabajos anteriores, ser capaz de proporcionar los mismos resultados que su versión flexible (**Capítulo 6** y **8**). De nuevo, se compararon los resultados obtenidos mediante experimentos y simulación con las predicciones teóricas obtenidas con anterioridad.

Capítulo 10: Interfacial Properties of l-Alkanol (l-Butanol to l-Heptanol) + Water Binary Mixtures by Molecular Dynamics Simulatio. J. M. Míguez, J. Algaba y F. J. Blas. *Journal of Physical Chemistry C*, Enviado.

En este trabajo se estudió mediante simulación molecular el equilibrio líquido-líquido y las propiedades interfaciales de la mezcla binaria de 1-alcanoles lineales (desde el 1-butanol hasta el 1-heptanol) con agua. Como ya se ha explicado anteriormente, este tipo de alcanoles pueden ser empleados como inhibidores de hidratos, por lo que este estudio puede considerarse un paso previo al estudio de como se ven afectadas las propiedades interfaciales y los equilibrios de las fases de los sistemas hidratos en presencia de estos alcanoles. Las distinas mezclas de 1-alcanol + agua fueron estudiadas a presión atmosférica y a diferentes temperaturas (desde 280 a 380 K). Las simulaciones se llevaron a cabo en dinámica molecular. La familia de 1-alcanoles lineales fue modelada utilizando la aproximación de átomos-unidos y los parametros de potencial del campo de fuerzas TraPPE. Para el agua se utilizó el conocido modelo TIP4P-2005. Los resultados obtenidos en este trabajo fueron comparados con datos experimentales tomados de la literatura.

Bibliography

[1] E. Sloan *Nature*, vol. 426, pp. 353–363, 2003.

[2] E. D. Sloan and C. Koh, *Clathrate Hydrates of Natural Gases, 3rd ed.* CRC Press, New York, 2008.

[3] K. McMullan and G. A. Jeffrey *J. Chem. Phys.*, vol. 42, pp. 2725–2733, 1965.

[4] T. W. Mak and R. K. McMullan *J. Chem. Phys.*, vol. 42, pp. 2732–2737, 1965.

[5] J. A. Ripmeester, J. S. Tse, C. I. Ratcliffe, and B. M. Powell *Nature*, vol. 325, pp. 135–136, 1987.

[6] Y. F. Makogon, *Hydrates of Hydrocarbon.* Pennwell Publishing Co.:Tulsa, OK, 1997.

[7] A. D. J. MacKerell *J. Phys. Chem.*, vol. 99, pp. 1846–1855, 1995.

[8] D. D. Link, E. P. Ladner, H. A. Elsen, and C. E. Taylor *Fluid Phase Equilib.*, vol. 211, pp. 1–10, 2003.

[9] W. Lin, G.-J. Chen, C.-Y. Sun, X.-Q. Guo, Z.-K. Wu, M.-Y. Liang, L.-T. Chen, and L.-Y. Yang *Chem. Eng. Sci.*, vol. 59, pp. 4449–4455, 2004.

[10] R. Kumar, P. Linga, J. A. Ripmeester, and P. Englezos *J. Environ. Eng.*, vol. 135, pp. 411–417, 2009.

[11] P. Linga, A. Adeyemo, and P. Englezos *Environ Sci. Technol.*, vol. 42(1), pp. 315–320, 2007.

[12] X. S. Li, C. G. Xu, Z. Y. Chen, and J. Cai *Int. J. Hydrogen Energ.*, vol. 37, pp. 720–727, 2012.

[13] N. Daraboina, J. A. Ripmeester, and P. Englezos *Int. J. Greenh. Gas Con.*, vol. 15, pp. 97–103, 2013.

[14] R. Larsen, C. A. Knight, and E. D. Sloan *Fluid Phase Equilib.*, vol. 150, p. 353, 1998.

[15] J.-P. Torré, D. Haillot, S. Rigal, R. W. de Souza Lima, C. Dicharry, and J.-P. Bedecarrats *Chem. Eng. Science*, vol. 126, pp. 688–697, 2015.

[16] T. Makino, T. Sugahara, and K. Ohgaki *J. Chem. Eng. Data*, vol. 50, pp. 2058–2060, 2005.

[17] L. J. Florusse, C. J. Peters, J. Schoonman, K. C. Hester, C. A. Koh, S. F. Dec, K. N. Marsh, and E. D. Sloan *Science*, vol. 306, pp. 469–471, 2004.

[18] H. Lee, J. W. Lee, D. Y. Kim, J. Park, Y. T. Seo, H. Zeng, I. L. Moudrakovski, C. I. Ratcliffe, and J. A. Ripmeester *Nature*, vol. 434, pp. 743–746, 2005.

[19] T. A. Strobel, C. A. Koh, and E. D. Sloan *Fluid Phase Equilib.*, vol. 261, p. 382, 2007.

[20] H. P. Veluswamy, R. Kumar, and P. Linga *Appl. Energy*, vol. 122, p. 112, 2014.

[21] R. K. Pachauri and L. Meyer, eds., *IPCC, 2014: Climate Change 2014: Synthesis Report. Contribution of Working Groups I, II and III to the Fifth Assessment Report of the Intergovernmental Panel on Climate Change.* IPCC, Geneve, Switzerland, 2014.

[22] B. Gwinner, D. Roizard, F. Lapicque, E. Favre, R. Cadours, P. Boucot, and P. L. Carrette *Ind. Eng. Chem. Res.*, vol. 45(14), pp. 5044–5049, 2006.

[23] M. G. Plaza, S. Garcia, F. Rubiera, J. J. Pis, and C. Pevida *J. Chem Eng.*, vol. 163(1-2), pp. 41–47, 2010.

[24] E. Favre, D. Roizard, R. Bounaceur, and W. J. Koros, *Reverse Selective Gas Separation Membranes: Technological Opportunities and Scientific Challenges.* Elsevier Science BV, Amsterdam, 2009.

[25] F. Anderson and J. Prausnitz *AIChE journal*, vol. 32(8), pp. 1321–1333, 1986.

[26] M. M. Ghiasi, A. Bahadori, S. Zendehboudi, A. Jamili, and S. Rezaei-Gomari *J. Nat. Gas Sci. Eng.*, vol. 15, pp. 69–75, 2013.

[27] P. G. Lafond, K. A. Olcott, E. D. Sloan, C. A. Koh, and A. K. Sum *J. Chem. Thermodyn.*, vol. 48, pp. 1–6, 2012.

[28] A. H. Mohammadi, W. Afzal, and D. Richon *J. Chem. Eng. Data*, vol. 53(3), pp. 683–686, 2008.

[29] A. H. Mohammadi and D. Richon *Ind. Eng. Chem. Res.*, vol. 49(18), pp. 8865–8869, 2010.

[30] P. Notz, S. Bumgardner, B. Schaneman, J. Todd, *et al. SPE Production & Facilities*, vol. 11(4), pp. 256–260, 1996.

[31] X.-S. Li, H.-J. Wu, and P. Englezos *Ind. Eng. Chem. Res.*, vol. 45(6), pp. 2131–2137, 2006.

[32] C. W. Foo, L. Ruan, and X. Lou *J. Nat. Gas Sci. Eng.*, vol. 35, pp. 1587–1593, 2016.

[33] A. H. Mohammadi, W. Afzal, and D. Richon *J. Chem. Eng. Data*, vol. 53(1), pp. 73–76, 2007.

[34] R. Anderson, A. Chapoy, H. Haghighi, and B. Tohidi *J. Phys. Chem. C*, vol. 113(28), pp. 12602–12607, 2009.

[35] K. Yasuda, S. Takeya, M. Sakashita, H. Yamawaki, and R. Ohmura *J. Phys. Chem. C*, vol. 113(28), pp. 12598–12601, 2009.

[36] J.-W. Lee and S.-P. Kang *J. Phys. Chem. B*, vol. 116(1), pp. 332–335, 2011.

[37] A. Chapoy, R. Anderson, H. Haghighi, T. Edwards, and B. Tohidi *Ind. Eng. Chem. Res.*, vol. 47(5), pp. 1689–1694, 2008.

[38] Y. Lee, S. Lee, Y. K. Jin, and Y. Seo *Chem. Eng. J.*, vol. 258, pp. 427–432, 2014.

[39] H. Cárdenas, M. Cartes, and A. Mejía *Fluid Phase Equilibr.*, vol. 396, pp. 88 – 97, 2015.

[40] W. G. Chapman, K. E. Gubbins, G. Jackson, and M. Radosz *Fluid Phase Equil.*, vol. 52, pp. 31–38, 1989.

[41] W. G. Chapman, K. E. Gubbins, G. Jackson, and M. Radosz *Ind. Eng. Chem. Res.*, vol. 29(8), pp. 1709–1721, 1990.

[42] M. S. Wertheim *J. Stat. Phys.*, vol. 35(1-2), pp. 19–34, 1984.

[43] M. S. Wertheim *J. Stat. Phys.*, vol. 35(1-2), pp. 35–47, 1984.

[44] M. S. Wertheim *J. Stat. Phys.*, vol. 42(3-4), pp. 459–476, 1986.

[45] M. S. Wertheim *J. Stat. Phys.*, vol. 42(3-4), pp. 477–492, 1986.

[46] F. J. Blas and L. F. Vega *Mol. Phys.*, vol. 92, p. 135, 1997.

[47] F. J. Blas and L. F. Vega *Ind. Eng. Chem. Res.*, vol. 37(2), p. 660, 1998.

[48] J. Gross and G. Sadowski *Ind. Eng. Chem. Res.*, vol. 41, no. 5, pp. 1084–1093, 2002.

[49] Georgios M. Kontogeorgis, Epaminondas C. Voutsas, Iakovos V. Yakoumis, and Dimitrios P. Tassios *Ind. Eng. Chem. Res.*, vol. 35(11), pp. 4310–4318, 1996.

[50] M. M. P. T. Lafitte and J. L. Daridon *J. Chem. Phys.*, vol. 124, pp. 024509/1–16, 2006.

[51] A. Gil-Villegas, A. Galindo, P. J. Whitehead, S. J. Mills, G. Jackson, and A. N. Burgess *J. Chem. Phys.*, vol. 106, pp. 4168–4186, 1997.

[52] A. Galindo, L. A. Davies, A. Gil-Villegas, and G. Jackson *Mol. Phys.*, vol. 93, pp. 241–252, 1998.

[53] B. Giner, F. M. Royo, C. Lafuente, and A. Galindo *Fluid Phase Equil.*, vol. 255, p. 200, 2007.

[54] B. Giner, I. Gascón, H. Artigas, C. Lafuente, and A. Galindo *J. Phys. Chem. B*, vol. 111(32), pp. 9588–9597, 2007.

[55] B. Giner, I. Bandrés, M. C. López, C. Lafuente, and A. Galindo *J. Chem. Phys.*, vol. 127(14), p. 144513, 2007.

[56] J. M. Míguez, M. C. D. Ramos, M. M. Piñeiro, and F. J. Blas *J. Phys. Chem. B*, vol. 115, p. 9604, 2011.

[57] T. Lafitte, A. Apostolakou, C. Avendaño, A. Galindo, C. S. Adjiman, E. A. Müller, and G. Jackson *J. Chem. Phys.*, vol. 139, p. 154504, 2013.

[58] J. S. Rowlinson and F. L. Swinton, *Liquids and Liquid Mixtures.* Butterworth, London, 1982.

[59] J. S. Rowlinson and B. Widom, *Molecular Theory of Capillarity.* Claredon Press, 1982.

[60] D. Henderson, *Fundamentals of Inhomogeneous Fluids.* Dekker, New York, 1992.

[61] H. T. Davis, *Statistical Mechanics of Phases, Interfaces, and Thin Films.* VCH, Weinheim, 1996.

[62] D. Frenkel and B. Smit, *Understanding Molecular Simulations.* 2nd Ed. Academic, San Diego, 2002.

Parte II

Metodología

Capítulo 2

Mecánica Estadística

El objetivo de la Mecánica Estadística consiste en servir de puente de unión entre las características y propiedades microscópicas de un sistema y el comportamiento macroscópico del mismo [1–4]. El número de variables necesarias para definir el estado macroscópico, o macroestado, de un sistema cerrado en equilibrio vendrá dado por la regla de las fases de Gibbs, la cual establece que el número de variables termodinámicas independientes (L) necesarias para definir el macroestado de un sistema cerrado, dependerá del número de fases en equilibrio (F) y del número de componentes químicos (C) mediante la siguiente relación:

$$L = C - F + 2 \tag{2.1}$$

Así, por ejemplo, un sistema puro constituido por una única fase podría quedar definido en función del número de moléculas que lo componen, N, y su temperatura, T, obteniéndose el resto de variables termodinámicas mediante las ecuaciones de estado. Por el contrario, para definir el estado microscópico de un sistema, o microestado, desde el punto de vista de la Mecánica Clásica, sería necesario especificar la posición y velocidad de cada una de las partículas que lo componen. Resulta evidente, por tanto, la diferencia en el número de parámetros necesarios para describir un microestado, con respecto al número necesario para describir un macroestado. La Mecánica Estadística permite a partir de una descripción microscópica detallada de un sistema, conocer su comportamiento macroscópico.

2.1 Postulados Básicos de la Mecánica Estadística

Un sistema químico cualquiera esta constituido por un número de partículas del orden del número de Avogadro ($6.022{\cdot}10^{23}$). Si por simplicidad suponemos que las partículas no tienen grados internos de libertad, la Mecánica Clásica especifica el estado dinámico de cada partícula mediante los momentos lineales y las coordenadas, quedando el estado microscópico del sistema total definido por el conjunto de momentos y coordenadas, es decir por un punto en un espacio de $6N$ dimensiones. Este espacio se denomina el espacio de las fases. Sin embargo, como ya hemos dicho, para especificar el estado macroscópico de un sistema, desde el punto de vista de la Termodinámica, solo serán necesarios

unos poco parámetros. Es decir, la descripción de un estado macroscópico es insuficiente para la determinación de un estado microscópico. Si se considera un sistema en equilibrio, entendiéndose por sistema en equilibrio aquel cuyas propiedades macroscópicas no varían a lo largo del tiempo y que por tanto puede ser definido por un reducido número de variables termodinámicas que permanecen constantes, se puede observar como a ese único macroestado le corresponde un elevado número de microestados compatibles. Desde el punto de vista de la Mecánica Estadística, cada microestado compatible con un macroestado dado será accesible para el sistema con una cierta probabilidad. Dado que se está utilizando una descripción clásica para describir al sistema y que en la Mecánica Clásica las coordenadas generalizadas q_i y los momentos generalizados p_i son variables continuas, lo que la Mecánica Estadística va a postular es que a cada sistema macroscópico le corresponde una función de densidad de probabilidad para las variables coordenadas y momentos generalizados, es decir una función *densidad de probabilidad* en el espacio de las fases [1–4]. Así pues, en el caso más general va a postular una función de la forma

$$\rho(q_i, p_i; t) = \rho(q, p; t) \tag{2.2}$$

de manera que, por la definición de densidad de probabilidad,

$$\rho(q_i, p_i; t) dq_1 \cdots dq_f \; dp_1 \cdots dp_f \equiv \rho(q, p; t) dq dp \tag{2.3}$$

representa la probabilidad de que en un instante t dado, el sistema se encuentre en un volumen infinitesimal del espacio fásico centrado en (q, p), donde $dqdp$ viene dado por

$$dpdq \equiv dq_1 \cdots dq_f \; dp_1 \cdots dp_f \tag{2.4}$$

De acuerdo con esta definición, $\rho(q, p; t)$ deberá, en todo instante, cumplir la condición de normalización

$$\int dpdq \; \rho(q, p; t) = 1 \tag{2.5}$$

Nótese que $\rho(q, p; t)$ debe de ser nula para aquellos valores de q, p y t que lleven a un microestado no compatible con el macroestado en el que se encuentra el sistema.

Como ya se ha dicho, para un macroestado dado existe un elevado número de posibles microestados accesibles para el sistema, cada uno de ellos con valores distintos de q y p. Así pues, si consideramos una variable, $A(q, p)$, que sea función de las coordenadas generalizadas q y de los momentos generalizados p, como es el caso de la energía, a cada microestado le corresponderá un valor diferente de $A(q, p)$. Esto nos lleva al primer postulado establecido por la Mecánica Estadística [1–4] que establece la relación entre el valor de $A(q, p)$ en cada uno de los microestados y el valor de A en el sistema macroscópico.

Primer Postulado: los valores de los parámetros macroscópicos que definen el estado de un sistema son iguales a los valores medios, sobre el conjunto de microestados asociados, de la correspondiente magnitud microscópica.

$$\langle A(t) \rangle = \int dpdq \; \rho(q, p; t) \; A(q, p) \tag{2.6}$$

El peso que tiene el valor de la variable $A(q,p)$ de un microestado dado dependerá del grado de accesibilidad de dicho microestado, es decir, de la probabilidad de que el sistema se encuentre en él. Si el sistema presenta una función de distribución de probabilidades independiente del tiempo (en equilibrio), y además no puede intercambiar ni materia ni energía con sus alrededores (se encuentra aislado), la probabilidad de que se encuentre en un microestado o en otro viene dado por *el postulado de igualdad de probabilidades a priori* de la Mecánica Estadística [1–4]:

Segundo Postulado: A un estado de equilibrio macroscópico de un **sistema aislado** le corresponde una descripción microscópica en la que todos los microestados accesibles al sistema son igualmente probables.

Esto quiere decir que todos los microestados accesibles por el sistema contribuirán de igual modo en el promedio de la obtención de la variable macroscópica A. Además, como consecuencia de este postulado, si esta igualdad de probabilidades se cumple para un instante dado, también se mantendrá en cualquier otro instante de tiempo. De este modo se estable la igualdad entre un gran número de medidas realizadas en distintos instantes sobre un único sistema y la medición en un instante dado sobre un gran número de sistemas idénticos. En otras palabras, se establece que el promedio de una propiedad realizada sobre los diversos microestados accesibles para el sistema, ver ecuación (2.6), será igual al promedio temporal de la correspondiente magnitud termodinámica.

$$\overline{A(t)} = \lim_{x\to\infty} \frac{1}{t} \int A(t')dt' \tag{2.7}$$

La ecuación anterior constituye la conocida Hipótesis Ergódica, establecida por Paul y Tania Ehrenfest [5]. Esta equivalencia, aunque razonable, no puede ser demostrada y ha sufrido numerosas reformulaciones, como su versión moderna en el teorema de Birkhoff [6], siendo realmente complejo establecer si un sistema es o no ergódico. Sin embargo, pese a que no puede ser demostrada, se acepta en cuanto que conduce a resultados correctos y se puede intentar racionalizar considerando que el tiempo necesario para llevar a cabo una medida de una propiedad macroscópica es grandísimo en comparación con el tiempo que tarda el sistema en pasar de un microestado a otro. Por tanto, se puede suponer que durante la medición, el sistema ha podido transitar por todos los microestados compatibles con el macroestado dado, permaneciendo en cada uno de ellos un tiempo proporcional a la probabilidad de ocupación de ese microestado, que para el caso de un sistema en equilibrio, es la misma para todos los microestados accesibles. De esta forma, la hipótesis ergódica elimina la variable temporal y es asumida en el estudio de sistemas en equilibrio, mediante simulación molecular, en el marco de la Mecánica Estadística del equilibrio [1–4, 7].

2.2 Colectivos de Gibbs

Un colectivo es un conjunto formado por un número muy grande de sistemas, todos los cuales se encuentran en el mismo estado termodinámico. Esta idea de asociar a cada macroestado de un sistema un conjunto de microestados con una distribución de probabilidades es debida a Gibbs, y el conjunto de réplicas macroscópicamente iguales con su distribución de probabilidades recibe el nombre de *conjunto o colectivo de Gibbs*. Para mayor simplicidad, se va a considerar únicamente sistemas que se encuentran en equilibrio termodinámico y, que por tanto, les corresponde una función de distribución de probabilidades independiente del tiempo.

La teoría de colectivos se basa en obtener las variables macroscópicas del sistema a partir del análisis estadístico de los microestados que conforman el colectivo. Para ello, Gibbs desarrolló una serie de formalismos que permiten calcular un conjunto completo de variables termodinámicas de un sistema dado, a partir de propiedades puramente mecánicas de sus componentes microscópicos. Estos formalismos dependerán del tipo de variables termodinámicas que definan al macroestado. El estado termodinámico de un sistema simple puede establecerse dando valor a tan solo tres variables termodinámicas: una elegida de cada una de las tres parejas $\{N, \mu\}$ (número de partículas o potencial químico), $\{V, p\}$ (volumen o presión), y $\{E, T\}$ (energía interna o temperatura). Cada pareja está formada por una variable extensiva y otra intensiva. Existen, por lo tanto, ocho formas diferentes de definir el estado termodinámico de los sistemas simples que forman el colectivo. Los dos colectivos de mayor interés a la hora de describir el comportamiento de sistemas reales son el colectivo canónico, o colectivo NVT, y el colectivo isotérmico-isobárico, o colectivo NPT.

2.2.1 Colectivo Canónico (NVT)

En el colectivo canónico, el sistema bajo estudio se encuentra aislado del exterior mediante una pared rígida e impermeable en contacto con un baño térmico externo a temperatura T, que asegura que la temperatura y el volumen del sistema permanezcan constantes. Este colectivo tiene especial interés debido al elevado número de experimentos con sistemas reales que suceden en estas condiciones. La densidad de probabilidad para este colectivo viene dado por

$$\rho(\mathbf{r}^N, \mathbf{p}^N) = \frac{\exp\left[-\beta\mathcal{H}(\mathbf{p}^N, \mathbf{r}^N)\right]}{N!h^{3N}} \, {Q_{NVT}}^{-1} \tag{2.8}$$

donde $\beta = (k_B T)^{-1}$, siendo k_B la constante de Boltzmann, el factor h es la constante de Planck, y $\mathcal{H}$ y Q_{NVT} son el Hamiltoniano del sistema y la función de partición del colectivo NVT respectivamente, y pueden expresarse como

$$\mathcal{H}(p, q) = \sum_{i=1}^{f} \frac{p_i^2}{2m} + \mathcal{U}(q) \tag{2.9}$$

y

$$Q_{NVT} = \frac{1}{N!h^{3N}} \int d\mathbf{p}^N d\mathbf{r}^N \exp\left[-\beta\mathcal{H}(\mathbf{p}^N, \mathbf{r}^N)\right] \tag{2.10}$$

La constante de Planck aparece debido a que, según el principio de incertidumbre de Heisenberg, es imposible conocer con exactitud la posición y la cantidad de movimiento de una partícula simultáneamente ($\Delta p_i \Delta q_i \geq h$). Esto resulta en que la mayor precisión a la que se puede llegar al describir el estado de un sistema, desde un punto de vista semiclásico, es a indicar que este se encuentra dentro de un cierto volumen del espacio fásico del orden de h^{3N}, dónde, $3N$ es el grado de números de libertad del sistema.

A partir de la función de partición se pueden expresar las propiedades macroscópicas del sistema. Así pues, si consideramos una variable, $A(q, p)$, que sea función de las coordenadas generalizadas q y de los momentos generalizados p, está podrá ser expresada como

$$\langle A \rangle_{NVT} = \frac{\int d\mathbf{p}^N d\mathbf{r}^N A(\mathbf{p}^N, \mathbf{r}^N) \exp\left[-\beta \mathcal{H}(\mathbf{p}^N, \mathbf{r}^N)\right]}{\int d\mathbf{p}^N d\mathbf{r}^N \exp\left[-\beta \mathcal{H}(\mathbf{p}^N, \mathbf{r}^N)\right]} \tag{2.11}$$

La expresión (2.11) puede escribirse de forma más compacta utilizando la función de partición

$$\langle A \rangle_{NVT} = -\frac{1}{Q_{NVT}} \frac{\partial Q_{NVT}}{\partial \beta} = -\frac{\partial \ln Q_{NVT}}{\partial \beta} \tag{2.12}$$

Para este colectivo, la energía libre de Helmholtz *F(N,V,T)* es la función de estado natural para establecer el nexo de unión entre la descripción microscópica y el estado termodinámico del sistema

$$F(N, V, T) = -k_B T \ln Q_{NVT} \tag{2.13}$$

Todas las propiedades termodinámicas de equilibrio pueden se calculadas a partir de la derivada parcial apropiada de la energía libre de Helmholtz sobre alguno de sus parámetros utilizando las relaciones de Maxwell

$$\left(\frac{\partial F}{\partial V}\right)_{T,N} = -P, \left(\frac{\partial F}{\partial T}\right)_{V,N} = -S, \left(\frac{\partial F}{\partial N}\right)_{V,T} = \mu \tag{2.14}$$

2.2.2 Colectivo Isotérmico-Isobárico (NPT)

Del mismo modo que resulta interesante mantener el número de moléculas, la temperatura y el volumen constante, como ocurría en el colectivo NVT, resulta igualmente interesante el estudio de sistemas donde en lugar de fijar su volumen, se fija su presión. Existe una basta cantidad de fenómenos que ocurren a presión constante (como por ejemplo a presión atmosférica). Es por ello que el colectivo isotérmico-isobárico, o NPT, en el que se fija el número de moléculas, la presión y la temperatura resulta de gran interés. Para este colectivo, la función de partición viene dada por

$$Q_{NPT} = \frac{\beta P}{N! \Lambda^{3N}} \int dV\, V^N \exp(-\beta P V) \int d\mathbf{s}^N \exp\left[-\beta \mathcal{U}(\mathbf{s}^N; L)\right] \tag{2.15}$$

Esta expresión puede escribirse de forma más compacta usando la función de partición del colectivo canónico del siguiente modo

$$Q_{NPT} = \int dV \exp(-\beta P V) Q_{NVT} \tag{2.16}$$

Y al igual que en el caso anterior, puede ser utilizada para expresar las propiedades macroscópicas del sistema, siendo en este caso la energía libre de Gibbs, G, la función de estado natural usada para establecer el nexo de unión entre la descripción microscópica del sistema y sus propiedades termodinámicas

$$G = -k_B T \ln Q_{NPT} \tag{2.17}$$

De nuevo todas las propiedades termodinámicas de equilibrio pueden se calculadas a partir de la derivada parcial apropiada de la energía libre de Gibbs sobre alguno de sus parámetros

$$\left(\frac{\partial G}{\partial T}\right)_{P,N} = -S,\ \left(\frac{\partial G}{\partial P}\right)_{T,N} = V,\ \left(\frac{\partial G}{\partial N}\right)_{T,P} = \mu \tag{2.18}$$

Al igual que en el colectivo NVT y en el colectivo NPT, se puede escoger una propiedad termodinámica que sirva de nexo de unión entre la descripción microscópica y el estado termodinámico del sistema para el resto de los colectivos, obteniéndose esta equivalencia mediante esquemas basados en la función de densidad de probabilidad muy similares a los dos anteriormente descritos. De esta forma, se estable la unión entre el mundo macroscópico y el mundo microscópico, pudiendo describir el comportamiento termodinámico de un sistema mediante una descripción mecano-clásica del comportamiento de las partículas que lo componen.

Bibliography

[1] J. de la Rubia Pacheco and J. J. B. Abalo, *Introducción a la Mecánica Estadística*. Ediciones del Castillo, 1978.

[2] F. Reif, *Fundamentals of Statistical and Thermal Physics*. McGraw-Hill, 1965.

[3] D. McQuarrie, *Statistical Mechanics*. Harper & Row, 1976.

[4] P. Attard, *Thermodynamics and Statistical Mechanics: Equilibirium by Entropy Maximisation*. Academic Press, 2002.

[5] P. Ehrenfest and T. Ehrenfest, *The Conceptual Foundations of the Statistical Approach in Mechanics*. Dover Publications, 2002.

[6] G. D. Birkhoff *Proc. Natl. Acad. Sci.*, vol. 17, p. 656, 1931.

[7] D. Frenkel and B. Smit, *Understanding Molecular Simulations*. 2nd ed. Academic, San Diego, 2002.

Capítulo 3

Simulación Molecular

Los métodos de simulación molecular son una poderosa herramienta aplicada en distintas áreas de la ciencia con el fin de estudiar el comportamiento microscópico de las moléculas que componen el sistema. La simulación molecular aporta una valiosa información acerca de las estructuras que adoptan las moléculas debido a las interacciones intramoleculares e intermoleculares, sobre la dinámica de ciertos procesos que suceden en una escala de tiempo tan pequeña que no pueden ser observados en un experimento, o simplemente aportan una mayor claridad acerca del comportamiento del sistema. Dentro de los métodos de simulación molecular, la dinámica molecular y el método de Monte Carlo constituyen los métodos de simulación molecular más ampliamente utilizados. En este capítulo se hará una breve descripción sobre el método de dinámica molecular, el cual ha sido utilizado en este trabajo para el estudio de las propiedades interfaciales y el equilibrio de fases de varios sistemas reales, y sobre algunas de las técnicas más empleadas en simulación molecular.

3.1 Dinámica Molecular

La dinámica molecular, MD, (del inglés, *molecular dynamics*) es un tipo de simulación molecular computacional que permite analizar el comportamiento o evolución de un sistema a través del tiempo, calculando las fuerzas entre las partículas que lo conforman y resolviendo las ecuaciones del movimiento de Newton. Esta técnica permite calcular las trayectorias de los átomos o partículas que forman un sistema macroscópico en distintos instantes de tiempo, obteniéndose un conjunto de posiciones y velocidades que corresponden a un muestreo del espacio de fase del sistema, simulando así su comportamiento microscópico. A partir de esta información y haciendo uso de la Mecánica Estadística, como hemos visto en el capítulo anterior, podemos obtener propiedades termodinámicas macroscópicas del sistema.

Conocida una configuración inicial del sistema, es decir, las posiciones, $\mathbf{r}$ y velocidades, $\mathbf{v}$, de cada una de las partículas que lo componen, es posible predecir las posiciones y velocidades en un instante futuro mediante la resolución de las ecuaciones de movimiento de Newton. Para un sistema de N partículas las ecuaciones de Newton vienen dadas por:

$$m_i \frac{d^2\mathbf{r}_i}{dt^2} = \mathbf{F}_i,\ i = 1...N. \tag{3.1}$$

$$\mathbf{v}_i = \frac{d\mathbf{r}_i}{dt} \tag{3.2}$$

siendo $\mathbf{F}_i$ la fuerza total que actúa sobre la partícula i. Si las fuerzas que actúan sobre la partícula i son conservativas, estas pueden ser calculadas en función del gradiente de la energía potencial (U):

$$\mathbf{F}_i = \nabla U \tag{3.3}$$

3.1.1 Integradores numéricos

Las ecuaciones de movimiento de Newton no tienen resolución analítica, pero pueden ser resueltas de forma numérica. Para ello, en primer lugar es necesario transformar la evolución temporal continua del sistema en una evolución discretizada, caracterizada por Δt, siendo éste el salto temporal, o paso de tiempo, que ocurre entre un estado microscópico del sistema y el siguiente. De esta forma se considera que la evolución en la dinámica del sistema ocurre en pequeños saltos de tiempo discretos, permitiendo así la resolución de las ecuaciones de Newton mediante métodos numéricos. Existen diversos algoritmos para la resolución de dichas ecuaciones. A la hora de escoger un algoritmo para la resolución numérica de estas ecuaciones, es importante tener en cuenta tanto la exactitud de los resultados que proporciona como la eficiencia y el rendimiento computacional. En este trabajo en concreto ha sido usado el algoritmo de leap-frog o de salto de rana [1, 2].

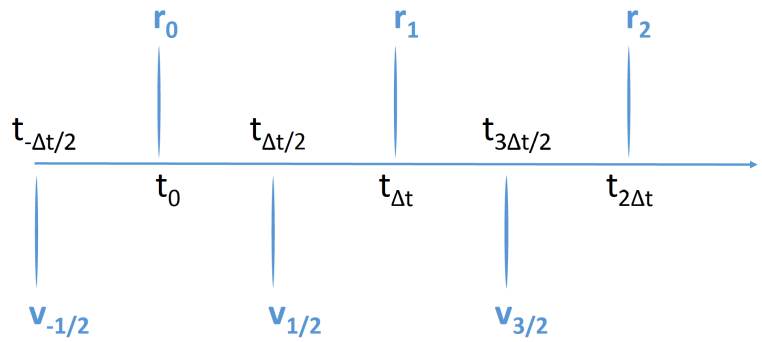

Figura 3.1: Representación visual de la obtención de las posiciones, $\mathbf{r}$, y las velocidades, $\mathbf{v}$, del sistema mediante el algoritmo del salto de rana

El algoritmo del salto de rana, figura 3.1, usa las posiciones $\mathbf{r}$ de un instante de tiempo t y las velocidades $\mathbf{v}$ de un instante de tiempo anterior, $t - 1/2\Delta t$, para obtener las velocidades en un instante de tiempo futuro, $t + 1/2\Delta t$, y finalmente, obtener las posiciones en el instante de tiempo $t + \Delta t$ mediante las siguientes relaciones:

$$\mathbf{v}(t + \frac{1}{2}\Delta t) = \mathbf{v}(t - \frac{1}{2}\Delta t) + \frac{\Delta t}{m}\mathbf{F}(t) \tag{3.4}$$

$$\mathbf{r}(t + \Delta t) = \mathbf{r}(t) + \Delta t \mathbf{v}(t + \frac{1}{2}\Delta t) \tag{3.5}$$

donde $\mathbf{F}(t)$ son las fuerzas que actúan sobre el sistema en el instante de tiempo t.

Durante el transcurso del paso de tiempo se considera que las fuerzas que actúan sobre cada partícula permanece constante. De esta manera, conociendo las posiciones de las partículas que componen nuestro sistema en un instante dado de tiempo, t, y sus velocidades en un instante anterior, $t - 1/2\Delta t$ podemos obtener las posiciones en un instante de tiempo futuro $t + \Delta t$. El salto de tiempo, Δt, debe de ser lo suficientemente pequeño para muestrear correctamente la evolución del sistema, siendo normalmente del orden de los femtosegundos.

Una vez calculadas las velocidades y posiciones del nuevo estado del sistema mediante la resolución de las ecuaciones de Newton, se vuelven a evaluar las fuerzas que actúan sobre cada una de las partículas y un nuevo ciclo de dinámica molecular comienza. Mediante la repetición de este proceso se obtiene la evolución temporal del sistema. Como ya se ha dicho, esta evolución temporal se produce de forma discretizada, es decir, el sistema avanza realizando pequeños saltos en el tiempo.

3.1.2 Termostato y Barostato

Como ya hemos dicho, mediante la resolución de las ecuaciones del movimiento de Newton se generan las trayectorias y velocidades de cada molécula que constituyen el sistema en diferentes instantes de tiempo. Si el sistema se encuentra cerrado y aislado del exterior mediante paredes rígidas, la resolución de estas ecuaciones genera una distribución de microestados correspondientes a un macroestado cuya energía permanece constante. Es decir, se estaría realizando la simulación de un sistema cuyo número de partículas (N), volumen (V) y energía (E) permanece constante a lo largo del tiempo, o lo que es lo mismo, se estaría realizando la simulación de un sistema en el colectivo microcanónico (NVE). Por desgracia, la mayoría de los experimentos con sustancias reales no ocurren en estas condiciones.

En lugar de fijar la energía total del sistema, resulta mucho más interesante y práctico fijar la temperatura. Para realizar una simulación a temperatura constante (como ocurre en los colectivos NVT y NPT), es necesario el uso de un termostato. El uso de un termostato en simulación molecular permite fijar la temperatura del sistema, lo que resulta de gran utilidad cuando se quiere estudiar el comportamiento de un sistema a una temperatura determinada. Entre los termostatos más usados se encuentran:

Termostato de Berendsen [3]. En este termostato, el sistema se encuentra acoplado a un baño térmico externo cuya temperatura se encuentra fijada a la temperatura de interés. En este caso, las velocidades de cada partícula serán reescaladas para ajustar la temperatura del sistema. El reescalado dependerá tanto del parámetro de acoplamiento, τ, como de la diferencia entre la temperatura real del sistema (T) y la temperatura del baño térmico (T_0).

$$\frac{dT(t)}{dt} = \frac{1}{\tau}(T_0 - T(t)) \tag{3.6}$$

Un inconveniente de este termostato es que, formalmente, el colectivo generado no es estrictamente un colectivo canónico debido a que no permite que la energía cinética pueda fluctuar.

Termostato de Reescalado de velocidades [4]. Este termostato es esencialmente igual al termostato de Berendsen más un término estocástico que asegura una correcta distribución de la energía cinética, la cual es regulada mediante la siguiente expresión

$$dK = (K_0 - K)\frac{dt}{\tau_T} + 2\sqrt{\frac{KK_0}{N_f}}\frac{dW}{\sqrt{\tau_T}} \tag{3.7}$$

donde K y K_0 son la energía cinética real del sistema y la energía cinética del sistema a la temperatura de referencia respectivamente, N_f es el número de grados de libertad y dW es un tipo de proceso estocástico que se usa para asegurar un correcto muestreo del colectivo canónico.

Termostato de Nosé-Hoover [5, 6]. Este termostato fue originalmente introducido por Nosé y posteriormente desarrollado por Hoover. La idea es introducir una variable dinámica ficticia de fricción, ξ, la cual acelera o disminuye la velocidad de las partículas hasta que la temperatura sea igual a la deseada

$$\frac{d^2\mathbf{r}_i}{dt} = \frac{\mathbf{F}_i}{m_i} - \frac{p\xi}{Q}\frac{d\mathbf{r}_i}{dt} \tag{3.8}$$

donde Q es el llamado parámetro de masas, el cual depende de la temperatura de referencia escogida, T_0, y del periodo de las fluctuaciones de temperatura en el equilibrio τ_T

$$Q = \frac{\tau_T^2 T_0}{4\pi^2} \tag{3.9}$$

y donde $p\xi$ es el momento asociado al parámetro de fricción ξ, el cual dependerá de la diferencia entre la temperatura real del sistema en el instante t y la temperatura de referencia

$$\frac{dp\xi}{dt} = (T(t) - T_0) \tag{3.10}$$

Las ecuaciones de movimiento modificadas por este termostato son reversibles en el tiempo y deterministas. Sin embargo, las fluctuaciones de temperatura que genera pueden llegar a ser casi periódicas.

De igual forma que resulta interesante fijar la temperatura de un sistema, puede ser igualmente interesante fijar la presión. En el colectivo isotérmico-isobárico o NPT, además de fijar el número de moléculas, también son fijadas la temperatura y la presión. Para fijar la presión a lo largo de una simulación será necesario el uso de un barostato. Entre los barostatos más usados se encuentran:

Barostato de Berendsen. [7] El algoritmo de Berendsen reescala las coordenadas y los vectores que forman la caja de simulación en cada paso de simulación mediante la matriz de reescalado μ

$$\mu_{ij} = \delta_{ij} - \frac{\Delta t}{3\tau_p}\beta_{ij}\left\{P_{0ij} - P_{ij}(t)\right\} \tag{3.11}$$

donde δ_{ij} vale 0 si $i \neq j$ y 1 si $i = j$, P_0 es la presión fijada, $P(t)$ es la presión del sistema en el instante de tiempo t y τ_p es la constante de tiempo del acoplamiento del barostato. Mediante este procedimiento, las velocidades no son ni reescaladas ni rotadas debido al cambio de tamaño y forma de la caja de simulación y no se puede asegurar que se este muestreando correctamente el colectivo NPT.

Barostato de Parrinello-Rahman. [8, 9] De forma similar al termostato de Nosé-Hoover, el barostato de Parrinello-Rahman ajusta la presión del sistema muestreando correctamente el colectivo

NPT. De nuevo, este barostato reescala las coordenadas y los vectores que forman la caja de simulación en cada paso de simulación mediante la matriz de reescalado $\mathbf{b}$

$$\frac{d\mathbf{b}^2}{dt^2} = V\mathbf{W}^{-1}\mathbf{b}'^{-1}(P - P_0) \tag{3.12}$$

donde V es el volumen de la caja y $\mathbf{W}$ es un parámetro matriz que determina la fuerza del acoplamiento. Mediante el uso de este barostato también son modificadas las ecuaciones de movimiento de la siguiente forma

$$\frac{d^2\mathbf{r}_i}{dt^2} = \frac{\mathbf{F}_i}{m_i} - M\frac{d\mathbf{r}_i}{dt}, \tag{3.13}$$

$$M = \mathbf{b}^{-1}\left[\mathbf{b}\frac{d\mathbf{b}'}{dt} + \frac{d\mathbf{b}}{dt}\mathbf{b}'\right]\mathbf{b}'^{-1} \tag{3.14}$$

Aunque este barostato asegura un correcto muestro del colectivo NPT. Para sistemas que se encuentren muy alejados de la presión de equilibrio, este barostato puede dar lugar a grandes oscilaciones de la caja de simulación que pueden hacer que las simulaciones fallen. Por eso es recomendable realizar una equilibración previa del sistema con el barostato de Berendsen antes de usar el barostato de Parrinello-Rahman.

3.2 Potencial de interacción

Tal y como se ha dicho con anterioridad, para predecir el estado futuro de un sistema y, por tanto, para predecir su evolución temporal, es necesario conocer las fuerzas que actúan sobre cada una de las partículas que lo componen. El hecho de que la mayoría de los sistemas reales no se comporte siguiendo el modelo de Gas Ideal implica que el comportamiento de estos sistemas depende en gran medida de estas fuerzas. En la descripción microscópica de sistemas condensados se asume que las fuerzas a las que se encuentran sometidas las partículas pertenecen a un tipo especial de interacciones denominadas fuerzas conservativas. Toda fuerza conservativa lleva asociada una energía denominada energía potencial de interacción (U), cuya relación vienen dada por la Eq. (3.3). Además, estas fuerzas podrán ser clasificadas como interacciones enlazantes o interacciones de no enlace. Las interacciones entre grupos químicos de diferentes moléculas o, en ocasiones, entre grupos químicos no contiguos de una misma molécula se denominan interacciones no enlazantes. Por otro lado, los sistemas reales están formados, en general, por moléculas más o menos complicadas, que poseen una estructura interna. En estos casos, además de las interacciones de no enlaces, es necesario tener en cuenta las interacciones enlazantes, las cuales aparecen entre grupos químicos pertenecientes a una misma molécula al interaccionar a través de los enlaces químicos. Ambas interacciones serán descritas en mayor detalle a continuación.

3.2.1 Interacciones de no enlace

Las fuerzas debidas a las interacciones de no enlace entre pares de moléculas, eléctricamente neutras, están caracterizadas por una contribución repulsiva de corto alcance, que varía rápidamente con la distancia de separación, y por una contribución atractiva, de largo alcance, que actúan de un modo mucho más suave a lo largo de la distancia de separación entre moléculas. Por tanto, cuando dos

moléculas eléctricamente neutras se encuentran lo suficientemente alejadas la una de la otra, no existe interacción entre ellas. Conforme se van acercando, aparece una fuerza de atracción que hace que cada vez se atraigan con más fuerza. Esta atracción aumenta rápidamente al disminuir la distancia interatómica. Esta fuerza atractiva aparece debido a que todos los átomos forman dipolos debido al movimiento de los electrones en torno al núcleo. Estos dipolos, a su vez, inducen la formación de nuevos dipolos en los átomos contiguos originando pequeñas fuerzas de atracción electrostática entre ellos. Por otra parte, a distancias muy pequeñas, los átomos experimentan una fuerte repulsión electrostática debido a la repulsión que existe entre las capas electrónicas de dos átomos muy próximos. El efecto más característico e importante de las fuerzas repulsivas es la creación de un orden de corte alcance característico de la estructura de los sistemas condensados. Por otro lado, las fuerzas atractivas proporcionan un fondo esencialmente uniforme y atractivo que contribuye a la cohesión existente en líquidos y sólidos. Si además las partículas que constituyen el sistema presentan cargas, aparecerá otra interacción adicional debido a la presencia de cargas eléctricas. El comportamiento de los sistemas reales debido a estas interacciones puede ser descrito mediante el uso de modelos matemáticos sencillos capaces de simular estas interacciones. Entre los más conocidos, y usados en este trabajo, se encuentran:

Potencial de pozo cuadrado

El potencial de pozo cuadrado, SW (por sus siglas en inglés, *Square Well*) es uno de los modelos de potencial esféricos más sencillos. En este potencial se considera que las partículas que componen un sistema son núcleos rígidos y duros. Estos núcleos se atraen entre si mediante una interacción atractiva constante para distancias comprendidas entre sus diámetros y una determinada distancia (ver figura 3.2). Para distancias mayores la interacción es nula. El potencial de pozo cuadrado viene dado por la siguiente expresión matemática

$$U_{SW}(r) = \begin{cases} \infty & r < \sigma \\ -\epsilon & \sigma < r < \lambda\sigma \\ 0 & r > \lambda\sigma \end{cases} \tag{3.15}$$

donde σ es el diámetro de la esfera dura, y donde ϵ y λ son la profundidad y la anchura del pozo de interacción.

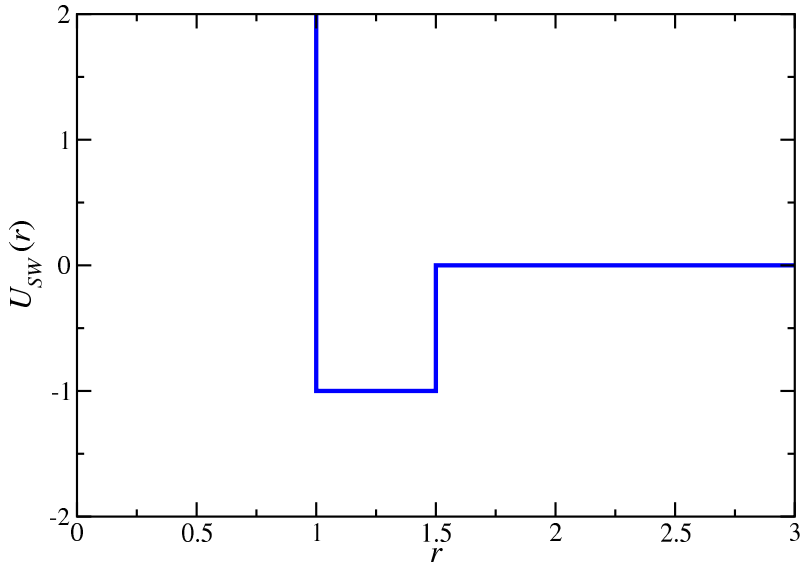

Figura 3.2: Representación de $U(\mathbf{r})$, frente a $\mathbf{r}$, para el potencial de pozo cuadrado.

Pese a no existir en la naturaleza ningún fluido cuyas partículas interaccionen mediante un potencial que tenga exactamente la forma descrita por la Eq. (3.15), este potencial ha sido ampliamente estudiado, tanto desde un punto de vista teórico como mediante simulación molecular. Esto se debe a que se trata del modelo más sencillo con contribuciones tanto para las interacciones repulsivas como atractivas. Pese a su simplicidad, es capaz de describir hasta cierto punto el comportamiento de sistemas reales. Además, este potencial ha sido ampliamente utilizado para describir interacciones de corto alcance, como las que ocurren por ejemplo durante la formación de puentes de hidrógeno.

Potencial de Lennard-Jones

El potencial de interacción intermolecular de Lennard-Jones [10], LJ, es probablemente uno de los potenciales más conocidos y utilizados que existen en la literatura. Este potencial ha sido ampliamente utilizado para la descripción de numerosos sistemas teóricos y reales. Al contrario que en el caso del potencial de SW, este se trata de un potencial continuo y su expresión matemática viene dada por

$$U_{LJ}(r_{ij}) = 4\epsilon_{ij}\left[\left(\frac{\sigma_{ij}}{r_{ij}}\right)^{12} - \left(\frac{\sigma_{ij}}{r_{ij}}\right)^{6}\right] \tag{3.16}$$

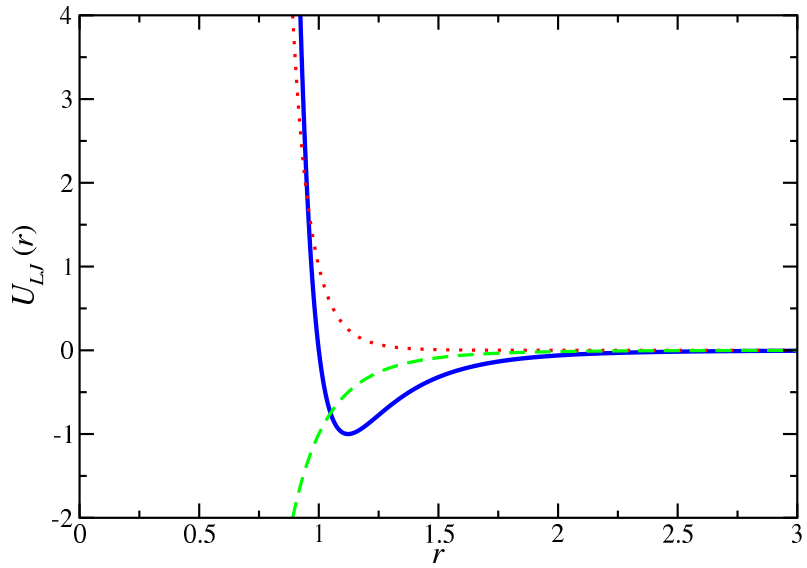

Figura 3.3: Representación de $U(\mathbf{r})$, frente a $\mathbf{r}$, para el potencial de Lennard-Jones (curva continua azul. Además del potencial completo se representa la contribución puramente repulsiva (curva punteada roja) y la contribución puramente atractiva (curva a trazos verde).

donde r_{ij} es la distancia entre los sitios de interacción i y j y σ_{ij} y ϵ_{ij} son el diámetro y la profundidad del pozo de interacción asociados al potencial de Lennard-Jones (ver Fig. 3.3). Como se puede ver, la ecuación (3.16) tiene dos contribuciones, la primera parte de la ecuación, $(\sigma_{ij}/r_{ij})^{12}$, describe la repulsión entre las capas de electrones, la cual decae rápidamente al aumentar la distancia, pero toma valores muy grandes a distancias muy cortas. La segunda parte, $(\sigma_{ij}/r_{ij})^{6}$, representa la atracción debido a la fuerzas de dispersión originadas por la formación de pequeños dipolos debido al movimiento de los electrones en torno al núcleo. La suma de ambas contribuciones da como resultado una distancia en la que la interacción atractiva es máxima (ver figura 3.3).

Potencial de Mie

El potencial de Lennard-Jones, anteriormente descrito, puede considerarse un caso particular del potencial de Mie [11], el cual se expresa matemáticamente como

$$U_{Mie}(r) = C\epsilon\left[\left(\frac{\sigma}{r}\right)^{\lambda_r} - \left(\frac{\sigma}{r}\right)^{\lambda_a}\right] \tag{3.17}$$

Aquí, igual que se definió en el potencial de Lennard-Jones (12-6), σ es un parámetro de tamaño que representa el diámetro de cada centro de interacción, ϵ es un parámetro energético que representa la profundidad del pozo de potencial, λ_r y λ_a son los exponentes repulsivos y atractivos, respectivamente, y el parámetro $C(\lambda_r, \lambda_a)$, que toma un valor de 4 para el potencial de Lennard-Jones ($C(12,6)$), se define como

$$C = \frac{\lambda_r}{\lambda_r - \lambda_a}\left(\frac{\lambda_r}{\lambda_a}\right)^{\frac{\lambda_a}{\lambda_r - \lambda_a}} \tag{3.18}$$

Los dos exponentes del potencial de Mie constituyen dos parámetros adicionales en comparación con el potencial de Lennard-Jones. Aunque el comportamiento de la fase fluida se puede describir con precisión utilizando el potencial de Lennard-Jones, a menudo es difícil obtener con precisión las propiedades derivadas segundas, las cuales son muy sensibles a las interacciones repulsivas. Por tanto, la posibilidad de poder ajustar los valores de λ_r y λ_a en el potencial de Mie es un ventaja respecto al potencial de Lennard-Jones.

Potencial de Coulomb

Cuando dos partículas presentan cargas, estas interaccionan mediante el potencial de Coulomb:

$$U_C(r_{ij}) = \frac{q_i q_j}{4\pi\epsilon_0 r_{ij}} \tag{3.19}$$

donde de nuevo r_{ij} es la distancia entre los sitios de interacción i y j, q_i y q_j son las cargas parciales de los sitios de interacción i y j respectivamente y ϵ_0 es la permitividad del vacío. Esta interacción podrá ser repulsiva o atractiva dependiendo de la relación que existe entre las partículas que interaccionan. Si ambas presentan el mismo tipo de carga (ambos positivas o negativas), la interacción será de tipo repulsiva. Sin embargo, si ambos presentan cargas contrarias, la interacción será atractiva.

3.2.2 Interacciones de enlace

Además de definir el potencial y los parámetros de interacción no enlazantes, es necesario describir el comportamiento de aquellos átomos o grupos químicos, pertenecientes a una misma molécula, que interaccionan a través de las interacciones de enlace. Para ello, dependiendo del número de enlaces químicos que existan entre estos centros, definiremos tres tipos posibles de interacción, los cuales serán descritos mediante modelos matemáticos con el fin de simular el comportamiento real de la molécula:

Potencial de enlace. Aquellos centros de interacción enlazados covalentemente unos con otros interaccionan mediante un potencial harmónico de vibración (U_b), caracterizado por la aparición de una fuerza recuperadora **F** que se opone a que la distancia entre estos dos centros unidos (r) se aleje

de una posición de equilibrio fijada (b). Las expresiones para el potencial harmónico de interacción y la fuerza recuperadora debido al enlace covalente entre el átomo i y el átomo j son:

$$U_b(r_{ij}) = \frac{1}{2}k^b_{ij}(r_{ij} - b_{ij})^2 \tag{3.20}$$

$$\mathbf{F}(r_{ij}) = k^b_{ij}(r_{ij} - b_{ij})\frac{\mathbf{r}_{ij}}{r_{ij}} \tag{3.21}$$

donde k^b_{ij} es la constante recuperadora del potencial harmónico de vibración.

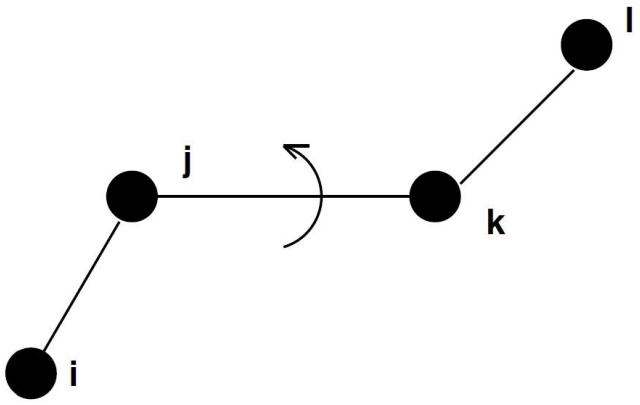

Figura 3.4: Representación gráfica de los sitios de interacción $i - j - k - l$ enlazados covalentemente formando una estructura lineal.

Potencial de flexión. Aquellos centros de interacción separados entre sí mediante dos enlaces covalentes, interaccionan mediante un potencial harmónico de flexión (U_α). Este potencial se caracteriza, de nuevo, por la aparición de una fuerza recuperadora que se opone a que el ángulo formado (θ) se aleje de un ángulo de equilibrio fijado (θ^0). La forma del potencial expresada para el ángulo formado entre los átomos $i - j - k$ (ver figura 3.4) toma la forma

$$U_\alpha(\theta_{ijk}) = \frac{1}{2}k^\theta_{ijk}(\theta_{ijk} - \theta^0_{ijk})^2 \tag{3.22}$$

donde k^θ_{ijk} es la constante recuperadora del potencial harmónico de flexión. La fuerza que actúa sobre cada átomo se obtiene a partir del potencial harmónico de flexión y aplicando la regla de la cadena

$$\mathbf{F}_i = -\frac{d_\alpha(\theta_{ijk})}{d\mathbf{r}_i} \tag{3.23}$$

$$\mathbf{F}_k = -\frac{d_\alpha(\theta_{ijk})}{d\mathbf{r}_k} \tag{3.24}$$

$$\mathbf{F}_j = -\mathbf{F}_i - \mathbf{F}_k \tag{3.25}$$

donde $\mathbf{r}_i$ y $\mathbf{r}_k$ son los vectores de posición de los átomos i y k respectivamente.

Potencial de torsión. Los centros de interacción separados entre sí mediante tres enlaces covalentes interaccionan a través de un potencial torsional dihédrico. Las moléculas constituidas por 4 átomos o más tienen la capacidad de realizar movimientos de torsión. El potencial de Ryckaert-Bellemans utiliza una expansión en serie de cosenos para describir los movimientos torsionales de las moléculas reales. Así, se define el potencial dihédrico, U_{rb} de 4 átomos enlazados consecutivamente (ver figura 3.4) como

$$U_{rb}(\phi_{ijkl}) = \sum_{N=0}^{5} C_n(cos(\phi - \pi))^n \tag{3.26}$$

donde ϕ es el ángulo formado entre los planos ijk y jkl, siendo la configuración cis (i y l en el mismo plano) considerada como el ángulo cero. Los valores de C_n son constantes que dependerán del modelo molecular utilizado.

Dependiendo del modelo molecular utilizado, se puede prescindir de todos o de algunos de estos grados internos de libertad, forzando a la molécula a mantener una estructura interna determinada, fijando así las distancias y los ángulos de enlace y evitando la torsión de la molécula. Dependiendo del número de grados de libertad fijados, hablaremos de modelos flexibles (ningún grado de libertad fijado), semi-flexible (uno o más grados de libertad fijados) o rígidos (todos los grados de libertad están fijados).

3.3 Condiciones de contorno periódicas

Mediante la simulación molecular se pretende estudiar y predecir el comportamiento macroscópico de un sistema real desde un punto de vista microscópico. Para mantener el sistema en una fase condensada y evitar que las moléculas que lo componen se alejen unas de otras, es necesario establecer un potencial que actúe de igual forma a como en la realidad lo haría un recipiente (condiciones de contorno), evitando que el sistema se expanda más allá de las paredes de este. Por desgracia, para simular el número real de moléculas que componen un sistema macroscópico sería necesario un total de moléculas del orden del número de Avogadro (N_A). Esto es inviable para la potencia computacional actual. El número típico de moléculas que componen una simulación está entre $100 \leq N \leq 10^4$, encontrándose muy alejado del número de moléculas de un sistema macroscópico real. Dado el tamaño finito de los sistemas simulados, el uso de una "pared de potencial" no es una solución factible debido los efectos que tienen estas condiciones de contorno sobre las propiedades del sistema. Una molécula no tendrá el mismo comportamiento en el seno de una fase homogénea que en contacto con una "pared de potencial" [12].

Para evitar este problema y poder simular una fase bulk sin que las propiedades de esta se vean afectadas por la proximidad de las moléculas que componen el sistema a una pared de potencial, es necesario hacer uso de condiciones de contorno periódicas [13–15]. Para ello, se replica en el espacio el sistema formando una red infinita de sistemas idénticos (ver Fig. 3.5), de tal manera que ahora el sistema de interés ya no se encuentra confinado por paredes, sino que se encuentra rodeado por idénticos sistemas, que hacen que se "sienta" como si se encontrara en el interior de una fase bulk. Dado que todos los sistemas replicados son idénticos, si durante el transcurso de la simulación, alguna de las moléculas que conforma el sistema original sale de este, una molécula idéntica a la anterior entrará de nuevo al sistema, por el lado contrario, desde uno de los sistemas replicados. De esta forma, la densidad y el número de partículas del sistema permanece constante, sin necesidad de paredes que

lo confinen y evitando así el efecto de las superficies de contorno sobre las propiedades del sistema. Durante la simulación no es necesario almacenar las coordenadas de cada una de las moléculas en todos los sistemas replicados, sino únicamente las del sistema original.

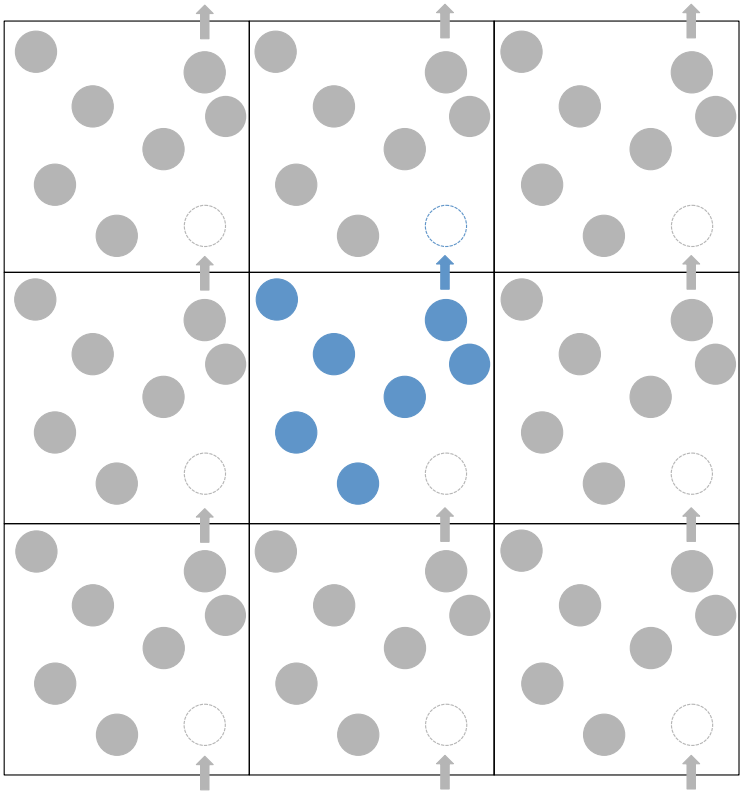

Figura 3.5: Representación gráfica en dos dimensiones de las condiciones de contorno periódicas mediante el replicado del sistema

Pese a que el uso de condiciones de contorno periódicas provee de un método sencillo para simular un sistema bulk con un número de moléculas a nuestro alcance, en este punto, es necesario preguntarse como de pequeño puede llegar a ser el sistema infinitamente replicado y que, aún así, siga siendo representativo del sistema macroscópico que representa. Esto dependerá tanto del rango del potencial intermolecular utilizado como de la propiedad o del fenómeno bajo estudio. Para un sistema constituido por partículas que interaccionan mediante un potencial de Lennard-Jones, con una caja cúbica de lado $L = 6\sigma$ es suficiente para que estas partículas sean incapaces de notar la periodicidad del sistema, ya que que la interacción es débil para largas distancias. Sin embargo, si entre las partículas que constituyen el sistema existiera algún tipo de interacción de largo alcance (como podría ocurrir en el caso de que las partículas se encontrasen cargadas e interaccionaran mediante el potencial de Coulomb), entonces se produciría la interacción de una partícula con su propia imagen en los sistemas replicados. Para evitar esto y disminuir el tiempo necesario para la realización de los cálculos de simulación, se hace uso del truncamiento del potencial de interacción, en combinación con el denominado criterio de mínima imagen.

3.4 Criterio de mínima imagen y truncamiento del potencial

Como se ha dicho anteriormente, la dinámica molecular estudia la evolución temporal de un sistema mediante el cálculo de las fuerzas que actúan sobre cada una de las moléculas que componen el sistema. Esta fuerza es calculada a partir de las contribuciones de energía potencial en las que están involucradas cada molécula. Si se considera un potencial aditivo por pares, como son los casos del potencial de Lennard-Jones o del potencial de Coulomb, la fuerza total que sufre la partícula i se calculará como las $N-1$ contribuciones debido a la interacción de todas las partículas del sistema con la partícula i. Además, sería necesario tener también en cuenta la interacción de la partícula i con todas las partículas de los sistemas replicados. Esto supone un número infinito de interacciones, algo imposible de calcular en la práctica. Para ello se establece el criterio de mínima imagen [13–15], que implica que la partícula i interaccione únicamente con las imágenes periódicas más cercanas de las otras $N-1$ partículas que constituyen el sistema.

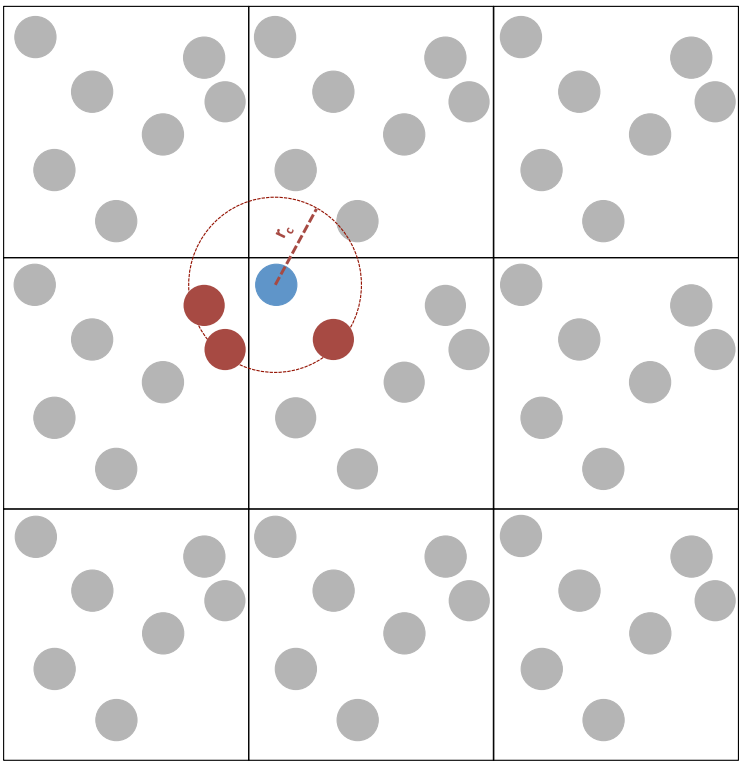

Figura 3.6: Representación gráfica en dos dimensiones del truncamiento del potencial de interacción

Con el fin de ahorrar tiempo de cómputo, es posible definir un radio de corte para el potencial de interacción, r_c, de tal manera que la interacción entre aquellas partículas situadas a una distancia superior a la del radio de corte, ya sean pertenecientes al sistema original o a sus mínimas imágenes, no son tenidas en cuenta (ver Fig.3.6). Para el caso de un sistema homogéneo en una caja de simulación cúbica de lado L, el número de partículas con las que interactúa una partícula i es reducido por un factor de aproximadamente $4\pi r_c^3/3L^3$. Para asegurar que se cumpla el criterio de mínima imagen existe una regla de oro que dice que la distancia máxima a la que se trunca el potencial de interacción debe de ser igual o menor que la mitad del lado más pequeño de la caja.

$$r_c \leq \frac{L}{2} \tag{3.27}$$

Para el caso de potenciales considerados de corto alcance, como el de Lennard-Jones, en los que la energía potencial de una determinada partícula proviene mayoritariamente de la interacción con sus partículas vecinas, el error que resulta de ignorar la interacción entre partículas a largas distancias es pequeño si se considera un r_c lo suficientemente grande. A modo de ejemplo, el valor del potencial por pares en el contorno de una esfera de radio de corte $r_c = 2.5\sigma$ es únicamente el 1.6 por ciento de la profundidad del pozo de interacción.

3.5 Método de Coexistencia Directa

Cuando dos fases inmiscibles de distinta naturaleza se encuentran en contacto se origina una interfase. El comportamiento de una molécula en las proximidades de la interfase será distinto al que presentaría en el seno de su fase bulk. Esto se debe a que cuando una molécula se encuentra cerca de una interfase, las fuerzas a las que se encuentra sometida son diferentes a las que experimentaría en el seno de la fase bulk, como ya se ha mencionado en la sección anterior. El conocimiento actual acerca del comportamiento que presentan las moléculas en las proximidades de una interfase es limitado. Propiedades interfaciales tales como la anchura interfacial, la adsorción selectiva de moléculas en la interfase y la tensión interfacial, juegan un papel esencial en diferentes procesos, y su conocimiento es de vital importancia en un gran número de aplicaciones industriales: detergentes (surfactantes y solubilización de sustancias), producción de alimentos (coloides y emulsiones), industria de cosméticos (fases estructuradas) y dispositivos optoelectrónicos (cristales líquidos) entre otros.

El método por el que se puede simular dos o más interfases en una única caja de simulación se denomina método de coexistencia directa [16, 17]. El método de coexistencia directa se puede aplicar fácilmente para estudiar propiedades interfaciales. Este método también puede ser aplicado para la determinación del equilibrio de fase de un sistema. Dependiendo del sistema y de las fases que lo componen, variará el procedimiento por el que se pondrán en contacto las diferentes fases para formar la interfase. En concreto, los procedimientos usados en este trabajo han sido:

Líquido-vapor (Sistema puro THF): Para formar las interfase líquido-vapor de los sistemas puros simulados con diferentes modelos de THF en el colectivo NVT, se realizaron en primer lugar simulaciones bulk de las fases líquidas a las diferentes temperaturas deseadas. Una vez obtenida esta fase bulk equilibrada, se expandió la caja de simulación a lo largo de la dirección z hasta obtener un valor igual a tres veces el tamaño de la caja original aproximadamente. La fase líquida se desplazó para colocarla en el centro de la nueva caja de simulación, obteniéndose un sistema constituido por una zona central formada por la fase líquida y dos fases de iguales dimensiones pero vacías a ambos lados de esta. La elección de este tipo de geometría garantiza el cumplimiento de las condiciones de contorno periódicas en las tres direcciones del espacio, de modo que una partícula que salga por cualquiera de las caras de la caja de simulación vuelve a entrar en una región que contiene la misma fase del fluido de la que partía. Una vez obtenido este estado inicial, se permitió al sistema evolucionar en el colectivo NVT, de tal manera que las fases inicialmente vacías se llenaron por algunas moléculas procedentes de la fase líquida, formando una fase vapor. El sistema evolucionó hasta alcanzar la presión y la densidad de equilibrio en ambas fases a la temperatura fijada para el modelo de THF escogido.

Líquido-vapor (Mezcla Binaria THF(1) + CO_2(2), CH_4(2)): En el caso de los sistemas formados por las mezclas binarias de THF+CO_2 y THF+CH_4, aunque técnicamente podría haberse construido las interfases líquido-vapor en el colectivo NVT siguiendo el procedimiento anteriormente descrito, es recomendable comenzar desde un punto de partida más cercano a las condiciones de equilibrio de los sistemas estudiados. Para ello, en primer lugar se llevaron acabo simulaciones bulk de las fases líquido y vapor que van a constituir los diferentes sistemas por separado. Para cada sistema, ambas fases fueron equilibradas a la misma temperatura y a la misma presión en el colectivo $NP_z\mathcal{A}T$, en el cual, L_x y L_y (longitudes de la caja en las dirección x e y respectivamente) permanecen constante y solo el tamaño de la caja en la dirección z puede cambiar a lo largo de la simulación. Una vez que ambas fases se encontraron equilibradas, la caja final de simulación se construyó mediante la unión de ambas fases bulk, formando un sistema vapor-líquido-vapor. La elección de esta geometría, de nuevo, garantiza las condiciones de contorno periódica en las tres dimensiones del espacio. Una vez obtenida la configuración de partida, se permitió a cada sistema evolucionar en el colectivo NVT hasta que alcanzó las densidades, composiciones y presiones de equilibrio para cada temperatura fijada.

Líquido-Líquido (Mezcla binaria n-alcohol+H_2O): Para construir las interfases líquido-líquido de los sistemas formados por la mezcla binaria n-alcohol+H_2O, se usó un procedimiento análogo al anteriormente descrito. Primero se construyó una caja de simulación para las fases líquidas que forman cada uno de los sistemas estudiados. Para cada sistema, ambas fases líquidas se equilibraron a la misma temperatura y a la misma presión en el colectivo $NP_z\mathcal{A}T$. Una vez que ambas fases estaban equilibradas, se unieron para formar la caja final de simulación líquido(1)-líquido(2)-líquido(1), donde la fase líquido(1) es una fase rica en n-alcoholes y la fase líquido(2) es rica en H_2O. Para fijar no solo la temperatura, sino también la presión del sistema, las simulaciones se llevaron a cabo en el colectivo $NP_z\mathcal{A}T$. Fijando el número de moléculas que componen el sistema, la presión a lo largo de la interfase y la temperatura, el sistema evolucionó hasta alcanzar las densidades y composiciones de coexistencia para las condiciones fijadas.

Bibliography

[1] R. Hockney, S. Goel, and J. Eastwood *J. Comput. Phys.*, vol. 14(2), pp. 148–158, 1974.

[2] H. J. Berendsen and W. F. Van Gunsteren *Molecular-Dynamics Simulation of Statistical-Mechanical Systems*, pp. 43–65, 1986.

[3] H. Berendsen, "Transport properties computed by linear response through weak coupling to a bath," in *Computer Simulation in Materials Science*, pp. 139–155, Springer, 1991.

[4] G. Bussi, D. Donadio, and M. Parrinello *J. Chem. Phys.*, vol. 126(1), p. 014101, 2007.

[5] S. Nosé *Mol. Phys.*, vol. 52(2), pp. 255–268, 1984.

[6] W. G. Hoover *Phys. Rev. A*, vol. 31(3), p. 1695, 1985.

[7] H. J. Berendsen, J. v. Postma, W. F. van Gunsteren, A. DiNola, and J. Haak *J. Chem. Phys.*, vol. 81(8), pp. 3684–3690, 1984.

[8] M. Parrinello and A. Rahman *J. Appl. Phys.*, vol. 52(12), pp. 7182–7190, 1981.

[9] S. Nosé and M. Klein *Mol. Phys.*, vol. 50(5), pp. 1055–1076, 1983.

[10] J. E. Lennard-Jones *Proceedings of the Physical Society*, vol. 43(5), p. 461, 1931.

[11] G. Mie *Annals of Physics*, vol. 11(8), pp. 657–697, 1903.

[12] M. Born and T. von Kármán *Physikalische Zeitschrift*, vol. 13, pp. 297–309, 1912.

[13] D. Frenkel and B. Smit, *Understanding Molecular Simulations.* 2nd ed. Academic, San Diego, 2002.

[14] M. P. Allen and D. J. Tildesley, *Computer Simulation of Liquids.* Oxford University Press, 1987.

[15] N. Metropolis, A. W. Rosenbluth, M. N. Rosenbluth, A. H. Teller, and E. Teller *J. Chem. Phys.*, vol. 21, p. 1087, 1953.

[16] A. Ladd and L. Woodcock *Chem. Phys. Lett.*, vol. 51(1), pp. 155–159, 1977.

[17] A. Ladd and L. Woodcock *Mol. Phys.*, vol. 36(2), pp. 611–619, 1978.

Capítulo 4

SAFT: Orígenes y Conceptos Básicos

Han pasado ya tres décadas desde la publicación de los primeros artículos [1, 2] que describen la Teoría Estadística de Fluidos Asociantes SAFT (por sus siglas en inglés, *Statistical Associating Fluid Theory*). SAFT nació de la implementación, como ecuación de estado, de la teoría de perturbación termodinámica de Wertheim [3–6] y surgió como respuesta a la necesidad de disponer de herramientas teóricas capaces de predecir de forma efectiva y precisa el comportamiento termodinámico de sistemas complejos. La ecuación de estado SAFT ha demostrado ser uno de los formalismos teóricos de mayor éxito a la hora de predecir las propiedades termodinámicas y el equilibrio de fase de fluidos, y ha sido aplicada en numerosos y diversos sistemas complejos. Esto es debido a la capacidad de esta ecuación de estado para tener en cuenta las interacciones asociantes (como los puentes de hidrógeno) y la forma y estructura de las moléculas (cadenas moleculares). La versatilidad de este formalismo a permitido el desarrollo de una gran variedad de diferentes versiones (SAFT-VR, SAFT-VR Mie, SAFT-γ Mie, PC-SAFT, soft-SAFT, etc) [7–15]. En este capítulo se pretende hacer una introducción a este formalismo y a sus orígenes.

4.1 Teoría de perturbaciones de Wertheim

Con el fin de poder estudiar el comportamiento de sistemas complejos, consideramos que estos pueden describirse en términos de otros más sencillos. Esta premisa junto a los resultados obtenidos experimentalmente y mediante simulación, que demostraban que la estructura de un fluido sencillo como el Argón apenas presentaba diferencias con las de un fluido de esferas duras, fueron los ingredientes necesarios para el desarrollo de las teorías de perturbaciones de Barker y Henderson [16, 17] y de Weeks *et al.* [18]. Mediante la teoría de perturbaciones, se expresa el potencial real del sistema en términos de un potencial de referencia y un término de perturbación que depende linealmente de un parámetro de acoplamiento λ, con $0 \leq \lambda \leq 1$, de la forma:

$$U(r, \lambda) = U_0 + \lambda U_1 \tag{4.1}$$

Además, se debe satisfacer que la suma U_0 y U_1 en el límite de $\lambda = 1$ debe ser igual al potencial

real del sistema que se desea estudiar. Fruto de estos estudios fueron los resultados obtenidos para una gran variedad de sistemas no asociantes formados por moléculas rígidas lineales y no lineales. [19–22]

Pese a la utilidad de estos trabajos y al avance que supusieron, estos eran incapaces de describir el comportamiento de sistemas más complejos, en los que las interacciones asociantes presentan un papel importante en la estructura del fluido. Estos formalismos también eran incapaces de predecir con precisión el comportamiento termodinámico de moléculas flexibles. Wertheim, inspirado por los estudios de Andersen [23, 24] propuso en una serie de trabajos [3–6, 25] aplicar la teoría de perturbaciones a un sistema formado por segmentos asociantes cuyo potencial de interacción intermolecular esta constituido por la suma de un potencial repulsivo de referencia simétricamente esférico, más un potencial atractivo direccional y de corto alcance ejercido entre puntos de asociación situados en estos segmentos. En estos trabajos, las moléculas son consideradas de diferentes especies en función del número de sitios asociantes enlazados y se establece una relación directa entre el cambio en la energía libre residual de Helmholtz debida a la asociación entre monómeros y a la densidad de estos.

En sus primeros trabajos, aplicó esta teoría a sistemas puros compuestos por segmentos caracterizados por un potencial de esfera dura y un único sitio de asociación descrito por un potencial de pozo cuadrado [3, 4] y, poco después, aplicó la misma metodología para segmentos con múltiples sitios de interacción [5, 6]. Estos trabajos fueron ampliados por Chapman *et al.* [26, 27] para mezclas binarias formadas por segmentos del tipo A y B, con sitios de asociación, de igual magnitud, colocados sobre la superficie de los segmentos en los que solo las asociaciones del tipo AB estaban permitidas. Como continuación de estos trabajos, Wertheim [25] y Chapman [28] dedujeron de forma simultánea que, en el límite de una interacción asociante infinita, el sistema se comportaba como un polímero. Dada una interacción asociante de corto alcance y altamente direccional, en el límite de una fuerza de asociación infinita, esta interacción se comporta de igual modo a como lo haría un enlace químico. Usando esta premisa como punto de partida, Chapman *et al.* [28] obtuvieron una ecuación de estado para cadenas de esfera duras al imponer la condición de que todos los segmentos se encuentran unidos y no existen en el sistema segmentos asociantes libres. Este trabajo fue posteriormente ampliado para el estudio de algunos sistemas reales (n-octano, metanol y ácido acético), considerándose estos trabajos como el nacimiento de la Teoría Estadística de Fluidos Asociantes (SAFT).

4.2 SAFT

Como ya hemos dicho, SAFT nació de la mano de Chapman *et al.* [1, 28] basándose en la teoría de perturbaciones de primer orden de Wertheim, pero no fue hasta su trabajo de 1990 [2] en donde explicaron los detalles de la ecuación de estado SAFT, así como las aproximaciones realizadas para aplicar esta teoría. En esta sección se recogerán los detalles más significativos.

4.2.1 La Ecuación de Estado

La ecuación de Estado SAFT está escrita en términos de la energía residual de Helmholtz, A^{res}. Esta energía residual queda definida como $A^{res}(N,V,T) = A(N,V,T) - A^{ideal}(N,V,T)$, donde $A(N,V,T)$ es la energía libre de Helmholtz total y $A^{ideal}(N,V,T)$ es la energía de Helmholtz para un gas ideal en las mismas condiciones de temperatura y densidad. Mientras que el cálculo de la energía de Helmholtz de un gas ideal es un cálculo sencillo, SAFT asume que hay tres contribuciones principales par la obtención de la energía residual de Helmholtz. Estas contribuciones son las debidas a la interacción de

repulsión y dispersión típica de cada segmento, la contribución debida al hecho de que estos segmentos se encuentran formando cadena y la contribución debido a la posibilidad de que algunos de estos segmentos estén formando asociaciones con otros segmentos. De esta forma, la energía residual de Helmholtz en unidades reducidas ($a = A/Nk_bT$, siendo k_B la constante de Boltzmann) viene expresada como:

$$a^{res} = a^{seg} + a^{chain} + a^{assoc} \tag{4.2}$$

donde a^{seg} representa la aportación a la energía de Helmholtz debido a las interacciones dispersivas entre segmentos, a^{chain} es la contribución debido a la formación de cadenas al unirse los segmentos mediante enlaces covalentes y a^{assoc} es la contribución debido a las interacciones entre sitios asociantes situados en los segmentos que componente el sistema.

4.2.2 Término de segmento a^{seg}

El término de segmento se corresponde con la energía de Helmholtz debida a las interacciones dispersivas y de repulsión isotrópicas entre segmentos esféricos no asociantes a^{seg}. Estos segmentos se pueden corresponder con átomos, grupos funcionales o incluso moléculas enteras. Dado que las moléculas están formadas por m segmentos, la contribución total de a^{seg} se corresponderá con la suma individual de cada uno de los monómeros que forman la molécula a^{mon}, siendo la expresión para un sistema puro

$$a^{seg} = ma^{mon} \tag{4.3}$$

Al igual que ocurre en simulación, la elección de un potencial de interacción adecuado es imprescindible cuando se quiere estudiar el comportamiento termodinámico de sustancias reales. Esto a llevado a la aparición de diferentes versiones de SAFT en función del potencial de interacción entre segmentos escogido. Así, Chapman *et al.* [2, 28] desarrollaron una ecuación de estado SAFT utilizando un sistema constituido por esferas duras no asociantes como sistema de referencia más un término dispersivo (siendo especialmente útil el uso del potencial de LJ para obtener el término dispersivo [2]). A partir de este trabajo, otros autores han desarrollado distintas versiones de SAFT para diferentes potenciales interacción, como por ejemplo el potencial de pozo cuadrado [29, 30], el potencial de Yukawa [31], el potencial de Lennard-Jones [7, 32, 33] o un potencial de cadena dura en el cual también se consideran interacciones intramoleculares [34–36].

Gil-Villegas *et al.* [15] desarrollaron una nueva versión de SAFT utilizando la función generalizada del potencial de pozo cuadro con una parte atractiva de rango variable. Esta nueva versión de SAFT fue llamada SAFT-VR (del inglés, *Variable Range*) y ha demostrado ser capaz de describir con gran precisión el comportamiento de sistemas muy complejos [37–39]. Otra versión interesante es la denominada SAFT-γ [40–42], en donde cada grupo funcional que forma la molécula es modelado como un segmento esférico de átomos unidos que interacciona mediante un potencial de pozo cuadrado. Esta versión fue ampliada al caso de grupos funcionales que interactúan mediante el potencial de Mie [43] (SAFT-γ Mie [44]). En este trabajo, como se verá más adelante, la versión de SAFT-VR fue utilizada para estudiar el comportamiento termodinámico y el equilibrio de fases de las mezclas del promotor de hidrato THF con agua, CO_2 y CH_4, mientras que la versión de SAFT-γ Mie fue utilizada para obtener

los parámetros del potencial de Mie de modelos CG de THF, para posteriormente realizar simulaciones líquido-vapor del equilibrio de fases de estos modelos mediante simulación por dinámica molecular.

Pese a que esta contribución tiene un gran peso en la energía residual de Helmholtz, un solo segmento de este tipo es insuficiente para describir la mayoría de las moléculas, debido a sus formas no esféricas o la presencia de atracciones direccionales no centrales. El modelo SAFT explica estos efectos al permitir que la conectividad de los segmentos forme una molécula más larga en forma de cadena, y / o al incluir una perturbación adicional debida a fuerzas asociantes.

4.2.3 Término de cadena a^{chain}

En el límite de una interacción asociante infinitamente fuerte y de muy corto alcance, esta puede ser tratada como un enlace químico. De esta forma, considerando los enlaces químicos como interacciones asociantes muy fuertes y estableciendo la condición de que estos enlaces no pueden ser rotos, obtenemos una expresión para el incremento de la energía de Helmholtz debido a la formación de cadenas para un sistema puro:

$$a^{chain} = (1 - m)\ln\, y^{ref}(d) \tag{4.4}$$

donde y^{ref} es la función de correlación de cavidad evaluada a la distancia de enlace d y que viene dada por

$$y^{ref} \equiv \exp(\phi^{ref}(r)/k_B T] g^{ref}(r)) \tag{4.5}$$

donde ϕ^{ref} es el potencial de interacción de referencia entre segmentos y g^{ref} es la función de distribución radial del fluido de referencia. Dependiendo del potencial y del fluido de referencia escogidos, esta expresión puede simplificarse, así, para un fluido de referencia formado por esferas tangentes que interaccionan mediante un potencial de LJ

$$y^{LJ}(\sigma) = g^{LJ}(\sigma) \tag{4.6}$$

y para un fluido de esferas duras tangentes

$$y^{HS}(d) = g^{HS}(d) \tag{4.7}$$

La contribución a la energía residual de Helmholtz, que se obtiene del término de cadena al aplicar la teoría de perturbaciones de primer orden, presenta una serie de limitaciones. En primer lugar, dado que en esta teoría no se consideran los ángulos de unión, sus predicciones pueden fallar en el límite en el que los ángulos de enlace sean tan pequeños que impidan un enlace simultáneo [45]. Una segunda limitación es que no se consideran las atracciones intramoleculares más allá de la formación de enlaces covalentes entre segmentos. Esto produce que a bajas densidades las predicciones teóricas fallen al no tener en cuenta las interacciones intramoleculares, que a bajas densidades, se vuelven más significativas que las interacciones intermoleculares. Ambas limitaciones pueden ser superadas al tener en cuenta términos de perturbaciones de ordenes superiores, lo que complica considerablemente las ecuaciones.

Por otro lado, el acuerdo entre predicciones teóricas y resultados de simulación es excelente para los casos en que los enlaces se producen cerca de los límites de las moléculas, como ocurre en el caso de cadenas formadas por esferas tangentes. Si embargo, la teoría falla al predecir el comportamiento de cadenas en las que las esferas se superponen significativamente. Para superar esta limitación, se han desarrollado trabajos en los que se consideran las cadenas formadas por un número no entero de segmentos, m, o en los que se busca relacionar el comportamiento de una molécula no esférica con un fluido de cadena equivalente [46–50].

4.2.4 Término asociante a^{assoc}

Una de las características más importantes de la ecuación de estado SAFT es ser capaz de tener en cuenta la interacción entre sitios asociantes de los segmentos o moléculas que componen el sistema. La capacidad de calcular la aportación a la energía libre de Helmholtz debido a estas interacciones asociantes es lo que convierte a SAFT en una poderosa herramienta capaz de describir, con precisión, el comportamiento termodinámico de un gran número de sistemas complejos, tanto puros como mezclas, en los cuales, las interacciones asociantes (como puentes de hidrógeno o entre partículas cargadas) juegan un papel importante en la estructura y el comportamiento del fluido.

Los sitios de asociación se caracterizan por un potencial no central ubicado cerca del perímetro de la molécula. Uno puede incluir uno o más tipos diferentes de sitios en cada molécula. No hay límite para la cantidad de sitios que caracterizan una molécula, aunque en la práctica, podría ser difícil justificar más de cuatro puntos de asociación diferentes en un solo segmento. Como ya se ha explicado para el caso de la contribución de cadena, la teoría de primer orden no distingue las posiciones reales de los sitios, es decir, los ángulos que forman entre ellos. De nuevo, y como ocurría para el caso de a^{chain}, esta limitación puede superarse al considerar términos de perturbación de ordenes superiores, con el consecuente incremento en la dificultad de las ecuaciones.

Aunque esta metodología ha sido extendida y aplicada a sistemas mezclas, a modo de esquema y siguiendo los pasos de las contribuciones anteriores (a^{seg} y a^{chain}), se van a presentar, tan solo, las expresiones correspondientes a un sistema puro. De este modo, el cambio en la energía de Helmholtz debido a las interacciones de asociación toma la forma

$$a^{assoc}RT = \sum_A \left(\ln X_A - \frac{X_A}{2} \right) + \frac{1}{2}M \tag{4.8}$$

donde M es el número de sitios asociantes que tiene cada molécula, X_A es la fracción molar de moléculas no enlazadas al sitio A, y el sumatorio se realiza sobre todo los sitios asociantes de la molécula. La fracción molar de moléculas no enlazadas al sitio A puede ser determinada aplicando la ley de acción de masas

$$X_A = \left[1 + \sum_B \rho X_B \Delta_{AB} \right]^{-1} \tag{4.9}$$

donde ρ es la densidad molar de moléculas, el sumatorio se realiza sobre todos los sitios de interacción que tenga la molécula ($i = A, B, C, ...$) y Δ_{AB} está relacionado con el volumen de asociación entre los sitios A y B, definido como

$$\Delta_{AB} = 4\pi F_{AB} \int_d^{r_c} r^2 \Omega(r) g(r)^{ref} dr \tag{4.10}$$

donde $4\pi r^2 \Omega(r) dr$ es el volumen total del sitio de interacción y la integración se realiza sobre el volumen efectivo disponible. La fuerza de la interacción asociante dependerá por tanto no solo de la energía de la interacción asociante, sino también del volumen de asociación disponible y de la función de distribución del fluido utilizado como fluido de referencia.

Modelado de las interacciones asociantes

Para un gran número de aplicaciones, las interacciones asociantes pueden ser descritas por un potencial del tipo de pozo-cuadrado caracterizado por dos parámetros, ϵ_{SW}, que se corresponde con la profundidad del pozo de potencial, y σ_{SW}, que se corresponde con el alcance de la interacción. Para que se produzca la interacción entre dos sitios asociantes, la distancia entre las dos moléculas donde se sitúan dichos sitios asociantes y su orientación deben de ser las adecuadas. El promedio de segmentos unidos dependerá de la fuerza de la interacción que forma el enlace. Esta fuerza dependerá tanto de la profundidad del pozo de potencial de la interacción asociante como del volumen de asociación, el cual es proporcional a σ_{SW}.

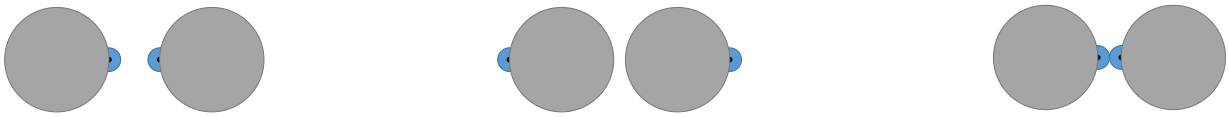

(a) Distancia incorrecta. (b) Orientación incorrecta. (c) Interacción asociante.

Figura 4.1: Modelo de interacción de un sistema de esferas duras con un único sitio de asociación.

Restricciones del modelo - Teoría de perturbaciones de primer orden

La teoría de primer orden permite la formación de multímeros dando lugar a cadenas lineales o ramificadas, pero no permite la formación de estructuras cerradas tipo anillo. Para la formación de cadenas tanto lineales como ramificadas son necesario más de un sitio de interacción por cada monómero. En esta teoría, no se especifican los ángulos formados entre los sitios asociantes, por lo que las propiedades del fluido son independientes del ángulo entre sitios. Además, la actividad de un sitio asociante no se verá afectada por que otro sitio asociante de la misma molécula esté formando un enlace o no, por lo que son ignorados los efectos del impedimento estérico cuando dos sitios de enlace están tan juntos que no pueden unirse simultáneamente a dos moléculas diferentes [3–6, 25]. La teoría de perturbaciones de primer orden, además, impone otra serie de restricciones

- Un doble enlace entre moléculas no está permitido. Una primera aproximación para superar esta limitación consiste en considerar los dobles enlaces como enlaces simples, sin embargo, hay determinados sistemas reales de interés en donde las moléculas tienden a unirse mediante una interacción simple o mediante una interacción doble dependiendo de las condiciones termodinámicas del sistema, por lo que esta aproximación resulta pobre a la hora de predecir el comportamiento del sistema.

- Más de dos moléculas no pueden unirse al mismo sitio de interacción. Aunque esta limitación pueda resultar razonable, lo cierto es que en los sistemas reales, esto puede suceder durante la formación de cadenas ramificadas y el crecimiento de polímeros.
- Un sitio asociante de una molécula no puede unirse simultáneamente a dos sitios asociantes de otra molécula.
- Un sitio asociante de una molécula no puede unirse a otro sitio asociante de la misma molécula. De esta restricción se deriva que las estructuras de tipo anillo no están permitidas, lo que supone una limitación importante pues hay una gran variedad de sustancias reales de interés que forman anillos.

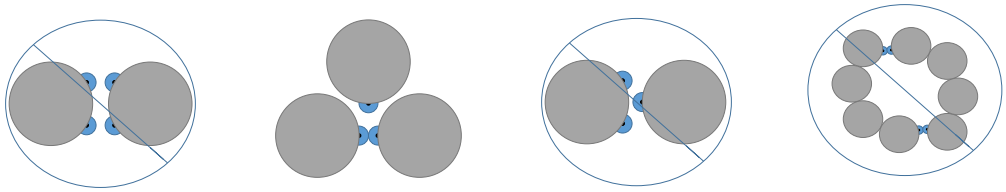

(a) (b) (c) (d)

Figura 4.2: Aproximaciones de la teoría de perturbaciones de primer orden de Wertheim. a) Los dobles enlaces están prohibidos. b) No puede unirse más de una molécula al mismo sitio de asociación. c) Un sitio de interacción de una molécula no puede unirse simultáneamente a dos sitios de interacción de una segunda molécula. d) La formación de cadenas esta prohibida.

Para superar estas restricciones, es necesario modificar la teoría. Fruto de estas modificaciones se han obtenido expresiones para tener en cuenta la formación de dobles enlaces [51], las interacciones asociantes entre tres moléculas y un único sitio de interacción [52] y las interacciones asociantes intramoleculares y la formación de anillos [53–58].

Bibliography

[1] W. G. Chapman, K. E. Gubbins, G. Jackson, and M. Radosz *Fluid Phase Equil.*, vol. 52, pp. 31–38, 1989.

[2] W. G. Chapman, K. E. Gubbins, G. Jackson, and M. Radosz *Ind. Eng. Chem. Res.*, vol. 29, no. 8, pp. 1709–1721, 1990.

[3] M. S. Wertheim *J. Stat. Phys.*, vol. 35, no. 1–2, pp. 19–34, 1984.

[4] M. S. Wertheim *J. Stat. Phys.*, vol. 35, no. 1–2, pp. 35–47, 1984.

[5] M. S. Wertheim *J. Stat. Phys.*, vol. 42, no. 3–4, pp. 459–476, 1986.

[6] M. S. Wertheim *J. Stat. Phys.*, vol. 42, no. 3–4, pp. 477–492, 1986.

[7] F. J. Blas and L. F. Vega *Mol. Phys.*, vol. 92, p. 135, 1997.

[8] F. J. Blas and L. F. Vega *Ind. Eng. Chem. Res.*, vol. 37, no. 2, p. 660, 1998.

[9] J. Gross and G. Sadowski *Ind. Eng. Chem. Res.*, vol. 41, p. 6 March, 1084–1093 2002.

[10] Georgios M. Kontogeorgis, Epaminondas C. Voutsas, Iakovos V. Yakoumis, and Dimitrios P. Tassios *Ind. Eng. Chem. Res.*, vol. 35, no. 11, pp. 4310–4318, 1996.

[11] M. M. P. T. Lafitte and J. L. Daridon *J. Chem. Phys.*, vol. 124, pp. 024509/1–16, 2006.

[12] E. A. Müller and K. E. Gubbins *Ind. Eng. Chem. Res.*, vol. 40, pp. 2193–2211, 2001.

[13] T. Lafitte, A. Apostolakou, C. Avendaño, A. Galindo, C. S. Adjiman, E. A. Müller, and G. Jackson *J. Chem. Phys.*, vol. 139, p. 154504, 2013.

[14] A. Galindo, L. A. Davies, A. Gil-Villegas, and G. Jackson *Mol. Phys.*, vol. 93, pp. 241–252, 1998.

[15] A. Gil-Villegas, A. Galindo, P. J. Whitehead, S. J. Mills, G. Jackson, and A. N. Burgess *J. Chem. Phys.*, vol. 106, pp. 4168–4186, 1997.

[16] J. A. Barker and D. J. Henderson *J. Chem. Phys.*, vol. 47, no. 8, p. 2856, 1967.

[17] J. A. Barker and D. J. Henderson *J. Chem. Phys.*, vol. 47, no. 11, p. 4714, 1967.

[18] J. D. Weeks, D. Chandler, and H. C. Andersen *J. Chem. Phys.*, vol. 54, no. 12, p. 5237, 1971.

[19] M. Lombardero, J. Abascal, and S. Lago *Mol. Phys.*, vol. 42, no. 4, pp. 999–1008, 1981.

[20] E. Enciso and M. Lombardero *Mol. Phys.*, vol. 44, no. 3, pp. 725–732, 1981.

[21] T. Boublík *J. Chem. Phys.*, vol. 87, no. 3, pp. 1751–1756, 1987.

[22] J. Fischer *J. Chem. Phys.*, vol. 72, no. 10, pp. 5371–5377, 1980.

[23] H. C. Andersen *J. Chem. Phys.*, vol. 59, no. 9, pp. 4714–4725, 1973.

[24] H. C. Andersen *J. Chem. Phys.*, vol. 61, no. 12, pp. 4985–4992, 1974.

[25] M. S. Wertheim *J. Chem. Phys.*, vol. 87, no. 12, pp. 7323–7331, 1987.

[26] W. G. Chapman, K. Gubbins, C. Joslin, and C. Gray *Fluid Phase Equil.*, vol. 29, pp. 337–346, 1986.

[27] C. Joslin, C. Gray, W. Chapman, and K. Gubbins *Mol. Phys.*, vol. 62, no. 4, pp. 843–860, 1987.

[28] W. G. Chapman, G. Jackson, and K. E. Gubbins *Mol. Phys.*, vol. 65, no. 5, pp. 1057–1079, 1988.

[29] M. Banaszak, Y. Chiew, and M. Radosz *Phys. Rev. E*, vol. 48, no. 5, p. 3760, 1993.

[30] F. W. Tavares, J. Chang, and S. I. Sandler *Fluid phase equilibria*, vol. 140, no. 1-2, pp. 129–143, 1997.

[31] L. A. Davies, G. Jackson, and L. F. Rull *Phys. Rev. Lett.*, vol. 82, no. 26, pp. 5285–5288, 1999.

[32] E. A. Müller and K. E. Gubbins *Ind. Eng. Chem. Res.*, vol. 34, no. 10, pp. 3662–3673, 1995.

[33] T. Kraska and K. E. Gubbins *Ind. Eng. Chem. Res.*, vol. 35, no. 12, pp. 4727–4737, 1996.

[34] G. Sadowski *Fluid Phase Equil.*, vol. 149, no. 1-2, pp. 75–89, 1998.

[35] J. Gross and G. Sadowski *Fluid Phase Equil.*, vol. 168, pp. 183–199, 2000.

[36] J. Gross and G. Sadowski *Ind. Eng. Chem. Res.*, vol. 40, no. 4, pp. 1244–1260, 2001.

[37] B. Giner, F. M. Royo, C. Lafuente, and A. Galindo *Fluid Phase Equil.*, vol. 255, p. 200, 2007.

[38] B. Giner, I. Gascón, H. Artigas, C. Lafuente, and A. Galindo *J. Phys. Chem. B*, vol. 111, no. 32, pp. 9588–9597, 2007.

[39] B. Giner, I. Bandrés, M. C. López, C. Lafuente, and A. Galindo *J. Chem. Phys.*, vol. 127, no. 14, p. 144513, 2007.

[40] A. Lymperiadis, C. S. Adjiman, A. Galindo, and G. Jackson *J. Chem. Phys.*, vol. 127, p. 234903, 2007.

[41] A. Lymperiadis, C. S. Adjiman, A. Galindo, and G. Jackson *Fluid Phase Equil.*, vol. 274, p. 85, 2008.

[42] V. Papaioannou, C. S. Adjiman, G. Jackson, and A. Galindo *Fluid Phase Equil.*, vol. 306, p. 82, 2011.

[43] G. Mie *Ann. Phys.*, vol. 316, p. 657, 1903.

[44] V. Papaioannou, T. Lafitte, C. Avendaño, C. S. Adjiman, G. Jackson, E. A. Müller, and A. Galindo *J. Chem. Phys.*, vol. 140, p. 054107, 2014.

[45] E. A. Müller and K. E. Gubbins *Mol. Phys.*, vol. 80, pp. 957—976, 1993.

[46] T. Boublík *Mol. Phys.*, vol. 68, no. 1, pp. 191–198, 1989.

[47] T. Boublík, C. Vega, and M. Diaz-Peña *J. Chem. Phys.*, vol. 93, no. 1, pp. 730–736, 1990.

[48] J. M. Walsh and K. E. Gubbins *J. Phys. Chem.*, vol. 94, no. 12, pp. 5115–5120, 1990.

[49] C. Vega, S. Lago, and B. Garzon *J. Chem. Phys.*, vol. 100, no. 3, pp. 2182–2190, 1994.

[50] S. Phan, E. Kierlik, and M. L. Rosinberg *J. Chem. Phys.*, vol. 101, no. 9, pp. 7997–8003, 1994.

[51] R. P. Sear and G. Jackson *Mol. Phys.*, vol. 82, no. 5, pp. 1033–1048, 1994.

[52] R. P. Sear and G. Jackson *J. Chem. Phys.*, vol. 105, no. 3, pp. 1113–1120, 1996.

[53] D. Ghonasgi and W. G. Chapman *J. Chem. Phys.*, vol. 102, no. 6, pp. 2585–2592, 1995.

[54] A. Garcia-Cuellar, D. Ghonasgi, and W. G. Chapman *Fluid Phase Equil.*, vol. 116, no. 1-2, pp. 275–281, 1996.

[55] R. P. Sear and G. Jackson *Mol. Phys.*, vol. 87, no. 2, pp. 517–521, 1996.

[56] A. J. Garcia-Cuellar and W. G. Chapman *Mol. Phys.*, vol. 96, no. 7, pp. 1063–1074, 1999.

[57] D. Ghonasgi, V. Perez, and W. G. Chapman *J. Chem. Phys.*, vol. 101, no. 8, pp. 6880–6887, 1994.

[58] R. P. Sear and G. Jackson *Phys. Rev. E*, vol. 50, no. 1, pp. 386–394, 1994.

Parte III

Resultados y Discusión

Capítulo 5

Understanding the Phase Behaviour of Tetrahydrofuran + Carbon Dioxide, + Methane, and + Water Binary Mixtures from the SAFT-VR Approach

Abstract

The high-pressure phase diagrams of the tetrahydrofuran(1) + carbon dioxide(2), + methane(2), and + water(2) mixtures are examined using the SAFT-VR approach. Carbon dioxide molecule is modeled as two spherical segments tangentially bonded, water is modeled as a spherical segment with four associating sites to represent the hydrogen bonding, methane is represented as an isolated sphere, and tetrahydrofuran is represented as a chain of m tangentially bonded spherical segments. Dispersive interactions are modeled using the square-well intermolecular potential. In addition, two different molecular model mixtures are developed to take into account the subtle balance between water-tetrahydrofuran hydrogen-bonding interactions. The polar and quadrupolar interactions present in water, tetrahydrofuran, and carbon dioxide are treated in an effective way via square-well potentials of variable range. The optimized intermolecular parameters are taken from the works of Giner *et al.* [*Fluid Phase Equil.* **255**, 200 (2007)], Galindo and Blas [*J. Phys. Chem. B* **106**, 4503 (2002)], Patel *et al.* [*Ind. Eng. Chem. Res.* **42**, 3809 (2003)] and Clark *et al.* [*Mol. Phys.* **104**, 3561 (2006)] for tetrahydrofuran, carbon dioxide, methane, and water, respectively. The phase diagrams of the binary mixtures exhibit different types of phase behaviour according to the classification of van Konynenburg and Scott, ranging from type I, III, and VI phase behaviour for the tetrahydrofuran(1) + carbon dioxide(2), + methane(2), and + water(2) binary mixtures, respectively. This last type is characterized by the presence of a Bancroft point, positive azeotropy, and the so-called closed-loop curves which represent regions of liquid-liquid immiscibility in the phase diagram. The system exhibits lower critical solution temperatures (LCSTs), which denote the lower limit of immiscibility together with upper critical solution temperatures (UCSTs). This behaviour is explained in terms of competition between the incompatibility with the alkyl parts of the tetrahydrofuran ring chain and the hydrogen bonding between water and the ether group. A minimum number of unlike interaction parameters are fitted to give the optimal representation of the most representative features of the binary phase diagrams. In the particular case of tetrahydrofuran(1) + water(2) , two sets of intermolecular potential

model parameters are proposed to describe accurately either the hypercritical point associated to the closed-loop liquid-liquid immiscibility region or the location of the mixture lower- and upper-critical end-points. The theory is not only able to predict the type of phase behaviour of each mixture, but also provides a reasonably good description of the global phase behaviour whenever experimental data are available.

5.1 Introduction

Tetrahydrofuran (c-$(CH_2)_4O$, denoted hereafter as THF for brevity) is a cyclic ether widely used as solvent in many industrial processes. Amongst its diverse applications, it is used as thermodynamic clathrate hydrate promoter [1, 2], and that represents a particular motivation for the present study. Clathrate hydrates are non-stoichiometric crystalline inclusion compounds consisting of a network of hydrogen-bonded molecules forming cages, in which various types of low molecular weight compounds (e.g., methane, carbon dioxide, hydrogen sulfide, THF, etc.) can be encapsulated under appropriate thermodynamic conditions. A mixture of THF and water forms the so-called "THF hydrate" (17 H_2O molecules per THF molecule), in which THF molecules occupy only the large cages of the structure II (sII) [1, 2]. This hydrate can be formed easily and dissociates around 277 K at atmospheric pressure. For this reason, it is used as a model system in many fundamental and practical applications. THF properties and the full THF + water phase diagram can be found elsewhere in literature [3, 4].

THF is a powerful gas hydrate promoter, as it follows forming mixed gas hydrates (i.e., hydrates containing both THF and another guest gas, such as THF + CO_2 hydrate) at lower pressure and higher temperature than the hydrate formed without this promoter (the CO_2 hydrate in that case) [5, 6]. This property has been widely exploited to produce hydrates in appropriated temperature and pressure ranges depending on the application envisaged. As an example, several authors [7–9] used THF to reduce significantly the equilibrium pressure of H_2 clathrate hydrate, considering its application in H_2 storage cells. The effect on the phase equilibria was clear, although as pointed out by Struzhkin *et al.* [10] some issues remain, concerning for instance the distribution of both guest molecules between both types of cells within sII structure. Nevertheless, the role of THF in H_2 storage using hydrates is clear, as pointed out recently in the review of Veluswamy *et al.* [11].

The same effect has been pointed out for carbon dioxide (CO_2) hydrates, and the environmental concern related with greenhouse gas emission control and the effects on global climate change have attracted intense research efforts in this direction. Kang and Lee [12] showed the thermodynamic feasibility of using THF to tune hydrate phase equilibria in the process of recovering CO_2 from post combustion or industrial flue gases. This topic is very active right now and many recent works [13–15] continue studying different aspects of this process.

The cornerstone of these applications is the multiphasic equilibria of THF mixtures, and if from an experimental perspective the number of studies published is very large, from a molecular modeling perspective the subject is undoubtedly far behind in development. Considering for instance the latest application cited, CO_2 capture using hydrates, a proper theoretical description of the process entails at a first stage an accurate description of phase equilibria of fluid solutions containing at least THF, CO_2 and water (H_2O). This is a complicated task, and although many attempts have been devoted to describe these complex phase equilibria scenarios, the discussion is still open. In any case, the complexity of an accurate description of aqueous solutions phase equilibria is well known, and even if binary mixtures are sometimes well described, the effects in multicomponent mixtures are poorly

understood [16].

The characteristics of THF make it a remarkably difficult target for molecular modeling. This is due to its cyclic structure, and the presence of the ether group, which produces a strong polarity, and a marked spacial anisotropy, inducing complex intermolecular interactions with the possibility of hydrogen bonding. Determining the degree of detail of a molecular model to represent this molecule with a physically realistic representation and accurate results without falling in over parametrization is a challenging objective. Avoiding an excessive degree of dependence between results and parametrization, and seeking for parameter transferability, are desirable objectives that should be also kept in mind. This applies to different levels of calculation, from equations of state (EoS) modeling to molecular simulation. Setting the proper molecular model is the first step towards a reliable representation of phase equilibria, and this should include first a robust representation of fluid phases before considering solid-fluid equilibrium, where hydrate description lays at the very end of this path. Another point in this discussion is the interest of defining molecular models that can be used with exactly the same definition, structural details and characteristic parameters in the framework of different approaches as EoS and molecular simulation [17], to obtain the best from each scheme. This includes the ability of EoS to describe phase equilibria and thermodynamic properties over broad temperature and pressure ranges with short calculation times, combined with the possibility of studying in detail microscopic fluid features with molecular simulation.

In this context, the description of THF has been attempted using different approaches, and proposing different molecular models. A representative example of this is the recent work by Herslund *et al.* [18], where different models are proposed for THF in the framework of CPA [19] EoS, discussing the degree of molecular detail in the description of phase equilibria of its aqueous solutions. The authors show how deciding a priori the association bonding scheme for the molecular models determines its performance for this highly non ideal solution. Let us recall that this binary global phase diagram can be ascribed as type VI according to van Konynenburg and Scott [20, 21] classification, and accordingly it presents the distinctive feature of a closed loop miscibility gap at moderate pressures, which has been accurately described experimentally [22–24]. From a theoretical point of view this behavior is a challenge and a major benchmark for any molecular modeling attempt.

Giner *et al.* [25] studied the phase equilibria of pure cyclic ethers using the SAFT-VR molecular EoS. This EoS consider the molecules formed by tangentially bonded variable range square-well (SW) segments, with specific additional interaction sites to account for associating interactions. In the cited work [25], cyclic ethers were considered as non associating, and polar effects were neither considered. The parameters determined were later used to estimate vapor liquid equilibria of mixtures with chloroalkanes [26, 27], obtaining fairly good results. This modelling approach is the same used in one of our previous works [16] to study the global phase diagram of the binaries including H_2O, CO_2 and methane (CH_4), and their ternary mixture. In that case, SAFT-VR EoS proved to be able to describe a very complex phase equilibria scenario resulting from the combination of type I and type III binary mixtures, using pure component parameters determined previously by other authors, and used in this case in a completely transferable manner, needing only one additional binary mixing rule coefficient for the H_2O + CO_2 binary. These results have induced us to apply the same approach for the estimation of THF solutions phase equilibria, considering its mixtures with the same three molecules, H_2O, CO_2 and CH_4, for the interest they have towards the understanding of hydrates phase equilibria. As it will be shown later, this implies describing type I, THF(1) + CO_2(2), type III, THF(1) + CH_4(2), and type VI, THF(1) + H_2O(2) binary phase diagrams with the same set of transferable molecular parameters.

5.2 Molecular Models and Theory

5.2.1 SAFT-VR Molecular Models

SAFT-VR approach requires the determination of a number of intermolecular parameters to describe the thermodynamic phase behaviour of real substances. In this EoS, molecules are modelled as chains of m spherical SW segments. Each segment is characterized by its size, σ, a dispersive energy characterized by a well depth ϵ, and a potential range λ. The interactions between SW segments i and j separated by a distance r_{ij} is given by,

$$u_{ij}(r_{ij}) = \begin{cases} +\infty & \text{if } r_{ij} < \sigma_{ij} \\ -\epsilon_{ij} & \text{if } \sigma_{ij} \leq r_{ij} \leq \lambda_{ij}\sigma_{ij} \\ 0 & \text{if } r_{ij} > \lambda_{ij}\sigma_{ij} \end{cases} \tag{5.1}$$

where σ_{ij} defines the contact distance between spheres, and λ_{ij} and ϵ_{ij} are the range and depth of the potential well for the i-j interaction, respectively. These molecular parameters are usually optimized to obtain the optimal representation of the experimental vapor pressure and saturated liquid density for each substance from the triple to the critical point.

We now detail the molecular models of the four molecules considered in this work, i.e., CH_4, CO_2, THF and H_2O. Firstly, we have considered the non-associating molecules, CH_4, CO_2, and THF. CH_4 molecule is represented as a single spherical SW segment of hard-core diameter σ_{11}, whose parameters were determined by Patel *et al.* [28]. The second molecule studied here, CO_2, is modelled as two tangentially bonded hard-sphere segments of equal diameter σ_{22}, with molecular parameters obtained from the work of Galindo and Blas [29, 30]. These sets of parameters have been shown to provide an excellent description of the thermodynamic phase behaviour of the CH_4 + CO_2 binary mixture for wide temperature and pressure ranges [16, 29]. Finally, as mentioned earlier, THF is also treated as a non self-associating molecule. However, it may associate with another associating molecule, such as water, as we will discuss later. THF is modelled following the parametrization proposed by Giner *et al.* [25]. The values of the molecular parameters σ_{33} and ϵ_{33} have been obtained by optimizing the vapor pressure and saturated liquid densities at different temperatures [25]. This model has been previously used to model the phase equilibrium and thermodynamic properties of a number of binary mixtures, including THF + 1-chlorohexane [31], THF + 2-chlorobutane [25], THF + 1-chloro-2-methylpropane [27], and THF + 1-chloropropane [32, 33]. The SAFT-VR approach is able to provide an excellent description of the experimental data in all cases. The intermolecular model parameters used in this work are summarized in Table 5.1.

In the case of the associating molecule, H_2O, we have used a four-site model [34, 35] with the optimal intermolecular parameters determined by Clark *et al.* [36]. The H_2O molecule is represented as a single spherical SW segment of hard-core diameter σ_{44}. The SW intermolecular potential is characterized by a depth ϵ_{44} and a range λ_{44}. Apart from these SW parameters, four additional off-center short-range attractive sites are used to mediate the hydrogen bonding interactions. Two associating H-sites represent the hydrogen atoms in the H_2O molecule and the other two e-sites represent the lone pairs of electrons of the oxygen, and only e-H interactions are permitted. The four association sites are placed at a distance $r_{d_{44}}^{HB}$ from the sphere center. The cutoff intermolecular range between the e and H sites is given by $r_{c_{44}}^{HB}$. These two parameters define the available associating volume K_{44}^{HB} for the e-H site-site bonding association [37]. When the distance of two sites of different

H_2O molecules is less than $r_{c_{44}}^{HB}$, both associating sites interact with an energy ϵ_{44}^{HB}. This model has shown to provide a good description of the thermodynamics and fluid phase equilibria of pure H_2O [36] and mixtures with other substances, such as the ternary mixture H_2O + CH_4 + CO_2 [16]. The parameter values for H_2O molecule are also gathered in Table 5.1.

Tabla 5.1: Optimized and rescaled Square-Well Intermolecular Potential Parameters for H_2O [36], CH_4 [28], CO_2 [29, 30], and THF [25]

Molecule	CH_4	CO_2	THF	H_2O
m	1	2	2.824	1
σ (Å)	3.6847	2.7864	3.206	3.033
ϵ/k_B (K)	167.3	179.27	184.900	300.4330
λ	1.4479	1.515727	1.738	1.718250
ϵ^{HB}/k_B (K)				1336.951
K^{HB} (Å^3)				0.893687
σ_c (Å)	4.05805	3.136386	3.5684	3.469657
ϵ_c/k_B (K)	156.464	168.8419	173.8285	276.2362
ϵ_c^{HB}/k_B (K)				1229.273
K_c^{HB} (Å^3)				1.337913

It is known that classical EoS or mean-field approaches, such as SAFT, do not consider the density fluctuations that occur near the critical point, and hence, an over-prediction of its coordinates is expected. This can be easily addressed in an effective way by re-scaling the conformal parameters, σ and ϵ, to the experimental critical temperature and pressure. The rescaled intermolecular parameters, σ_c, ϵ_c, ϵ_c^{HB}, and K_c^{HB} are also presented in Table 5.1. It is obvious that the use of rescaled parameters produces an accuracy loss in the estimated saturated liquid density of pure components [29, 30, 36]. However, this set of parameters provides a good description of the coexistence compositions and critical curves. In this work we only use the rescaled molecular parameters given in Table 5.1.

5.2.2 Unlike binary interaction

In order to model the phase behavior of the binary mixtures considered in this work, THF(1) + CO_2(2), + CH_4(2), and + H_2O(2), a number of unlike intermolecular association parameters have to be determined. In the case of THF(1) + H_2O(2), experimental studies [38–41] confirm the formation of hydrogen bonds between H_2O and THF molecules. These works suggest that the interaction between THF and H_2O molecules is relatively weak compared to H_2O-H_2O interaction. As a cyclic ether, the oxygen of a THF molecule uses one of its unshared electron pairs to accept a proton from a H_2O molecule to form a hydrogen bond [38]. In view of this discussion, a number of off-center SW attractive sites are used to mediate the unlike hydrogen bonding between THF and H_2O: two and three e^* sites are included to represent the electronegative oxygen atom (two lone pairs of electrons) of THF molecule, following previous works [42–46]. These e^* sites are all placed at a distance $r_{d,34}^{HB}$ from the center of the THF molecule. When the e^* sites (THF) and H sites (H_2O) are within a distance of $r_{c,34}^{HB}$ they interact with an energy ϵ_{34}^{HB}. Note that only e^*-H associations are allowed. The values of $r_{d,34}^{HB}$ and $r_{c,34}^{HB}$ define the volume K_{34}^{HB} available for site-site bonding association. Since we are mostly interested in the description of the closed-loop liquid-liquid immiscibility behaviour present in this mixture, we have used the experimental data taken from literature [22–24, 47] as the reference data to determine the strength ϵ_{34}^{HB} and volume available K_{34}^{HB} of the e^*-H association. In the so-called set A

of molecular parameters for THF-H_2O, in which two associating sites of type e^* can form hydrogen bonding with H_2O molecules, the unlike interaction parameters are determined by fitting them to the lower-critical (LCEP) and upper-critical (UCEP) end-points. The second model proposed in this work, the so-called set B of molecular parameters for THF-H_2O, in which three associating sites of type e^* can form hydrogen bonding with H_2O molecules, the associating unlike interaction parameters are obtained by fitting them to the maximum pressure-point of the closed-loop liquid-liquid immiscibility or hypercritical point of the mixture. The complete list of the THF-H_2O unlike associating and dispersive interaction parameters are given in Table 5.2.

Tabla 5.2: Unlike binary interaction parameter values for THF(1) + H_2O(2) binary mixture. Two and three e sites, denoted as e^*, are included to represent the electronegative oxygen atom on the THF molecule. These e^* sites are allowed to bond only to H_2O molecules (e^*-H) (and not to THF molecules). ϵ_{34}^{HB} and K_{34}^{HB} are determined by fitting to the experimental closed-loop behavior [22–24, 47] that presents this system.

Model system	number of e^*sites	ξ_{34}	$\epsilon_{34,HB}^{HB}/K$	K_{34}^{HB}/A
Model A	2	1.02	1602.5	0.52902
Model B	3	1	1505	0.52902

In addition to the associating unlike interaction molecular parameters, the study of phase equilibria of mixtures also requires the determination of a number of unlike dispersive interaction parameters. The standard arithmetic mean or Lorentz rule is used for the unlike hard-core diameter,

$$\sigma_{ij} = \frac{\sigma_{ii} + \sigma_{jj}}{2} \tag{5.2}$$

The unlike SW potential range parameter is given by,

$$\lambda_{ij} = \frac{\lambda_{ii}\sigma_{ii} + \lambda_{jj}\sigma_{jj}}{\sigma_{ii} + \sigma_{jj}} \tag{5.3}$$

The unlike SW dispersive energy parameter is given by a modified Berthelot rule as,

$$\epsilon_{ij} = \xi_{ij}\sqrt{\epsilon_{ii}\epsilon_{jj}} \tag{5.4}$$

where the binary interaction parameter ξ_{ij} provides a measure of the deviation from the Berthelot rule, and is usually determined by comparison with experimental mixture data.

5.2.3 The SAFT-VR equation of state

In this work, we have used the particular extension of SAFT for potentials of variable range, the well-known SAFT-VR [48, 49] approach, to predict the phase equilibria of the THF(1) + CO_2(2), + CH_4(2), and + H_2O(2) binary mixtures. As any other SAFT version, the SAFT-VR approach is written in terms of the Helmholtz free energy, which can be expressed as a sum of four microscopic contributions:

$$\frac{A}{Nk_BT} = \frac{A^{\text{IDEAL}}}{Nk_BT} + \frac{A^{\text{MONO}}}{Nk_BT} + \frac{A^{\text{CHAIN}}}{Nk_BT} + \frac{A^{\text{ASSOC}}}{Nk_BT} \tag{5.5}$$

where N is the total number of molecules, T is the temperature, and k_B is the Boltzmann constant. The term A^{IDEAL} corresponds to the ideal free energy of the mixture, the monomer term A^{MONO} takes into account the attractive and repulsive forces between the molecule segments, the chain contribution A^{CHAIN} accounts for the connectivity of segments within the molecules, and the association contribution A^{ASSOC} accounts for the hydrogen bonding interactions between molecules.

The Helmholtz free contribution of an ideal mixture of n components is given by [50],

$$\frac{A^{IDEAL}}{Nk_BT} = \sum_{i=1}^{n} x_i \ln \rho_i \Lambda_i^3 - 1 \tag{5.6}$$

The sum is over all species i of the mixture, $x_i = \frac{N_i}{N}$ is the mole fraction, $\rho_i = \frac{N_i}{V}$ the number density, N_i the number of molecules, Λ_i the thermal de Broglie wavelength of species i, and V the volume of the system.

In the SAFT-VR, approach the SW monomer dispersive contribution for all the segments in the mixture is obtained from a Barker-Henderson [51–53] high-temperature perturbation expansion up to second order,

$$\frac{A^{MONO}}{Nk_BT} = \frac{A^{HS}}{Nk_BT} + \frac{A_1}{Nk_BT} + \frac{A_2}{Nk_BT} \tag{5.7}$$

The hard-sphere reference free energy $\frac{A^{HS}}{Nk_BT}$ is obtained from the expression of Boublik [54] and Mansoori *et al.* [55]. $\frac{A_1}{Nk_BT}$ corresponds to the mean attractive energy of the mixture and is obtained in the context of the M1Xb mixing rules. The second-order fluctuation term $\frac{A_2}{Nk_BT}$ is calculated using the local compressibility approximation. Details of each of these terms and of the mixing rules can be found in the original works [48, 49].

The residual contribution to the free energy due to the formation of chain molecules is given by [56],

$$\frac{A^{CHAIN}}{Nk_BT} = -\sum_{i=1}^{n} x_i \left(m_i - 1\right) \ln y_{ii}^{SW}(\sigma_{ii}) \tag{5.8}$$

where m_i is the number of segments of component i, and $y_{ii}^{SW}(\sigma_{ii}) = g_{ii}^{SW}(\sigma_{ii}) \exp\left(-\beta\epsilon_{ii}\right)$. The contact pair radial distribution function for a mixture of SW molecules corresponding to the $i-i$ interaction. $g_{ii}^{SW}(\sigma_{ii})$ is obtained from the high-temperature expansion [51–53] (see references [48, 49] for further details). In our system, the only chain formation to account for is due to the CO_2 molecule, because H_2O, CH_4 and THF are modeled as spherical segments.

Finally, the residual contribution to the free energy due to the association takes the form [57–60],

$$\frac{A^{ASSOC}}{Nk_BT} = \sum_{i=1}^{n} x_i \left[\sum_{a=1}^{s_i} \left(\ln X_{a,i} - \frac{X_{a,i}}{2}\right) + \frac{s_i}{2}\right] \tag{5.9}$$

where s_i is the total number of sites on a molecule of species i and $X_{a,i}$ is the fraction of molecules of species i not bonded at site of type a given by [37, 56]

$$X_{a,i} = \frac{1}{1 + \rho \sum_{j=1}^{n} x_j \sum_{b=1}^{s_j} X_{b,j} \Delta_{a,b,i,j}} \tag{5.10}$$

where $\Delta_{a,b,i,j}$ characterizes the association between site a on molecule i and site b on molecule j and can be written as,

$$\Delta_{a,b,i,j} = K_{a,b,i,j} f_{a,b,i,j} g_{ij}^{\mathrm{SW}}(\sigma_{ij}) \tag{5.11}$$

where the Mayer f-function of the $a-b$ site-site association interaction ($\epsilon_{a,b,i,j}$) is given by $f_{a,b,i,j} = \exp(-\frac{\epsilon_{a,b,i,j}}{k_{\mathrm{B}}T}) - 1$, and $K_{a,b,i,j}$ is the available volume for bonding, whose expression can be found elsewhere [37, 48, 49, 56].

As mentioned earlier, we have considered one associating component (i.e, H_2O molecule) in this work. This means that no unlike binary associating interaction parameters are considered for the THF(1) + CO_2(2) and + CH_4(2) binary mixtures, and only unlike association interaction parameters need to be used for the THF(1) + H_2O(2) system. In this mixture, hydrogen bonds are formed by H-e (self-associating) interactions between H_2O molecules and unlike associating interactions between the H sites on the H_2O molecule and the e^* sites on the THF molecules. Therefore, $\Delta_{a,b,i,j}$ characterizes only the hydrogen bond association (i.e., H-e and H-e^*) present in this system and the fractions of molecules not bonded at given sites are obtained from Eq. 5.10.

The fraction of H_2O molecules not bonded at a site of type e and H are given by $X_{e,1}$ and $X_{H,1}$, respectively

$$X_{e,1} = \frac{1}{1 + 2\rho x_1 X_{H,1} \Delta_{e,H,1,1}} \tag{5.12}$$

and

$$X_{H,1} = \frac{1}{1 + 2\rho x_1 X_{e,1} \Delta_{H,e,1,1} + s_2 \rho x_2 X_{e^*,2} \Delta_{H,e^*,1,2}} \tag{5.13}$$

where s_2 is the number of sites type e^* on THF molecule.

Finally, the fraction of THF molecules not bonded at a site of type e^* can be written as,

$$X_{e^*,2} = \frac{1}{1 + 2\rho x_1 X_{H,1} \Delta_{e^*,H,2,1}} \tag{5.14}$$

The association parameter $\Delta_{a,b,i,j}$ defines only two different types of hydrogen bonding present in this system due to the symmetry of the interactions: $\Delta_{1,1} = \Delta_{e,H,1,1} = \Delta_{H,e,1,1}$, that characterizes the association between the e and H sites of the H_2O molecules, and $\Delta_{1,2} = \Delta_{H,e^*,1,2} = \Delta_{e^*,H,2,1}$, that characterizes the association between the H sites of H_2O and the e^* sites of THF.

5.3 Results and discussion

5.3.1 THF + CO_2 binary mixture

The THF(1) + CO_2(2) binary mixture exhibits type I phase behaviour according to the van Konynenburg and Scott classification [20, 21]. In a PT projection of the phase diagram, as shown in Fig. 5.1, the gas-liquid critical line is continuous, running from the critical point of component 1, THF, to the critical point of the component 2, CO_2. In particular, there is no liquid-liquid separation in the

system, or in other words, the liquid mixture of THF and CO_2 is homogeneous at any composition. We first determine the critical line of the mixture from the molecular parameters of the pure components in order to assess the ability of SAFT-VR, in conjunction with the Berthelot rule given by Eq. (5.4) for the unlike dispersive interactions with $\xi_{12} = 1$, in predicting the critical behaviour of the system.

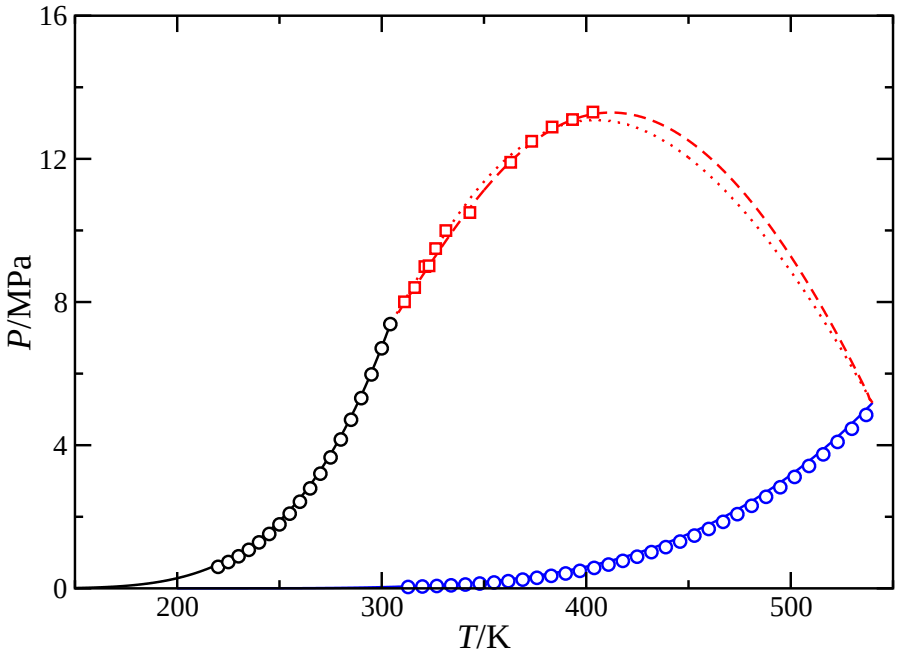

Figura 5.1: *PT* projection of the phase diagram for the THF(1) + CO_2(2) binary mixture. The blue and black circles correspond to the experimental vapour pressure data of pure THF [61] and pure CO_2 [62–67], respectively, and red squares [68, 69] to the experimental gas-liquid critical line. The continuous black and blue curves are the SAFT-VR calculations for the vapour pressures, and the dotted and dashed red curves are the predictions from SAFT-VR, in conjunction with the Berthelot rule, for the critical line using $\xi_{12} = 1$ and $\xi_{12} = 0.95$, respectively.

It is important to recall here that we are using re-scaled molecular parameters to the critical points of pure components to obtain the best-possible representation of the critical behaviour of the system. However, this produces an accuracy loss in the calculated saturated liquid density of pure components, as it has been shown in previous works [29, 30, 36, 70]. However, these sets of parameters provide a good description of the coexistence compositions and critical curves. A more satisfactory description of these systems could be obtained using the versions of SAFT-VR proposed by McCabe and Kiselev, using a crossover treatment [71, 72], or the more recent versions of Forte *et al.* [73, 74] in combination with the renormalization-group theory.

As can be seen in Fig. 5.1, agreement between experimental data taken from the literature and predictions from the theory is good in the whole range of compositions, especially taking into account that SAFT-VR results are pure predictions. However, it seems that the shape of the continuous gas-liquid critical line is not captured by the theoretical predictions, especially near the maximum of the critical curve. Unfortunately, no experimental data for temperatures above 400 K are available. In order to obtain more accurate results, we have adjusted ξ_{12} to improve the description of the gas-liquid critical line of the mixture. The value obtained ($\xi_{12} = 0.95$) is treated as temperature-independent and

used to study the complete pressure-temperature-composition (PTx) phase behaviour of the mixture in a wide range of thermodynamic conditions. As can be seen, agreement between theoretical results and experimental data taken from the literature for the gas-liquid critical line is excellent in the whole range of temperatures with available experimental data.

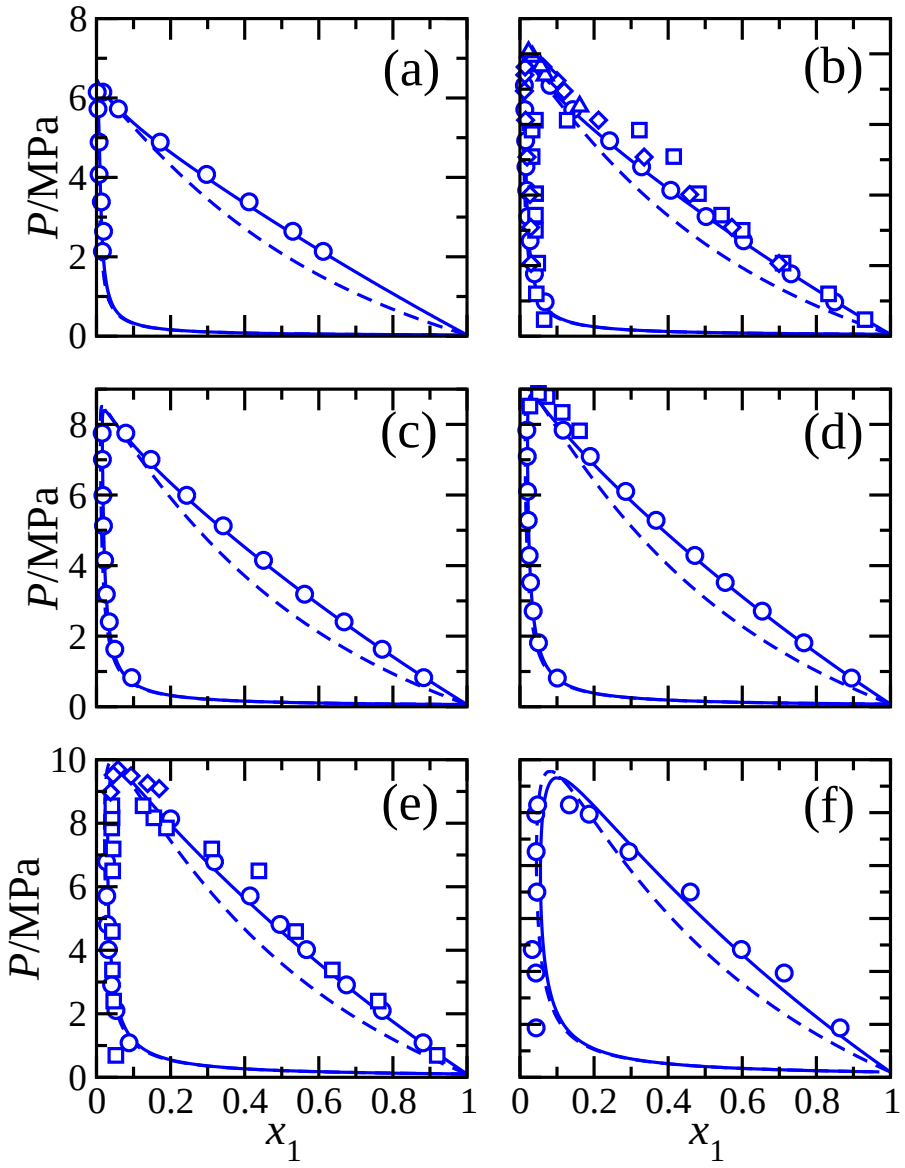

Figura 5.2: Px slices of the phase diagram for the THF(1) + CO_2(2) binary mixture at (a) 298.15 K, (b) 311 K,(c) 316 K,(d) 321 K, (e) 331 K, and (f) 353 K. The dashed and continuous curves represent SAFT-VR estimations using $\xi_{12} = 1$ and $\xi_{12} = 0.95$, respectively, and the symbols represent the experimental data taken from literature [68, 75–77].

Fig. 5.2 shows the Px slices of the phase diagram, at temperatures varying from 298 to 353 K approximately, compared with experimental data taken from literature. We have determined the phase

behaviour of the mixture using two different values of the binary unlike dispersive energy parameter, $\xi_{12} = 1$, which corresponds to the original Berthelot value for the dispersive energy ϵ_{12}, and $\xi_{12} = 0.95$, a value found to give the optimal representation of the gas-liquid critical line. As can be seen, the mixture is subcritical at the lowest temperature considered, 298.15 K, since it is below the critical temperature of CO_2 ($T_c \approx 304$ K). Both values of ξ_{12} give a good representation of the Px slices at different temperatures, although calculations obtained using $\xi_{12} = 0.95$ are clearly better than those predicted using $\xi_{12} = 1$. In particular, SAFT-VR estimations provide similar values of composition along the gas branch of the phase envelope at nearly all temperatures considered. Notice, however, that theoretical results slightly overestimate the composition of THF in the gas phase at 353 K, especially at low pressures ($p \approx 2$ MPa). Predictions corresponding to the liquid branch of the phase diagram are clearly different when using different values of the unlike dispersive energy parameter ξ_{12}. This is an expected results since properties of liquids, and particularly liquid composition along the vapour-liquid phase envelope, depend critically on the unlike binary dispersive energy ϵ_{12}.

5.3.2 THF + CH_4 binary mixture

In this section, we study the phase behaviour of the THF(1) + CH_4(2) binary mixture. As previously mentioned, the phase diagram of this system has not been investigated from the experimental point of view and no experimental data are available. We determine the phase behaviour of the mixture from the SAFT-VR approach using the molecular parameters of THF and CH_4, and the Berthelot combining rules to evaluate the unlike dispersive energy of the system (Eq. (5.4)), i.e., using $\xi_{12} = 1$. We follow this approach because experimental data are not available to judge the magnitude of the required correction in ξ_{12}. In addition to that, we have also obtained the phase diagram of the mixture using $\xi_{12} = 0.95$. One would expect that the true value for ξ_{12} for this mixture should lie between the unity and that of the THF(1) + CO_2(2) mixture, probably lying close to the latter. Hence, it would be very helpful in this regard to indicate what would happen to the phase diagram if one would choose $\xi_{12} = 0.95$.

As mentioned before, the THF(1) + CH_4(2) binary mixture exhibits type III phase behaviour. Fig. 5.3 shows the PT projection of the phase diagram. As can be seen, the behaviour of the system is governed by a huge LL immiscibility region located at temperatures below one of the branches of the fluid-fluid critical line of the mixture and high pressures. This branch of the fluid-fluid critical line, that runs from the critical point of the heaviest component (THF), changes continuously its character from vapour-liquid (at low pressures and temperatures close to the critical point of THF) to liquid-liquid as temperature decreases. The other branch of the gas-liquid critical line, which is very short, starts at the critical point of the lightest component (CH_4), ending at an upper critical end-point (UCEP) and meeting a three-phase liquid-liquid-vapour (LLV) line coming from low temperatures and pressures (see the inset of Fig. 5.3).

As it is well-known [79], the PT projection of the phase diagram corresponding to the three-phase line can be located at different relative positions with respect to the vapour pressure curve of the more volatile component. In this particular case, the LLV three-phase line lies entirely between the vapour pressure curves of both pure components, producing the presence of hereto-azeotropy and terminating at an UCEP located at a higher temperature than the critical temperature of the lightest component. The sensitivity of the SAFT-VR predictions using two different unlike dispersive interaction parameter ξ_{12} can be also observed in this Figure. As can be seen, a decrease of the value of ξ_{12} (from 1 to 0.95) produces an enlargement of the liquid-liquid immiscibility region of the phase diagram, i.e., for

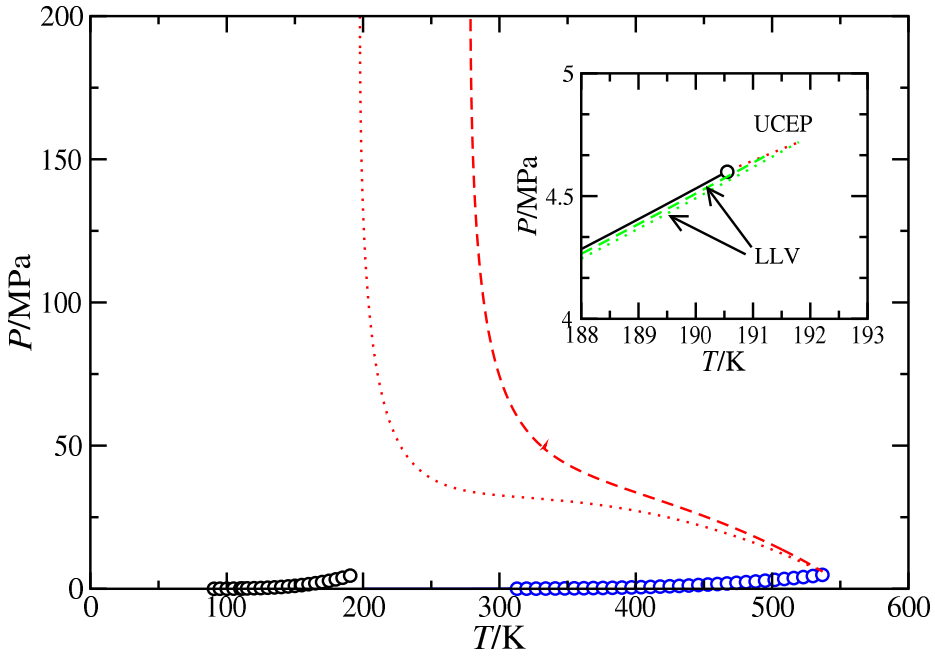

Figura 5.3: PT projection of the phase diagram for the THF(1) + CH_4(2) binary mixture. The circles correspond to the experimental vapour pressure data of pure THF [61] and pure CH_4 [78]. The continuous blue curves are the SAFT-VR predictions for vapour pressures, the dotted and dashed red curves are the theoretical predictions for the critical lines using $\xi_{12} = 1$ and 0.95, respectively, and the dashed and dotted green curves are the LLV three-phase lines predicted using $\xi_{12} = 1$ and 0.95, respectively. The inset shows the region close to the critical point of pure CH_4.

$\xi_{12} = 1.0$ THF and CH_4 become immiscible at $P \gtrsim 50\,\text{MPa}$ and $P \lesssim 200\,\text{K}$; however, for $\xi_{12} = 0.95$, the mixture exhibits liquid-liquid immiscibility below 280 K, approximately, for similar values of the pressure. This is an expected behavior since a decrease of the value of ξ_{12} provokes unfavourable dispersive interactions between THF and CH_4, and hence, a promotion of the liquid-liquid phase separation at higher temperatures.

The different VL and LL coexistence regions of the phase diagram of the THF(1) + CH_4(2) binary mixture become more apparent in constant-temperature Px and constant-temperature Tx slices of the PTx surface. We first consider constant-temperature Px slices at high temperatures and above the critical temperature of pure CH_4 and the UCEP of the mixture, $\sim 192\,\text{K}$. Fig. 5.4a shows six Px slices at different temperatures. The five highest temperatures, i.e., $T \geq 300\,\text{K}$, correspond to coexistence phases with gas-liquid character. As can be seen, as temperature decreases the gas-liquid character of the phase envelope continuously changes to a typical LL coexistence, especially at high pressures. This effect is clearly seen as the temperature is further decreased. $T = 260\,\text{K}$ can be viewed as an intermediate temperature at which the continuous transition from VL to LL character takes place. It is important, however, to recall that this transition is not only observed at constant pressure but also at a given temperature and varying the pressure. This is particularly clear in the Px slice, at which the system behaves as a liquid in coexistence with its vapour at low temperature, but exhibits LL immiscibility at high pressures.

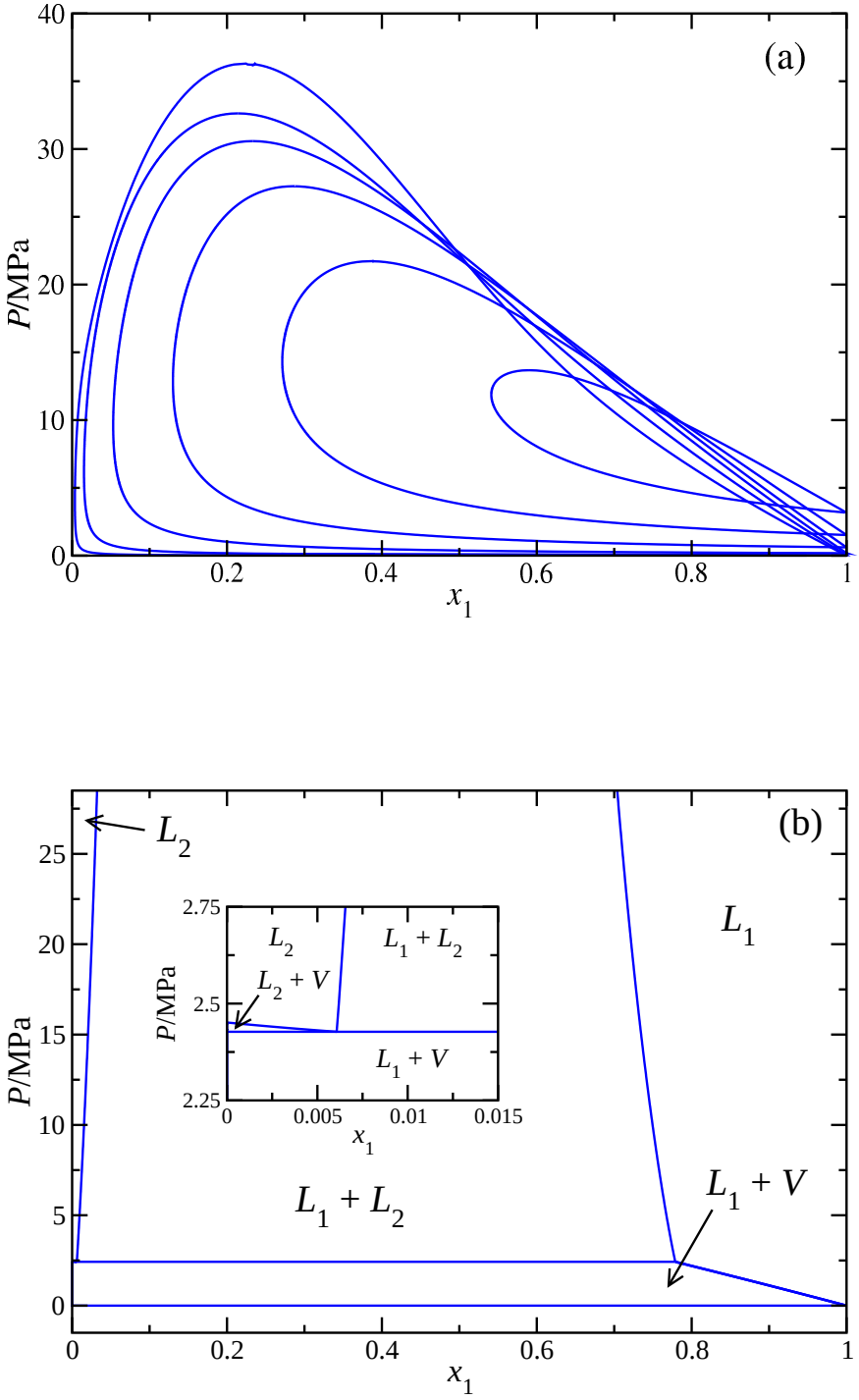

Figura 5.4: *Px* slices of the phase diagram for the THF(1) + CH_4(2) binary mixture as obtained from the SAFT-VR approach at (a) temperatures, from top to bottom of the relative maxima of the curves, 260, 300, 350, 400, 450, and 500, K , and (b) at 170, K. In all cases, only the Lorentz Berthelot combining rule for the unlike dispersive interaction is used ($\xi_{12} = 1.0$). The inset of part (b) shows the region close to the three-phase line in the methane-rich liquid phase.

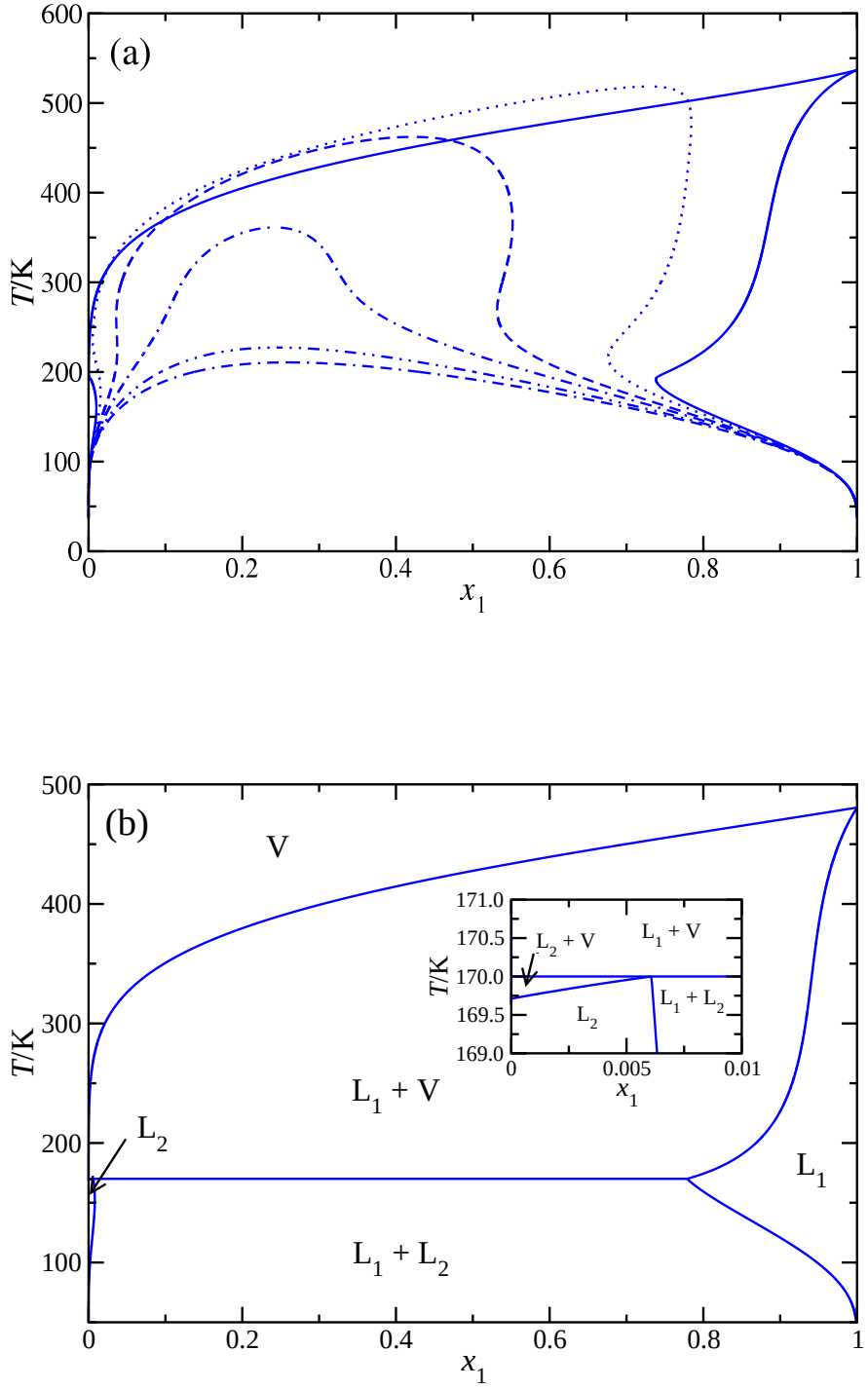

Figura 5.5: *Tx* slices of the phase diagram for the THF(1) + CH_4(2) binary mixture as obtained from the SAFT-VR approach at (a) pressures, from top to bottom of the relative maximum of the curves, 5, 10, 20, 30, 50, and 75 MPa, and (b) at 2.427 MPa. In all cases, only the Lorentz Berthelot combining rule for the unlike dispersive interaction is used ($\xi_{12} = 1.0$). The inset of part (b) shows the region close to the three-phase line in the methane-rich liquid phase.

We now turn our attention to the phase behaviour at much lower temperatures, close to but below the UCEP of the mixture and the critical point of pure CH_4. In Fig. 5.4b, a constant-temperature Px slice at 170 K is shown. As can be seen, since temperature is below the UCEP of the system, both VL and LL phase separation are seen in the same Px slice. At low pressures, below ~ 2.427 MPa, the system exhibits VL equilibria, the three-phase coexistence is observed at $P \approx 2.427$ MPa, and a huge LL immiscibility region is seen at higher pressures. There exists a second tiny VL region above the three-phase coexistence region, at THF compositions $x_1 \sim 0.005$, as can be seen in the inset of the Figure.

We have also studied a number of constant-pressure Tx slices of the PTx phase diagram of the mixture. Fig. 5.5a shows the phase envelopes at different pressures, from 5 up to 75 MPa. Note that since all pressures lie above the critical pressure of both components (critical pressures of pure THF and CH_4 are 5.02 and 4.6 MPa, respectively). The lowest pressure, 5 MPa, lies slightly below the critical pressure of pure THF. This results in a coexistence with vapour-liquid character at high temperatures and a region of liquid-liquid character at low temperatures, characteristic of mixtures that exhibit type III phase behaviour. At higher pressures (from 10 up to 75 MPa), the distinction between the gas and liquid phases becomes more difficult because the two phases in coexistence are fluids (liquid-like) with different densities.

We have analyzed, as in the case of the Px slices of the diagram diagram for the binary mixture, the phase behaviour at a lower pressure, 2.427 MPa, close to the UCEP of the mixture and the critical point of pure CH_4. Note that this pressure corresponds to the pressure of the LLV three-phase point of the system at 170 K, as discussed previously in the context of Fig. 5.4b. This means that the corresponding constant-temperature Tx slice of the phase diagram must show a LLV three-phase line at the same temperature, 170 K. As can be seen in Fig. 5.5b, above this temperature the system exhibits vapour-liquid phase separation, whereas below 170 K the system separates into two immiscible liquid phases, a L_1 liquid phase rich in THF and a second L_2 liquid phase rich in CH_4. As previously mentioned, at 170 K the system exhibits LLV phase separation, in agreement with results shown in Fig.5.4b. We have not shown the Px and Tx slices in the case $\xi_{12} = 0.95$ since a similar qualitative behavior is expected. Note that it is possible to have an approximate picture of them from a careful inspection and analysis of the PT projection of the phase diagram of the mixture shown in Fig. 5.3.

5.3.3 THF + H_2O binary mixture

Finally, we analyze in this section the phase behaviour of the last mixture considered, the THF(1) + H_2O(2) binary mixture. We focus in two different parametrizations used to the describe the global phase equilibria of the mixture. As we have discussed earlier, in the first case, referred to as set A, the intermolecular potential model parameters are obtained to ensure the best description of the maximum exhibited by the liquid-liquid critical line of the mixture. In the second case, referred to as set B, intermolecular potential model parameters are obtained to ensure the best description of the upper- and lower-critical end-points of the mixture.

Figure 5.6 shows the PT projection of the phase diagram for the THF(1) + H_2O(2) binary mixture. It is immediately clear that the SAFT-VR approach, using the set A of intermolecular potential model parameters developed in this work, predicts type VI phase behaviour, with a continuous gas-liquid critical line running between the critical point of the two pure components of the mixture, and a region of liquid-liquid immiscibility bounded below and above by a critical line which corresponds to the locus

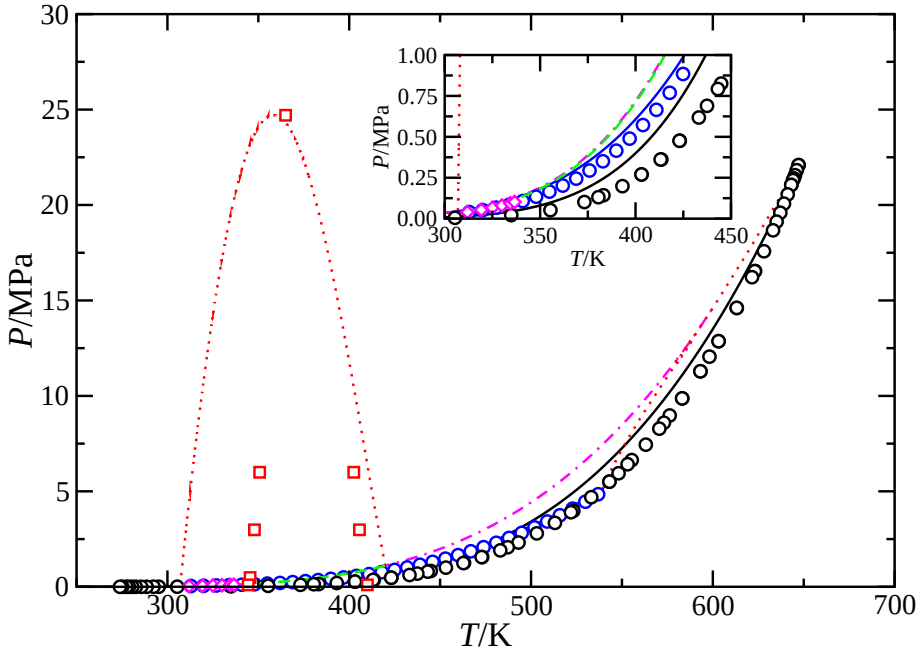

Figura 5.6: *PT* projection of the phase diagram for the THF(1) + H_2O(2) binary mixture. The curves are the SAFT-VR predictions using the set A of intermolecular potential model parameters and the symbols are the literature experimental data. The black and blue circles correspond to the experimental vapour pressure data of pure THF [61] and pure H_2O [80–88], the red squares are the UCST and LCST at different pressures [23, 24], and the magenta diamonds are the azeotropic points [89]. The continuous black and blue curves are the SAFT-VR predictions for the vapour pressures of THF and H_2O, respectively, the red dotted curves are the critical lines, the green dashed curve is the LLV three-phase line, and the magenta dot-dashed curve is the azeotropic line.

of the upper and lower critical solution temperatures (at different pressures). At low pressures, the liquid-liquid critical line ends at two critical end-points linked by a LLV three-phase line running from 314 to 420 K, approximately. In addition to that, the system exhibits positive azeotropy (the boiling point of the azeotrope is located at lower temperatures than the boiling point temperatures of both pure components). As can be seen in Fig. 5.6, the azeotropic line of THF(1) + H_2O(2) begins at 600 K approximately, being tangent to the continuous gas-liquid critical line of the system, and runs towards lower temperatures and pressures. This azeotropic line is well above the vapour pressure curves of pure THF and H_2O, including the low temperature and pressure regions (between the upper- and lower-critical end-points of the mixture), corroborating the positive character of the azeotropy, as it is shown in the inset of the Figure. This line is also close but slightly above the LLV three-phase line of the system.

The THF(1) + H_2O(2) system also exhibits a Bancroft point located at 480 K and 2.4 MPa, approximately. This feature is usually related to molecules that are dissimilar in chemical type or in shape but have similar vapour pressures. In this particular case, as can be seen in the Figure, the vapour pressure of H_2O is higher than that of THF above 480 K, i.e., H_2O is more volatile than THF at high temperatures. On the contrary, below the Bancroft temperature, THF is more volatile than H_2O (see both vapour pressure curves in the inset of the Figure).

Undeniably, the most salient feature of the PT projection of the phase diagram of the THF(1) + H_2O(2) binary mixture is the characteristic region of closed-loop liquid-liquid immiscibility exhibited by the system. As can be seen, the mixture is completely miscible at low temperatures, below the left-side liquid-liquid critical line running from the LCEP of the mixture up to high pressures, but also at high temperatures, above the right-side liquid-liquid critical line running from the UCEP of the mixture up to high pressures. At intermediate temperatures, inside the region of the phase diagram located between the LLV three-phase line and liquid-liquid critical line of the mixture, the system is immiscible. Note that the liquid-liquid immiscibility region is seen to disappear at a maximum in the pressure, usually called a hypercritical point.

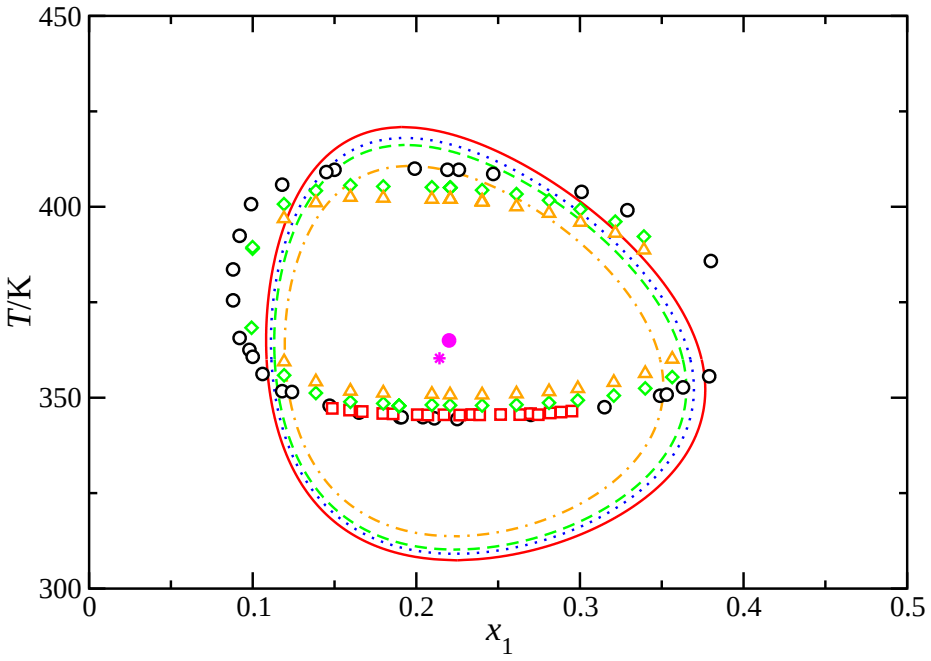

Figura 5.7: Tx closed-loops regions of liquid-liquid immiscibility for the THF(1) + H_2O(2) binary mixture. The symbols and curves correspond to experimental data taken from the literature [23, 24, 47] and SAFT-VR estimations using set A of molecular parameters, respectively, at pressures equal to 0.1 (black circles), 0.5 (red squares and continuous red curve), 2 (blue dotted curve), 3 (green diamonds and dashed green curve), and 6 MPa (orange triangles and dot-dashed orange curve). The magenta star and the filled magenta circle correspond to the hypercritical point, at 24.7 MPa, from experiment and theory, respectively.

As the Fig. 5.6 shows, the set A of intermolecular potential model parameters provides a reasonable description of the limited literature experimental data. The SAFT-VR approach is able to predict the conditions at which the azeotropic line exists, in good agreement with experimental data [89]. Note that, as seen in the inset of the figure, only experimental data for this line exists in the range of temperatures running form the LCEP temperature of the system up to 336 K, approximately. In addition to that, the theory is able to predict the point at which the closed-loop region of liquid-liquid immiscibility for the THF(1) + H_2O(2) system reaches a maximum pressure of $\sim$ 24.7 MPa, at 358 K and mixture composition $x_1 \sim 0.214$. This point, where LCST and UCST meet, is the so-called the hypercritical point of the mixture, as previously mentioned. This prediction is in excellent agreement with experimental values taken from literature, for which the maximum pressure, 24.7 MPa, is reached

at 365 K and mixture composition $x_1 = 0.22$ [23]. Thus, deviations between theory and experiment for the hypercritical point temperature and composition are as low as 1.4% and 2.7%, respectively.

We have also compared the predictions obtained from the SAFT-VR EoS with literature experimental data corresponding to the temperature-composition Tx slices of the phase diagram at conditions at which the system exhibits liquid-liquid immiscibility. As can be seen in Fig. 5.7, the set A of intermolecular potential model parameters presented in the previous section provides a reasonable description of the experimental liquid-liquid coexistence data in a wide range of temperatures and pressures. As in other cases in which SAFT-VR has been used to predict closed-loops of liquid-liquid immiscibility [43, 46, 90, 91], it is noticeable that the LCSTs are underpredicted while the upper critical temperatures are overestimated by the theory. Note that differences between theoretical predictions and experiments are larger in the case corresponding to the LCSTs than in the case of UCSTs. This behaviour is also in agreement with the estimation of the LCEP and the UCEP of the mixture. In the first case, the SAFT-VR EoS predicts a LCEP temperature equal to 306.9 K, a value an 11% lower than the experimental one ($T^{exp}_{LCEP} = 344.95$ K). In the second case, the theory overestimates the UCEP temperature of the mixture, predicting 419 K, a value 4.5% higher than the experiment ($T^{exp}_{UCEP} = 410.25$ K). It is important, however, to recall that the set A of molecular parameters is able to predict the phase diagram globally, including the coordinates of the hypercritical point associated to the liquid-liquid immiscibility, the LLV three-phase line, and the liquid-liquid closed-loop of immiscibility in a reasonable fashion.

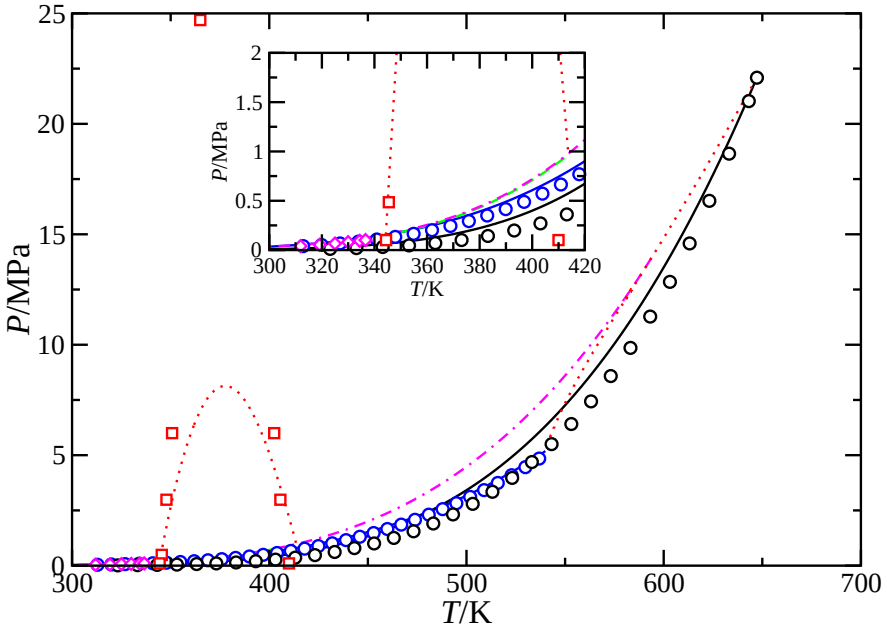

Figura 5.8: PT projection of the phase diagram for the THF(1) + H_2O(2) binary mixture. The curves are the SAFT-VR predictions using the set B of intermolecular potential model parameters and the symbols are the literature experimental data . The black and blue circles correspond to the experimental vapour pressure data of pure THF [61] and pure H_2O [80–88], the red squares are the UCST and LCST at different pressures [23, 24], and the magenta diamonds are the azeotropic points [89]. The continuous black and blue curves are the SAFT-VR predictions for the vapour pressures of THF and H_2O, respectively, the red dotted curves are the critical lines, the green dashed curve is the LLV three-phase line, and the magenta dot-dashed curve is the azeotropic line.

We now turn to the prediction of the global phase diagram of the THF(1) + H_2O(2) binary mixture using the set B of intermolecular potential model parameters. As previously mentioned, these parameters have been obtained to ensure the best possible description of the upper- and lower-critical end-points of the system. Figure 5.8 shows the pressure-temperature PT projection of the phase diagram of the mixture using this parametrization. As can be seen, the set B of model parameters also predicts type VI phase behaviour. Similarly to the case corresponding to the set A, SAFT-VR predicts the presence of positive azeotropy, with the azeotropic line running from the continuous vapour-liquid critical line, at 595 K and 14.1 MPa, towards lower pressures and temperatures. Note that the conditions at which the azeotropic line starts predicted using the set B of molecular parameters is nearly identical that those obtained using the set A. However, this is not the case for the LL and LLV coexistence at low temperatures.

As can be seen in Figure 5.8 and in the inset showing the region at which the UCEP and LCEP of the mixture exist, the set B of molecular parameters predicts very precisely the location of these two critical end-points. In particular, the theory predicts 343.3 and 413.8 K for the temperature of the upper- and lower-critical end-points of the mixture, respectively. This is in excellent agreement with experimental data taken from the literature (344.95 K and 410.25 K, respectively). As can be seen, SAFT-VR underestimates the temperature of the LCEP by 0.5% and overestimates the temperature of the UCEP by 0.9%. Unfortunately, this accuracy is not for free; the cost is a wrong prediction of the location of the hypercritical point of the system associated to the liquid-liquid critical point for the close-loop immiscibility. SAFT-VR predicts that this hypercritical point is at 8.1 MPa and 378 K, approximately, in bad agreement with experimental data taken from the literature (24.7 MPa and 358 K).

As in the case of the use of set A of molecular parameters, previously discussed in this section, we have also obtained the temperature-composition (Tx) slices of the phase diagram at high pressures, at which the system exhibits close-loop liquid-liquid immiscibility. As can be seen in Figure 5.9, SAFT-VR is able to predict very accurately the lower- and upper-critical solution temperatures of the mixture at different pressures, ranging from 0.1 up to 6 MPa. Unfortunately, the EoS overestimates the range in composition of component 1, THF, at which the system exhibits liquid-liquid immiscibility.

It is interesting to compare the predictions obtained from the SAFT-VR approach when using the two sets of parameters optimized in this work. In particular, comparison between Figures 5.7 and 5.9 provides an interesting insight on how the experimental data employed for estimating a particular set of model parameters determines SAFT estimations. The set A, is specifically selected for describing very accurately the location of the hypercritical point of the mixture in the PT projection of the phase diagram, and the set B is obtained for predicting the experimental LCEP and UCEP associated to the liquid-liquid immiscibility of the mixture. In the first case, in addition to an excellent description of the PT coordinates of hypercritical point of the mixture, the set A parameters are also able to predict reasonably well the width in compositions of the liquid-liquid immiscibility close-loops at all the pressures considered. However, predictions of the LCST and UCST are not so accurate. In particular, SAFT-VR overestimates and underestimates the LCST and UCST at all conditions, respectively. On the contrary, in the second case, in which the set B of intermolecular potential model parameters is used, agreement between theory and experiment is very good for the UCEP and LCEP of the mixture, as well as for the LCST and UCST of the system at all pressures considered; however, the predictions for the hypercritical point of the mixture and the width in compositions of the close-loop diagrams are clearly in worse agreement with experiment. One may be tempted to obtain different sets of model parameters for predicting all the properties mentioned above: the hypercritical point and the UCEP

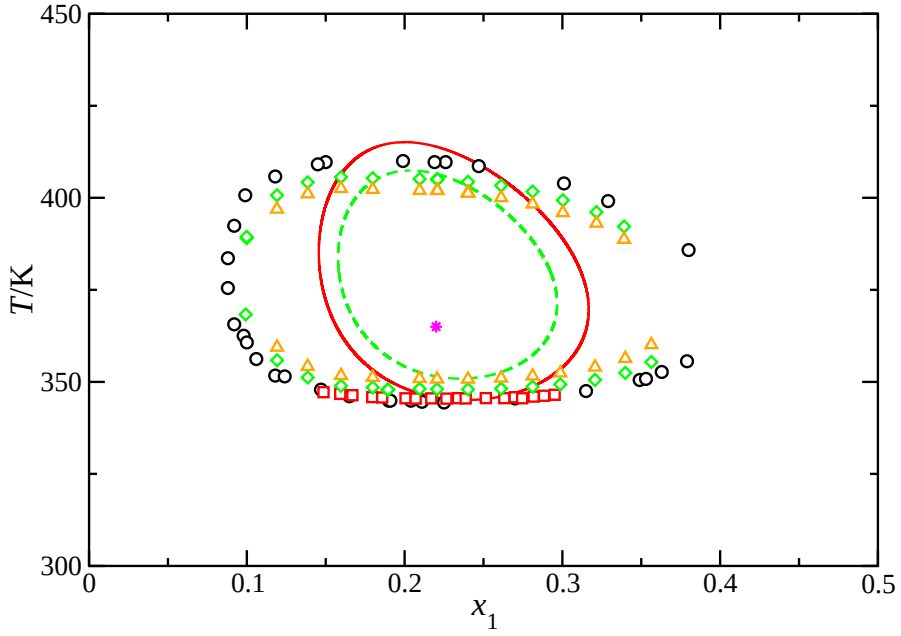

Figura 5.9: Tx closed-loops regions of liquid-liquid immiscibility for the THF(1) + H_2O(2) binary mixture. The symbols and curves correspond to experimental data taken from the literature [23, 24, 47] and SAFT-VR estimations using set B of molecular parameters, respectively, at pressures equal to 0.1 (black circles), 0.5 (red squares and continuous red curve), 3 (green diamonds and dashed green curve), and 6 MPa (orange triangles). The magenta star corresponds to the experimental hypercritical point at 24.7 MPa.

and LCEP of the system, as well as the LCST and UCST and the width in compositions corresponding to the liquid-liquid immiscibility close-loops. Is this ideal compromise possible? Certainly, using an analytical-based EoS, such as SAFT-VR or any other version that predicts classical behaviour near critical regions, the answer is no.

It is important to recall here that we are using molecular parameters of pure components that have been re-scaled to the experimental critical temperature and pressure. This allows using them to provide a good description of the coexistence compositions and critical curves. However, the use of these parameters produces a detriment in the calculated saturated liquid density of pure components, as it has been shown in previous works [30, 70, 94]. In summary, one may have a set of parameters describing accurately the critical region (i.e., re-scaled parameter) but with a poor description of the phase envelope at temperatures and/or pressure below the critical point, or a different set of parameters that predict precisely the phase envelope of the system (i.e., the usual optimized molecular parameters) but giving a poor description of the critical region. Similarly to that, systems that exhibit liquid-liquid immiscibility close-loops, as in the case of the THF(1) + H_2O(2) mixture, present the same problem. The sets A and B are able to describe reasonably well the experimental data taken from the literature associated to different regions and properties, but they are not able to predict all the magnitudes of interest within the whole phase diagram of the mixture. As in the case of pure systems and binary mixtures that exhibit vapour-liquid phase behaviour, a more satisfactory description of these systems could be obtained using a version of SAFT in combination with the renormalization-group theory or crossover treatment [71–74, 95].

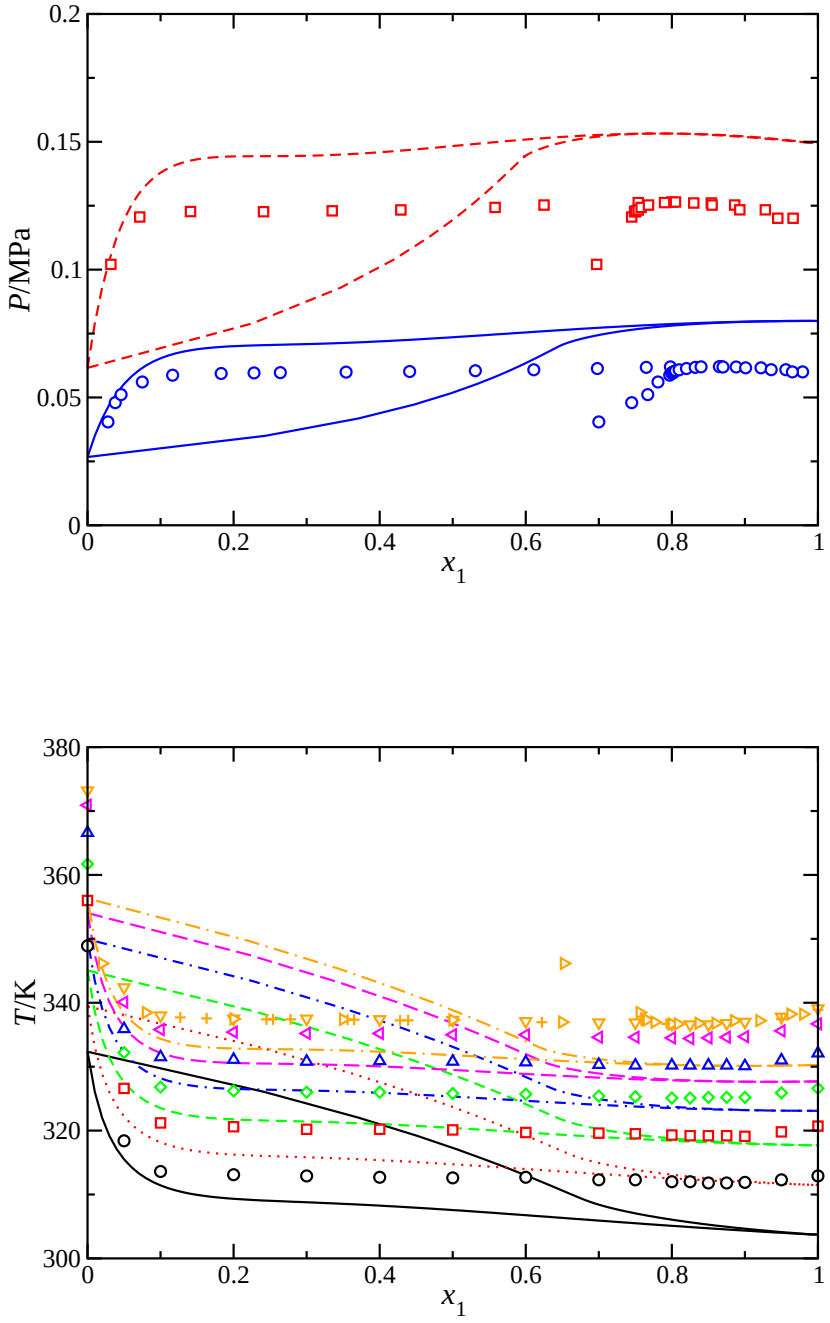

Figura 5.10: (a) *Px* and (b) *Tx* slices of the phase diagram for the THF(1) + H_2O(2). The symbols are the experimental data taken from the literature and curves are the predictions from SAFT-VR using the set B of intermolecular potential model parameters at: (a) 323.15 (blue circles [22] and continuous blue curve) and 343.15 K (red squares [22] and red dashed curve); (b) 0.04 MPa (black circles [89] and continuous black curve), 0.0533 MPa (red squares [89] and red dotted curve), 0.067 MPa (green diamonds [89] and green dashed curve), 0.08 MPa (blue up triangles [89] and blue dot-dashed curve), 0.093 MPa (magenta left triangles [89] and magenta long-dashed curve), and 0.1013 MPa (orange triangle down [89], orange triangle right [92], and orange plus [93], and orange dot-long-dashed curve).

We have also used the set B of molecular parameters to predict the vapour-liquid phase equilibria of the THF(1) + H_2O(2) binary mixture at low pressures. Fig. 5.10a shows the pressure-composition Px slices of the phase diagram at two different temperatures, both below the temperature lower-critical end-point of the mixture ($T_{LCEP} \approx 344.95\,\mathrm{K}$). As can be seen, the system exhibits positive azeotropy at both temperatures, at $x_1 \approx 0.86$ and $P \approx 0.062\,\mathrm{MPa}$ ($T = 323.15\,\mathrm{K}$) and $x_1 \approx 0.78$ and $P \approx 0.126\,\mathrm{MPa}$ ($T = 343.15\,\mathrm{K}$). Although SAFT-VR is able to predict the existence of this behaviour, the theory overestimates the pressures at which the system exhibits vapour-liquid separation. In particular, the EoS overestimates the pressure at the azeotropic point.

We have also considered the temperature-composition Tx slices of the phase diagram at low pressures, from 0.04 up to 0.1013 MPa. Unfortunately, only experimental data corresponding to the liquid-side of the phase diagram are available in literature. As can be seen in Fig. 5.10b, predictions obtained from SAFT-VR are able to predict the behaviour of the mixture at low pressures. One should take into account that the set of intermolecular potential model parameters used has not been fitted to predict the vapour-liquid phase behaviour but to describe accurately the lower- and upper-critical end-points of the mixture.

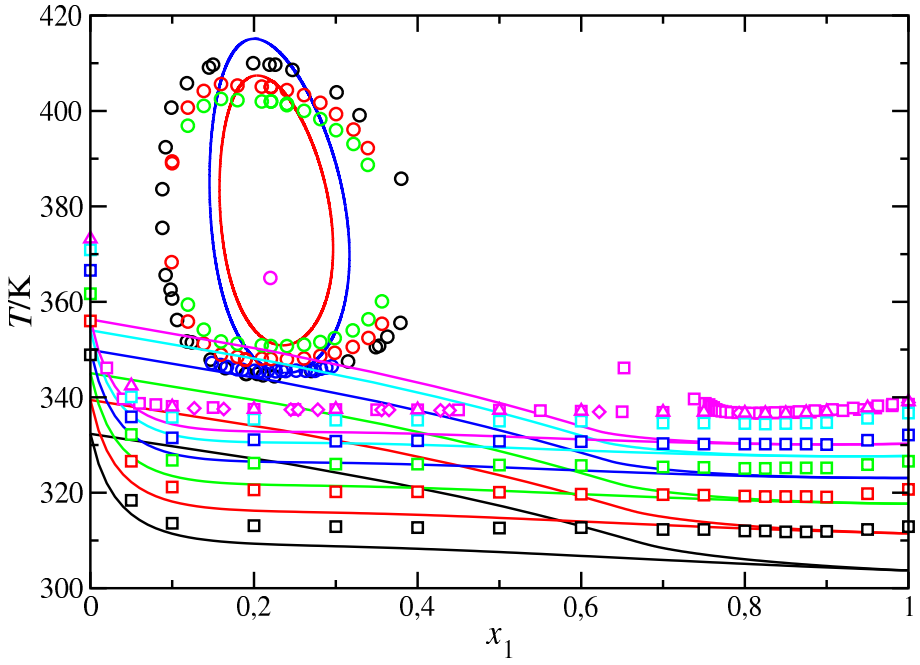

Figura 5.11: Tx slices of the phase diagram for the THF(1) + H_2O(2). The symbols are the experimental data taken from the literature and curves are the predictions from SAFT-VR using the set B of intermolecular potential model parameters at low pressures (vapour-liquid equilibria), 0.04 MPa (black squares [89] and black continuous curve), 0.0533 MPa (red squares [89] and red continuous curve), 0.067 MPa (green squares [89] and green continuous curve), 0.08 MPa (blue squares [89] and blue continuous curve), 0.093 MPa (light blue squares [89] and light blue curve), and 0.1013 MPa (magenta up triangles [89], magenta squares [92], and magenta diamonds [93], and magenta continuous curve), and at high pressures (liquid-liquid closed-loops), 0.1 (black circles), 0.5 (blue circles and continuous blue curve), 3 (red circles and red curve), and 6 MPa (green circles). The magenta circle corresponds to the experimental hypercritical point at 24.7 MPa. Experimental data have been taken from literature [23, 24, 47].

Fig. 5.11 shows the temperature-composition Tx slices of the phase diagram at low and high pressures, showing the vapor-liquid coexistence at pressures below 0.1 MPa and the closed-loops of liquid-liquid immiscibility at pressure above 0.1 MPa. As can be seen, the SAFT-VR approach in combination with the set B of molecular parameters is able to provide an excellent global description of the Tx slices of the phase diagram. It is important to recall again that the set B of molecular parameters have been used to provide the best possible description of the UCEP and LCEP of the mixture. However, this parametrization allows to describe reasonably well the whole phase diagram of the mixture.

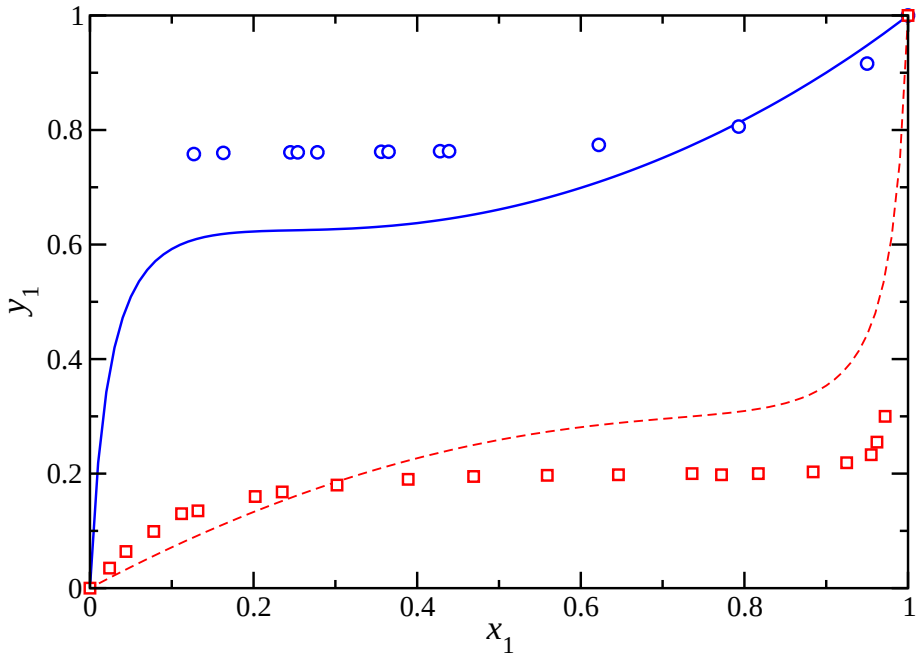

Figura 5.12: x_1y_1 slices of the phase diagram for the THF(1) + H_2O(2) binary mixture. The symbols are experimental data taken from the literature and curves are SAFT-VR estimations using the set B of intermolecular potential model parameters at 0.101325 MPa (blue circles [92] and continuous blue curve) and 303.15 K (red squares [96] and dashed red curve).

Finally, we have also represented composition-composition x_1y_1 slices of the phase diagram at 303.15 K and 0.101325 MPa. Fig. 5.12 shows the comparison between experimental data taken from the literature and SAFT-VR predictions using the set B of intermolecular potential model parameters. As can be seen, the theory is able to capture qualitatively the shape of the curves at the temperatures considered.

5.4 Conclusions

A global view of the fluid phase behaviour of the THF + CO_2(2), + CH_4(2), and + H_2O(2) binary mixtures is given using the SAFT-VR approach. We use a simple united-atoms approximation to model CO_2 and CH_4 molecules as chains formed by attractive spherical segments tangentially bonded

and a single sphere interacting via SW potentials, respectively. The H_2O molecule is modeled as spherical with four off-centre association sites (two sites are type H and two of type O). The THF molecule is also modeled as a chain formed by attractive spherical segments tangentially bonded together and interacting through the same type of intermolecular potential. Standard arithmetic combining rules are used to obtain the unlike segment size and potential range mixture parameters. We have also used standard geometric combining rules for the unlike energy parameter in most cases, although this parameter has also adjusted according to the modified geometric mean rule to give the best representation of the global fluid phase behaviour of some mixtures. In addition to that, two different mixture models have been developed to account for specific interactions (hydrogen bonding) between THF and H_2O molecules. The first set of intermolecular potential model parameters ensures an accurate description of the maximum exhibited by the liquid-liquid critical line of the mixture at high pressures (location of the hypercritical point), whereas the second one allows the best possible description of the upper- and lower-critical end-points of the mixture at low pressures.

We have used the mixture models to predict the fluid phase behaviour of the binary mixtures containing THF. We first examine the phase diagram of the simplest system, the THF(1) + CO_2(2) binary mixture, using two different mixture parameters. A set in which unlike mixture parameters are fully predicted from the molecular parameters of pure components and the original arithmetic and geometric combining rules, and a second one in which the unlike dispersive energy parameter is fitted to give the best possible representation of the continuous gas-liquid critical line of the mixture. Both theoretical results are able to describe accurately the critical line of the mixture. In addition to that, we have also examined the pressure-composition Px slices of the phase diagram at several temperatures. In all cases, agreement between theory and experiment is excellent for both sets of parameters, although the second set is able to provide a more accurate description of the mixture behaviour.

We have also analyzed the fluid phase behaviour of the second mixture, THF(1) + CH_4(2). Unfortunately, there is no experimental data in the literature for this mixture. The theory predicts type III phase behaviour for the mixture, i.e., a more complex phase diagram than the previous mixture, including now a continuous liquid-liquid critical line running from the upper-critical end-point of the system to the critical point of pure THF, and a fluid-fluid critical line that starts at the critical point of pure H_2O and extends towards high pressures. The theoretical predictions indicate that the system exhibits a huge region of liquid-liquid immiscibility at low temperatures and a vapour-liquid-liquid three-phase line at low temperatures and pressures, as expected for a mixture that exhibits type III phase behaviour.

Finally, we have determined the high-pressure phase behaviour of the THF(1) + H_2O(2) binary mixture using two sets of molecular parameters developed to account for the specific interactions (hydrogen bonding) between THF and H_2O molecules. The theoretical results correspond to type VI phase behaviour, in agreement with experimental data. In particular, the theory, using both sets of molecular parameters for association, accounts for the presence of the Bancroft point, the existence of positive azeotropy, and the closed-loop liquid-liquid immiscibility of the mixture. The first set of parameters, obtained to provide the best possible description of the hypercritical point of the mixture, is able to predict reasonably well the closed-loop liquid-liquid immiscibility, and particularly, its width in compositions at different pressures. The second set, however, which has been calculated to account for accurately the upper- and lower-critical end-points of the mixture, also predicts qualitatively the shape of the closed-loops, particularly the upper- and lower-critical solutions temperatures of the mixture at all pressures considered. We have also studied the vapour-liquid phase equilibria at low

pressures and temperatures using the set B of model parameters. All the calculations show good qualitative agreement with experimental data.

It is important to emphasize how a simple molecular approach, such as the SAFT-VR formalism, is able to account for the global phase behaviour of the THF(1) + CO_2(2), + CH_4(2), and + H_2O(2) binary mixtures, relying on very limited experimental mixture information and only one or two adjustable mixture parameter. Three of the four components considered in this work, THF, CO_2, and H_2O, are not particularly easy to model. In particular, THF and H_2O have strong electric dipole moments and CO_2 has a permanent electric quadrupolar moment. The good overall agreement we observe in the comparison with experimental data suggests that the approach used in this work contains the essential ingredients to predict the most-important features of the properties studied.

As a final comment, it is interesting to mention that the results obtained in this work have been used to provide detailed information for a Molecular Dynamics study of the interfacial properties of these mixtures. In particular, the vapor-liquid and liquid-liquid coexistence data of the binary mixtures is being used as initial guesses to set up the molecular simulation boxes of interfaces involving THF + CO_2, + CH_4, and + H_2O mixtures. This will provide important information on how united-atoms realistic simulation models available in the literature may predict accurately the interfacial properties of these mixtures, with particular emphasis on interfacial tension. Note that this property is probably one of the most sensitive thermodynamic property to the molecular details of a model and it allows to check its capability for predicting other thermodynamic properties. The second stage of our long-term goal, i.e., the selection of appropriate molecular simulation models for determining the phase equilibria and interfacial properties of these mixtures, allows to check which of the realistic molecular models under current study will be used to simulate the phase equilibria of clathrate hydrates in a near future.

5.5 Acknowledgement

We acknowledge Ministerio de Economía y Competitividad of Spain for financial support from projects FIS2012-33621 (M. M. P. and J. M. M.) and FIS2013-46920-C2-1-P (F. J. B. and J. A.), both cofinanced with EU Feder funds. J. M. M. acknowledges and Xunta de Galicia for a Postdoctoral Grant (ED481B2014/117-0). The french CARNOT Institute ISIFoR is also acknowledged for the funds provided through the THEMYS project (novel approaches in THErmodynamical modelling and Molecular simulation for the study of gas hYdrates and their applicationS). Further financial support from Universidad de Huelva and Junta de Andalucía is also acknowledged.

Bibliography

[1] R. Larsen, C. A. Knight, and E. D. Sloan *Fluid Phase Equilib.*, vol. 150, pp. 353–360, 1998.

[2] E. D. Sloan and C. Koh, *Clathrate Hydrates of Natural Gases.* New York: CRC PRess, 3 ed., 2008.

[3] J.-P. Torré, D. Haillot, S. Rigal, R. W. de Souza Lima, C. Dicharry, and J.-P. Bedecarrats *Chem. Eng. Science*, vol. 126, pp. 688–697, 2015.

[4] T. Makino, T. Sugahara, and K. Ohgali *J. Chem. Eng. Data*, vol. 50, pp. 2058–2060, 2005.

[5] J.-P. Torré, C. Dicharry, and D. Broseta *Chem. Eng. Science*, vol. 82, pp. 1–13, 2012.

[6] Y.-J. Lee, T. Kawamura, Y. Yamamoto, and J.-H. Yoon *J. Chem. Eng. Data*, vol. 57, pp. 3543–3548, 2012.

[7] L. J. Florusse, C. J. Peters, J. Schoonman, K. C. Hester, C. A. Koh, S. F. Dec, K. N. Marsh, and E. D. Sloan *Science*, vol. 306, no. 5695, pp. 469–471, 2004.

[8] H. Lee, J. W. Lee, D. Y. Kim, J. Park, Y. T. Seo, H. Zeng, I. L. Moudrakovski, C. I. Ratcliffe, and J. A. Ripmeester *Nature*, vol. 434, pp. 743–746, APR 7 2005.

[9] T. A. Strobel, C. A. Koh, and E. D. Sloan *Fluid Phase Equilib.*, vol. 261, pp. 382–389, DEC 1 2007. 11th International Conference on Propeties and Phase Equilibria for Product and Process Design, Crete, GREECE, MAY 20-25, 2007.

[10] V. V. Struzhkin, B. M. W. L., Mao, H.-K. Mao, and R. J. Hemley *Chem. Revs.*, vol. 107, pp. 4133–4151, OCT 2007.

[11] H. P. Veluswamy, R. Kumar, and P. Linga *Appl. Energy*, vol. 122, pp. 112–132, 2014.

[12] S. P. Kang and H. Lee *Environ. Sci. Technol.*, vol. 34, no. 20, pp. 4397–4400, 2000.

[13] M. Ricaurte, C. Dicharry, D. Broseta, X. Renaud, and J.-P. Torré *Ind. Eng. Chem. Res.*, vol. 52, no. 2, pp. 899–910, 2013.

[14] P. Babu, R. Kumar, and P. Linga *Energy*, vol. 50, pp. 364–373, 2013.

[15] P. J. Herslund, K. Thomsen, J. Abildskov, N. von Solms, A. A. Galfre, P. Brantuas, M. Kwaterski, and J.-M. Herri *Int. J. Greenh. Gas Control*, vol. 17, pp. 397–410, 2013.

[16] J. M. Míguez, M. C. dos Ramos, M. M. Piñeiro, and F. J. Blas *J. Phys. Chem. B*, vol. 115, no. 31, pp. 9604–9617, 2011.

[17] J. M. Míguez, J. M. Garrido, F. J. Blas, H. Segura, A. Mejía, and M. M. Piñeiro *J. Phys. Chem. C*, vol. 118, pp. 24504–24519, 2014.

[18] P. J. Herslund, K. Thomsen, J. Abildskov, and N. von Solms *Fluid Phase Equilib.*, vol. 356, pp. 209–222, OCT 25 2013.

[19] G. M. Kontogeorgis, E. C. Voutsas, I. V. Yakoumis, and D. P. Tassios *Ind. Eng. Chem. Res.*, vol. 35, pp. 4310–4318, July 1996.

[20] R. L. Scott and P. H. van Konynenburg *Discuss. Faraday Soc.*, vol. 49, pp. 87–97, 1970.

[21] P. H. van Konynenburg and R. L. Scott *Phil. Trans.*, vol. A298, pp. 495–540, 1980.

[22] J. Matouš, J. P. Noviák, J. Šobr, and J. Pick *Collect. Czech. Chem. Commun.*, vol. 37, pp. 2653–2663, 1972.

[23] A. Wallbruch and G. M. Schneider *J. Chem. Thermodynamics*, vol. 27, pp. 377–382, 1995.

[24] N. Riesco and J. P. M. Trusler *Fluid Phase Equil.*, vol. 228, pp. 233–238, 2005.

[25] B. Giner, F. M. Royo, C. Lafuente, and A. Galindo *Fluid Phase Equil.*, vol. 255, pp. 200–206, 2007.

[26] B. Giner, I. Gascón, H. Artigas, C. Lafuente, and A. Galindo *J. Phys. Chem. B*, vol. 111, no. 32, pp. 9588–9597, 2007.

[27] B. Giner, I. Bandrés, M. C. López, C. Lafuente, and A. Galindo *J. Chem. Phys.*, vol. 127, p. 144513, OCT 14 2007.

[28] B. H. Patel, P. Paricaud, A. Galindo, and G. C. Maitland *Ind. Eng. Chem. Res.*, vol. 42, pp. 3809–3823, 2003.

[29] F. J. Blas and A. Galindo *Fluid Phase Equil.*, vol. 194, pp. 501–509, 2002.

[30] A. Galindo and F. J. Blas *J. Phys. Chem. B*, vol. 106, pp. 4503–4515, 2002.

[31] I. Bandrés, B. Giner, M. C. López, H. Artigas, and C. Lafuente *J. Chem. Thermodyn.*, vol. 40, pp. 1253–1260, 2008.

[32] N. Nonay, I. Giner, B. Giner, H. Artigas, and C. Lafuente *Fluid Phase Equil.*, vol. 295, pp. 130–135, 2010.

[33] I. Giner, D. Mondaño, M. Haro, H. Artigas, and C. Lafuente *Fluid Phase Equil.*, vol. 278, pp. 62–67, 2009.

[34] W. Bol *Mol. Phys.*, vol. 45, pp. 605–616, 1982.

[35] I. Nezbeda, J. Kolafa, and Y. V. Kalyuzhnyi *Mol. Phys.*, vol. 68, pp. 143–160, September 1989.

[36] G. N. I. Clark, A. J. Haslam, A. Galindo, and G. Jackson *Mol. Phys.*, vol. 104, pp. 3561–3581, 2006.

[37] G. Jackson, W. G. Chapman, and K. E. Gubbins *Mol. Phys.*, vol. 65, no. 1, pp. 1–31, 1988.

[38] F. A. Carey, *Organic Chemistry*. New York: McGraw-Hill, 1987.

[39] T. Fukasawa, Y. Tominaga, and A. Wakisaka *J. Phys. Chem. A*, vol. 108, pp. 59–63, 2004.

[40] M. Ohtake, Y. Yamamoto, T. Kawamura, A. Wakisaka, W. F. de Souza, and A. M. V. de Freitas *J. Phys. Chem. B*, vol. 109, pp. 16879–16885, 2005.

[41] T. Takamuku, A. Nakamizo, M. Tabata, K. Yoshida, T. Yamaguchi, and T. Otomo *J. Mol. Liquids*, vol. 103, pp. 143–159, 2003.

[42] M. N. García-Lisbona, A. Galindo, G. Jackson, and A. N. Burges *Mol. Phys.*, vol. 93, pp. 57–71, 1998.

[43] G. N. I. Clark, A. Galindo, G. Jackson, S. Rogers, and A. N. Burgess *Macromolecules*, vol. 41, pp. 6582–6595, 2008.

[44] A. F. Cristino, S. Rosa, P. Morgado, A. Galindo, E. M. J. Filipe, A. M. F. Palavra, and C. A. N. de Castro *J. Chem. Thermodynamics*, vol. 60, pp. 15–18, 2013.

[45] A. F. Cristino, S. Rosa, P. Morgado, A. Galindo, E. M. J. Filipe, A. M. F. Palavra, and C. A. N. de Castro *Fluid Phase Equil.*, vol. 341, pp. 48–53, 2013.

[46] M. C. dos Ramos and F. J. Blas *J. Supercrit. Fluids*, vol. 55, pp. 802–816, 2010.

[47] J. Matouš, J. Hrnčiřík, J. P. Novák, and J. Šobr *Collect. Czech. Chem. Commun.*, vol. 35, pp. 1904–1905, 1970.

[48] A. Gil-Villegas, A. Galindo, P. J. Whitehead, S. J. Mills, G. Jackson, and A. N. Burgess *J. Chem. Phys.*, vol. 106, pp. 4168–4186, 1997.

[49] A. Galindo, L. A. Davies, A. Gil-Villegas, and G. Jackson *Mol. Phys.*, vol. 93, pp. 241–252, 1998.

[50] J. P. Hansen and I. McDonald, *Theory of Simple Liquids*. No. p 233 ss, Academic Press, 1990.

[51] J. A. Barker and D. J. Henderson *J. Chem. Phys.*, vol. 47, no. 8, p. 2856, 1967.

[52] J. A. Barker and D. J. Henderson *J. Chem. Phys.*, vol. 47, no. 11, p. 4714, 1967.

[53] J. A. Barker and D. J. Henderson *Rev. Mod. Phys*, vol. 48, no. 4, pp. 587–671, 1976.

[54] T. Boublík *J. Chem. Phys.*, vol. 53, pp. 471–472, 1970.

[55] G. A. Mansoori, N. F. Carnahan, K. E. Starling, T. W. Leland *J. Chem. Phys.*, vol. 54, p. 1523, 1971.

[56] W. G. Chapman, K. E. Gubbins, G. Jackson, and M. Radosz *Ind. Eng. Chem. Res.*, vol. 29, no. 8, pp. 1709–1721, 1990.

[57] M. S. Wertheim *J. Stat. Phys.*, vol. 35, no. 1–2, pp. 19–35, 1984.

[58] M. S. Wertheim *J. Stat. Phys.*, vol. 35-47, no. 1–2, p. 35, 1984.

[59] M. S. Wertheim *J. Stat. Phys.*, vol. 42, no. 3–4, pp. 459–476, 1986.

[60] M. S. Wertheim *J. Stat. Phys.*, vol. 42, no. 3–4, pp. 477–492, 1986.

[61] J. Safarov, M. Geppert-Rybczyńska, E. Hassel, and A. Heintz *J. Chem. Thermodynamics*, vol. 47, pp. 56–61, 2012.

[62] C. F. Jenkin and D. R. Pye *Philos. Trans. R. Soc. London Ser. A*, vol. 213, p. 67, 1914.

[63] J. M. Sengers, H. Levelt, and W. T. Chen *J. Chem. Phys.*, vol. 56, pp. 595–608, 1972.

[64] C. H. Meyers and M. S. van Dusen *J. Res. Nat. Bur. Std.*, vol. 10, pp. 381–412, 1933.

[65] L. A. Webster and A. J. Kidnay *J. Chem. Eng. Data*, vol. 46, pp. 759–764, 2001.

[66] J. G. Harris and K. H. Yung *J. Phys. Chem.*, vol. 99, pp. 12021–12024, 1995.

[67] P. Nowak, T. Tielkes, R. Kleinrahm, and W. Wagner *J. Chem. Thermodynamics*, vol. 29, pp. 885–889, 1997.

[68] J. Im, W. Bae, J. Lee, and H. Kim *J. Chem. Eng. Data*, vol. 49, p. 35, 2004.

[69] J. W. Ziegler, T. L. Chester, D. P. Innis, S. H. Page, and J. G. Dorsey *ACS Symposium series.*, vol. 608, pp. 93–110, 1995.

[70] A. Galindo, P. J. Whitehead, G. Jackson, and A. N. Burgess *J. Phys. Chem.*, vol. 100, pp. 6781–6792, 1996.

[71] C. McCabe and S. B. Kiselev *Fluid Phase Equil.*, vol. 219, pp. 3–9, 2004.

[72] C. McCabe and S. B. Kiselev *Ind. Eng. Chem. Res.*, vol. 43, no. 1, pp. 2839–2851, 2004.

[73] E. Forte, F. Llovell, L. F. Vega, J. P. M. Trusler, and A. Galindo *J. Chem. Phys.*, vol. 134, p. 154102, 2011.

[74] E. Forte, F. Llovell, J. P. M. Trusler, and A. Galindo *Fluid Phase Equil.*, vol. 337, pp. 274–287, 2013.

[75] Z. Knez, M. Škerget, L. Ilič, and C. Lütge *J. Supercrit. Fluids*, vol. 43, pp. 383–389, 2008.

[76] D. Kodama, T. Yagihashi, T. Hosoya, and M. Kato *Fluid Phase Equil.*, vol. 297, pp. 168–171, 2010.

[77] J. Li, M. Rodrigues, A. Pavia, H. A. Matos, and E. G. de Azevedo *J. Supercrit. Fluids*, vol. 41, pp. 343–351, 2007.

[78] B. D. Smith and R. Srivastava, *Physical Science Data: Thermodynamic Data for Pure Componentes, Part A: Hydrocarbons and Ketones. Vol. 25.* Elsevier:; New York, 1986.

[79] J. S. Rowlinson and B. Widom, *Molecular Theory of Capillarity.* Claredon Press, 1982.

[80] A. J. Apelblat *J. Chem. Thermodynamics*, vol. 31, no. 7, pp. 869–893, 1999.

[81] F. Keyes *J. Mech. Eng. Sci.*, vol. 53, pp. 132–135, 1931.

[82] I. M. Abdulagatov *J. Chem. Thermodynamics*, vol. 29, no. 12, pp. 1387–1407, 1997.

[83] I. M. Abdulagatov *J. Chem. Eng. Data*, vol. 43, no. 5, pp. 830–838, 1998.

[84] W. J. Gildseth *J. Chem. Eng. Data*, vol. 17, no. 4, pp. 402–409, 1972.

[85] N. S. Osborne *J. Res. Nat. Bur. Std.*, vol. 10, pp. 155–188, 1933.

[86] D. R. Douslin *J. Sci. Instrum.*, vol. 42, pp. 369–373, 1965.

[87] A. Egerton *Philos. Trans. R. Soc. London Ser. A*, vol. 231, p. 147, 1932.

[88] L. Besley *J. Chem. Thermodynamics*, vol. 5, pp. 397–410, 1973.

[89] H. Matsuda, N. Kamihama, K. Kurihara, K. Tochigi, and K. Yokoyama *J. Chem. Eng. Jpn.*, vol. 44, pp. 131–139, 2011.

[90] M. N. García-Lisbona, A. Galindo, G. Jackson, and A. N. Burges *Mol. Phys.*, vol. 93, pp. 57–72, 1998.

[91] M. N. García-Lisbona, A. Galindo, G. Jackson, and A. N. Burgess *J. Am. Chem. Soc.*, vol. 120, pp. 4191–4199, 1998.

[92] E. Sada, T. Morisue, and K. Miyahara *J. Chem. Eng. Data*, vol. 20, pp. 283–287, 1975.

[93] J. Pick *Collect. Czech. Chem. Commun.*, vol. 37, pp. 2653–2663, 1972.

[94] F. J. Blas *Mol. Phys.*, vol. 100, no. 14, pp. 2221–2240, 2002.

[95] F. Llovell, J. C. Pàmies, and L. F. Vega *J. Chem. Phys.*, vol. 121, pp. 10715–10724, 2004.

[96] J. N. Nayak, M. I. Aralaguppi, B. V. K. Naidu, and T. M. Aminabhavi *J. Chem. Eng. Data*, vol. 49, pp. 468–474, 2004.

Capítulo 6

On Interfacial Iroperties of Tetrahydrofuran: Atomistic and Coarse-Grained Models from Molecular Dynamics Simulation

Abstract

We have determined the interfacial properties of tetrahydrofuran (THF) from direct simulation of the vapor-liquid interface. The molecules are modeled using six different molecular models, three of them based on the united-atom approach and the other three based on a coarse-grained (CG) approach. In the first case, THF is modeled using the Transferable Parameters Potential Functions (TIPS) approach proposed by Chandrasekhar and Jorgensen [*J. Chem. Phys.* **77** 5073 (1982)] and a new parametrization of the TraPPE force fields for cyclic alkanes and ethers [*J. Phys. Chem. B* **115**, 11234 (2012)]. In both cases, dispersive and coulombic intermolecular interactions are explicitly taken into account. In the second case, THF is modeled as a single sphere, a diatomic molecule, and a ring formed from three Mie monomers according to the SAFT-γ Mie top-down approach [*J. Chem. Phys.* **140**, 054107 (2014)]. Simulations were performed in the Molecular Dynamics (MD) canonical ensemble and the vapor-liquid surface tension is evaluated from the normal and tangential components of the pressure tensor along the simulation box. In addition to the surface tension, we have also obtained density profiles, coexistence densities, critical temperature, density, and pressure, and interfacial thickness as functions of temperature, paying special attention to the comparison between the estimations obtained from different models and literature experimental data. The simulation results obtained from the three CG models as described by the SAFT-γ Mie approach are able to predict accurately the vapor-liquid phase envelope of THF, in excellent agreement with estimations obtained from TraPPE model and experimental data in the whole range of coexistence. However, Chandrasekhar and Jorgensen model presents significant deviations from experimental results. We also compare the predictions for surface tension as obtained from simulation results for all the models with experimental data. The three CG models predict reasonably well (but only qualitatively) the surface tension of THF, as a function of temperature, from the triple point to the critical temperature. On the other hand, only the TraPPE united-atoms models are able to predict accurately the experimental surface tension of the system in the whole temperature range.

6.1 Introduction

Tetrahydrofuran, c-$(CH_2)_4O$ or simply THF, is a cyclic ether widely used as solvent in many industrial processes. One of its various applications is the use as thermodynamic hydrate promoter [1, 2]. This molecule is able to form structure II (sII) hydrates [1] when mixed in stoichiometric ratio with water (17 H_2O molecules per THF molecule), at 277.15 K and atmospheric pressure. From an applied point of view, its effect on systems exhibiting hydrate phases is very important, because it produces a pronounced shift on the hydrates coexistence curves when used as an additive. This ability has been widely exploited to produce hydrates in appropriated temperature and pressure ranges depending on the application envisaged. As an example, several authors [3–5] used THF for applications as the reduction of the equilibrium pressure of H_2 clathrate hydrates, considering its application in H_2 storage cells [6, 7], and of carbon dioxide (CO_2) hydrates for environmental concerns related with greenhouse gas emission control and effects on global climate change [8–11].

During the last decades, remarkable progresses have been made on the development and application of the so-called molecular modeling techniques for the prediction of thermodynamic properties (*i.e.* phase equilibrium and interfacial properties) of an important number of complex mixtures of industrial interest. Examples of these methods are theoretical approaches based on a microscopic vision of the system, such as perturbation theories, Density Gradient Theory (DGT) or Density Functional Theory (DFT), and computer simulation methodologies [12–16], including Monte Carlo (MC) and Molecular Dynamics (MD). This wide range of techniques are being applied and used nowadays for the determination of equilibrium and non-equilibrium properties of hydrates, including phase equilibrium, and particularly the dissociation line of the hydrate phases (see e. g. Míguez *et al.* [17] and references therein), and other properties, such as kinetic and structural properties [2].

The success of these methods in predicting accurately the behaviour of complex mixtures depends critically on how precisely the chemical structure and intermolecular and intramolecular potential energies between the components of the system are known. This includes not only traditional systems that exhibit fluid-fluid phase equilibrium, but also systems that show hydrate phases, including carbon dioxide, methane, and THF hydrates. Different approaches to describe intermolecular potential of molecules as carbon dioxide, methane, and even water, have been extensively studied during last decades. However, the case of THF is different. Although this molecule is widely used as solvent in many processes, very limited work has been devoted to the determination of its thermodynamic properties, and phase equilibria in the case of mixtures of industrial interest.

For this reason, THF molecular models are scarce in literature. The first one was proposed in the 1980s by Jorgensen and collaborators in the context of the Transferable Parameters Potential Functions (TIPS), a series of force fields suitable for use in liquid simulations for water, alcohols, and ethers. In the seminal work of TIPS [18–20], the interaction sites for this molecule are located on oxygen, hydroxyl hydrogens, and the carbons in the alkyl groups, each site combining Coulombic and Lennard-Jones parameters chosen to yield reasonable structural and energetic results for both gas-dimers and pure liquids of water, alcohol (methanol and ethanol), and ethers. The model for THF in this framework was proposed by Chandrasekhar and Jorgensen [21, 22]. In particular, they considered Monte Carlo simulations of liquid THF and solutions in water, methanol, and also THF with and without pseudo-rotation of the cyclic ether. As for other TIPS models, the intermolecular potentials consist of Lennard-Jones and Coulomb terms, in the same way than those reported previously for ethers [23]. Several years later, Jorgensen and coworkers proposed the well-known Optimized

Potential for Liquid Simulations -or OPLS- force fields [24, 25], which can be regarded as an evolved version of the former TIPS approach. Unfortunately, the authors did not determine THF vapor-liquid coexistence, neither using TIPS or OPLS approaches.

More recently, Helfrich and Hentschke [26] and Girard and Müller-Plathe [27] examined several THF force fields and simulated different bulk and structural properties, although none of them considered the simulation of the vapor-liquid coexistence. Finally, Keasler *et al.* [28] developed a new version of the TraPPE-UA force fileld (Transferable Parameters for Phase Equilibria-United Atoms) specifically for five- and six-membered cyclic alkanes and ethers, including THF. In particular, they took into account that partial charges are molecule specific and thus they were parametrized using liquid-phase dielectric constants. This THF model is able to provide accurate saturated liquid densities and vapor pressures, critical temperatures and densities, and other important thermodynamic properties. Unfortunately, none of the works cited determined THF interfacial properties.

On the other hand, there has been an increasing effort during the last years in developing new coarse-grained (CG) intermolecular potential functions for the fluid state based on alternative top-down techniques. The usual bottom-up methodology, which is based on quantum-mechanical or atomic-level description of the interactions between real molecules, integrates out some (unwanted) degrees of freedom of the real system through different techniques and uses iterative simulation procedures to refine the parameters of the model. Examples of this methodology are the well known all-atom and united-atom force fields existing in the literature since the early 1980s. Following an opposite philosophy, the top-down methods are based on the use of an accurate equation of state to link macroscopic properties of the fluid state and force field parameters [29]. One of the most promising alternative is based on the group-contribution formulation of the statistical associating fluid theory (SAFT-γ) [30–32]. The specific version of this approach for molecules formed from heteronuclear chemical groups that interact through the Mie intermolecular potential, [33] referred to as SAFT-γ Mie [34], based on the latest enhanced version of the SAFT-VR Mie [35], can be used to estimate the corresponding force field. This information can then be used in direct simulations to obtain a great variety of thermodynamic, structural, interfacial, and dynamic properties. This top-down approach has neither been used so far to describe THF thermodynamic or interfacial properties. Another interesting point is that the ability of CG molecular models to describe complex real interfacial behavior has been pointed out recently for the case of multicomponent mixtures, [36] leading to a pertinent discussion concerning the comparison of their quantitative performance if compared with their counterpart atomistic molecular models.

Although the accurate description of bulk thermodynamic properties and phase equilibrium is essential to any sound molecular model, not every standard properties determined routinely from computer simulation exhibit the same sensitivity to the details of theoretical molecular models. However, fluid-fluid interfacial properties, and particularly surface tension, is one of the most sensitive properties to subtle differences in molecular details. These properties play a key role in many different fields, including nucleation or dynamics of phase transitions, and their knowledge is essential in a great number of practical and industrial applications. This has attracted the attention from simulators of the liquid community over the last years, allowing nowadays the accurate determination of these properties from computer simulation using different methodologies. Among all of them, surface tension is obviously the most important and challenging property to be determined and predicted in the context of inhomogeneous systems [12, 14, 15].

This work is the first of a series of papers in which models of THF and mixtures with other substances are developed and tested to predict accurately the phase equilibrium and interfacial properties of

these systems using computer simulation. The long-term goal of this work is to use the proposed molecular models to predict the phase equilibrium of THF hydrates and hydrates of mixtures of THF with methane and/or carbon dioxide. The particular objectives of this work are two. Firstly, to use some models existing in literature for predicting the vapor-liquid interfacial properties of THF; and secondly, to propose new CG molecular models for THF, based on the SAFT-γ Mie, able to describe the vapor-liquid phase equilibrium and interfacial properties of THF. In all cases, results obtained from MD simulation are compared with recommended experimental data [37] to critically assess the models ability. To our knowledge, this is the first time that the vapor-liquid interfacial properties, and particularly the surface tension, of THF is determined from computer simulations.

The rest of the paper is organized as follows. In the next section we summarize the molecular models considered, as well as the simulation details. Results and discussion are presented in Section III. Finally, in Section IV we present the main conclusions.

6.2 Molecular models and simulation details

6.2.1 SAFT-γ Coarse Grained Mie force field

As follows from the generic SAFT approach, [38, 39] the Helmholtz energy function of a fluid can be described on an additive basis as a contribution of several molecular effects

$$a = \left(a^{MONO} + a^{CHAIN} + a^{IDEAL}\right) \rho \frac{N_{av}}{\beta} \tag{6.1}$$

In the particular case of the SAFT-γ Mie model - which has been selected for performing Coarse-Grained molecular simulation - the mathematical structure of each contribution has been discussed in detail by Lafitte *et al.* [35] Briefly in Eq. (6.1), $a = A/(Nk_BT)$ and A is the total Helmholtz energy, N is the total number of molecules, N_{av} is the Avogadro constant, T is the temperature, k_B is the Boltzmann constant, $\beta = 1/(k_BT)$, and ρ is the molar density of the fluid. a^{MONO} represents a monomer (unbound) contribution for a chain composed of m_s tangential segments, a^{CHAIN} accounts for the formation of chain molecules and a^{IDEAL} is the ideal gas contribution.

In the framework of CG force fields, the pure fluids will be modeled as freely jointed tangential non associating spheres characterized by five parameters: the molecular chain length (or number of segments) m_s, the repulsion and attraction parameters of the intermolecular potential λ_r and λ_a, the energy scale or potential well depth ε, and the length scale, roughly equivalent to a segment diameter σ, which can be found from three alternative routes. The first or traditional way is to force the EoS to fit the available fluid phase equilibrium data (experimental measurements or molecular simulation data), (*i.e.*, vapor pressure and liquid density data), and second derivative properties. [40] A second option is using the corresponding states principle [41, 42], in terms of conformational parameters of the Mie potential. In the latter case, as it was recently demonstrated, once m_s and λ_a are fixed, the remaining parameters can be calculated using the acentric factor (which defines the λ_r value), critical temperature (which defines the ε value) and the liquid density evaluated at 0.7 of the critical temperature (which defines the σ value). Finally, following the general methodology proposed by Segura *et al.* [43, 44], the molecular parameters of pure fluids can be calculated by forcing the EoS to exactly reproduce the experimental vapor pressure, the local slope of the vapor pressure curve, and

the density and compressibility of the liquid phase at one single reference temperature in terms of the theory of displacements [45, 46].

Tabla 6.1: SAFT-γ Mie CG force field parameters for THF

m_s	ε/k_B (K)	σ (A)	λ_r	λ_a
1^a	668.797	5.401	47.07	6.00
2^b	348.920	3.840	14.85	6.00
3^c	261.632	3.350	13.63	6.00
3^d	277.080	3.359	13.63	6.00

[a]Monomer Configuration
[b]Dimer configuration
[c]Ring configuration
[d]Refined parameters for the Ring configuration

In this work we modeled THF as a single- and double-segment pearl-necklace model, without any additional electrostatic interactions, estimated from the corresponding states principle (or critical data) proposed by Mejía *et al.* [41]. This methodology has shown great flexibility to characterize vapor-liquid interfacial properties of pure fluids [47] and complex mixtures of dilute surfactant solutions [48] and natural gases and condensates. [47, 49–51] Table 6.1 summarizes the SAFT parameters for THF as used in molecular simulations in this work. Nevertheless, the methodology proposed by Mejía *et al.* [41] can not be used directly in a rigid configuration, because energy contribution in Eq. (6.1) due to the formation of m_s-membered ring from a theoretical point of view is different. [52–54] Firstly, the approximation in the Helmholtz energy contribution of ring structures (*i.e.* $a^{RING} \approx -m_s \ln g^{Mie}(\sigma)$) suggested by Lafitte *et al.* [55] has been used to obtain initial values of force field parameters. It has been noted that the protocol generalized by Segura *et al.* [43, 44] allows a great compromise between the properties of the pure fluid and the SAFT-γ Mie model. This means, of course, that the theoretical description will not provide a perfect match between theory and molecular simulation. Indeed, following the *recipe* provided in Refs. [40, 55–57] force field parameters of the rigid model (σ, ε) have been rescaled to match the simulation results with the theoretical prediction and recommended experimental data from DECHEMA. [37] Table 6.1 summarizes also a set of SAFT-γ parameters for the THF three-segment ring configuration. On one hand, model 3c in Table 6.1 corresponds to a set of model parameters recommended for use in theoretical predictions for fluid properties of THF. On the other hand, force fields of model 3d (refined parameters) are recommended for use in molecular simulations. The reader is referred to Ref. [55] for further details.

6.2.2 United-atom force field models

As we have mentioned, THF has been also modeled following the united-atom approach. We use three different models to describe this cyclic ether. In all cases, the force fields use the Lennard-Jones and Coulomb potentials to describe the non-bonded interactions,

$$U(r_{ij}) = 4\epsilon_{ij}\left[\left(\frac{\sigma_{ij}}{r_{ij}}\right)^{12} - \left(\frac{\sigma_{ij}}{r_{ij}}\right)^{6}\right] + \frac{q_i q_j}{4\pi\epsilon_0 r_{ij}} \tag{6.2}$$

where r_{ij} is the distance between interacting sites i and j, σ_{ij} and ϵ_{ij} are the diameter and well depth

associated to the LJ intermolecular potential, q_i and q_j are the partial charges on interaction sites i and j, and ϵ_0 the permittivity of vacuum. All the LJ parameters for unlike interactions are obtained always using the Lorentz-Berthelot combining rules.

In all the united-atoms models used in this work, THF molecule is described with three different types of united-atom chemical groups. The ether group or oxygen atom, O, the α-methyl (α-CH_2) united atoms bonded directly to the oxygen atom, and the β-methyl (β-CH_2) united atoms bonded to the α-methyl chemical group. In addition to that, partial charges are placed on the interaction sites of the oxygen atom and the α-CH_2 and β-CH_2 chemical groups. Molecular parameters for the LJ diameter and well depth of different chemical units, as well as values of partial charges are given in Table 6.2.

We first consider the rigid version of the model proposed by Chandrasekhar and Jorgensen [21, 22], in which THF can be viewed as a planar and rigid cyclic ether. In this case, since the molecule is rigid, nor bending neither torsional intramolecular potentials are needed. Molecular parameters due to the non-bonded interactions between THF molecules are collected in Table 6.2. Note that, apart from the negative partial charge located at the ether group to account for its electronegativity, the α-CH_2 chemical groups have positive partial charges allowing the model to mimic the molecular electric dipole moment. However, the β-CH_2 groups do not have any partial charge associated. This is probably one of the most important differences between this model and the TraPPE-UA model. As we will see in the following, this and other differences in the molecular parameters produce important differences in the thermodynamic and interfacial properties estimations.

We also consider the original TraPPE model of Keasler *et al.* [28]. In this model, as usual in TraPPE force fields, the bond lengths between different chemical groups are fixed. Monomeric units separated by two bonds interact through a harmonic bending potential with the usual form, with bending force constants taken from the TraPPE-UA force field for n-alkanes and ethers [28]. Interactions between beads separated by three bonds are described through a torsional intramolecular potential energy represented by a cosine series [28]. For further details on the TraPPE-UA force field we recommend the original paper of Keasler *et al.* [28]

Finally, following a similar approach than the case of the Chandrasekhar and Jorgensen model, we consider an approximated, planar, and rigid TraPPE model, in which non-bonded LJ intermolecular parameters and partial charges located at the different chemical groups are identical to those of the original TraPPE model. In addition to that, bending and torsional degrees of freedom are frozen, i.e., we consider that the equilibrium bond angles are fixed and the molecule has no torsional degrees of freedom. As an additional approximation, THF is considered in this case not only rigid but also planar.

Tabla 6.2: TraPPE-UA and Jorgensen force field parameter for nonbonded interactions of THF.

Atom	ε/k_β(K)	σ[Å]	q[e]
THF (TraPPE-UA)			
O	190	2.20	-0.410
$CH_2(\alpha)$	56.3	3.88	0.160
$CH_2(\beta)$	56.3	3.88	0.045
THF (Jorgensen)			
O	85.47	3.00	-0.5
$CH_2(\alpha)$	59.39	3.80	0.25
$CH_2(\beta)$	59.39	3.905	0.0

6.2.3 Simulation details

All MD simulations are carried out in conditions at which the vapor-liquid interface is present, following the standard methodology [16, 58] for all models studied. In particular, simulations are performed in the NVT canonical ensemble using GROMACS (version 4.6.1) [59] at a fixed temperature T, in a parallelepipedic simulation cell of constant volume $V = L_x \times L_y \times L_z$, where L_x, L_y, and L_z are the dimensions of the simulation box. We use periodic boundary conditions in all three directions. A homogeneous liquid system is first equilibrated in a rectangular simulation box of dimensions $L_x = L_y = 14\sigma$ and $L_z = 32\sigma$. We consider N=12500, 6250, 2800 for systems formed from 1, 2, and 3 monomers in the case of CG models (See Table 6.1) and 2430 molecules for UA simulations. After equilibration of this bulk-liquid system, the box is expanded to three times its original size along the z direction leaving the liquid phase slab at the center. The final overall dimensions of the vapor-liquid-vapor configuration box are therefore $L_x = L_y = 14\sigma$, and $L_z = 92\sigma$ for each system. In order to reduce the truncation and system size effects involved in the phase equilibrium and interfacial properties calculations, the cut-off radius (r_c) has been taken equal to a large value of 7σ. It has been shown by several authors [60–62] that a cut-off above six diameters provides a reliable description for the interfacial properties. However, it was shown by Dinpajooh *et al.* [63], it is thus natural to consider larger cut off values when the objective is obtain a reliable predictions of critical properties. Long-range interactions are determined using three-dimensional Ewald technique with a convergence parameter of 0.1 Å^{-1} and a maximum value for the reciprocal lattice equal to 31 is used.

We have used a Verlet leapfrog [64] algorithm with a time step of 0.002 ps for the case of CG models, Jorgensen-UA (rigid model) and the simplified TraPPE-UA model (rigid model). It is important to note in this case that a time step of 0.001 ps has been necessary to sample correctly the torsional potential in the case of rigorous TraPPE-UA model (flexible model). A Nosé-Hoover thermostat [65] with large time constant equal to 1.0 ps has been used. After the system reaches equilibrium, the properties of the coexisting vapor and liquid phases can be obtained as appropriate averages during 10 ns (including an equilibration period of 5 ns). In order to estimate errors on the variables computed, the sub-blocks average method has been applied. [66] In that approach, the production period is divided into n independent blocks. The statistical error is then deduced from the standard deviation of the average $\bar{\sigma}/\sqrt{M}$, where $\bar{\sigma}$ is the variance of the block averages and M has been fixed in this work to $M = 10$.

The equilibrium vapor pressure, P_v, and interfacial tension, γ, are obtained from the diagonal components of the pressure tensor. The vapor pressure corresponds to the normal component, $P_v = P_{zz}$, of the pressure tensor, while the interfacial tension is obtained using the mechanical route [13, 67–69] as:

$$\gamma = \frac{L_z}{2}\left[P_{zz}(z) - \frac{P_{xx}(z) + P_{yy}(z)}{2}\right] \tag{6.3}$$

In Eq. (6.3), the additional factor 1/2 comes from having two interfaces in the system, and L_z is the size of the simulation box in the z direction, defined along the longitudinal dimension across the interface. The critical pressure, P_c, temperature, T_c, and density, ρ_c have been obtained from the vapor-liquid equilibrium results, presented in Table 6.3 and Table 6.4, using the scaling laws [12, 70] given by:

$$\rho_L - \rho_V = A\,(T - T_c)^{\beta} \tag{6.4}$$

and the corresponding law of rectilinear diameters

$$\frac{\rho_L + \rho_V}{2} = \rho_c + B\,(T - T_c) \tag{6.5}$$

β is the corresponding critical exponent, with a universal value of $\beta = 0.325$ [13], and A, B, T_c and ρ_c are four unknown constants obtained fitting to the simulation results. ρ_L and ρ_V are the liquid and vapor coexistence densities at the corresponding temperature T. Alternatively, an independent way to calculate T_c is to apply the scaling laws for the case of interfacial calculations. [71] Following this route, γ is related to T_c by the following expression:

$$\gamma = \gamma_0\,(1 - T/T_c)^{\mu} \tag{6.6}$$

where γ_0 is the so-called "zero-temperature" surface tension and μ is the corresponding critical exponent. Here, we fix μ to the universal value $\mu = 1.258$ as obtained from renormalization-group theory. [13]. Once again, the unknown constants, γ_0 and T_c are found by fitting the interfacial tension data with temperature. Finally, the critical pressure is estimated from an extrapolation of the Clausius-Clapeyron relation to the critical temperature obtained from Eq. (6.4) or Eq. (6.6)

$$\ln P = C_1 + \frac{C_2}{T} \tag{6.7}$$

where C_1, and C_2 are correlation parameters. Results obtained in this work from the analysis of the simulation data using Eqs. (6.4)-(6.7) are presented in Table 6.5.

6.3 Results and discussion

In this section we present the main results from the simulations of tetrahydrofuran (THF) using three different coarse grained models and three different UA models. We focus on the interfacial properties, such as density profiles, interfacial thickness, and surface tension. We also examine the temperature dependence of these properties, and compare our results for the different models with literature experimental data. [37] In particular, we compare the results corresponding to predictions from the different coarse grained models and the three UA models considered in this work.

We follow the same analysis and methodology than in our previous works [72–75], and consider different temperatures for all the models analyzed. In order to characterize the bulk phase and interfacial behaviour, density profiles are calculated by dividing the system in 250 slabs along the z direction. The molecular density profiles, $\rho_i\,(z)$, are obtained by assigning the position of each united atom center, z_i, to the corresponding slab and constructing the molecular density from mass balance considerations. The bulk vapor and liquid densities in each system are obtained by averaging $\rho_i\,(z)$ over appropriate regions sufficiently removed from the interfacial region. In addition to that, the final bulk vapor density value, at each temperature and chain length, is obtained after averaging the density profiles on both sides of the liquid film. Another interesting property that can be obtained from the calculation of density profiles is the interfacial width along the liquid-vapor equilibrium. Implicitly this

property is defined by fitting the curves from the original mean field van der Waals theory, [12, 13] described by

$$\rho(z) = \frac{\rho_L + \rho_V}{2} - \frac{\rho_L - \rho_V}{2} \tanh\left[\frac{\alpha(z - z_0)}{d}\right] \tag{6.8}$$

where the constant $\alpha = 2\tanh^{-1}(0.8)$ is chosen so that d is the 10-90 interfacial thickness and z_0 the position of the Gibbs dividing surface. As mentioned, coexistence densities have been calculated previously, therefore d and z_0 are treated as adjustable parameters in Eq. (6.8). As for the calculation of the bulk vapor density, our reported values of d correspond to the average of the values for both interfaces in the system. Values determined this way are always found to be coincident to within statistical uncertainty; indicating that the inhomogeneous systems are properly equilibrated at all temperatures. The statistical uncertainty of these values is estimated from the standard deviation of the mean values. For the six THF models studied here, Tables 6.3 and 6.4 summarize the numerical values of the MD simulations and the corresponding statistical deviations.

Tabla 6.3: Vapor pressure P, liquid density ρ_L, vapor density ρ_V, 10-90 interfacial thickness d, and surface tension γ at different temperatures for CG force fields of THF formed from tangentially bonded segments (m_s). The errors are estimated as explained in the text.

m_s	T / K	P / MPa	ρ_L / (kg/m^3)	ρ_V / (kg/m^3)	d / nm	γ / (mN/m)
	300	0.0017(2)	868.8(3)	0.347(8)	0.768(5)	27.5(9)
	325	0.07(1)	829.7(2)	1.91(1)	0.887(5)	25.5(7)
	350	0.156(2)	813(2)	4.12(2)	1.305(3)	21.9(7)
	375	0.29(1)	775(2)	7.74(4)	1.153(2)	17.7(7)
1[a]	400	0.56(2)	749(2)	13.6(5)	1.848(3)	14.5(5)
	425	0.88(3)	724.4(3)	21.89(5)	1.64(3)	11.0(9)
	450	1.451(4)	673(3)	34.8(6)	2.17(2)	8.1(7)
	475	2.18(4)	629(3)	52.7(6)	2.52(2)	6.9(4)
	500	3.118(7)	579(3)	80.9(1)	3.356(9)	3.5(6)
	520	4.028(9)	531(3)	110.3(1)	3.96(3)	2.6(9)
	300	0.002(2)	881.3(2)	0.656(9)	0.747(2)	28.78(1)
	325	0.043(2)	853(2)	1.791(1)	0.823(6)	26.94(1)
	350	0.132(2)	822(2)	3.16(3)	0.959(4)	22.27(7)
	375	0.24(2)	792.6(2)	7.44(4)	1.121(4)	20.03(8)
2[b]	400	0.487(2)	758.5(2)	12.34(2)	1.57(3)	15.13(9)
	425	0.87(3)	722.6(2)	20.3(5)	1.675(3)	13.1(5)
	450	1.40(2)	686(3)	33.2(4)	1.903(2)	8.94(7)
	475	2.07(5)	640(3)	50.7(6)	2.221(1)	7.05(7)
	500	3.111(8)	588(3)	79.9(1)	2.78(9)	3.93(9)
	520	4.081(1)	536.4(3)	105.7(1)	3.87(1)	1.95(9)
	300	0.006(9)	883.1(3)	0.444(8)	0.685(4)	28.91(1)
	325	0.026(2)	854.8(2)	1.614(1)	0.789(4)	25.7(7)
	350	0.14(2)	823.8(2)	3.01(2)	0.917(3)	23.39(4)
	375	0.25(2)	792(2)	6.62(4)	1.07(5)	19.22(7)
3[c]	400	0.531(2)	758(2)	12.12(2)	1.317(7)	15.59(5)
	425	0.89(4)	719.1(3)	19.9(5)	1.532(2)	12.59(9)
	450	1.405(3)	681(3)	31.2(4)	1.67(3)	8.39(4)
	475	2.153(7)	634.8(3)	52.7(6)	2.381(7)	5.49(6)
	500	3.177(7)	579(3)	83.6(1)	1.72(3)	3.35(7)
	520	4.22(8)	514(4)	121.4(1)	4.36(5)	1.37(9)

[a] Monomer configuration
[b] Dimer configuration
[c] Refined parameters for the Ring configuration (See Table 6.1)

Tabla 6.4: Vapor pressure P, liquid density ρ_L, vapor density ρ_V, 10-90 interfacial thickness d, and surface tension γ at different temperatures by the different UA force fields for THF. The errors are estimated as explained in the text.

UA-Model	T / K	P / MPa	ρ_L / (kg/m^3)	ρ_V / (kg/m^3)	d / nm	γ / (mN/m)
	200	0.4050(9)	978(6)	0.0(0)	00	46(3)
	250	0.00(9)	930(3)	0.0(0)	0.537(3)	38.4(17)
	300	0.02(1)	881(3)	0.0(0)	0.6926(14)	30.7(13)
Jorgensen	350	0.11(10)	830(3)	3.07(13)	0.883(4)	24.1(11)
	400	0.4(4)	775(3)	9(1)	1.1221(13)	18.0(12)
	450	1.2(6)	713(3)	25.8(8)	1.527(19)	11.54(10)
	500	2.5(8)	633(3)	58.5(9)	2.008(13)	6.4(7)
	200	0.0(1)	964(3)	0.0(0)	0.431(8)	41.3(1)
	250	0.0(1)	913(3)	0.113(2)	0.58(6)	32.9(1)
	300	0.045(1)	861(3)	1.22(1)	0.754(1)	26.5(1)
	325	0.086(2)	834(3)	2.35(2)	0.857(2)	22.9(1)
	350	0.209(2)	805.4(3)	5.2(3)	1.14(1)	19.9(1)
Rigid TraPPE	375	0.37(3)	775.4(2)	9.1(4)	1.208(7)	16.5(9)
	400	0.67(5)	742.3(2)	16.2(6)	1.37(5)	13(1)
	425	1.085(6)	708(3)	26.4(6)	1.514(3)	11(1)
	450	1.67(9)	669.4(2)	41.1(8)	2.01(3)	7.5(2)
	475	2.4(1)	622(3)	60.5(8)	2.166(4)	4.6(1)
	500	3.49(11)	560(3)	98(1)	3.2(2)	3.3(1)
	200	0.0(0)	974.4(3)	0.0(0)	0.404(3)	40.52(5)
	250	0.0(0)	923.51(3)	0.08(6)	0.56(5)	34.3(4)
	300	0.0(7)	872.3(4)	1.01(4)	0.743(4)	27.43(7)
TraPPE	350	0.0(7)	817(5)	4.97(5)	0.952(4)	20.45(3)
	400	0.26(1)	756(1)	14.74(9)	1.346(2)	14.29(3)
	450	1.28(5)	681.3(3)	38.32(1)	1.734(2)	8.79(3)
	500	2.918(4)	584(8)	83.04(3)	3.31(2)	3.743(3)

We show in Fig. 6.1 the density profiles $\rho(z)$ for the coarse grained model of THF with two Mie spherical segments (dimer model) and for the rigid UA TraPPE model. For the sake of clarity, we only present one half of the profiles corresponding to one of the interfaces. Also for convenience, all density profiles have been shifted to place z_0 at the origin. As can be seen, density profiles for both approaches provide similar values of the liquid and vapor densities at the same temperatures. Liquid density decreases and vapor density increases as the temperature is increased as expected. In addition to that, the absolute value of the slope of the density profiles in the interfacial region decreases as the temperature is increased. This is an expected behavior as the critical temperature of the system is approached. This is also in agreement with the divergence, as it is shown later, of the interfacial thickness as $T \to T_c$. For the other CG and UA models, we have checked that results are equivalent.

We have also estimated the location of the critical point resulting from our direct MD simulations. The critical coordinates (temperature, T_c, density, ρ_c, and pressure, P_c) are obtained following the procedure explained in Section II. In Table 6.5 we report the values of the critical temperatures, densities, and pressures as obtained from this procedure. In addition to that, we have also included the literature THF critical coordinates.

The vapor-liquid phase envelopes of the different CG and UA models for THF are depicted in Fig. 6.2. We have also included the experimental data [37] corresponding to the coexistence curve of THF. We first analyze the phase behavior of THF as obtained from MD NVT simulations of the three CG models. As can be seen, the predictions obtained from the three models, i.e., monomer, dimer, and ring CG, are very similar an in excellent agreement with literature experimental data in the whole range of temperatures from near the triple-point to the critical temperature. [37] We

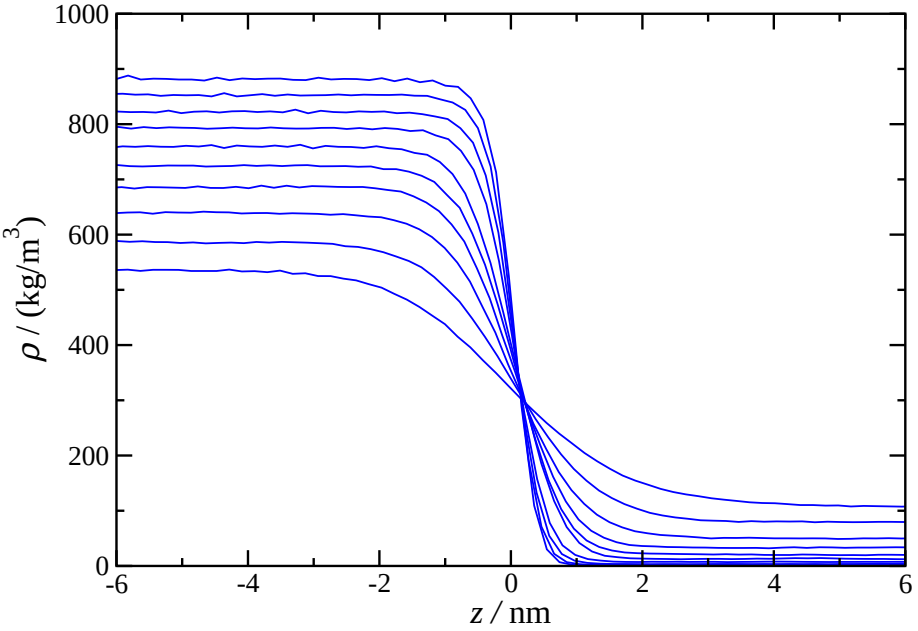

(a)

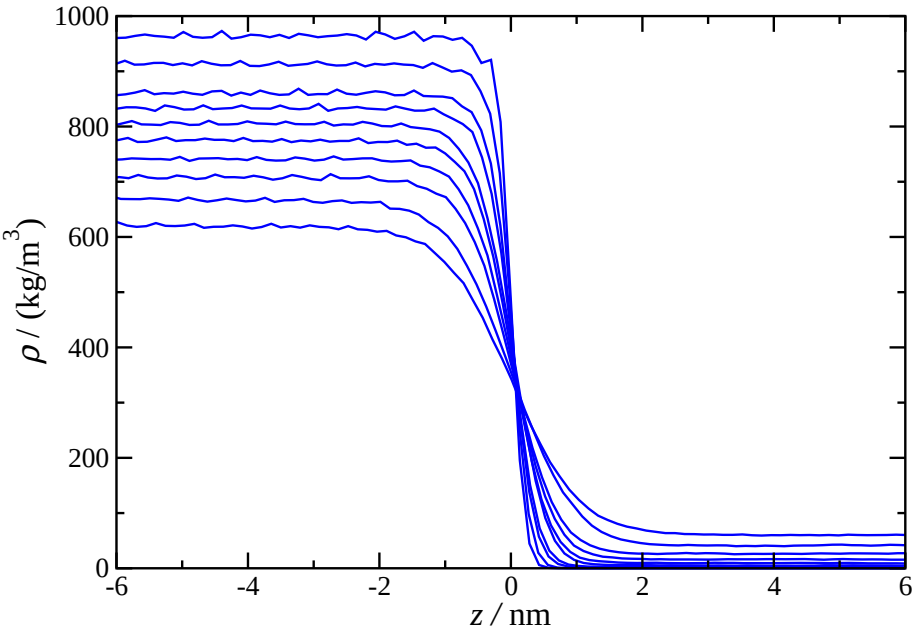

(b)

Figura 6.1: Simulated equilibrium density profiles across the vapor-liquid interface of THF as obtained from MD NVT simulations using the Coarse Grained dimer (a) and the rigid TraPPE models (b). From bottom to top (in the liquid region): (a) 300, 325, 350, 375, 400, 425, 450, 475, 500, and 525 K; (c) 200, 250, 300, 325, 350, 375, 400, 425, 450, and 475 K.

Tabla 6.5: Experimental and predicted critical properties of THF with different Force Fields models

Models	ρ_c (kg/m^3)	T_c^a / K	T_c^b / K	P_c / MPa
Experimental [37, 76]	320	541	-	5.2
CG-monomer	307(14)	545(8)	552(7)	5.9(2)
CG-dimer	307(12)	546(5)	549(4)	5.4(4)
CG-RING	307(16)	540(4)	542(5)	5.3(1)
Rigid-UA	335(11)	569(4)	576(8)	4.9(5)
Semiflexible-UA	308(15)	540(6)	537(6)	5.9(3)
Flexible-UA	312(11)	543(6)	552(5)	5.5(6)

Critical densities (ρ_c) of THF with different Force Fields models as obtained from the analysis of the coexistence densities using Eqs. (6.4) and (6.5); critical temperatures (T_c^a) of THF with different Force Fields models as obtained from the analysis of the coexistence densities using Eqs. (6.4) and (6.5); critical temperatures (T_c^b) of THF with different Force Fields models as obtained from the analysis of the computed tension data using Eq. (6.6) and fixing the critical point to $\mu = 1.258$; and critical pressure (P_c) of THF with different Force Fields models as obtained from the analysis of Eq. (6.7)

have also represented in the same figure the phase behavior predicted from simulations of the UA models. As can be seen, the UA of Jorgensen is only able to predict quantitatively the vapor-liquid phase behavior at low temperatures, below 350 K, approximately. At higher temperatures, the model overestimates the coexistence liquid density and underestimates the vapor density. Contrarily, the other two UA models studied are able to provide a quantitative description of the phase envelope of THF. Agreement between experimental data and estimations from the TraPPE model are better in the case of the original version since the rigid or approximated TraPPE model proposed in this work slightly underestimates the saturated liquid density of THF.

Surprisingly, the approximated TraPPE model proposed here is able to predict reasonably well the experimental vapor-liquid phase envelope of THF. This is important since flexible models, that include bending and torsional intramolecular potentials, need MD time steps considerably shorter that rigid models. This is a restriction coming from the necessity to solve correctly the Newton's equations of motion associated to the internal degrees of freedom of these molecules. In this particular case, MD NVT simulations for the (fully) flexible TraPPE model need twice more CPU time that those corresponding to the rigid TraPPE model to simulate the same real time evolution of the system. This is an important issue that should be taken into account when dealing when simulating explicit interfaces, as they need remarkably longer CPU times if compared to homogeneous phases.

We have also calculated the vapor pressure of the THF models. In this particular case, since we are dealing with a planar interface and simulations are performed using MD NVT simulations, the vapor pressure is equal to the normal (perpendicular to the interface) component of the pressure tensor P_N. These results are shown in Tables 6.3 and 6.4. It is somewhat striking to check that these simulations may produce negative values of vapor pressure at low temperatures, as seen for UA models in Table 6.4. The reason for this is that, as already pointed out by Vega and de Miguel [77], the direct coexistence is not the most accurate method to determine vapor liquid coexistence conditions, specially when dealing with low temperatures corresponding to very low vapor pressures, where the sampling of this technique produces larger deviations. Instead, if the vapor liquid coexistence is to be evaluated accurately, Gibbs ensemble would be a more convenient choice, as it allows remarkable efficiency if conveniently implemented, as discussed recently for instance by Cortés-Morales *et al.* [78].

Recalling that the main objective of this work is the determination of interfacial properties, we will focus first on interfacial thickness of THF (cf. Table 6.1). We have included the results obtained from

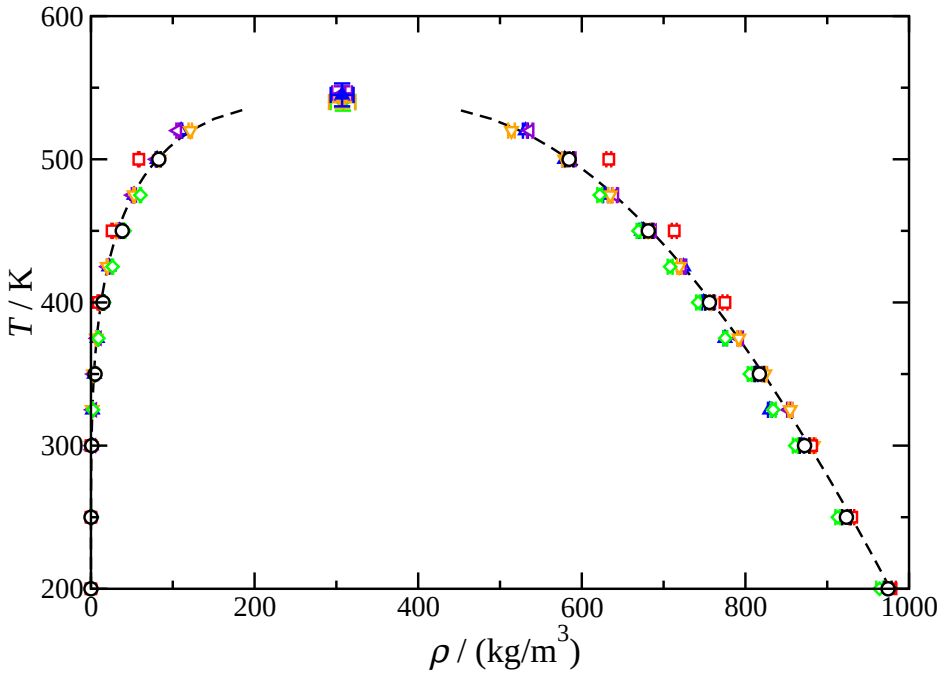

Figura 6.2: Vapour-liquid coexistence densities for THF. The sysmbols correspond to the coexistence densities obtained from the MD NVT simulations for the CG monomer (up triangles), the CG dimer (left triangles), and the CG ring (down triangles) models, the UA of Jorgensen (squares), the flexible UA TraPPE model (circles), and the rigid UA approximated TraPPE model (diamonds). The dashed curve correspond to the experimental coexistence densities taken from the literature [37, 76]. Symbols at the highest temperatures for each of the coexistence curve represent the critical points estimated from Eqs. (6.4) and (6.5).

simulations for the three CG models, as well as for UA models. Fig. 6.3 shows its temperature trend for the different models tested. As shown, d increases with temperature, which simply reflects the fact that the interfacial region gets wider, as can be also observed in Fig. 6.2. At low temperatures the density profiles exhibit a sharp interface which corresponds to a low value of the interfacial thickness. As the temperature is increased towards the critical value the interfacial region becomes wider, and hence, the value of the interfacial thickness increases and diverges as $T \to T_c$. Note that all models exhibit the same qualitative behavior. The only exception is the case of the Jorgensen UA. This may be explained in terms of the predictions obtained from this model in Fig. 6.2. As can be seen, the UA model of Jorgensen overestimates liquid density and underestimates vapor density, predicting consequently a wider vapor-liquid phase separation at higher temperatures ($T \sim 400\,\mathrm{K}$). A higher width in densities in a $T\rho$ phase diagrams indicates a higher slope in the density profile at the interfacial region, and consequently, a higher surface tension, as shown also in Fig. (6.4). As we have mentioned previously in this section, the differences between the predictions of the Jorgensen models with the other models considered here are probably due to a wrong description of the distribution of the point charges in the α- and β-methyl chemical groups.

We finally consider the behavior of the vapor-liquid surface tension of THF. In particular, we compare the results obtained in this work for the coarse grained models and the UA of Jorgensen, Keasler *et al.*, and the rigid version of the formed model. As we have mentioned previously in this

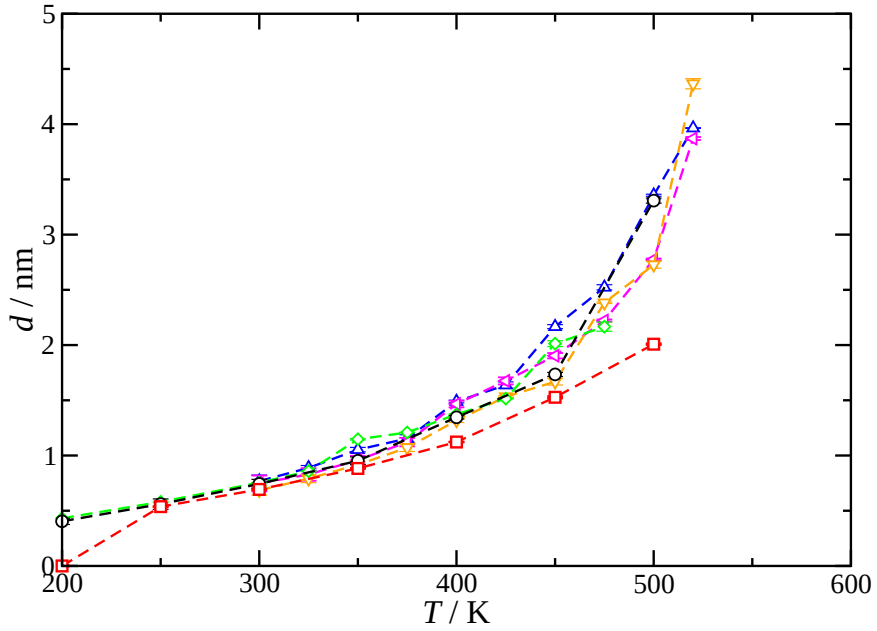

Figura 6.3: The interfacial thickness d as a function of the temperature for THF. The meaning of the symbols is the same as in Fig. 6.2. The dashed curves are included as a guide to the eyes.

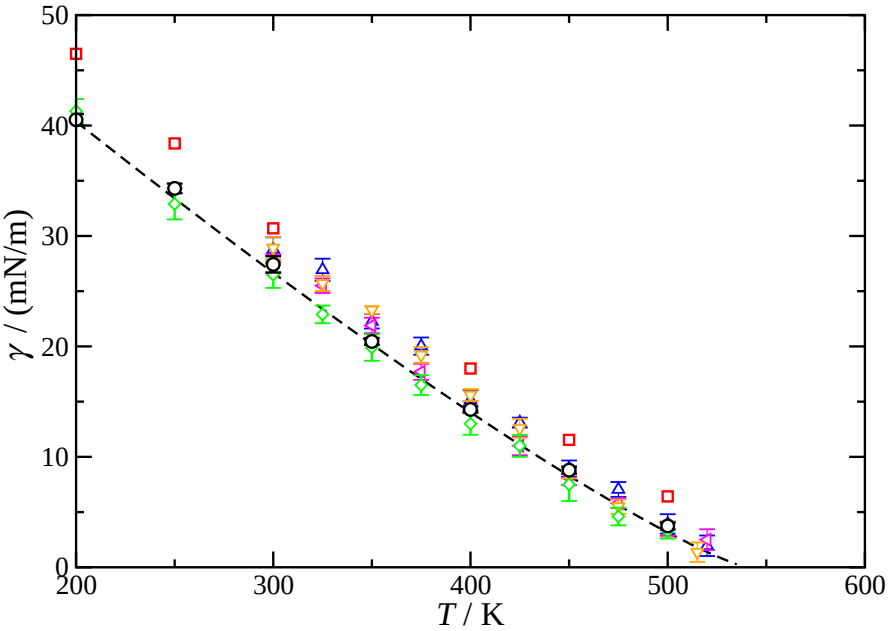

Figura 6.4: Surface tension as a function of temperature for THF. The meaning of the symbols and dashed curves is the same as in Fig. 6.2.

section and in the Section I, interfacial properties, and particularly surface tension, are extremely sensitive to molecular model details of the system. The temperature dependence of the surface tension for all models is shown in Fig. 6.4. As can be seen, the values of the interfacial tension predicted by the coarse grained and the Jorgensen model are above the experimental values. This is especially true for the case of the UA model of Jorgensen, that fails in predicting the surface tension for the whole temperature range considered. Deviation between simulation results and experimental data, in the case of coarse grained models, is lower, especially at high temperatures. Finally, both TraPPE models (rigid and flexible) are able to provide a quantitative description of the experimental vapor-liquid surface tension of THF in the whole range of temperatures, from the triple-point up to the critical temperature. The original TraPPE model seems to be slightly more accurate that the approximated rigid TraPPE model near the critical temperature. However, MD NVT simulations for the former model are faster (up to twice those corresponding to the flexible model), and this should also be taken into account when simulating the vapor-liquid interface of this kind of molecules.

6.4 Conclusion

We have determined the interfacial properties of the vapor-liquid interface of THF considering two different approaches for modeling the system. In the first approach, three different coarse grained force fields based on the SAFT-γ Mie molecular equation of state are used. Under this approach, THF is modeled as a single sphere, as a diatomic molecule, and as a ring formed from three Mie monomeric units. In the second approach, we use three different united atoms models, including the TIPS model proposed by Chandrasekhar and Jorgensen, the TraPPE model by Keasler and collaborators, and an approximated rigid version of this latter model proposed in this work.

We use MD NVT simulations of the inhomogeneous system containing two vapor-liquid interfaces. The surface tension is evaluated from the calculation of the normal and tangential components of the pressure tensor from the virial route. We have examined the density profiles, interfacial thickness, and surface tension in terms of temperature. In addition to that, we have calculated the coexistence phase envelope and vapor pressure, including the location of the critical point from an analysis of the density profiles and the surface tension. All properties have been determined for the six molecular models studied. Predictions obtained from MD simulation are compared with experimental data taken from the literature for all properties except for the case of interfacial thickness.

Tha vapor-liquid phase envelope of THF is predicted remarkably well by the three CG models proposed. In particular, agreement between experimental literature data and predictions from the CG dimer model is comparable with the best united atoms models used in this work. Both TraPPE models, the approximated rigid version and the full flexible model, are able to provide an excellent accuracy in the whole coexistence range. The original TraPPE model proposed by Keasler *et al.* predicts more accurately the saturated liquid density at low temperatures than the approximated version of the model. This is expected since the model parameters have been obtained to ensure the correct vapor-liquid coexistence behavior. Unfortunately, the united-atoms model by Jorgensen is unable to predict correctly the phase envelope at intermediate to high temperatures, close to the critical region. In particular, the model overestimates the liquid density and underestimates the vapor density. The CG models are also able to predict very accurately the vapor pressure, as a function of temperature, and particularly the CG dimer model. The original TraPPE model reproduces the experimental vapor pressure of the system at all temperatures very accurately. The approximated

rigid version of the model provides a reasonably good agreement with experimental data at low and intermediate temperatures, but unfortunately overestimates the vapor pressure at high temperatures. The Jorgensen model underestimates the vapor pressure in the whole range of temperatures at which the seem exhibits vapor-liquid coexistence.

Finally, we have used the six models to predict the vapor-liquid surface tension of THF. The CG models are only able to predict qualitatively the behavior of the surface tension, as a function of temperature. In particular, these models overestimate the experimental data taken from the literature at intermediate and low temperatures. Nevertheless, the agreement between both results is remarkable, bearing in mind that molecular models are usually fitted only to experimental saturated liquid density and vapor pressure, [37] without using any information on interfacial properties. The only united atoms model able to predict accurately THF vapor-liquid surface tension is the TraPPE model, including the original version and the approximated rigid model proposed in this work. The Jorgensen model is unable to predict quantitatively the surface tension, overestimating their values at all temperatures. This is in agreement with the poor description of the vapor-liquid phase envelope, probably due to a wrong election of the molecular parameters of the ether and methyl functional groups, including the distribution of the partial charges assigned. On the contrary, both TraPPE models provide a quantitative and excellent description of the surface tension along the complete temperature range. Although the original TraPPE model seems to predict the surface tension better than the approximated rigid model proposed in this work, the planar and rigid model is faster for simulating since internal degrees of freedom are frozen (nor bending neither torsional intramolecular interactions need to be evaluated). This is an important and clear advantage, especially when interfacial properties need to be calculated and in the case of mixtures containing other chemical compounds. We are currently investigating the advantage of this model for simulating vapor-liquid and liquid-liquid interfaces of binary mixtures containing THF.

6.5 Acknowledgment

We thank Dr. Andres Mejía (Universidad de Concepción, Chile) for stimulating discussions. This work was supported by Ministerio de Economía and Competitividad (MINECO, Spain) through Grants Nos. FIS2013-46920-C2-1-P and FIS2015-68910-P, both cofinanced with EU FEDER funds. We also acknowledge CESGA (www.cesga.es) in Santiago de Compostela, Spain, and MCIA (Mésocentre de Calcul Intensif Aquitain) of the Universités de Bordeaux and Pau et Pay de l'Adour, France, for providing access to computing facilities. J. M. G. acknowledges the doctoral scholarship from Conicyt (Chile) and from Red Doctoral REDOC.CTA, MINEDUC project UCO1202 at U. de Concepción. J. M. M. acknowledges Xunta de Galicia (Spain) for the Postdoctoral Grant. Further financial support from Junta de Andalucía, Universidad de Huelva, and Carnot Institure (ISIFoR, France) are also acknowledged.

Bibliography

[1] R. Larsen, C. A. Knight, and E. D. Sloan *Fluid Phase Equilib.*, vol. 150, p. 353, 1998.

[2] E. D. Sloan and C. Koh, *Clathrate Hydrates of Natural Gases.* New York: CRC PRess, 3 ed., 2008.

[3] L. J. Florusse, C. J. Peters, J. Schoonman, K. C. Hester, C. A. Koh, S. F. Dec, K. N. Marsh, and E. D. Sloan *Science*, vol. 306, pp. 469–471, 2004.

[4] H. Lee, J. W. Lee, D. Y. Kim, J. Park, Y. T. Seo, H. Zeng, I. L. Moudrakovski, C. I. Ratcliffe, and J. A. Ripmeester *Nature*, vol. 434, pp. 743–746, 2005.

[5] T. A. Strobel, C. A. Koh, and E. D. Sloan *Fluid Phase Equilib.*, vol. 261, p. 382, 2007.

[6] V. V. Struzhkin, B. M. W. L., Mao, H.-K. Mao, and R. J. Hemley *Chem. Revs.*, vol. 107, p. 4133, 2007.

[7] H. P. Veluswamy, R. Kumar, and P. Linga *Appl. Energy*, vol. 122, p. 112, 2014.

[8] S. P. Kang and H. Lee *Environ. Sci. Technol.*, vol. 34, p. 4397, 2000.

[9] M. Ricaurte, C. Dicharry, D. Broseta, X. Renaud, and J.-P. Torré *Ind. Eng. Chem. Res.*, vol. 52, p. 899, 2013.

[10] P. Babu, R. Kumar, and P. Linga *Energy*, vol. 50, pp. 364–373, 2013.

[11] P. J. Herslund, K. Thomsen, J. Abildskov, N. von Solms, A. A. Galfre, P. Brantuas, M. Kwaterski, and J.-M. Herri *Int. J. Greenh. Gas Control*, vol. 17, p. 397, 2013.

[12] J. S. Rowlinson and F. L. Swinton, *Liquids and Liquid Mixtures*. Butterworth, London, 1982.

[13] J. S. Rowlinson and B. Widom, *Molecular Theory of Capillarity*. Claredon Press, 1982.

[14] D. Henderson, *Fundamentals of Inhomogeneous Fluids*. Dekker, New York, 1992.

[15] H. T. Davis, *Statistical Mechanics of Phases, Interfaces, and Thin Films*. VCH, Weinheim, 1996.

[16] D. Frenkel and B. Smit, *Understanding Molecular Simulations*. 2nd ed. Academic, San Diego, 2002.

[17] J. M. Míguez, M. M. Conde, J.-P. Torré, F. J. Blas, M. M. Piñeiro, and C. Vega *J. Chem. Phys.*, vol. 142, p. 124505, 2015.

[18] W. L. Jorgensen *J. Am. Chem. Soc.*, vol. 103, pp. 335–340, 1981.

[19] W. L. Jorgensen *J. Am. Chem. Soc.*, vol. 103, pp. 341–345, 1981.

[20] W. L. Jorgensen *J. Am. Chem. Soc.*, vol. 103, pp. 345–350, 1981.

[21] J. Chandrasekhar and W. L. Jorgensen *J. Chem. Phys.*, vol. 77, pp. 5073/1–10, 1982.

[22] J. Chandrasekhar and W. L. Jorgensen *J. Chem. Phys.*, vol. 77, pp. 5080/1–11, 1982.

[23] W. L. Jorgensen and M. Ibrahim *J. Am. Chem. Soc.*, vol. 103, p. 3976, 1981.

[24] W. L. Jorgensen and J. Tirado-Rives *J. Am. Chem. Soc.*, vol. 110, pp. 1657–1666, 1988.

[25] W. L. Jorgensen, D. S. Maxwell, and J. Tirado-Rives *J. Am. Chem. Soc.*, vol. 118, pp. 11225–11236, 1996.

[26] J. Helfrich and R. Hentschke *Macromolecules*, vol. 28, pp. 3831–3841, 1995.

[27] S. Girard and F. Müller-Plathe *Mol. Phys.*, vol. 101, pp. 779–787, 2003.

[28] S. J. Keasler, S. M. Charan, C. D. Wick, I. G. Economou, and J. I. Siepmann *J. Phys. Chem. B*, vol. 116, pp. 11234–11246, 2012.

[29] E. A. Müller and G. Jackson *Annu. Rev. Chem. Biomol. Eng.*, vol. 5, pp. 405–427, 2014.

[30] A. Lymperiadis, C. S. Adjiman, A. Galindo, and G. Jackson *J. Chem. Phys.*, vol. 127, p. 234903, 2007.

[31] A. Lymperiadis, C. S. Adjiman, A. Galindo, and G. Jackson *Fluid Phase Equil.*, vol. 274, p. 85, 2008.

[32] V. Papaioannou, C. S. Adjiman, G. Jackson, and A. Galindo *Fluid Phase Equil.*, vol. 306, p. 82, 2011.

[33] G. Mie *Ann. Phys. (Berlin)*, vol. 316, p. 657, 1903.

[34] V. Papaioannou, T. Lafitte, C. Avendaño, C. S. Adjiman, G. Jackson, E. A. Müller, and A. Galindo *J. Chem. Phys.*, vol. 140, p. 054107, 2014.

[35] T. Lafitte, A. Apostolakou, C. Avendaño, A. Galindo, C. S. Adjiman, E. A. Müller, and G. Jackson *J. Chem. Phys.*, vol. 139, p. 154504, 2013.

[36] J. M. Míguez, J. M. Garrido, F. J. Blas, H. Segura, A. Mejía, and M. M. Piñeiro *J. Phys. Chem. C*, vol. 118, p. 24504, 2014.

[37] "Dechema gesellschaft für chemische technik und biotechnologie e.v., frankfurt am main, germany, https://cdsdt.dl.ac.uk/detherm/, (retrieved september, 2015)."

[38] E. A. Müller and K. E. Gubbins *Ind. Eng. Chem. Res.*, vol. 40, pp. 2193–2211, 2001.

[39] C. McCabe and A. Galindo in *Applied Thermodynamics of Fluids* (A. Goodwin, J. V. Sengers, and C. J. Peters, eds.), ch. 8, Royal Society of Chemistry, London, 2010.

[40] C. Avendaño, T. Lafitte, A. Galindo, C. S. Adjiman, G. Jackson, and E. A. Müller *J. Phys. Chem. B*, vol. 115, no. 38, pp. 11154–11169, 2011.

[41] A. Mejía, C. Herdes, and E. A. Müller *Ind. Eng. Chem. Res.*, vol. 53, no. 10, p. 4131, 2014.

[42] N. S. Ramrattan, C. Avendaño, E. A. Müller, and A. Galindo *Mol. Phys.*, vol. 113, pp. 932–947, 2015.

[43] H. Segura, D. Seiltgens, A. Mejía, F. Llovell, and L. F. Vega *Fluid Phase Equil.*, vol. 265, p. 66, 2008.

[44] H. Segura, D. Seiltgens, A. Mejía, F. Llovell, and L. F. Vega *Fluid Phase Equil.*, vol. 265, p. 155, 2008.

[45] J. M. Garrido, H. Quinteros-Lama, A. Mejía, J. Wisniak, and H. Segura *Energy*, vol. 45, pp. 888–899, 2012.

[46] W. Malesinski, *Azeotropy and Other Theoretical Problems of Vapour-Liquid Equilibrium.* New York Interscience, 1965.

[47] C. Herdes, T. S. Totton, and E. A. Müller *Fluid Phase Equilib.*, vol. 406, pp. 91–100, 2015.

[48] C. Herdes, E. E. Santiso, C. James, J. Eastoe, and E. A. Müller *J. Colloid Interface Sci.*, vol. 445, pp. 16–23, 2015.

[49] A. Mejía, M. Cartes, H. Segura, and E. A. Müller *J. Chem. Eng. Data*, vol. 50, no. 10, pp. 2928–2941, 2014.

[50] C. Cumicheo, M. Cartes, E. A. Müller, and A. Mejía *Fluid Phase Equilib.*, vol. 380, pp. 82–92, 2014.

[51] O. Lobanova, A. Mejía, G. Jackson, and E. A. Müller *J. Chem. Thermodyn.*, vol. 93, pp. 320–336, 2016.

[52] R. P. Sear and G. Jackson *Mol. Phys.*, vol. 81, no. 4, pp. 801–811, 1994.

[53] R. P. Sear and G. Jackson *Phys. Rev. E*, vol. 50, pp. 386–394, July 1994.

[54] E. A. Müller and K. E. Gubbins *Mol. Phys.*, vol. 80, pp. 957—976, 1993.

[55] T. Lafitte, C. Avendaño, V. Papaionnou, A. Galindo, C. S. Adjiman, G. Jackson, and E. A. Müller *Mol. Phys.*, vol. 110, no. 11–12, p. 1189, 2012.

[56] C. Avendaño, T. Lafitte, C. S. Adjiman, A. Galindo, E. A. Müller, and G. Jackson *J. Phys. Chem. B*, vol. 117, no. 9, pp. 2717–2733, 2013.

[57] O. Lobanova, T. Lafitte, C. Avendaño, E. A. Müller, and G. Jackson *Mol. Phys.*, vol. 113, pp. 1228–1249, 2015.

[58] M. P. Allen, *Computer Simulation of Liquids*. Claredon, Oxford, 1987.

[59] D. Van Der Spoel, E. Lindahl, B. Hess, G. Groenhof, A. E. Mark, and H. J. Berendsen *J. Comput. Chem.*, vol. 26, no. 16, pp. 1701–1718, 2005.

[60] G. Galliero, M. M. Piñeiro, B. Mendiboure, C. Miqueu, T. Lafitte, and D. Bessieres *J. Chem. Phys.*, vol. 130, pp. 104704/1–10, 2009.

[61] G. Galliero *J. Chem. Phys.*, vol. 133, pp. 074705/1–7, 2010.

[62] J. M. Míguez, M. M. Piñeiro, and F. J. Blas *J. Chem. Phys.*, vol. 138, pp. 034707/1–11, 2013.

[63] M. Dinpajooh, P. Bai, D. A. Allan, and J. I. Siepmann *J. Chem. Phys.*, vol. 143, p. 114113, 2015.

[64] M. A. Cuendet and W. F. van Gunsteren *J. Chem. Phys.*, vol. 127, pp. 184102/1–9, 2007.

[65] S. Nosé *Mol. Phys.*, vol. 52, pp. 255–268, 1984.

[66] H. J. C. Berendsen, J. P. M. Postma, W. F. van Gunsteren, A. di Nola, and J. R. Haak *J. Chem. Phys.*, vol. 81, pp. 3684/1–8, 1984.

[67] H. Hulshof *Ann. Phys. (Berlin)*, vol. 4, pp. 165–186, 1901.

[68] E. de Miguel, F. J. Blas, and E. M. del Río *Mol. Phys.*, vol. 104, pp. 2919–2927, 2006.

[69] E. de Miguel and G. Jackson *J. Chem. Phys.*, vol. 125, pp. 164109/1–12, 2006.

[70] H. W. Xiang, *The Corresponding-States Principle and its Practice Thermodynamic. Transport and Surface Properties of Fluids*. Elsevier, Amsterdam, 2005.

[71] B. Widom *J. Chem. Phys.*, vol. 43, p. 3892, 1965.

[72] F. J. Blas, L. G. MacDowell, E. de Miguel, and G. Jackson *J. Chem. Phys.*, vol. 129, p. 144703, 2008.

[73] L. G. MacDowell and F. J. Blas *J. Chem. Phys.*, vol. 131, pp. 074705/1–10, 2009.

[74] J. G. Sampayo, F. J. Blas, E. de Miguel, E. A. Müller, and G. Jackson *J. Chem. Eng. Data*, vol. 55, p. 4306, 2010.

[75] F. J. Blas, A. I. Moreno-Ventas Bravo, J. M. Míguez, M. M. Piñeiro, and L. G. MacDowell *J. Chem. Phys.*, vol. 137, p. 084706, 2012.

[76] P. Linstrom and W. Mallard, "Nist chemistry webbook, nist standard reference database number 69, https://webbook.nist.gov, (retrieved september, 2015)."

[77] C. Vega and E. de Miguel *J. Chem. Phys.*, vol. 126, no. 15, p. 154707, 2007.

[78] A. D. Cortés-Morales, I. G. Economou, C. J. Peters, and I. J. Siepmann *Mol. Phys.*, vol. 39, no. 14-15, pp. 1135–1142, 2013.

Capítulo 7

Measurement and Modeling of High Pressure Density and Interfacial Tension of Carbon Dioxide + Tetrahydrofuran Mixture

Abstract

We report experimental interfacial tension, coexisting densities and relative Gibbs adsorption measurements for carbon dioxide + tetrahydrofuran mixture in the vapor-liquid equilibrium at 298.15 K and 353.15 K and pressure up to 12.0 MPa. Measurements are based on the use of a high-pressure pendant drop tensiometer coupled to a high-pressure densimeter. The results were compared to literature values where possible. In order to complement experimental measurements, theoretical modeling on the interfacial behavior was carried out using the Square Gradient Theory based on a Peng-Robinson equation of state. Investigating the applicability of the model to describe the vapor-liquid interfacial tensions of carbon dioxide + tetrahydrofuran revealed very good agreement between calculated and experimental data, where the interfacial tension decreases as the pressure (or the liquid mole fraction of carbon dioxide) increases. Furthermore, the model was applied to examine accumulation of compounds at the interface. Thereby, peculiar adsorption effects of carbon dioxide in the liquid interface of tetrahydrofuran were observed.

7.1 Introduction

In the last years, the precise theoretical description of the interfacial properties of inhomogeneous fluid systems, including greenhouse gases (CH_4, CO_2, N_2, N_2O, etc...) has received much attention due to their environmental implications. Particularly, CO_2 emissions from the combustion of fossil fuels for power generation has been identified as the main source to global warming, according to the Intergovernmental Panel on Climate Change (IPCC) [1]. This report states clearly that efforts in all scientific and technical fields to reduce the emissions of antropogenic CO_2, and to capture and safely store it [2, 3] must be significantly enhanced. Nowadays, CO_2 capture is perhaps the first and crucial step, and although several useful technologies have been proposed, amine solvents are mostly used for

its capture after combustion in fossil fuel power plants [4]. However, this effective method presents issues as high corrosion and remarkable energy consumption [5, 6]. Consequently, new environmentally friendly and efficient technologies must be explored to expand conventional approaches [7–9]. In this context, capture through hydrate crystallization is a promising method, due to not only to its high and safe gas storage capacity [10–13] but also to the reduced energy consumption involved in hydrate formation/dissociation processes [3, 14–16].

Gas hydrates are non-stoichiometric inclusion solid compounds, consisting of a crystalline structure formed by a network of water molecules which, under certain thermodynamic conditions, can enclathrate individual small guest molecules of suitable size and shape [17]. Several hydrate structures are known [17, 18], and the most common ones encountered in nature are *sI* [19], *sII* [20], and *sH* structures [21]. The nature of guest molecule determines the type of gas hydrate structure. Normally, these crystals are stable under high pressures and low temperatures. The empty hydrate water lattice itself is a thermodynamically unstable structure in these conditions, and it is the interaction between water and guest molecules that stabilize the lattice structure [22]. Many details and properties of these compounds can be found elsewhere in literature [18].

The concept of CO_2 capture by forming hydrates was first proposed by Spencer in 1997 [23, 24]. Many investigations were carried out to improve the method concerning thermodynamic, kinetic, economic and process design aspects [25–28]. Tajima *et al.* [29] presented an estimation of energy consumption of CO_2 separation from flue gases in a gas-fired thermal power plant. However, industrial applications of hydrates have been hindered by several problems, such as the requirement of high-pressure conditions, and slow crystallization kinetics, which represent two of the main barriers to the commercialization of this technology [30]. However, it is possible to add chemical compounds, called hydrate promoters, that participate actively in the hydrate formations process altering the phase equilibria conditions, causing the reduction of the formation pressure and the increasing of the formation temperature. Among the various thermodynamic hydrate promoters (because there are also kinetic promoters), tetrahydrofuran, denoted hereafter as THF for brevity, is one of the most popular [31–36]. It allows forming mixed gas hydrates (i.e., hydrates containing both THF and CO_2) occurring at significantly lower pressure and higher temperature than the hydrate formed without this promoter. In addition, its efficiency has been already tested and demonstrated for various gases (such as CO_2, N_2, CH_4, H_2) and several gas mixtures (such as CO_2+CH_4, CO_2+N_2) [37–39].

The cornerstone of the development of these applications is the accurate determination of the multiphasic equilibria of CO_2+THF and H_2O+THF mixtures. From a molecular modeling and experimental perspective the subject is clearly undeveloped. Only a reduced number of studies have been published on this topic due to the complexity of the thermodynamic behavior of these binary mixtures [40–45]. Concerning CO_2+THF, the recent work of Míguez *et al.* [45] presented a detailed analysis of its thermodynamic phase behavior from a molecular modeling perspective, showing that it exhibits type *I* phase behavior according to the van Konynenburg and Scott classification [46]. This means that the critical points of both pure compounds are connected by a continuous liquid-vapor critical line. The SAFT-VR equation of state used in that work is able to capture the correct type of phase behavior, and also provides a reasonably good quantitative description of the available experimental data [40, 42–44].

The measurement or computation of interfacial properties is of great importance since previous works have proven that they are closely related to the kinetic hydrate formation mechanisms. Qin *et al.* [47] investigated various hydrate-forming systems with natural gas and aqueous solutions with

kinetic additives and concluded that a lower interfacial tension corresponds to a longer onset time of hydrate formation, i.e., better kinetic inhibition performance. Overall, the presence of more or stronger hydrophobic groups in the kinetic hydrate inhibitors (KHIs), with the help of alcohols as synergists, enhance their adsorption on the surface of aqueous phase leading to lower gas/liquid interfacial tension. Similarly, the strong surface adsorption of KHI molecules produce a stronger barrier between liquid water and hydrate particles, slowing their growth. On the opposite side, tuning the interfacial interaction between gas-water phases can improve gas hydrate crystallization, as shown by Arora *et al.* [48]. An interesting point in this discusion is the probable modification with THF as hydrate promotor, in the equilibrium formed by CO_2 + H_2O. [49] An important element in hydrates global phase diagram, in a PT projection, is the three phase line. Along this line, the hydrate coexists with two fluid phases, one rich in H_2O and the other rich in the hydrate former guest molecule (CO_2). Knowledge of the promoter (THF) and guest (CO_2) interaction, could imply an increase or decrease in the temperature of formation of hydrates. Bearing this in mind, in this work we comprehensively address the experimental study of interfacial behavior for the CO_2+THF binary mixture, which to our knowledge has not been previously reported.

This paper is organized as follows: we first describe the experimental equipment and measurement details (Section 2). We then summarize the main expressions of the square gradient theory and the equation of state models (Section 3). Following, we present and discuss the main results of both bulk phase equilibrium densities and interfacial properties (interfacial tension, surface activity and relative Gibbs adsorption isotherm) in Section 4. Finally, we summarize the main conclusions of this work in Section 5.

Tabla 7.1: Comparison of liquid mass densities ($\hat{\rho}$) and interfacial tensions (γ) of pure THF with literature values at 298.15 K and 0.1013 MPa.[a]

$\hat{\rho}$ / (kg/m^3)					
Compound	Source	This work	Literature	Method	AAD / (%)[b]
THF (0.999)	Sigma Aldrich	881.93	881.93[c]	Vibrating-tube	0.012
			881.95[d]		
			881.98[e]		
			881.99[f]		
			882.01[g]		
			882.43[h]		
			881.98[i]		
γ / (mN/m)					
		26.30	26.59	Capillary rise[j]	1.751
			26.73	Drop volume[k]	
			27.04	Pendant drop[l]	
				Drop volume[m]	
				Drop volume[n]	
			26.68	Drop volume[o]	

[a]Measurement uncertainties are: $\hat{\rho}\pm5\times10^{-3}$ kg m^{-3}; $\gamma\pm0.01$mN m^{-1}; $p\pm10^{-4}$ MPa; $T\pm0.10$K. [b]Absolute Average Desviation (AAD): $AAD(\theta)=(100/N_{exp})\sum_{i}^{N_{exp}}\left|\theta_i^{exp}-\theta_i^{cal}\right|/\theta_i^{exp}$ with $\theta=\hat{\rho},\gamma$

[c]Ref. [50], [d]Ref. [51, 52], [e]Ref. [53], [f]Ref. [54], [g]Ref. [55], [h]Ref. [56], [i]Ref. [57], [j]Ref. [58], [k]Ref. [52], [l]Ref. [59], [m]Ref. [60], [n]Ref. [61], [o]Ref. [62].

7.2 Experimental section

7.2.1 Materials

Tetrahydrofuran (THF) and carbon dioxide (CO_2) used in the experimental measurements were obtained from Aldrich and Linde S.A. (Chile), respectively with a certified purity greater than 99.9 % for both compounds. The quoted fluids, were used without further purification, considering that THF was purchased without stabilizers. Table 7.1 shows the obtained experimental results for the liquid mass densities ($\hat{\rho}$) and interfacial tensions (γ) of pure THF at 298.15 K and 0.1013 MPa. In this table, the obtained data were compared with the available literature data, showing accurate agreement each other.

Particularly, an Absolute Average Desviation (AAD) of 0.012 % was obtained from liquid density, whereas 1.715 % was obtained from interfacial tensions comparing various techniques and the available experimental data. As an additional verification in density measurements of THF, a wide temperature range was performed comparing our measurements with the existing source of experimental data [63]. Considering that the normal boiling point has been set in 338.7 K [64], a good agreement in Fig. (7.1) is found between our measurements and the available experimental data. This point is relevant in our work, because one of our selected temperature is above the boiling point of THF, and probably density measurement should not be easy.

7.2.2 Apparatus and procedure

Density measurements

The mass density ($\hat{\rho}$) of THF was measured from 298.15 to 353.15 K at atmospheric pressure condition using a DMA 5000 densimeter vibrating-tube (Anton Paar, Austria). calibrated at $T = 293.15$ K with ambient air and ultrapure water. For the case of CO_2 + THF mixture at pressures over the atmospheric condition, $\hat{\rho}$ in the liquid and vapor phases are measured at the experimental temperature and pressure using a DMA HP densimeter (Anton Paar GmbH, Austria). In both densimeters, the mass density determination is based on measuring the period of oscillation of a vibrating U-shaped tube filled with the fluid mixture sample. The temperature was measured with the built-in platinum resistance thermometer, which was calibrated by the manufacturer. The calibration of the thermometer was verified in this work by inserting a second calibrated platinum resistance thermometer into the thermowell in the densimeter block; differences were within ±0.01 K. The expanded uncertainty of the temperature was estimated to be 0.02 K at 95 % confidence. Pressure, in turn, is measured by means a Swagelok type S pressure transducer with a relative uncertainty of 0.1% over the full scale up to p=70MPa connected to the densimeter, and maintained constant by means of the high-pressure syringe pump (Teledyne Isco Pump. Model 100DM, USA). The estimated expanded uncertainties of density for the measurements on CO2-free liquids was 5×10^{-3} kg/m^3 at 95 % confidence, including the effects of calibration uncertainty, repeatability, temperature amd pressure uncertainty. The density measurements are repeated 25 times for each condition and averaged accordingly.

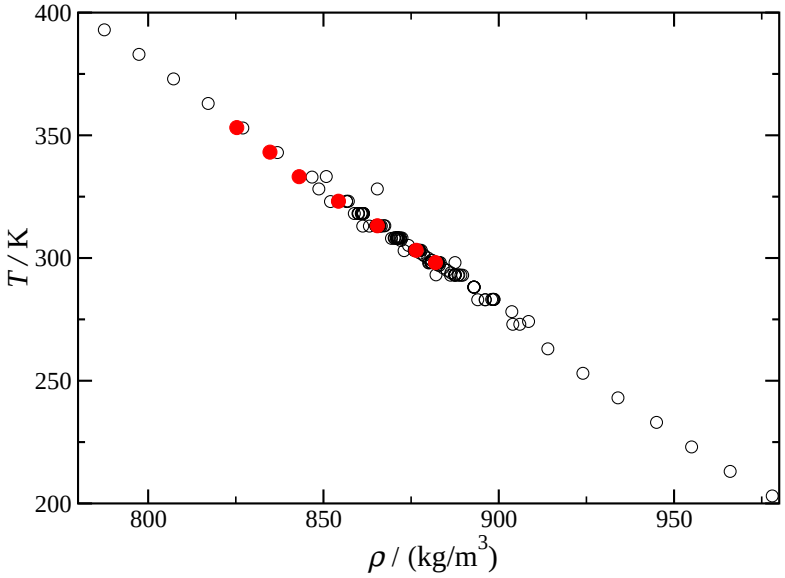

Figura 7.1: Comparison of densities for pure THF at 0.1013 MPa over a wide temperature range. (red circles) This work, (open circles) Available experimental data [63].

Interfacial tension cell

A pendant drop tensiometer model IFT-10, manufactured by Temco Inc. (USA) is used for interfacial tension measurements. The pendant drop cell is a stainless steel cylindrical chamber (with an inner volume of ~ 42 cm^3), with two injection orifices, one at the top and the other at the bottom of the chamber. On the top orifice a stainless steel needle (1.4 mm i.d. and 2.45 mm o.d.) is placed for generating pendant drops. The bottom orifice is connected to the high-pressure syringe pump (Teledyne Isco Pump. Model 100DM, USA), which is used to compress CO_2 from a commercial ultra high purity CO_2 cylinder, and maintained the experimental pressure constant within $\pm$ 0.001 kPa.

The chamber is equipped with appropriately sealed borosilicate glass windows, which allow visualization of the inner space during operation. The light beam source, located at one side of the visualization axis, is a Led Fiber Optic Iliminator (AmScope 20W) covered by a white diffuser made of Teflon. The camera, located at opposite side of the visualization axis, is a monochrome video camera model CS8320Bi (Toshiba Teli, Corp., Japan) connected to a personal computer through a frame grabber card. The temperature of the cell is measured by means a K-type thermocouple, and maintained constant to within $\pm$ 0.1 K by means of electric band heaters operated by a Watlow temperature controller model TC-211-K-989 (USA). The tensiometer, the light source and the camera are mounted on a free vibration table (Vibraplane, model 2210, USA) in order to avoid the effect of noisy measurements due to external vibrations. Interfacial tension measurements were made by analyzing images of liquid THF pendant drops generated at the tip of an injection needle, which is surrounded by CO_2, by using the DROPimage Advanced software version 1.5 (Ramé-Hart instruments, co. USA) [65].

The experimental procedure for determining interfacial tension is as follows. The cell is heated to the desired experimental temperature, and then it is slightly pressurized with CO_2. After degasification in an ultrasonic bath, THF is pumped through a stainless steel tube to the needle tip. The pump is

a positive displacement ELDEX HP Series Model B-100-S-2 CE (USA). Initially, a small portion of the pure liquid is pumped into the chamber in order to saturate the gas that fills the cell. Then, the cell is pressurized to the desired experimental pressure and a liquid drop is generated at the tip of the needle. The pressure in the IFT cell is maintained constant to within ± 0.10 kPa by means of the high-pressure syringe pump. Once the drop is formed and the desired experimental temperature and pressure are reached, it is necessary to wait, a period approximately from 5 to 10 min. until the drop reaches an equilibrium state. For the systems study here, we use the mass transfer model to estimate the diffusion time needed to reach the equilibrium conditions, in this case the interfacial tensions reaches an equilibrium state very fast (less than 5 min). After this equilibration step, the drop dimensions are recorded (at least during 6 h) in order to check the stability of its geometry.

Once the shape and volume of the drop are deemed constant, the equatorial diameter of the drop, d_e (the largest one), and the horizontal diameter of the drop, d_s, which is located at a distance d_e from the apex of the drop are recorded and, simultaneously, the liquid and the gas phases are transported to the high-pressure densimeter, through a heated stainless steel tube, in order to measure the mass density of the THF saturated with CO_2 ($\hat{\rho}_L$) and the mass density of CO_2 saturated with THF ($\hat{\rho}_G$). Both densities are measured at the experimental temperature and pressure. For further description and details on the experimental design, the reader is redirected to the following references [66–68]

Based on the experimental measurements of d_e, d_s, $\hat{\rho}_L$ and $\hat{\rho}_G$, the interfacial tension, γ, is obtained through the following expression:

$$\gamma = \left(\hat{\rho}_L - \hat{\rho}_G\right) g_c d_e^2 f\left(d_s, d_e\right) \tag{7.1}$$

where g_c is the local gravitational constant ($\approx 981\ \text{cm} \cdot \text{s}^{-2}$), and $f\left(d_s, d_e\right)$ corresponds to a function related to the silhouette of the drop, whose value is determined from numerical tables. [69] In this work, γ and ($\hat{\rho}$) are measured at two isothermal conditions (298.15 and 353.15 K) and over the pressure range 0.1−10 MPa.

Additionally, the experimental values of γ and ($\hat{\rho}$) can be also used to predict, as a first approximation, the magnitude of the relative Gibbs adsorption isotherm of a species i on species j (Γ_{ij}). According to Masterton *et al.* [70] for a gas-liquid system in which the pressure is changing, Γ_{ij} can be described by the following expression:

$$\Gamma_{ij} = -\frac{\hat{\rho}_i}{M_i}\left(\frac{\partial \gamma}{\partial p}\right)_T \tag{7.2}$$

where the slope $(\partial\gamma/\partial p)_T$ is obtained from experimental values of γ - p projection. $\hat{\rho}_i$ and M_i are the mass density and molecular weight of the pure gas (here CO_2), respectively. $\hat{\rho}_i$ can be directly measured as a function of T and p or alternatively, it can be obtained from a data base.

It is also important to recall that γ in a pendant drop tensiometer is not measured directly; therefore it is important to establish that the uncertainties of γ values are affected by the value of temperature, pressure, density difference, experimental reproducibility of γ itself and their standard uncertainties. In order to quantify these effects in the expanded or combined relative uncertainty of γ, u_c, the following relationship [71, 72] has been considered for the case of isothermal measurements:

$$u_c^2\left(\gamma\right) = \left[\frac{1}{\gamma}\left(\frac{\partial \gamma}{\partial p}\right)_T \delta p\right]^2 + \left[\frac{\delta \Delta\rho}{\Delta\rho}\right]^2 + \left[\frac{\sigma\left(\gamma\right)}{\gamma}\right]^2 \tag{7.3}$$

In eq (7.3) δp and $\delta\Delta\rho$ correspond to the standard uncertainties in pressure and density, respectively. $\sigma(\gamma)$ is the standard deviation of γ which, together with the maximum value of partial derivatives of γ in p, have directly been estimated from experimental data. For the binary systems investigated here, the average u_c, value was found to be 0.77%. Therefore, the expanded relative uncertainty of γ at 95% confidence was 1.5%. Additional details concerning the pendant drop technique have been extensively described by Andreas *et al.* [69], Rusanov and Prokhorov [73], Ambwani and Fort [74] and Evans [75].

7.3 Theoretical section

7.3.1 Square gradient theory for modeling phase equilibrium and interfacial behavior

The application of the Square Gradient Theory (SGT) to different EOS models has been described in previous papers [76–81]. So, we briefly outline the specific details that were considered for the purpose of calculating density profiles and interfacial tensions. As its theoretical starting point, the SGT assumes the Helmholtz energy density f (where $f = \rho A$) to have a continuous interfacial evolution among phases in equilibrium. The geometry of the f function is approximated by means of a second order Taylor expansion about the Helmholtz energy density of the homogeneous system f_0 (formally, one of the bulk phases in equilibrium). For the case of binary mixtures characterized by flat interfaces between adjacent phases, the Taylor expansion may be performed along the interface width by considering a normal z-coordinate (that stands for the interface length) as follows:

$$f = f_0 + \frac{1}{2}\left[c_{11}\left(\frac{d\rho_1}{dz}\right)^2 + 2c_{12}\frac{d\rho_1}{dz}\frac{d\rho_2}{dz} + c_{22}\left(\frac{d\rho_2}{dz}\right)^2\right] \tag{7.4}$$

In Eq. (7.4), ρ_i is the molar density of the i-th component ($\rho_i = x_i\rho$), c_{ii} and c_{ij} stand for the pure component and cross influence parameters, respectively. The influence parameters of pure fluids, c_{ii}, are calculated using the procedure originally suggested by Carey *et al.* [76, 77], and later applied extensively by other authors (See Refs. [67, 78–80, 82]). For the case of the pure fluids considering in this work, the parameters were fitting from experimental interfacial tension data taken from Ref. [83] and then correlated as a linear function of the temperature: $c_{11} = 28.17275 \times 10^{-21}$ $\mathrm{Jm^5mol^{-2}}$ whereas $c_{22} = 3.83262 \times 10^{-22} + 7.5753 \times 10^{-20}T$ $\mathrm{Jm^5mol^{-2}}$

The density profiles of the components ρ_i along the interface length may be obtained by constraining Eq. (7.4) to a condition of minimum energy density. The so-defined variational problem [84, 85] yields a set of partial differential equations which may be conveniently simplified by considering the following assumptions: (a) the influence parameters of pure fluids (c_{11} and c_{12}) do not depend on density and (b) the cross influence c_{ij} parameter is given by a geometric average (*i.e.* $c_{12} = \sqrt{c_{11}c_{12}}$). According to these assumptions, which have been extensively validated for the case of the vapor-liquid interface, the density profiles implying a minimum value of f may be determined by solving the following algebraic equation

$$\sqrt{c_{11}}\left[\mu_2 - \mu_2^0\right] = \sqrt{c_{22}}\left[\mu_1 - \mu_1^0\right] \tag{7.5}$$

where μ and μ_i^0 stand for the interfacial and homogeneous chemical potentials of the ith component,

respectively. The chemical potential can be calculated from any EOS model by considering the following definition

$$\mu_i = \left(\frac{\partial f_0}{\partial \rho_i}\right)_{T^0, V^0, \rho^0_{j\neq i}} \tag{7.6}$$

where f_0 represents the homogeneous Helmholtz energy density, which can be directly obtained from the EoS model through the following integral expression

$$\frac{f_0}{\rho RT} = \int_0^\rho \left(\frac{p}{RT\rho^2} - \frac{1}{\rho}\right) d\rho + \frac{\rho_1 \ln \rho_1 + \rho_2 \ln \rho_2}{\rho} \tag{7.7}$$

Based on the results of Kodama *et al.* [43] the use of cubic EoS provides an accurate description of phase densities in a wide range of temperature and pressures. Specifically, in this work f_0 and μ_i are obtained from the Peng-Robinson EoS [86]. The Peng-Robinson EoS is given by:

$$p = \frac{RT}{1-\rho b} - \frac{a\rho^2}{1 - 2\rho b + \rho^2 b^2} \tag{7.8}$$

where p is the total pressure, R is the universal gas constant, T is the temperature. ρ is the molar density, a is the cohesion parameter and b is the covolume that, for the case of pure fluids, are defined as

$$a = 0.457235 \frac{(RT_{c,i})^2}{P_{c,i}} \alpha\left(T, T_{c,i}\right) \tag{7.9}$$

$$b = 0.077796 \frac{(RT_{c,i})}{P_{c,i}} \tag{7.10}$$

In Eqs. (7.9)-(7.10), $T_{c,i}$ and $P_{c,i}$ are the critical temperature and pressure of pure fluids, respectively, and α is the thermal cohesion parameters given by the Stryjek-Vera function [87]

$$\alpha = \left(1 + k_1\left[1 - \sqrt{T/T_{c,i}}\right] + k_2\left(1 - T/T_{c,i}\right)\left(0.7 - T/T_{c,i}\right)\right)^2 \tag{7.11}$$

where k_1 and k_2 are parameters, which were directly fitted from vapor pressure data of pure components (See Wisniak *et al.* [88] for details). Table 7.2 reports the values of $T_{c,i}$, $P_{c,i}$, k_1 and k_2 parameters for CO_2 and THF, the latter parameters were obtained from the experimental vapor pressure data reported in Ref. [83]. Equations (7.9)-(7.10) are be extended to mixtures by using adequate mixing rules. In this work, we considering the van der Waals quadratic mixing rule (QMR). In QMR, the cohesion parameter and the co-volume of the mixture are given by the following expressions [89]

$$a\rho^2 = \sum_{i,j=1}^{n_c} \rho_i \rho_j \sqrt{a_i a_j}\left(1 - k_{ij}\right) \tag{7.12}$$

$$b\rho = \sum_{i,j=1}^{n_c} \rho_i b_i \tag{7.13}$$

where k_{ij} is the binary interaction parameter. In this work, the k_{ij} is fitted from the vapor liquid data reported by Im *et al.* [40], and then correlated as a linear function of the temperature: $k_{12} = 2.2134 \times 10^{-3} + 1.69434 \times 10^{-5} T$. The interaction parameter is able to predict phase behavior with an absolute average deviation in vapor pressure (AADP=0.5%) and a deviation in the vapor molar fraction ($\Delta y = 0.31\%$).

Tabla 7.2: Physical properties of the pure components.[a],[b]

Fluid	P_c / bar	T_c / K	k_1	k_2
CO_2	73.76	304.20	0.70205	0
THF	51.90	540.00	0.71381	0.01605

[a] The critical pressure (P_c) and the critical temperature (T_c) were taken from Ref. [83]
[b] k_1 and k_2 are the parameters involve in the Stryjek-Vera thermal cohesion function [87], which were fitting from experimental vapor pressure data taken from Ref. [83] and following the procedure described by Wisniak *et al.* [88]

Using Eq. (7.8) in Eqs. (7.6) and (7.7), the final expression for f_0 and μ_i

$$f_0 = \sum_{i=1}^{2} RT\rho_i \ln\left(\frac{\rho_i}{\rho}\right) - RT\rho\ln(1-b\rho) - \frac{a\rho}{2b\sqrt{2}}\ln\left(\frac{1+b\rho+\sqrt{2}b\rho}{1+b\rho-\sqrt{2}b\rho}\right) - RT\rho\ln\left(\frac{P_{ref}}{rt\rho}\right) \tag{7.14}$$

$$\begin{aligned}\mu_i &= -RT\ln(1-b\rho) - \left(\frac{\partial\rho^2 a}{\partial\rho_i}\right)\frac{1}{2\sqrt{2}b\rho}\ln\left(\frac{1+b\rho+\sqrt{2}b\rho}{1+b\rho-\sqrt{2}b\rho}\right) - RT\rho\ln\left(\frac{P_{ref}}{rt\rho}\right) + RT \\ &+ \left(\frac{\partial\rho b}{\partial\rho_i}\right)\frac{1}{2\sqrt{2}b^2}\ln\left(\frac{1+b\rho+\sqrt{2}b\rho}{1+b\rho-\sqrt{2}b\rho}\right) - \left(\frac{\partial\rho b}{\partial\rho_i}\right)\frac{a\rho}{[1-(b\rho-2)\,b\rho]\,b} + \left(\frac{\partial\rho b}{\partial\rho_i}\right)\frac{RT\rho}{(1-b\rho)}\end{aligned} \tag{7.15}$$

where P_{ref} is some freely chosen reference pressure (*i. e.* $P_{ref} = 1bar$). In addition, from Eq. (7.4) it is possible to obtain the parametric relationship between density profiles and interface length as

$$z(\rho_k) = z_0\left(\rho_k^0\right) + \int_{\rho_k^0}^{\rho_k}\left[\frac{1}{2\Delta\Phi}\sum_{i,j}^{2} c_{ij}\left(\frac{d\rho_i}{d\rho_k}\right)\left(\frac{d\rho_j}{d\rho_k}\right)\right]^{1/2} d\rho_k \tag{7.16}$$

where $\Delta\Phi$ is given by the following definition

$$\Delta\Phi = P^0 + f^0 - \sum_{i=1}^{2}\rho_i\mu_i^0 \tag{7.17}$$

and P^0 corresponds to the equilibrium pressure. It should be noted that the application of Eq. (7.5) allows defining a parametrical relationship between the density profiles of the components $\{\rho_i(\rho_j), i = 1,2,\ j = 1,2 \neq i\}$ once the equilibrium densities are known. Then, the application of eq (7.16) allows calculating the normal coordinate z for a given interfacial state of the density profile. In the framework of SGT, the interfacial tension, γ, can be calculated knowing the parametrical relationship between the density profiles in Eq. (7.5):

$$\gamma = \int_{\rho_k^0}^{\rho_k} \left[2\Delta\Phi \sum_{i,j}^{2} c_{ij} \left(\frac{d\rho_i}{d\rho_k} \right) \left(\frac{d\rho_j}{d\rho_k} \right) \right] d\rho_k \tag{7.18}$$

From a mathematical viewpoint, integration of Eq. (7.16) allows quantification of the population of species at the interface ($\rho_i(z)$) from which the surface activity (or absolute adsorption / desorption of species along the interface region), relative Gibbs adsorption isotherm and the interfacial or surface tension can be calculated and also compared with experimental results in Eq. (7.2).

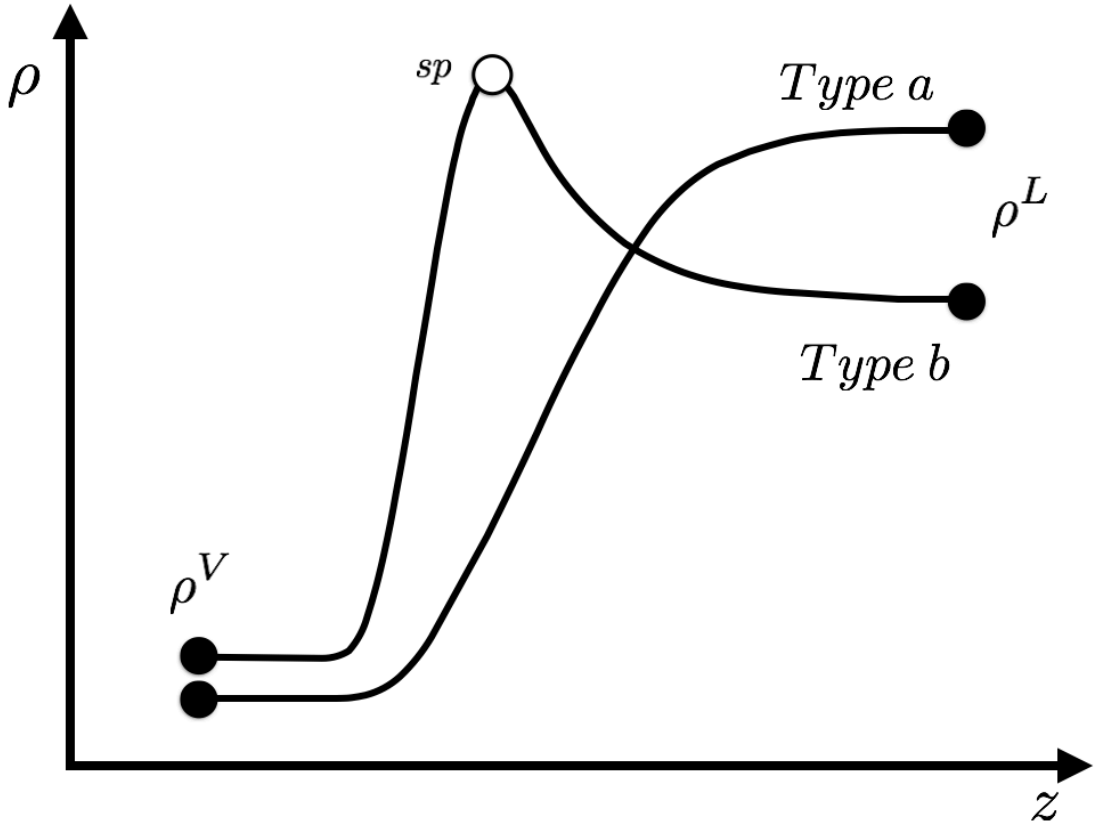

Figura 7.2: Schematic representation of concentration profiles along the interfacial region. (circles) bulk phases: vapor (ρ^V) and liquid (ρ^L); (open circles) sp: Stationary Point.

Figure (7.2) shows, schematically, the most usual $\rho_i(z)$ distribution obtained from the integration of Eq. (7.16). In this projection, it is possible to observe that the concentration profile may be a monotonic (Type a) or non-monotonic (Type b) function. According to our experience, Type a profiles (or hyperbolic *tanh* profiles) are found in pure fluids and in mixtures of consecutive n-alkanes [90] and chains (up to 6 segments) using the Mie potential [91, 92]. Type *b* profiles, in turn, are typically found, for at least one component, in asymmetric mixtures such as water + n-alkanes, water + alcohols, mixtures of heavy n-alkanes, CO_2 + n-alkanes, and n-alkanes + branched ethers. [67, 68, 90, 93–99] The reliability of the concentration profiles obtained from the integration of Eqs. (7.16) (Type a and b) has been also verified by using molecular dynamics and/or Monte Carlo simulations. [67, 93–97]

It should be pointed out that the non-monotonic behavior of the concentration profiles (Type b) is interesting because it reflects the surface activity at the interface. Specifically, the accumulation of a species i at the interface region is characterized by the condition, $d\rho_i/dz = 0$ (see SP point in

Fig. (7.2)), and it may be positive (most common case) or negative. The positive surface activity reflects absolute adsorption of species along the interface region and is reflected in a negative second derivative, $d^2\rho_i/dz^2 < 0$. In this case, the component i is found in the surface zone in higher concentration than what might be expected from its concentration in the bulk phases. Inversely, the negative surface activity denotes desorption of species along the interface region and its condition is given by $d^2\rho_i/dz^2 > 0$. In this case, the component i is found in the surface zone in lower concentration than might be expected from its concentration in the bulk phases. The relative Gibbs adsorption isotherm of a species i relative to a species j (Γ_{ij}) can be expressed in terms of $\rho_i(z)$ by the following integral equation [100, 101]:

$$\Gamma_{ij} = \int_{-\infty}^{z_0^j} [\rho_i(z) - \rho_i^{\alpha}]dz + \int_{z_0^j}^{+\infty} [\rho_i(z) - \rho_i^{\beta}]dz \tag{7.19}$$

In Eq. (7.19), z_0^j is the location of the divide position relative to a species j. z_0^j is calculated from Eq. (7.19) considering that species j does not have adsorption along the interfacial region (Type a profile). In other words, Eq. (7.19) is solved for the case that $\Gamma_{jj} = 0$. Once z_0^j is fixed, the relative Gibbs adsorption isotherm of a species i relative to a species j (Γ_{ij}) is calculated from Eq. (7.19).

Figures (7.3) show, schematically, the location and application to z_0^j. In Figure 7.3(a), z_0^j is defined as the geometric locus where Area 1 (A_1) equals Area 2 (A_2). According to Eq. (7.19), $\Gamma_{jj} = A_2 + (-A_1)$ implies that $\Gamma_{jj} = 0$. In Figure 7.3(b), the location of z_0^j conducts to $A_2 > A_1$, and therefore $\Gamma_{ij} > 0$.

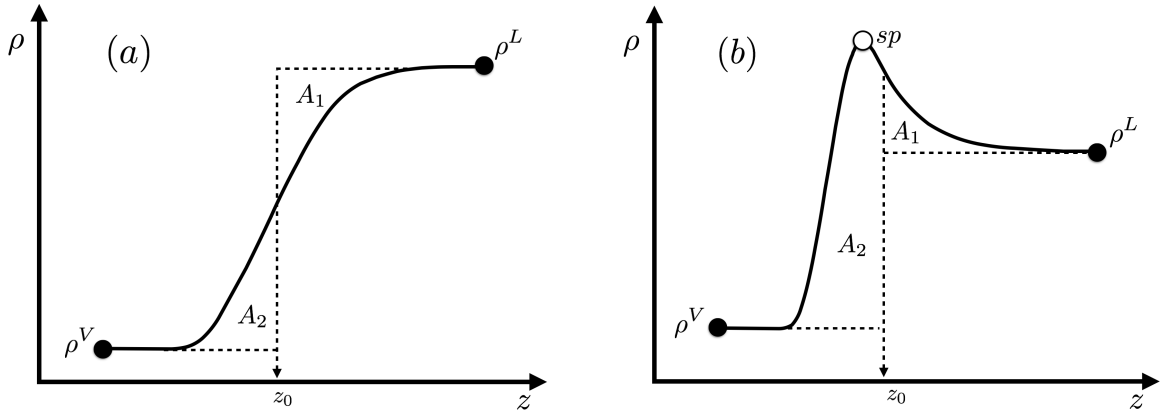

Figura 7.3: Schematic representation of the location of the divide position (z_0) in the relative Gibbs adsorption isotherm. (a): Interfacial concentration for specie j with Area 1 (A_1) equal to Area 2 (A_2); (b) Interfacial concentration for specie i with $A_2 > A_1$.

7.4 Results and Discussions

A central requirement to theoretically and physically describe significant interfacial behavior (*i.e.* concentrations profiles, interfacial tensions and surface activity) is to predict accurately bulk phase boundary conditions. Vapor-liquid phase equilibrium data (p, T, x, y, ρ_L and ρ_V) for CO_2 + THF have been reported by Lazzaroni *et al.* [41], Kodama *et al.* [43] and Knez *et al.* [42]. In this work, complementary data about bulk phase equilibrium densities and for the first time, interfacial tensions measurements have been obtained.

Tabla 7.3: Experimental bulk phase mass densities ($\hat{\rho}$) and interfacial tensions (γ) for carbon dioxide (1) + tetrahydrofuran (2) mixture.[a]

x_1	p (MPa)	$\hat{\rho}_L$ (kg m^{-3})	$\hat{\rho}_V$ (kg m^{-3})	γ (mN m^{-1})	u_c (mN m^{-1})
T= 298.15 K					
0.108	0.50	891.429	8.474	23.81	0.18
0.196	1.00	896.555	17.192	21.78	0.17
0.282	1.50	901.183	28.287	19.44	0.18
0.367	2.00	906.515	39.443	16.91	0.19
0.449	2.50	912.302	52.124	14.27	0.14
0.532	3.00	915.294	64.014	11.62	0.14
0.612	3.50	914.871	80.959	9.05	0.15
0.690	4.00	914.708	94.981	6.65	0.13
0.767	4.50	913.603	114.306	4.53	0.15
0.843	5.00	807.685	134.912	2.78	0.17
T= 353.15 K					
0.069	1.00	846.841	15.161	17.76	0.19
0.147	2.00	848.384	32.758	15.07	0.18
0.225	3.00	849.726	51.006	12.59	0.19
0.306	4.00	856.038	70.392	10.34	0.21
0.388	5.00	851.067	91.121	8.30	0.14
0.473	6.00	848.628	118.961	6.48	0.11
0.559	7.00	838.346	147.043	4.87	0.19
0.646	8.00	821.886	180.898	3.48	0.19

[a] Variables and measurement uncertainties are: $\hat{\rho}\pm 5\times 10^{-3}$ kg m^{-3}; $p\pm 10^{-4}$ MPa; $T\pm$0.10K.
[b] Experimental data from Ref. [41–43]

Tabla 7.4: Optimized (Model 1) and Rescaled (Model 2) Square-Well Intermolecular Potential Parameters [45] for CO_2 and THF.

	Molecule	m	σ	ε	λ
Model 1	CO_2	2	2.7864	179.27	1.515727
	THF	2.824	3.2060	184.900	1.738000
Model 2	CO_2	2	3.1363	168.841	1.515727
	THF	2.824	3.5684	173.828	1.738000

Table 7.3 summarizes the experimental determinations for the bulk phase mass densities for the CO_2 + THF mixture at 298.15 and 353.15 K, and the corresponding CO_2 concentration (in the THF (2)) obtained from experimental data (Ref. [41–43]). In Figure 7.4, the continuous lines denote the calculation results by the Peng-Robinson [86], while dashed (Model 1) and dashed-dotted lines (Model 2) the SAFT-VR EoS [102, 103] calculations. Peng-Robinson parameters are detailed on the table Table 7.2, while in the predictions generated by SAFT-VR we used the parameters summarized Table 7.4 with a binary interaction parameter $\xi_{12} = 0.95$. First of all we compare the predictions of concentration diagrams at 298.15 K (Figure 7.4(a)) and 353.15 K (Figure 7.4(b)). We note that Peng-Robinson is able to describe this kind of mixture at the two temperature conditions, however the optimized parameters of SAFT-VR (Model 1) can not reproduce phase diagrams above critical

temperature of CO_2, obviously compared to the rescaled parameters (Model 2). Discussed previously, in the work of Mejía *et al.* [80], a correct prediction of phase equilibrium is not a direct consequence of predicting other properties such as densities and interfacial tensions. As shown in Figure 7.4(c)-(d), Peng-Robinson equation of state yields good results in the two temperatures selected, especially for liquid and vapor density if compared with the two models used with the SAFT-VR. On the one hand, the vapor phase is under-predicted as pressure increases with Model 1 (Optimized parameters). On the other hand, being the worst scenario of the mixture, model 2 (rescaled parameters) practically reduces by 50% the liquid density prediction, only with the fact of adjusting its parameters in order to predict accurately the concentration diagrams. Table 7.5 summarizes the absolute average deviation (AAD) in liquid and vapor mass density for each model, concluding that SAFT-VR (model 1 and model 2) it is not the most appropriate model for characterized density behavior, and therefore the prediction of interfacial tensions wont be appropriated.

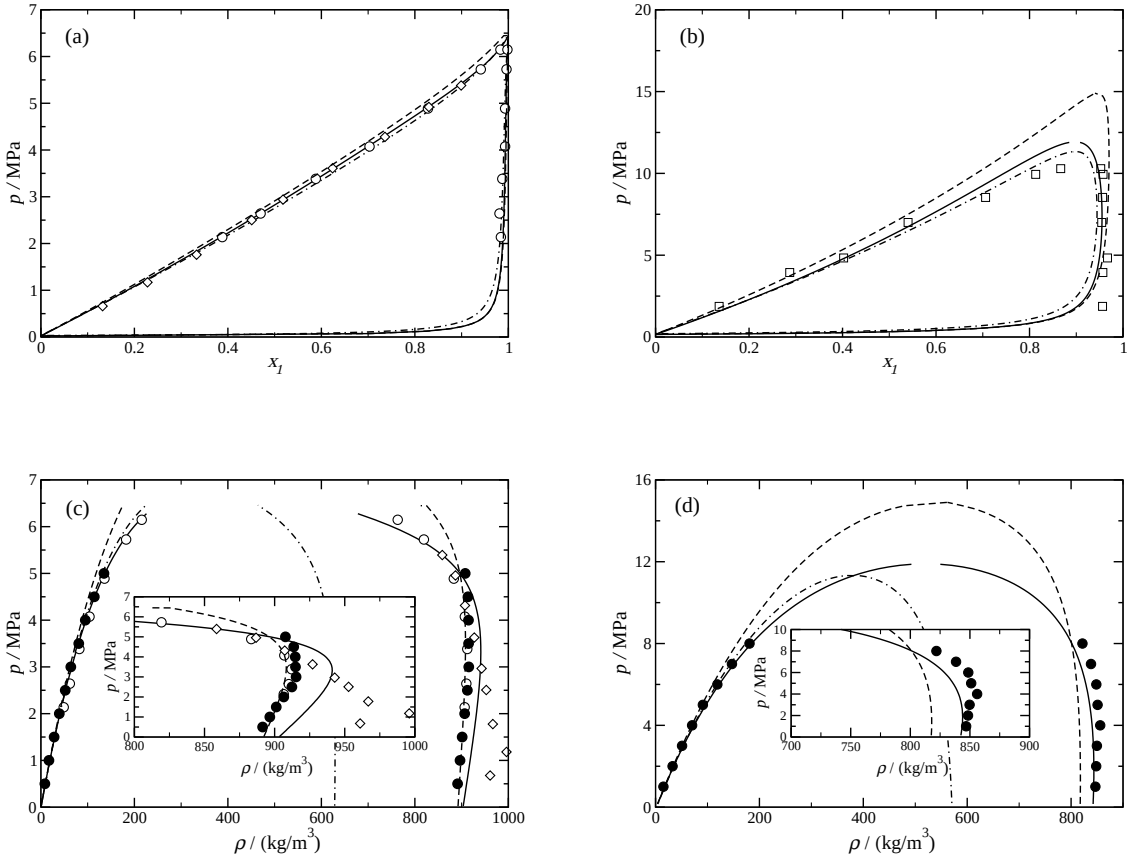

Figura 7.4: Concentration and saturated bulk densities projections for carbon dioxide (1) + THF (2) at 298.15 K (a,c) and 353.15 K (b,d). (full circles) This work; (open diamonds) Lazzaroni *et al.* [41]; (open circles) Kodama *et al.* [43], (open squares) Knez *et al.* [42]; (continuous line) Peng-Robinson EoS; (dashed line) SAFT-VR EoS (model 1); (dashed dotted line) SAFT-VR EoS (model 2).

From experimental viewpoint and in order to check out our experimental technique [67, 68] for measuring bulk densities in this kind of mixture, Figure 7.4(c) compares our experimental results with those obtained previously in the literature [41, 43]. Particularly, our vapor and liquid densities are in excellent agreement with the data of Kodama *et al.* [43] at 298.15 K from low to high pressure. It is interesting to note that the saturated liquid density at this temperature is shifted in the low pressure

range from the data of Lazzaroni *et al.* [41], probably because their density data were not measured directly.

Tabla 7.5: Absolute average deviation (AAD) in bulk densities predictions for CO_2 (1) + THF (2) at 298.15 and 353.15 K.[a]

	298.15 K		353.15 K	
EoS Model	ADD ($\hat{\rho}_L$)	ADD ($\hat{\rho}_V$)	ADD ($\hat{\rho}_L$)	ADD ($\hat{\rho}_V$)
PR	3.98	2.24	1.59	0.89
SAFT-VR (Model 1)	1.63	6.95	4.35	8.02
SAFT-VR (Model 2)	32.63	4.15	39.35	4.02

[a] Absolute Average Desviation (AAD): $AAD\theta = (1/N_{exp}) \sum_{i}^{N_{exp}} \left|\theta_i^{exp} - \theta_i^{cal}\right| / \theta_i^{exp}$ with $\theta = \hat{\rho}_L, \hat{\rho}_V$. Experimental data ($\theta_i$) taken from this work.

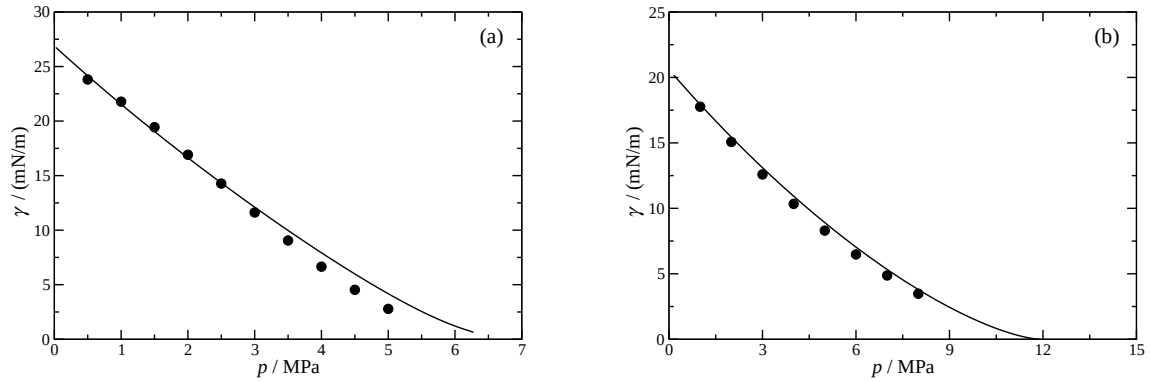

Figura 7.5: Interfacial tensions for CO_2 (1) + THF (2) at 298.15 K (a) and 353.15 K (b). (full circles) This work; (continuous line) SGT + Peng-Robinson EoS.

Experimental measurements for interfacial tensions are collected in Table 7.3 while Figure 7.5 depicts the experimental and predicted interfacial tensions as a function of pressure using the SGT coupled with PR EoS using a quadratic mixing rule (QMR). The values reported in these tables have been obtained from eq (7.1) considering the experimental values of d_s, d_e, $\hat{\rho}_L$ and $\hat{\rho}_V$. At this point it is important to remark that the interfacial tensions reported in Table 7.3 have been obtained from eq (7.1) using the actual mass densities of the mixture. The common practice of using the mass densities of the pure components instead of mixture densities is a convenient approximation that may be useful for treating extremely immiscible systems or to deal with cases where no experimental mixture density data have been reported. However, the impact of such an approximation on the accuracy of experimentally determined data requires careful assessment (see Georgiadis *et al.* [104]). As it has been reported by Míguez *et al.* [45] CO_2 (1) + THF (2) mixture exhibits a continuum critical line connecting their pure components critical points. According to van Konynenburg and Scott, [46] this type of mixtures is characterized by a completely miscible liquid phase in every temperature condition. This fact implies that all subcritical states exhibit only vapor-liquid equilibrium.

In Figure 7.5(a) it is possible to observe that interfacial tensions monotonously decrease with pressure and particularly, the SGT over-predicts the experimental data of γ at 298.15 K with an

AAD of 4.52%, From experimental viewpoint, it is likely that the overestimation of the interfacial tensions may be and effect of the proximity of the critical condition for pure CO_2, because the time of formation and stabilization on the drop occurs in a very short time. As shown in Figure 7.5(b), when the temperature exceeds CO_2 critical point good agreement between experimental data and theory is observed. In this case, the interfacial tension initiates its route at low pressures from pure THF ending in the critical point of the mixture with an AAD of 1.87%. As described before, in addition to predict the interfacial tension of the mixture, the SGT provides a rigorous route to analyze other interfacial properties such as the interfacial concentration population and the Gibbs adsorption isotherm.

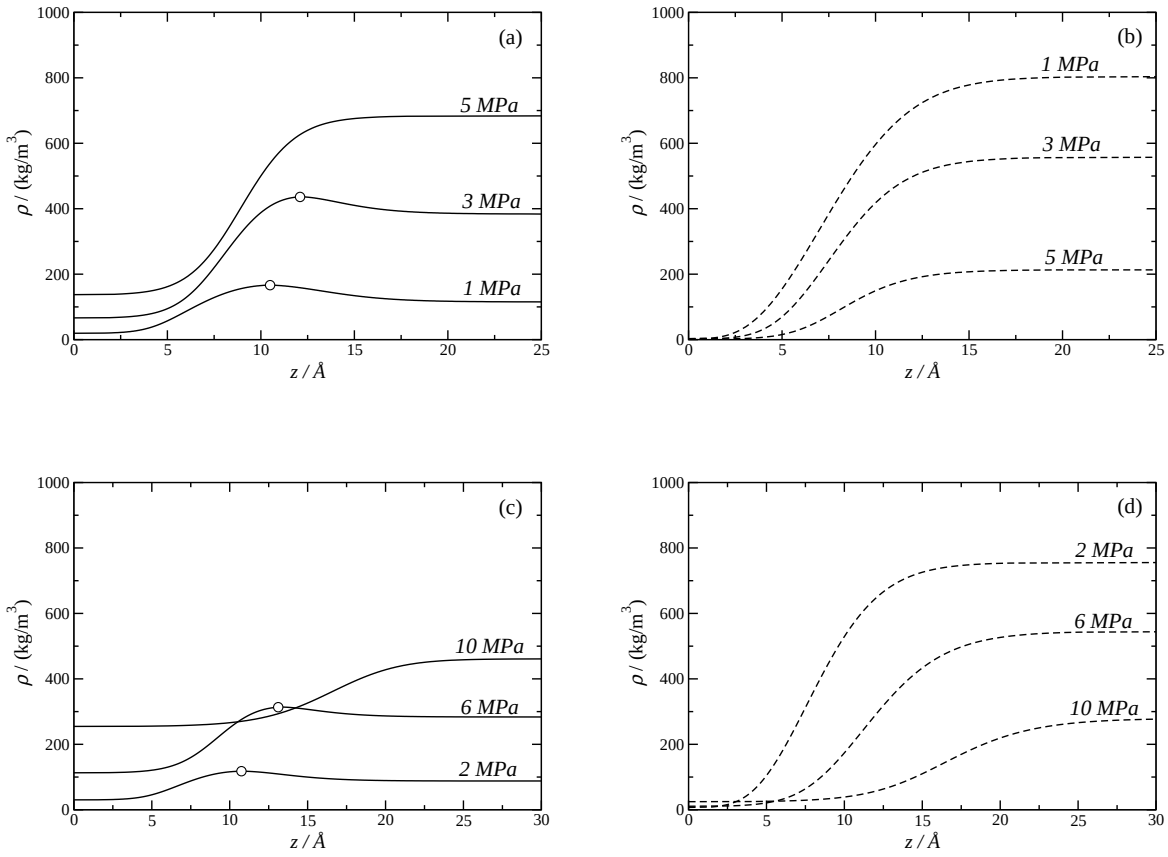

Figura 7.6: Concentration profiles (ρ_i) along the interfacial region, z, for CO_2 (1) + THF (2) mixture at 298.15 K (a,b) and 353.15 K (c,d) as a function of pressure (p). (continuous lines) concentration profiles of CO_2 and (dashed lines) THF.

Figure 7.6 show the $z - \rho_i$ projection as a function of pressure. In that figure, we observe that CO_2 exhibits positive surface activity (i.e. $d\rho_1/dz = 0$; $d^2\rho_1/dz^2 < 0$ in the interfacial zone), whereas THF does not show surface activity. As it is shown in Figures 7.6(a) and 7.6(c), the surface activity of CO_2 increases with pressure and mole fraction. According to our calculations, the surface activity or absolute adsorption of CO_2 is present over the range $0 < p/$ MPa < 4.5 at 298.15 K and $1 < p/$ MPa < 8.5 at 353.15 K, where its maximum value is found. Finally, Figure 7.7(a) shows the relative Gibbs adsorption isotherm of CO_2 (1) with respect to THF (2). It is seen how Γ_{12} increases as pressure increases, but decreases when the temperature increases. An interesting condition that we can see in Figure 7.7(a) is that relative Gibbs adsorption generates an inflexion. which can probably be attributed to the supersaturation of CO_2 on the interfacial zone. As expected from inspection of Figure 7.6(a)

and 7.6(c), the magnitude of the relative Gibbs adsorption of CO_2 in THF is moderate, in comparison with supercritical gases (*i.e.* nitrogen, methane and CO_2) or with other fluids. [67, 68, 97, 105]

In order to understand CO_2 supersaturation, we use the so-called interfacial enrichment (E) introduced by Becker *et al.* [106]. Physically this parameter represent the ratio between the maximum local component density of fluid absorbed ($\rho_{CO_2}(z)$) in the interfacial region and the larger of the component densities in the two bulk phases ($\rho^L_{CO_2}, \rho^V_{CO_2}$)

$$E_{CO_2} = \frac{\max\left(\rho_{CO_2}(z)\right)}{\max\left(\rho^L_{CO_2}, \rho^V_{CO_2}\right)} \tag{7.20}$$

In this work the enrichment can only be determined from the component density profiles obtained from SGT calculations, because there is no experimental way to estimate the interfacial concentration. Figure 7.7(b) shows that the enrichment decreases with increasing pressure and increases when the temperature increases. It is important to recognize that the enrichment approaches unity when the stationary condition in the interfacial zone disappears. Comparing both figures we can see that enrichment shows the range in which adsorption reaches the saturation limit of CO_2.

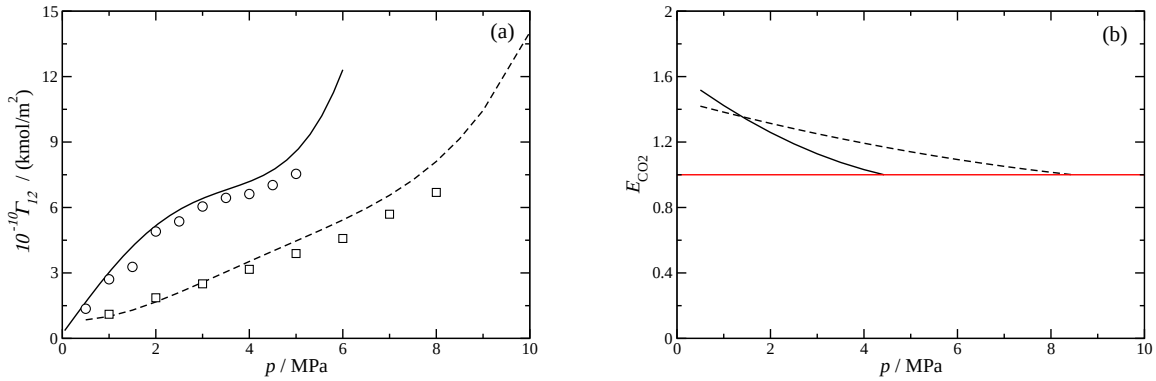

Figura 7.7: a) Relative Gibbs adsorption isotherm (Γ_{12}) and (b) interfacial enrichment (E) for CO_2 (1) + THF (2) mixture as a function of pressure (p). (circles) Experimental data from Eq. (7.2) at 298.15 K; (squares) Experimental data from Eq. (7.2) at 353.15 K, (continuous line) SGT + PR EoS at 298.15 K; (continuous line) SGT + PR EoS at 353.15 K; (red line) supersaturation of CO_2.

7.5 Conclusions

In this work, bulk phase mass densities and interfacial tensions at vapor-liquid equilibrium for CO_2 + THF at high pressure, and temperatures of 298.15 and 353.15 K have been measured and theoretically modeled. According to experimental data, the vapor mass densities at both temperatures increases with pressure, whereas the liquid mass densities initially increases with the pressure and reaches a maximum value, which is probably related to the maximum adsorption of CO_2 in the liquid THF phase. For higher pressure, liquid densities starts to decrease until the pure CO_2 condition is obtained at 298.15 K or at 353.15 K, or if reached the critical point in the mixture. The new bulk phase densities experimental data exhibit very good agreement with previous works, but some appreciable deviations are observed at low pressure, with a maximum deviation in the liquid phase of 15% from

one source [41] and 3.1% from the other one [43]. For the mixture considered here, it is possible to conclude that interfacial tensions decreases monotonically in the experimental pressure range.

Besides the new experimental data reported for interfacial tensions of the mixture, a fully predictive theoretical scheme was used to predict both phase densities and interfacial properties. The application of the square gradient theory coupled to the Peng-Robinson EoS, appropriately extended to mixtures within the framework of a predictive quadratic mixing rule, provides a route to determine interfacial tensions as a function of pressure. This theoretical method can be used to explore or predict other interfacial properties such as the interfacial concentration profiles. According to the results, accurate predictions of the interfacial tensions data were obtained (showing an AAD $< 3\%$). In addition, the present approach applied to a characterization of the interfacial behavior allows concluding that CO_2 is adsorbed at the interface region, showing that its surface activity decreases as pressure increases, eventually reaching the saturation limit where both profiles show hyperbolic *tanh* behavior.

Interfacial tension and accumulation of CO_2 at THF interface plays a key role on the crystallization kinetics of hydrates, due it allows to analyze a possible interaction between the thermodynamic promoter (THF) and the guest molecule (CO_2). CO_2 captures into an aqueous solution is still a development area of research, due that theoretical models, experimental measurements and molecular simulation are still deficient in predicting the interfacial behavior of hydrates. [107] his extension is not pursued here but will be the subject of future work.

7.6 Acknowledgments

This work was financed by FONDECYT, Santiago, Chile (Project 1150656). This work was supported by the Spanish Ministerio de Economía y Competitividad through Grant Nos. FIS2013-46920-C2-1-P, FIS2015-68910-P, and FIS2015-71749-REDT. J.A., I.M.-V.B., J.M.M., and F.J.B also gratefully acknowledge Universidad de Huelva and Junta de Andalucía. J.A. also acknowledges Contrato Predoctoral de Investigación from XIX Plan Propio de Investigación de la Universidad de Huelva and a FPU Grant (Ref. FPU15/03754) from Ministerio de Educación, Cultura y Deporte.

Bibliography

[1] R. K. Pachauri and L. Meyer, eds., *IPCC, 2014: Climate Change 2014: Synthesis Report. Contribution of Working Groups I, II and III to the Fifth Assessment Report of the Intergovernmental Panel on Climate Change*. IPCC, Geneve, Switzerland, 2014.

[2] K. Ding, D.-L. Zhong, Y.-Y. Lu, and J.-L. Wang *Energy & Fuels*, vol. 29, no. 5, pp. 2971–2978, 2015.

[3] P. Linga, A. Adeyemo, and P. Englezos *Environ Sci. Technol.*, vol. 42, no. 1, pp. 315–320, 2007.

[4] H. Adous, *CO2 at Power Stations, Greenhouse Gas Control Technologies*. Proceedings of the 5th International Conference on Greenshouse Gas Control Technologies, Cairns, 2001.

[5] J. Kittel, R. Idem, D. Gelowitz, P. Tontiwachwuthikul, G. Parrain, and A. Bonneau, *Corrosion in MEA Units for CO2 Capture: Pilot Plant Studies*. Elsevier Science BV, Amsterdam, 2009.

[6] R. Idem, D. Gelowitz, and P. Tontiwachwuthikul, *Evaluation of the Performance of Various Amine Based Solvents in an Optimized Multipurpose Technology Development Pilot Plant.* Elsevier Science BV, Amsterdam, 2009.

[7] B. Gwinner, D. Roizard, F. Lapicque, E. Favre, R. Cadours, P. Boucot, and P. L. Carrette *Ind. Eng. Chem. Res.*, vol. 45, no. 14, pp. 5044–5049, 2006.

[8] M. G. Plaza, S. Garcia, F. Rubiera, J. J. Pis, and C. Pevida *J. Chem Eng.*, vol. 163, no. 1-2, pp. 41–47, 2010.

[9] E. Favre, D. Roizard, R. Bounaceur, and W. J. Koros, *Reverse Selective Gas Separation Membranes: Technological Opportunities and Scientific Challenges.* Elsevier Science BV, Amsterdam, 2009.

[10] Y. F. Makogon, *Hydrates of Hydrocarbon.* Pennwell Publishing Co.:Tulsa, OK, 1997.

[11] A. D. J. MacKerell *J. Phys. Chem.*, vol. 99, pp. 1846–1855, 1995.

[12] D. D. Link, E. P. Ladner, H. A. Elsen, and C. E. Taylor *Fluid Phase Equilib.*, vol. 211, pp. 1–10, 2003.

[13] W. Lin, G.-J. Chen, C.-Y. Sun, X.-Q. Guo, Z.-K. Wu, M.-Y. Liang, L.-T. Chen, and L.-Y. Yang *Chem. Eng. Sci.*, vol. 59, pp. 4449–4455, 2004.

[14] R. Kumar, P. Linga, J. A. Ripmeester, and P. Englezos *J. Environ. Eng.*, vol. 135, pp. 411–417, 2009.

[15] X. S. Li, C. G. Xu, Z. Y. Chen, and J. Cai *Int. J. Hydrogen Energy*, vol. 37, pp. 720–727, 2012.

[16] N. Daraboina, J. A. Ripmeester, and P. Englezos *Int. J. Greenhouse Gas Control*, vol. 15, pp. 97–103, 2013.

[17] E. Sloan *Nature*, vol. 426, pp. 353–363, 2003.

[18] E. D. Sloan and C. Koh, *Clathrate Hydrates of Natural Gases, 3rd ed.* CRC Press, New York, 2008.

[19] K. McMullan and G. A. Jeffrey *J. Chem. Phys.*, vol. 42, pp. 2725–2733, 1965.

[20] T. W. Mak and R. K. McMullan *J. Chem. Phys.*, vol. 42, pp. 2732–2737, 1965.

[21] J. A. Ripmeester, J. S. Tse, C. I. Ratcliffe, and B. M. Powell *Nature*, vol. 325, pp. 135–136, 1987.

[22] A. Sum, C. A. Koh, and E. D. Sloan *Ind. Eng. Chem. Res.*, vol. 48, pp. 7457–7465, 2009.

[23] D. F. Spencer, *Methods of selectively separating CO2 from a multicomponent gaseous stream.* US Patent, USA, 1997.

[24] D. F. Spencer, *Methods of selectively separating CO2 from a multicomponent gaseous stream using CO2 hydrate promoters.* US Patent, USA, 1997.

[25] M. Ricaurte, C. Dicharry, D. Broseta, X. Renaud, and J.-P. Torré *Ind. Eng. Chem. Res.*, vol. 52, pp. 899–910, 2013.

[26] D.-L. Zhong, Z. Li, Y.-Y. Lu, and D.-J. Sun *J. Chem. Eng. Data*, vol. 59, pp. 4110–4117, 2014.

[27] Y. Seo and S.-P. Kang *Chem. Eng. J.*, vol. 161, pp. 308–312, 2010.

[28] A. Iizukaa, S. Hayashia, H. Tajimac, F. Kiyonoc, Y. Yanagisawa, and A. Yamasakic *Sep. and Purif. Tech.*, vol. 139, pp. 70–77, 2015.

[29] H. Tajima, A. Yamasaki, and F. Kiyono *Energy*, vol. 29, pp. 1713–1729, 2004.

[30] P. Linga, N. Daraboina, J. A. Ripmeester, and P. Englezos *Chem. Eng. Sci.*, vol. 68, pp. 617–623, 2012.

[31] D. Mech, P. Gupta, and J. S. Sangwai *J. Nat. Gas Sci. Eng.*, vol. 35, pp. 1519–1534, 2016.

[32] P. J. Herslund, K. Thomsen, J. Abildskov, N. von Solms, A. Galfre, P. Brantuas, M. Kwaterski, and J.-M. Herric *Int. J. Greenhouse Gas Control*, vol. 17, pp. 397–410, 2013.

[33] N. Daraboina and N. von Solms *J. Chem. Eng. Data*, vol. 60, pp. 247–251, 2015.

[34] M. Yang, W. Jing, J. Zhao, Z. Ling, and Y. Song *Energy*, vol. 106, pp. 546–553, 2016.

[35] A. Mandal and S. Laik *Energy & Fuels*, vol. 22, no. 4, pp. 2527–2532, 2008.

[36] J.-P. Torré, D. Haillot, S. Rigal, R. S. Lima, C. Dicharry, and J.-P. Bedecarrats *Chem. Eng. Sci.*, vol. 126, pp. 688–697, 2015.

[37] R. Anderson, A. Chapoy, and B. Tohidi *Langmuir*, vol. 23, pp. 3440–3444, 2007.

[38] S.-P. Kang, H. Lee, C.-S. Lee, and W.-M. Sung *Fluid Phase Eq.*, vol. 185, pp. 101–109, 2001.

[39] Y.-J. Lee, T. Kawamura, Y. Yamamoto, and J.-H. Yoon *J. Chem. Eng. Data*, vol. 57, pp. 3543–3548, 2012.

[40] J. Im, W. Bae, J. Lee, and H. Kim *J. Chem. Eng. Data*, vol. 49, pp. 35–37, 2004.

[41] M. J. Lazzaroni, D. Bush, J. S. Brown, and C. A. Eckert *J. Chem. Eng. Data*, vol. 50, pp. 60–65, 2005.

[42] Z. Knez, M. Škerget, L. Ilič, and C. Lütge *J. Supercrit. Fluids*, vol. 43, pp. 383–389, 2008.

[43] D. Kodama, T. Yagihashi, T. Hosoya, and M. Kato *Fluid Phase Eq.*, vol. 297, pp. 168–171, 2010.

[44] J. Li, M. Rodrigues, A. Pavia, H. A. Matos, and E. G. de Azevedo *J. Supercrit. Fluids*, vol. 41, pp. 343–351, 2007.

[45] J. M. Míguez, M. M. Piñeiro, J. Algaba, B. Mendiboure, J. P. Torré, and F. J. Blas *J. Phys. Chem. B*, vol. 119, no. 44, pp. 14288–14302, 2015.

[46] P. H. van Konynenburg and R. L. Scott *Philos. Trans. A*, vol. 298, no. 1442, pp. 495–540, 1980.

[47] H.-B. Qin, C.-Y. Sun, Z.-F. Sun, B. Liu, and G.-J. Chen *Chem. Eng. Sc.*, vol. 48, pp. 182–189, 2016.

[48] A. Arora, S. S. Cameotra, R. Kumar, C. Balomajumder, A. K. Singh, B. Santhakumari, P. Kumar, and S. Laik *Scientific Reports*, vol. 6, p. 20893, 2016.

[49] J. M. Míguez, M. M. Conde, J.-P. Torré, F. J. Blas, M. M. Piñeiro, and C. Vega *J. Chem. Phys.*, vol. 142, pp. 124505–124517, 2015.

[50] S. K. Suri and H. Naorem *J. Chem. Eng. Data*, vol. 32, no. 462–464, 1987.

[51] A. Amigo, R. Bravo, and M. Pintos *J. Chem. Eng. Data*, vol. 38, no. 141–142, 1993.

[52] A. Piñeiro, P. Brocos, A. Amigo, M. Pintos, and R. Bravo *J. Chem. Eng. Data*, vol. 31, pp. 931–942, 1999.

[53] P. Brocos, A. Piñeiro, R. Bravo, A. Amigo, A. K. Roux, and G. Roux-Desgranges *J. Chem. Eng. Data*, vol. 47, no. 351–358, 2002.

[54] H. Shekaari and M. T. Zafarani-Moatta *Int. J. Thermophys.*, vol. 29, pp. 534–545, 2008.

[55] M. T. Zafarani-Moatta and R. Majdan-Cegincara *J. Chem. Eng. Data*, 2359–2364 2007.

[56] S. Rodríguez *J. Chem. Thermodyn.*, vol. 31, pp. 139–149, 1999.

[57] M. Geppert-Rybczyńska, A. Heintz, J. K. Lehmann, and A. Golus *J. Chem. Eng. Data*, vol. 55, pp. 4114–4120, 2010.

[58] D. H. S. Ramkumar and A. P. Kudchadker *J. Chem. Eng. Data*, vol. 34, pp. 463–465, 1989.

[59] C. Pan, Q. Ke, G. Ouyang, X. Zhen, Y. Yang, and Z. Huang *J. Chem. Eng. Data*, no. 49, pp. 1839–1842, 2004.

[60] A. Villares, B. Giner, H. Artigas, C. Lafuente, and F. M. Roy *J. Solution. Chem.*, vol. 34, pp. 185–198, 2005.

[61] B. Giner, I. Bandres, H. Artigas, P. Cea, and C. Lafuente *Int. J. Thermophys.*, vol. 28, pp. 1188–1198, 2007.

[62] M. Geppert-Rybczyńska, J. K. Lehmann, and A. Heintz *J. Chem. Eng. Data*, vol. 56, no. 4, pp. 1443–1448, 2011.

[63] V. Diky, R. D. Chitico, C. D. Muzny, A. F. Kazakov, K. Kroenlein, J. W. Magee, I. Abdulagatov, and M. Frankel *J. Chem. Inf. Model.*, vol. 53, no. 12, pp. 3418–3430, 2013.

[64] B. E. Poling, J. M. Prausnitz, and J. P. O'Connell, *The Properties of Gases and Liquids*. McGraw-Hill , New York, 5th ed., 2001.

[65] F. K. Hansen. Ramé-Hart instrument Co., USA, advanced edition ed., 2005.

[66] J. J. C. Hsu, N. Nagarajan, and R. L. RobinsonJr *J. Chem. Eng. Data*, vol. 30, no. 4, pp. 485–491, 1985.

[67] A. Mejía, M. Cartes, H. Segura, and E. A. Müller *J. Chem. Eng. Data*, vol. 50, no. 10, pp. 2928–2941, 2014.

[68] C. Cumicheo, M. Cartes, E. A. Müller, and A. Mejía *Fluid Phase Equilib.*, vol. 380, pp. 82–92, 2014.

[69] J. M. Andreas, E. A. Hauser, and W. B. Tucker *J. Phys. Chem.*, vol. 42, pp. 1001–1019, 1938.

[70] W. L. Masterton, J. Bianchi, and E. J. S. Jr. *J. Phys. Chem.*, vol. 67, pp. 615–618, 1963.

[71] X. Li, E. Boeck, G. C. Maitland, and J. P. M. Trusler *J. Chem. Eng. Data*, vol. 57, pp. 1078–1088, 2012.

[72] X. Li, E. Boeck, G. C. Maitland, and J. P. M. Trusler *J. Chem. Eng. Data*, vol. 57, pp. 1369–1375, 2012.

[73] A. I. Rusanov and V. A. Prokhorov, *Interfacial Tensiometry*. Elsevier, Amsterdam, 1996.

[74] D. S. A. Jr and T. Fort in *Surface and Colloid Science* (R. Good and R. Stromberg, eds.), vol. 11, New York: Plenum Press, 1979.

[75] M. J. B. Evans, *Measurement of surface and interfacial tension.* Elsevier, Amsterdam, 2006.

[76] B. S. Carey, L. E. Scriven, and H. T. Davis *AIChE J.*, vol. 24, no. 6, pp. 1076–1080, 1978.

[77] B. S. Carey and L. E. Scriven *AIChE J.*, vol. 26, no. 5, pp. 705–711, 1980.

[78] P. M. W. Cornelisse, C. J. Peters, and J. de Swaan Arons *Fluid Phase Equilib.*, vol. 82, pp. 119–129, 1993.

[79] P. M. W. Cornelisse, C. J. Peters, and J. de Swaan Arons *Mol. Phys.*, vol. 80, no. 4, pp. 941–955, 1993.

[80] A. Mejía, H. Segura, L. F. Vega, and J. Wisniak *Fluid Phase Equilib.*, vol. 227, pp. 225–238, 2005.

[81] C. Miqueu, B. Mendiboure, A. Graciaa, and J. Lachaise *Fluid Phase Equilib.*, vol. 218, pp. 189–203, 2004.

[82] C. Miqueu, B. Mendiboure, A. Graciaa, and J. Lachaise *Fluid Phase Equilib.*, vol. 207, no. 1-2, pp. 225–246, 2003.

[83] T. E. Daubert and R. P. Danner, *Physical and Thermodynamic Properties of Pure Chemicals. Data Compilation.* Taylor and Francis, Bristol, PA, 1989.

[84] V. Bongiorno and H. T. Davis *Phys. Rev. A*, vol. 12, no. 5, pp. 2213–2224, 1975.

[85] V. Bongiorno, L. E. Scriven, and H. T. Davis *J. Colloid Interface Sci.*, vol. 57, no. 3, pp. 462–475, 1976.

[86] D. Y. Peng and D. B. Robinson *Ind. Eng. Chem. Fundam.*, vol. 15, no. 1, pp. 59–64, 1976.

[87] R. Stryjek and J. H. Vera *Fluid Phase Equilib.*, vol. 25, no. 3, pp. 279–290, 1986.

[88] J. Wisniak, A. Apelblat, and H. Segura *Chem. Eng. Sci.*, vol. 53, pp. 743–751, 1998.

[89] H. Orbey and S. I. Sandler, *Modeling Vapor Liquid Equilibria: Cubic Equations of State and Their Mixing Rules.* Cambridge University Press, New York, 1998.

[90] E. A. Müller and A. Mejía *J. Phys. Chem. B*, vol. 115, no. 44, pp. 12822–12834, 2011.

[91] G. Mie *Ann. Phys. (Berlin)*, vol. 316, no. 8, pp. 657–697, 1903.

[92] J. M. Garrido, A. Mejía, M. M. Piñeiro, F. J. Blas, and E. A. Müller *AIChE J.*, vol. 62, no. 5, pp. 1781–1794, 2016.

[93] C. Miqueu, J. M. Míguez, M. M. Piñeiro, T. Lafitte, and B. Mendiboure *J. Phys. Chem. B*, vol. 115, no. 31, pp. 9618–9625, 2011.

[94] M. J. Tardón, J. M. Garrido, H. Quinteros-Lama, A. Mejía, and H. Segura *Fluid Phase Equilib.*, vol. 336, pp. 84–97, 2012.

[95] J. M. Míguez, J. M. Garrido, F. J. Blas, H. Segura, A. Mejía, and M. M. Piñeiro *J. Phys. Chem. C*, vol. 118, no. 42, pp. 24504–24519, 2014.

[96] J. M. Garrido, M. M. Piñeiro, A. Mejía, and F. J. Blas *Phys. Chem. Chem. Phys.*, vol. 18, pp. 1114–1124, 2016.

[97] J. M. Garrido, L. Cifuentes, M. Cartes, H. Segura, and A. Mejía *J. Supercrit. Fluids*, vol. 89, no. 1, pp. 78–88, 2014.

[98] O. Lobanova, A. Mejía, G. Jackson, and E. A. Müller *J. Chem. Thermodyn.*, vol. 93, pp. 320–336, 2016.

[99] L. M. C. Pereira, A. Chapoy, R. Burgass, and B. Tohidi *J. Chem. Thermodyn.*, vol. 97, pp. 55–69, 2016.

[100] J. S. Rowlinson and B. Widom, *Molecular Theory of Capillarity*. Clarendon, Oxford, 1982.

[101] J. S. Rowlinson, *Cohesion: A Scientific History of Intermolecular Forces*. Cambridge University Press, 2005.

[102] A. Galindo, L. A. Davies, A. Gil-Villegas, and G. Jackson *Mol. Phys.*, vol. 93, no. 2, pp. 241–252, 1998.

[103] A. Gil-Villegas, A. Galindo, P. J. Whitehead, S. J. Mills, G. Jackson, and A. N. Burgess *J. Chem. Phys.*, vol. 106, pp. 4168–4186, 1997.

[104] A. Georgiadis, F. Llovell, A. Bismarck, F. J. Blas, A. Galindo, G. C. Maitland, J. P. M. Trusler, and G. Jackson *J. Supercrit. Fluids*, vol. 55, no. 2, pp. 743–754, 2010.

[105] E. A. Müller and A. Mejía *Fluid Phase Equilib.*, vol. 282, no. 2, pp. 68–81, 2009.

[106] S. Becker, S. Werth, M. Horsch, K. Langenbach, and H. Hasse *Fluid Phase Equilib.*, vol. 427, pp. 476–487, 2016.

[107] M. Pérez-Rodríguez, A.Vidal-Vidal, J. M. Míguez, F. J. Blas, J.-P. Torré, and M. M. Piñeiro *Phys. Chem. Chem. Phys.*, vol. 19, pp. 3384–3393, 2017.

Capítulo 8

Interfacial Properties of Tetrahydrofuran and Carbon Dioxide Mixture from Computer Simulation

Abstract

We have determined the interfacial properties of the tetrahydrofuran + carbon dioxide (THF + CO_2) binary mixture from direct simulation of the vapor-liquid interface. We consider two different models of THF based on the TraPPE-UA (Transferable parameters for Phase Equilibria, United Atoms version) approach. In the first case, we use the original (flexible) TraPPE-UA model force field for this ether [*J. Phys. Chem. B* **115**, 11234 (2012)]. The second model is a planar and rigid approximated TraPPE-UA model recently proposed by us [*J. Chem. Phys.* **144**, 144702 (2016)]. It is demonstrated that the sophisticated flexible model does not have an over-all advantage in comparison with the simplified planar model. Indeed, both models are able to predict the phase behavior and interfacial tension of pure THF with a high accuracy in a wide range of temperatures and pressures. It is noticed that the planar model is faster for simulating since internal degrees of freedom are frozen (neither bending nor torsional intramolecular interactions need to be evaluated). Most of simulations have been performed in the Molecular Dynamics (MD) canonical ensemble and the vapor-liquid interfacial tension is evaluated from the normal and tangential components of the pressure tensor according to the mechanical virial route. We have also used the Gibbs ensemble Monte Carlo simulation technique to determine the phase behavior of the mixture at selected conditions in order to compare results from both methodologies. In addition to the interfacial tension, we have also obtained density profiles and pressure-density and pressure-composition slices of the phase diagram of the mixture at different temperatures and pressures. Simulation results obtained from both models are able to predict accurately the vapor-liquid phase envelope of the system, in good agreement with experimental results. We also compare the predictions for interfacial tension as obtained from simulation results for the two models with experimental data. Agreement between computer simulation predictions and experiments for the interfacial tension of THF + CO_2 mixtures, as a function of pressure, is excellent in nearly all cases. In addition to that, the density profiles associated to the carbon dioxide exhibit a relative maximum related to preferential adsorption at the liquid interface of tetrahydrofuran. This accumulation in the interface is probably related to the asymmetry in size of the components of the mixture.

8.1 Introduction

Gas hydrates are non−stoichiometric crystalline inclusion compounds consisting of a network of hydrogen-bonded molecules forming cages in which various types of low molecular weight compounds, such as methane (CH_4), carbon dioxide (CO_2), hydrogen sulfide (H_2S), or hydrogen (H_2), among many others, can be enclathrated under appropriate thermodynamic conditions. Due to the characteristics properties of hydrates to selectively encage guest molecules within this solid hydrate crystalline structures, hydrates are nowadays considered strategic and key materials for the industry of gas storage/transportation and mixture separation applications. This includes CH_4, CO_2, and H_2 among the most relevant substances. Although storage, transportation, and mixture separation are key applications for industry, the view of gas hydrates as a possible future source of energy and the environmental use of hydrates for CO_2 sequestration make the understanding of these systems from kinetic, thermodynamic, and structural points of view even more attractive for the scientific community.

The thermodynamic conditions at which the clathrate hydrates structures are formed and become stable depend in a complex fashion on the shape, structure, and molecular interactions of the low molecular weight compounds or guests that are enclathrated in the cages of the water-like crystalline network formed, as well as on the intermolecular interactions between guest and water molecules. In many occasions, the temperatures and pressures at which different clathrate hydrates are stable are far from being considered as mild conditions. As an example, H_2 can be stabilized in clathrate hydrates at extremely high pressures, typically 220 MPa at 249 K [1, 2]. To avoid these extreme conditions, it is usual to add some chemical additives, called hydrate thermodynamic promoters, to water. This provokes a reduction of the formation pressure and/or an increase of the formation temperature of the clathrate hydrates. Among different candidates, tetrahydrofuran, or simply THF, is probably one of the most popular hydrate thermodynamic promoter. A clear example of this effect was shown several years ago by Florusse *et al.* [3] and Lee *et al.* [4]. In this particular case, the addition of small amounts of THF in the water + hydrogen mixture provokes a stabilization of clathrate hydrates of hydrogen in a range of pressures between 5 and 100 MPa at temperatures between 280 and 295 K, approximately, in contrast with the conditions at which pure hydrogen hydrate is formed.

THF is a cyclic ether usually used as solvent in many industrial processes. It is a volatile and extremely flammable substance which can form peroxides if stored with long exposure to air [5]. In addition, it is a severe eye irritant and a mild skin irritant. Also, the use of this ether in laboratory experiments causes technical problems with apparatus and/or analytical devices since it is highly aggressive on some plastic, rubbers and coatings. In spite of these adverse properties, THF is routinely used as clathrate hydrates promoter since it allows mixed gas hydrates to form at significantly lower pressure and higher temperature than the hydrates formed without this promoter. This is particularly true in the case of CH_4, CO_2, and H_2 hydrates, among other examples [6–9].

Apart from the utility of THF as hydrate promoter, aqueous mixtures of this compound exhibit interesting properties from practical and fundamental point of view. THF + water mixture exhibits a highly non-ideal phase behavior and displays some uncommon and interesting phenomena. First at all, this cyclic ether is water-soluble at low ambient pressures and temperatures. At this conditions, THF is able to form by itself a pure hydrate in which THF molecules are enclathrated in large cages of the equilibrium structure, leaving small cages vacant because of its large molecular size (structure sII). The singular aspect of this clathrate hydrate, which is not common in other gas hydrates, is the existence of a univariant two-phase (hydrate + aqueous solution) coexistence curve. This means that

the composition of the aqueous solution in equilibrium with the solid THF hydrate phase is equal to the mole stoichiometric ratio of the THF hydrate (1 molecule of THF per 17 water molecules). Due to that, structure sII THF hydrate is frequently studied as it is easily made by freezing a solution of composition THF·17H_2O. This hydrate is stable at atmospheric pressure up to a congruent melting point of 277.5 K [10]. The miscibility of both compounds at these thermodynamic conditions is a consequence of the hydrogen bonding occurring between the oxygen atom on THF (the ether chemical group) and the hydrogen atoms on water. In the particular case of the cyclic compound, the oxygen atom is more "exposed" to what is normal in the case of linear ethers. This hypothesis is supported by the fact that miscibility of linear ethers in water is much more limited compared with the case of THF in water, in which cyclic structure promotes some degree of polarity, enhancing its mutual miscibility.

The popularity of THF as hydrate thermodynamic promoter has produced a relative large amount of experimental data on the subject, making of it an excellent candidate to be studied from a molecular perspective using alternative methodologies, such as molecular modelling tools, including molecular-based theories and computer simulation techniques (Monte Carlo and Molecular Dynamics), to understand the thermodynamic, structural, and dynamical properties of clathrate hydrates. During the last decades, remarkable progress have been made on the development and application of the molecular modelling techniques for the prediction of thermodynamics properties, including phase equilibria and interfacial properties, of complex mixtures of industrial interest. Among the different methodologies based on a microscopic vision of the system, Monte Carlo (MC) and Molecular Dynamics (MD) techniques are particularly suited to study the behavior of substances with complex chemical structures and different length-scale intermolecular interactions, such as attractive and repulsive dispersive interactions, long-range electrostatic forces, and specific interactions such as hydrogen bonding.

As it has been explain above, the molecular characteristics of THF make it a remarkably difficult target for molecular modeling, being the cyclic structure and the presence of the ether chemical group two of the most challenging molecular details to be modelled. The last ingredient produces a strong polarity and a marked spacial anisotropy, inducing complex molecular interactions including hydrogen bonding, as it has been mentioned before. This is obviously a key question here if an accurate description of the fluid and hydrate phase behavior of mixtures containing this cyclic ether, water, and other guest molecules, such as CO_2, is desired.

In spite of the interest of use of THF as hydrate thermodynamic promoter during last years, THF molecular models are scarce in literature. The first model proposed in literature was proposed in the 1980s by Jorgensen and collaborators in the context of the Transferable Parameters Potential Functions (TIPS), a series of force fields suitable for the use in liquid simulations for water, alcohols, and ethers [11–13]. In particular, the model for THF in this framework was proposed in 1982 by Chandrasekhar and Jorgensen [14, 15]. Several years ago, Jorgensen and co-workers proposed the well-known Optimized Potential for Liquid Simulations -or OPLS- force fields [16, 17], an evolved version of the TIPS approach. However, the authors did not determine THF vapor-liquid coexistence. More recently, several authors [18, 19] have examined some THF force fields and simulated different bulk and structural properties, although none of them considered the simulation of phase diagram of this compound. Only Keasler *et al.* [20] developed a new version of THF in the context of the TraPPE-UA force field (Transferable Parameters for Phase Equilibria-United Atoms) specifically for five- and six-membered cyclic alkanes and ethers, including THF. This model is able to provide accurate saturated liquid densities and vapor pressures, critical temperatures and densities, and other important thermodynamic properties, although interfacial properties have not been considered.

Although accurate description of bulk thermodynamic properties and phase equilibrium is essential for a molecular model, not all properties determined from molecular simulation exhibit the same sensitivity to details of molecular models. In this context, fluid-fluid interfacial properties, and particularly interfacial tension, are one of the most sensitive properties to subtle differences in molecular details.

Following this approach, we have used recently the TraPPE-UA model proposed by Keasler *et al.* [20], to determine the interfacial properties of THF in a wide range of temperatures, from near the triple point up to the critical temperature of the system, with special emphasis on the variation of the structure of the interface with temperature and the surface tension [21]. In addition to that, and following the approach of Chandrasekhar and Jorgensen in their seminal work [14, 15], we have also proposed an approximated, planar, and rigid TraPPE-UA model in which non-bonded interaction intermolecular parameters and partial charges located at the different chemical groups are identical to those of the original TraPPE-UA model. In addition to that, bending and torsional degrees of freedom are frozen, i.e., we consider that the equilibrium bond angles are fixed and the molecule has not torsional degrees of freedom. As an additional approximation, THF is considered in this case not only rigid but also planar. [21] This means that although the fixed bonded angles in this new model are the same than those of equilibrium in the flexible model, the bond lengths are slightly different (Table 8.4). Finally, it is important to remark that the 1- 4 intramolecule interactions are excluded in both models, and the nonbonded interactions are not scaled.

Our previous work demonstrates that both TraPPE-UA models, the rigid the flexible models, are able to provide an excellent accuracy in the whole coexistence range for the vapor-liquid phase envelope of THF [21]. The original TraPPE-UA model proposed by Keasler *et al.* [20] predicts more accurately the saturated liquid density at low temperatures than the approximated rigid version of the model. In addition to that, both united-atoms models are able to predict precisely the vapor-liquid surface tension of THF, one of the most sensitive thermodynamic property. Although the original TraPPE-UA model seems to predict the surface tension better that the approximated rigid model proposed in our previous work, the rigid model is faster for simulating since internal degrees of freedom are frozen (neither bending nor torsional intramolecular interactions need to be evaluated). This is an important and clear advantage, especially when interfacial properties need to be calculated and in the case of mixtures containing other chemical compounds. This is particularly suited if hydrates containing THF and/or similar compounds have to be studied.

The research we are carrying out in these series of papers is devoted to the test and develop models of THF and mixtures with other substances to accurately predict the phase equilibrium and interfacial properties of these systems using computer simulation. The long-term goal of these works is to use the proposed molecular models to predict the phase equilibrium of THF hydrates and hydrates of mixtures of THF with CH_4 and/or CO_2. In this second paper we concentrate in the study of vapor-liquid interfacial properties of the THF + CO_2 binary mixture.

Experimental, theoretical, and computer simulation studies of the phase equilibrium properties and interfacial properties of the THF(1) + CO_2(2) mixture are scarce. This binary mixture exhibits type I phase behavior according to the van Konynenburg and Scott classification [22, 23]. In a *PT* projection of the phase diagram, the gas-liquid critical line is continuous, running from the critical point of component 1, THF, to the critical point of the component 2, CO_2. In particular, there is no liquid-liquid separation in the system, or in other words, the liquid mixture of THF and CO_2 is homogeneous at any composition. Different authors have studied this mixture and determined that

exhibits such as behavior [24–27]. More recently, Míguez *et al.* [28] have also determined the global phase behavior of the mixture using the Statistical Associating Fluid Theory for Variable Range, the SAFT-VR approach, corroborating that the mixture only exhibits a continuous gas-liquid critical line without liquid-liquid separation.

From the experimental point of view, few works have been published to study the vapor-liquid phase equilibria of this mixture. During the first decade of the 21th century, several research groups have studied the vapor-liquid phase behavior of the mixture [24–27]. Most of the authors have concentrated on the determination of pressure-composition or Px slices of the phase diagram for the THF(1) + CO_2(2) mixture at several temperatures, from 298.15 K up to 353.15 K. In addition to that, Kodama *et al.* [27] have also determined the saturated liquid and vapor densities at high pressures, from 2 up to 7.6 MPa at two different temperatures, 298.15 K and 313.15 K. Apart from these five papers, no other experimental data existed in the literature until 2017. Last year, Garrido *et al.* [29] have determined the pressure-density or $P\rho$ slices of the phase diagram of this mixture at two temperatures, 298.15 K and 353.15 K and pressure up to 12 MPa, approximately. The authors have also measured the saturated liquid and vapor densities, as well as interfacial tensions and relative Gibbs adsorption of the mixture. To the best of our knowledge, this is the first time the interfacial properties of the THF(1) + CO_2(2) mixture have been determined experimentally. In addition to that, the authors have also modelled the interfacial behavior of the mixture using the Square Gradient Theory based on a Peng-Robinson phenomenological equation of state. They have demonstrated that the theoretical formalism is able to provide very good agreement between the calculated and experimental data for the properties investigated, including the accumulation of compounds at the interface, observing peculiar adsorption effects of carbon dioxide in the liquid interface of THF.

From the theoretical point of view, only one paper has been published to predict the phase equilibria of the mixture from a truly molecular perspective. Míguez *et al.* [28] considered the phase behavior of three mixtures of THF with complex and important substances from the fundamental and practical point of view, namely, CO_2, CH_4, and water (H_2O). To the best of our knowledge, this is the first time the phase behavior of the THF(1) + CO_2(2) binary mixture is studied using a theoretical approach, such as the SAFT-VR equation of state, based on a molecular perspective. In particular, they have predicted the Px slices of the phase diagram for the THF(1) + CO_2(2) mixture at several temperatures, from 298.15 K up to 353.15 K. They have also determined the pressure-temperature or PT projection of the phase diagram for the mixture, including the continuous gas-liquid critical line. In all cases, the theory is able to describe accurately the critical line of the mixture, as well as the Px slices of the phase diagram at several temperatures.

Finally, to the best of our knowledge, works published in the literature do not exist dealing either the phase equilibria nor interfacial properties of the THF(1) + CO_2(2) mixture from the molecular simulation perspective. As we have mentioned previously along this Introduction, since we are considering the possibility of studying the phase behavior of clathrate hydrates of mixtures of CO_2 and THF, it is necessary to check if models available in the literature are capable to accurately predict the phase behavior and interfacial properties of the system. This may be considered as the continuation of our previous work [21], as well as a step forward in the global study of phase equilibria and interfacial properties covering experiments, theoretical modelling, and computer simulation.

The particular goal of this work is to determine the ability of the TraPPE-UA models, including the flexible and the approximated rigid models of THF, for predicting the vapor-liquid interfacial properties of the THF + CO_2 binary mixture, with particular emphasis on the interfacial tension of

the systems at different temperatures and high pressures.

The rest of the paper is organized as follows. In Section 2 we summarize the molecular models considered, as well as the simulation details. Results and discussion are presented in Section 3. Finally, in Section 4 we present the main conclusions.

8.2 Models and simulation details

8.2.1 Models-co2

In this work, CO_2 has been modeled as a linear rigid molecule using the TraPPE-UA force field proposed by Pottof *et al.* [30]. We use two different models for THF also based on the TraPPE-UA approach. The first one is the original flexible model introduced by Keasler *et al.* [20] and the second is a rigid approximated model proposed by us in a previous work [21]. In both models, the THF molecule is described with three different types of united-atom chemical groups: the ether group or oxygen atom, O, two α-methyl (α-CH_2) bonded directly to the ether group, and two β-methyl (β-CH_2) chemical groups bonded to the α-methyl groups and closing the ring of the cyclic ether.

Non-bonded interactions between different chemical groups of the molecules are accounted for through the Lennard-Jones and Coulomb intermolecular potentials:

$$U(r_{ij}) = 4\epsilon_{ij}\left[\left(\frac{\sigma_{ij}}{r_{ij}}\right)^{12} - \left(\frac{\sigma_{ij}}{r_{ij}}\right)^{6}\right] + \frac{q_i q_j}{4\pi\epsilon_0 r_{ij}} \tag{8.1}$$

where r_{ij} is the distance between interaction sites i and j, σ_{ij} and ϵ_{ij} are the diameter and well depth associated to the LJ intermolecular potential, q_i and q_j are the partial charges on interaction sites i and j, and ϵ_0 is the permittivity of vacuum. The parameters for the potentials of each chemical group of each molecule are presented in Table 8.1. All the LJ parameters for unlike interactions are obtained always using the Lorentz-Berthelot combining rules.

Tabla 8.1: Lennard-Jones well depth, ε, and size, σ, partial charges, q, parameters for the TraPPE-UA force field for non-bonded interactions of THF and CO_2.

Atom	ε/k_B(K)	σ(Å)	q(e)
THF			
O	190	2.20	-0.410
$CH_2(\alpha)$	56.3	3.88	0.160
$CH_2(\beta)$	56.3	3.88	0.045
CO_2			
C	27.0	2.80	0.700
O	79.0	3.05	-0.350

In addition, bonded interactions in molecules are described following the usual TraPPE-UA formalism (see the parameter values for bending and torsional parameters of the model in Tables 8.2 and 8.3). According to the work of Pottof *et al.* [30], CO_2 is modeled as a rigid molecule in which bond lengths between carbon and oxygen groups are fixed. In the case of original TraPPE-UA model for THF, we

Tabla 8.2: Bending potential parameters for the flexible TraPPE-UA model of THF

Bending	θ (degrees)	k_θ/k_B (K/rad)
CH_2-CH_2-CH_2	105.5	62500
CH_2-CH_2-O	108.5	50300
CH_2-O-CH_2	112.0	60400

Tabla 8.3: Torsional potential parameters for the flexible TraPPE-UA model of THF

Torsion	c_0/k_B (K)	c_1/k_B (K)	c_2/k_B (K)	c_3/k_B (K)
CH_2-CH_2-CH_2-CH_2	31394	45914	16518	1496
CH_2-CH_2-CH_2-O	21903	24297	8147	246
CH_2-CH_2-O-CH_2	21933	40808	16851	2392

follow the work of Keasler *et al.* [20]. In this model, the bond lengths between the different chemical groups are fixed. Monomeric units separated by two bonds interact through a harmonic bending potential with the usual form, with bending force constants taken from the TraPPE-UA force field for n-alkanes and ethers [20]. Interactions between beads separated by three bonds are described through a torsional intramolecular potential energy represented by a cosine series [20]. For further details on the TraPPE-UA force field we recommend the original paper of Keasler *et al.* [20] In the case of the approximated, planar, and rigid TraPPE-UA model, in which non-bonded LJ intermolecular parameters and partial charges located at the different chemical groups are identical to those of the original TraPPE model. In addition to that, bending and torsional degrees of freedom are frozen, i.e., we consider that the equilibrium bond angles are fixed and the molecule has no torsional degrees of freedom. As an additional approximation, THF is considered in this case not only rigid but also planar [21]. This means that although the fixed bonded angles in this new model are the same than those of equilibrium in the flexible model, the bond lengths are slightly different (Table 8.4). Finally, it is important to remark that the 1-4 intramolecule interactions are excluded in both models, and the nonbonded interactions are not scaled.

Tabla 8.4: Bond angles and lengths for the rigid TraPPE-UA model of THF and CO_2

Angle	θ (degrees)	Bond	Length(nm)
rigid TraPPE-UA model			
CH_2-CH_2-CH_2	105.5	α-CH_2-β-CH_2	0.1540
CH_2-CH_2-O	108.5	α-CH_2-O	0.1440
CH_2-O-CH_2	112.0	β-CH_2-β-CH_2	0.1565
CO_2 model			
O=(C)=0	180.0	C-O	0.116

8.2.2 Simulation details

We determine the vapor-liquid phase equilibrium and interfacial properties of the mixture from MD simulations using the direct coexistence technique in the NVT canonical ensemble [31, 32]. Simulations are performed in two steps. In the first step, homogeneous liquid and vapour systems,

at a given temperature and pressure, are equilibrated in a parallelepipedic simulation box of volume $V = L_x \times L_y \times L_z$, where L_x, L_y, and L_z are the dimensions of the simulation box. We use as initial values for density and composition in each independent simulation box (one for the liquid phase and another one for the vapor phase) the predictions obtained from the SAFT-VR approach at the same temperature and pressure [28]. We use periodic boundary conditions in all three dimensions. Box length measured along the z-axis in both liquid and vapor phases are chosen appropriately to ensure phase separation at the corresponding temperature and pressure. Both phase are equilibrated at the same temperature and pressure using an $NP_z\mathcal{A}T$ ensemble in which L_x and L_y are kept constant and only L_z is varied along the simulation. After equilibration, the final simulation box is builded linking up both bulk boxes forming a vapor-liquid-vapor system. The total number of THF and CO_2 molecules is different since depends on the composition of the mixture. To obtain a reliable description of the interfacial properties of the mixture, we use a cut-off radius $r_c = 7\sigma$, where σ corresponds to the larger value of the size parameter of the Lennard-Jones intermolecular potential [33–35]. Long-range interactions are determined using three-dimensional Ewald technique with a convergence parameter of $1\,\mathrm{nm}^{-1}$ and a maximum value for the reciprocal lattice equal to 31 [31, 32].

All MD simulations are performed using GROMACS (version4.6.1) [36]. We use a Verlet leapfrog algorithm [37] with a time step of 0.002 ps for the case of the rigid TraPPE-UA model of THF. However, a time step of 0.001 ps has been used for the case of the flexible TraPPE-UA model to sample correctly the torsional potential. We use a Nosé-Hoover thermostat [38] with a time constant equal to 1.0 ps. We use 5 ns for equilibration and 15 ns for averages in the case of the rigid model of THF. However, larger simulation times are required in the case of the flexible model (10 ns and 50 ns for equilibration and averages, respectively) to ensure the correct sampling of the torsional potentials. It is important in this context to compare the computational efficiency of simulations using both models. The rigid TraPPE-UA model of THF is computationally more efficient that the flexible model due mainly to three reasons. First at all, and due to the difference in the time step employed in both models, simulations of the flexible model are twice faster than those of the flexible model. Secondly, MD simulations of the rigid model are 1.2 times faster (in terms of time steps) than those of the flexible model due to the extra CPU time employed to solve the corresponding motion equations associated to the internal degrees of freedom. And finally, as it is mentioned above, time for average and production in the case of the rigid model is 4 times lower than for flexible model. As a consequence of this, we estimate than a typical simulation of the rigid model of THF is approximately 10 times faster than one for the flexible model.

In order to estimate the errors, we apply the sub-blocks average method of Berendsen *et al.* [39], dividing the average period into M independent blocks and obtain the statistical error as the standard deviation of the average $\bar{\sigma}/\sqrt{M}$, where $\bar{\sigma}$ is the variance of the block averages. M is fixed in this work to $M = 10$.

The equilibrium vapor pressure, P_v, and interfacial tension, γ, are obtained from the diagonal components of the pressure tensor. The vapor pressure corresponds to the normal component, $P_v = P_{zz}$, of the pressure tensor, while the interfacial tension is obtained using the mechanical route [40–43] as:

$$\gamma = \frac{L_z}{2}\left[P_{zz}(z) - \frac{P_{xx}(z) + P_{yy}(z)}{2}\right] \tag{8.2}$$

In Eq. (8.2), the additional factor 1/2 comes from having two interfaces in the system, and L_z is the size of the simulation box in the z direction, defined along the longitudinal dimension across the

interface.

We have also performed some Gibbs ensemble MC (GEMC) simulations using MedeA® GIBBS suite [44] to ensure the methodology employed in the MD simulation is correct. In particular, we use the GEMC method to calculate the vapor-liquid equilibrium of the mixtures using the flexible model of THF. We use a total number of 400 molecules for the systems studied, with non-bonded potential cut-off radius equal to half the simulation box and tail corrections for the LJ interactions [31, 32]. Ewald summation technique, with a number of reciprocal vectors k ranging from -7 to $+7$ in all three directions and a Gaussian width α equal to 2 in reduced units, is used in the calculation of the long-range electrostatic interactions [31, 32]. A typical NPT GEMC simulation run lasts for 60 million MC steps, including an equilibration run of 30 million MC steps. One MC step corresponds to a single Monte Carlo move. We use the following Monte Carlo moves, with the corresponding attempt probabilities used during the simulations: translation (20%), rigid rotation (20%), configurational-bias regrowth (15%), flips (14.5%), transfer with insertion bias (30%), and volume change (0.5%). We adjust the amplitude of translations, rotations, and volume changes to achieve an acceptance ratio of 50% for these specific motions.

8.3 Results and discussion

We first determine the equilibrium molecular density profiles of each of components of the mixture, $\rho_1(z)$ and $\rho_2(z)$, corresponding to THF and CO_2, respectively, as well as the total density of the system, $\rho(z) = \rho_1(z) + \rho_2(z)$. The profiles are obtained from MD simulations using the direct coexistence technique in the NVT canonical ensemble and particular values of the profiles are computed from averages of the histogram of densities along the z direction over the production stage. We have fit each of the two equilibrium density profiles using hyperbolic tangent functions of the form given by Eq. (8) of Garrido *et al.* [21]. In all cases, we have checked that all profiles are essentially symmetric around the mid-point of the corresponding liquid slabs. In addition to that, we have also checked that: (a) the bulk vapour density obtained after averaging the density profiles on both sides of the liquid film are always found to be the same within statistical uncertainties; (b) the measure of the thickness of the interface, the $10-90$ interfacial thickness associated to both interfaces, is also found to be the same within statistical uncertainties. This three points provide evidence that the inhomogeneous systems are properly equilibrated.

We only depict the density profiles taken from half of the simulation box to avoid unnecessary repetitions. In addition to that, all density profiles have been shifted along the z-axis to place z_0, the Gibbs dividing surface at origin.

The bulk liquid and vapor densities, and total density are obtained by averaging $\rho_1(z)$, $\rho_2(z)$, and $\rho(z)$ over the appropriate regions sufficiently removed form the interfacial region. Care has been taken to ensure that the central region of each bulk phase (liquid and vapor) is thick enough at all pressures and temperatures considered. The statistical uncertainties of these values is estimated from the standard deviation of the mean values. In the particular case of the vapor phases, since for each simulation we have two interfaces and two vapor phases, the final statistical uncertainty takes into account calculations obtained in both vapor phases.

Simulation results for the total densities in the liquid and vapor phases, and molar fractions of both components in each phase at different pressures and temperatures are collected in Tables 8.5 and 8.6.

Tabla 8.5: Liquid density, ρ_L, vapor density, ρ_V, molar fraction of THF in the liquid phase, x_1^L, molar fraction of THF in the vapor phase, x_1^V, interfacial tension, γ, and relative Gibbs adsorption, Γ_{12}, at 298.15 K and different pressures as obtained from MD NVT (rigid and flexible TraPPE-UA models) and Gibbs ensemble MC (flexible TraPPE-UA model) simulations.

P/MPa	ρ_L/(kg/m^3)	ρ_V/(kg/m^3)	x_1^L	x_1^V	γ/(mN/m)	$10^{-10}\,\Gamma_{12}$/(kmol/m^2)
MD NVT simulations (rigid TraPPE-UA model)						
0.432(7)	869(3)	8.27(16)	0.9105(4)	0.0825(9)	24.79(21)	0.2278(11)
1.019(12)	880(3)	19.97(20)	0.7687(7)	0.0332(3)	21.69(11)	1.4351(12)
1.718(12)	889(3)	34.25(24)	0.6512(18)	0.02083(15)	17.83(25)	3.5562(14)
2.392(16)	896(3)	49.5(4)	0.5247(14)	0.01668(13)	15.5(3)	6.2915(19)
3.223(24)	900(3)	70.2(5)	0.4110(12)	0.00956(10	11.95(15)	6.7712(10)
4.005(27)	903(3)	92.3(5)	0.2919(20)	0.00935(17)	9.05(25)	7.3971(21)
4.814(16)	887(3)	120.8(6)	0.1834(12)	0.00712(5)	5.83(12)	7.9762(18)
5.623(10)	844.7(21)	153.7(7)	0.0839(13)	0.00606(7)	3.52(13)	8.1836(18)
MD NVT simulations (flexible TraPPE-UA model)						
0.418(13)	877(3)	7.6(10)	0.9094(9)	0.069(8)	25.28(21)	1.1225(10)
3.232(22)	909(3)	71.0(5)	0.412(4)	0.01081(5)	12.03(12)	6.3470(17)
5.503(14)	847(4)	152.3(11)	0.0829(27)	0.00452(8)	3.71(7)	10.1837(23)
Gibbs ensemble MC (flexible TraPPE-UA model)						
1.5	878(3)	30.14(25)	0.6637(20)	0.02639(21)	–	–
3.0	884(3)	77.09(19)	0.4312(22)	0.0165(3)	–	–
4.5	863(4)	122.1(4)	0.213(5)	0.0090(5)	–	–

Tabla 8.6: Liquid density, ρ_L, vapor density, ρ_V, molar fraction of THF in the liquid phase, x_1^L, molar fraction of THF in the vapor phase, x_V^V, interfacial tension, γ, and relative Gibbs adsorption, Γ_{12}, at 353.15 K and different pressures as obtained from MD NVT (rigid and flexible TraPPE-UA models) and Gibbs ensemble MC (flexible TraPPE-UA model) simulations.

P/MPa	ρ_L/(kg/m^3)	ρ_V/(kg/m^3)	x_1^L	x_1^V	γ/(mN/m)	$10^{-10}\,\Gamma_{12}$/(kmol/m^2)
MD NVT simulations (rigid TraPPE-UA model)						
1.431(9)	804(3)	25.32(23)	0.8777(5)	0.1664(9)	16.5(3)	0.5035(11)
2.304(11)	804(3)	40.71(3)	0.7978(7)	0.1050(13)	14.78(13)	1.3425(11)
3.243(13)	804.4(20)	58.7(3)	0.7216(7)	0.0844(3)	12.33(9)	2.3987(12)
4.112(12)	803(3)	76.1(4)	0.6500(11)	0.0719(4)	10.90(15)	2.3288(14)
5.155(21)	795(4)	97.5(5)	0.569(3)	0.0621(6)	9.2(3)	3.3822(9)
6.151(24)	793.6(21)	124.5(6)	0.5091(14)	0.0607(10)	7.2(3)	3.1111(16)
7.22(3)	787(4)	152.0(7)	0.4448(24)	0.0542(10)	5.29(19)	3.4634(19)
8.199(24)	772(5)	182.9(13)	0.374(3)	0.0543(15)	3.71(15)	3.5845(17)
9.23(3)	750(3)	224.3(10)	0.3108(20)	0.0538(10)	2.53(13)	3.9874(13)
MD NVT simulations (flexible TraPPE-UA model)						
1.627(12)	818.6(19)	27.75(6)	0.8607(6)	0.1389(6)	16.50(20)	0.6942(15)
5.245(19)	817.1(6)	89.9(14)	0.5709(7)	0.0506(11)	9.03(12)	3.8745(14)
9.48(4)	781.3(19)	185.1(13)	0.3042(12)	0.03990(10)	2.74(9)	4.5145(17)
Gibbs ensemble MC (flexible TraPPE-UA model)						
2.5	817(3)	49.2(3)	0.7532(24)	0.12573(22)	–	–
5.0	808(3)	99.93(19)	0.602(7)	0.0828(3)	–	–
7.5	785(3)	171.62(21)	0.4100(12)	0.0743(9)	–	–

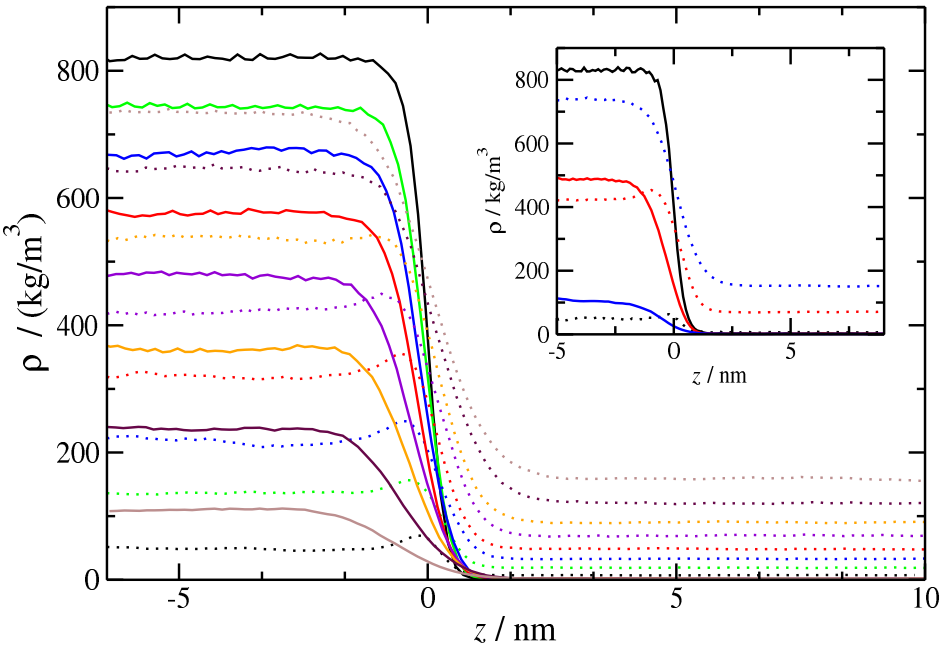

Figura 8.1: Simulated equilibrium density profiles of THF (continuous curves) and density profiles of CO_2 (dotted curves) across the vapor-liquid interface of the THF(1) +CO_2(2) binary mixture at $T = 298.15\,K$ as obtained from MD NVT simulations using the rigid TraPPE model . Density profiles in the inset correspond to results for the original flexible TraPPE model. From bottom to top (in the liquid region of the principal plot): 0.432 MPa (black), 1.019 MPa (green), 1.718 MPa (blue), 2.392 MPa (red), 3.223 MPa (violet), 4.005 MPa (orange), 4.814 MPa (maroon), and 5.623 MPa (brown). From bottom to top (in the liquid region of the inset of the figure): 0.418 MPa (black), 3.232 MPa (red), 5.503 MPa (blue).

We first show in Figure 8.1 the density profiles of THF and CO_2 for the THF + CO_2 binary mixture at 298.15 K and several pressures, from 0.4 up to 5.6 MPa, approximately. The curves presented in the main part of the Figure correspond to the simulation results obtained using the rigid model of THF. Density profiles corresponding to the simulation of the flexible model (original TraPPE-UA model) are presented in the inset of the Figure. As can be seen in Fig. 8.1, profiles exhibit identical qualitative behavior. At these conditions, both components are subcritical, i.e., temperature considered is below the critical temperature of THF ($T_c^{THF} \approx 540\,K$) and CO_2 ($T_c^{CO_2} \approx 304\,K$). The slope in absolute value of the density profiles of THF in the interfacial region decrease as the pressure is increased since the jump in densities decreases when passing from the vapor to the liquid size along the interface. At low pressures, the liquid phase is rich in THF, being the density of THF high ($\sim 800\,kg/m^3$) and that of CO_2 low ($\sim 50\,kg/m^3$). As the pressure increases, the liquid becomes richer in CO_2, with a high value of the total density. This produces an increase of the interfacial thickness of the interface as the pressure is higher.

The behavior of the density profiles corresponding to CO_2 is more interesting than that of THF: $\rho_2(z)$ exhibits a nearly monotonic increasing behavior when passing from the vapor to the liquid phase along the interface at high pressures. However, at mid and low pressures ($P \lesssim 4.0\,MPa$), the density profile exhibits a relative maximum at the interface. This maximum reflects a preferential adsorption

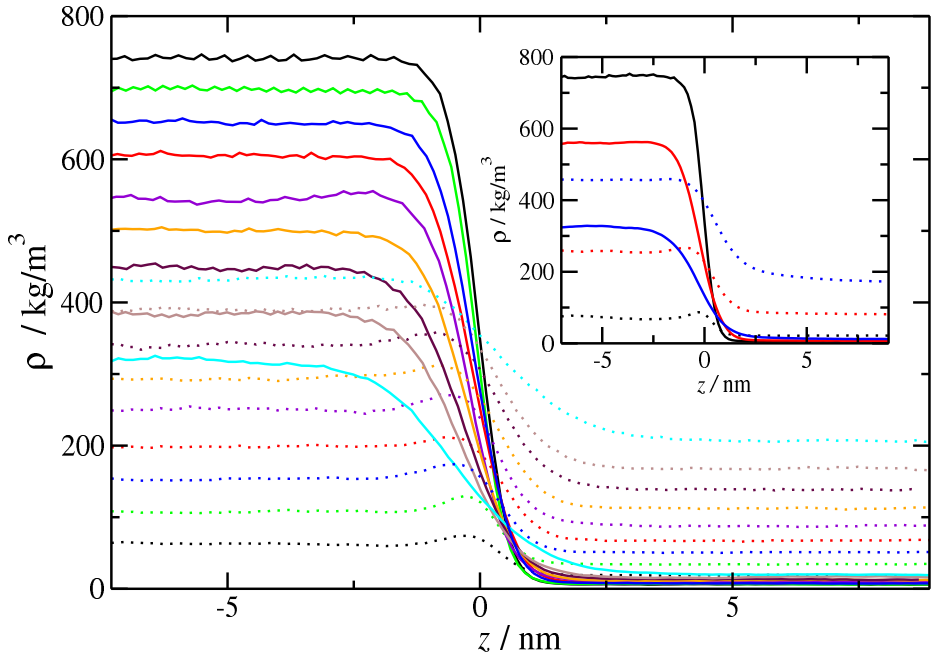

Figura 8.2: Simulated equilibrium density profiles of THF (continuous curves) and density profiles of CO_2 (dotted curves) across the vapor-liquid interface of the THF(1) +CO_2(2) binary mixture at $T = 353.15$ K as obtained from MD NVT simulations using the rigid TraPPE model. Density profiles in the inset correspond to results for the original flexible TraPPE model. From bottom to top (in the liquid region of the principal plot): 1.431 MPa (black), 2.304 MPa (green), 3.243 MPa (blue), 4.112 MPa (red), 5.155 MPa (violet), 6.151 MPa (orange), 7.22 MPa (maroon), 8.199 MPa (brown), and 9.23 MPa (cyan). From bottom to top (in the liquid region of the inset of the figure): 1.627 MPa (black), 5.245 MPa (red), 9.48 MPa (blue).

of CO_2, which is the more volatile component of the mixture, indicating a preference to accumulate at the interface as the pressure is decreased. This enhanced adsorption of CO_2 relative to THF is usually seen in binary mixtures with significant differences in the values of the vapor pressure at a given temperatures, i.e., systems with compounds with different volatility. Note that this behavior, that is observed for both models of THF, is also very common in other mixtures. [29, 45–49]

We also consider the interfacial behavior of the system at a higher temperature, 353.15 K. Contrary to the previous case, at this temperature one of the components is supercritical (CO_2), and consequently, the mixture exhibits a critical point at $10.5 - 10.0$ MPa, approximately. Figure 8.2 shows the density profiles of THF and CO_2 at this temperature, in a wider range of pressures, from 1.4 up to 9.2 MPa, approximately. All density profiles at 353.15 K exhibit qualitatively the same behavior than at lower temperature. In this case, CO_2 is also preferentially adsorbed at the interface (using both models of THF), although in the current case the range of pressures at which this happens is higher.

From the analysis of the density profiles obtained from the MD simulations, we have calculated the vapor-liquid phase envelopes of the THF + CO_2 mixture at two different temperatures, 298.15 K and 353.15 K. We first analyze in Figure 8.3 the pressure-density or $P\rho$ projection of the phase diagram at 298.15 K. We plot the predictions obtained using both models for THF. We have also included

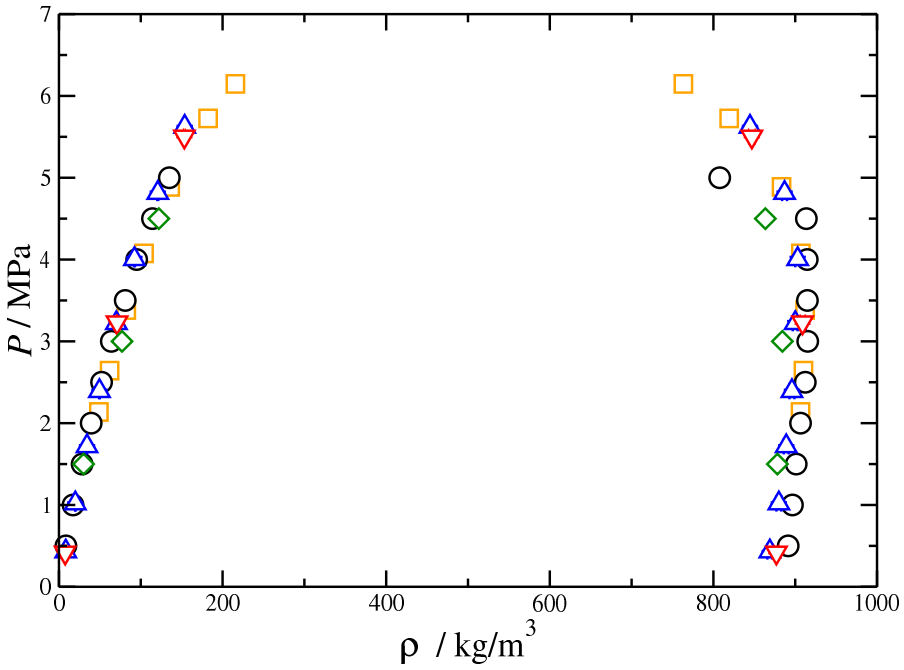

Figura 8.3: Pressure-density slices of the phase diagram of the THF(1) +CO_2(2) binary mixture at $T = 298.15\,\mathrm{K}$ as obtained from experiment and simulation. Black circles [29] and orange squares [27] correspond to experimental data taken from literature. Blue up triangles and green diamonds correspond to predictions obtained from MD NVT simulations using the planar and rigid TraPPE-UA and the original (flexible) TraPPE-UA models, respectively. Red down triangles are the predictions obtained from the GEMC simulations for the original (flexible) TraPPE-UA model.

experimental data taken from the literature at the same thermodynamic conditions [29]. In addition to that, and to check that the simulations performed in the MD NVT canonical ensemble are correct, we have also obtained the vapor-liquid coexistence density for the original TraPPE-UA model of Keasler *et al.* using the Gibbs ensemble Monte Carlo (MC) method.

As can be seen in the Figure 8.3, both models provide nearly identical predictions for the vapor coexistence density in the whole range of pressures. In addition to that, simulation results obtained using the original and approximated models of THF also provide similar values for the liquid coexistence density. Agreement between simulation and experiments is excellent in the whole range of pressures, including results obtained from MD and Gibbs ensemble MC simulations. It is important to mention here that results obtained from simulations are truly predictions since Lorentz-Berthelot combining rules are used for the unlike size and dispersive energy molecular parameters.

We have also obtained the $P\rho$ projection of the phase diagram of the mixture at the highest temperature studied in this work, 353.15 K. Fig. 8.4 indicates that the shape of the coexistence diagram is qualitative similar to that at the lowest temperature (298.15 K). However, as we have mentioned previously, now CO_2 is supercritical, i.e, 353.15 K is above its critical temperature ($T_c^{CO_2} \approx 304\,\mathrm{K}$), and consequently, the system exhibits a critical point at the high-pressure region of the phase diagram. Unfortunately, we have only investigated the phase behavior of the mixture below 9.2 MPa, which

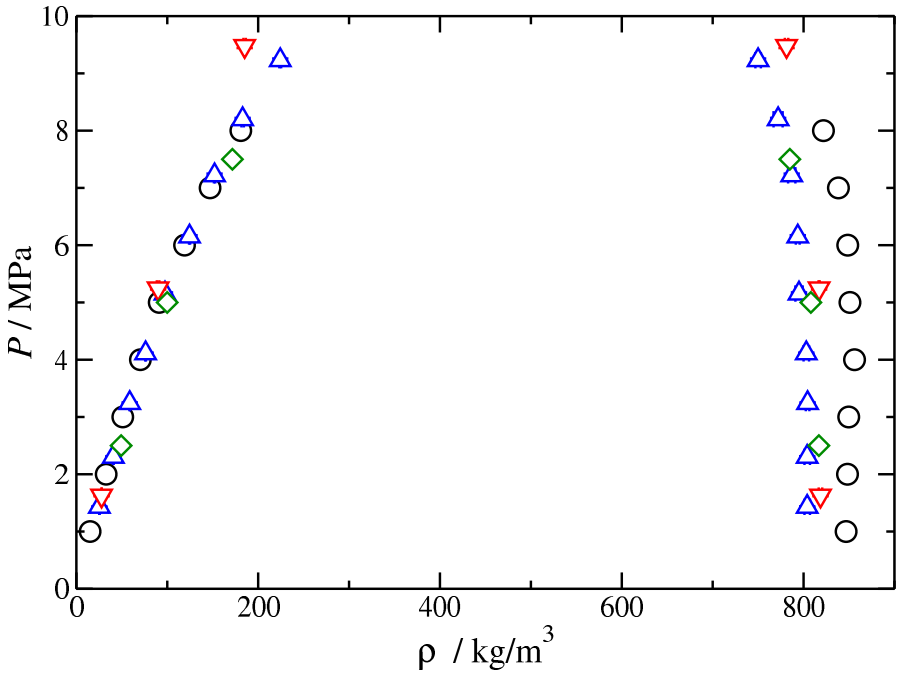

Figura 8.4: Pressure-density slices of the phase diagram of the THF(1) +CO_2(2) binary mixture at $T = 353.15\,\mathrm{K}$ as obtained from experiment and simulation. Black circles correspond to experimental data taken from literature [29]. Blue up triangles and green diamonds correspond to predictions obtained from MD NVT simulations using the planar and rigid TraPPE-UA and the original (flexible) TraPPE-UA models, respectively. Red down triangles are the predictions obtained from the GEMC simulations for the original (flexible) TraPPE-UA model.

is below the estimated critical point of this mixture. Note that both THF models and molecular simulations (MC and MD) systematically underestimate liquid densities at high density ($800\,\mathrm{kg/m^3}$). We believe that it is due to an inaccuracy of the TraPPE-UA force field. Indeed, we checked the same behavior using the coarse grained models taken from our previous work [21], where the accuracy with experimental data is remarkable.

MD NVT simulation data obtained using the two THF models describe very accurately the vapor coexistence densities in the whole range of pressures, in excellent agreement with experimental data taken from the literature. This is an expected result since at low pressures and densities vapor phase behaves as an ideal mixture. In addition to that, both models of THF are able to predict nearly the same liquid coexistence densities, although underestimate the experimental liquid densities around a 5%, approximately. As in the case corresponding to 298.15 K, results obtained using the original TraPPE model of Keasler *et al.* (flexible model) from MD and Gibbs ensemble MC simulations provide essentially identical predictions for both vapor and liquid coexistence densities. This indicates clearly that the methodology used in our MD computer simulations is correct.

We have also obtained the pressure-composition or Px slice of the phase diagram of the mixture at the same thermodynamic conditions and using both models of THF. Figs. 8.5 and 8.6 show the predictions from MD NVT simulations and the analysis of the density profiles. Here we also show the

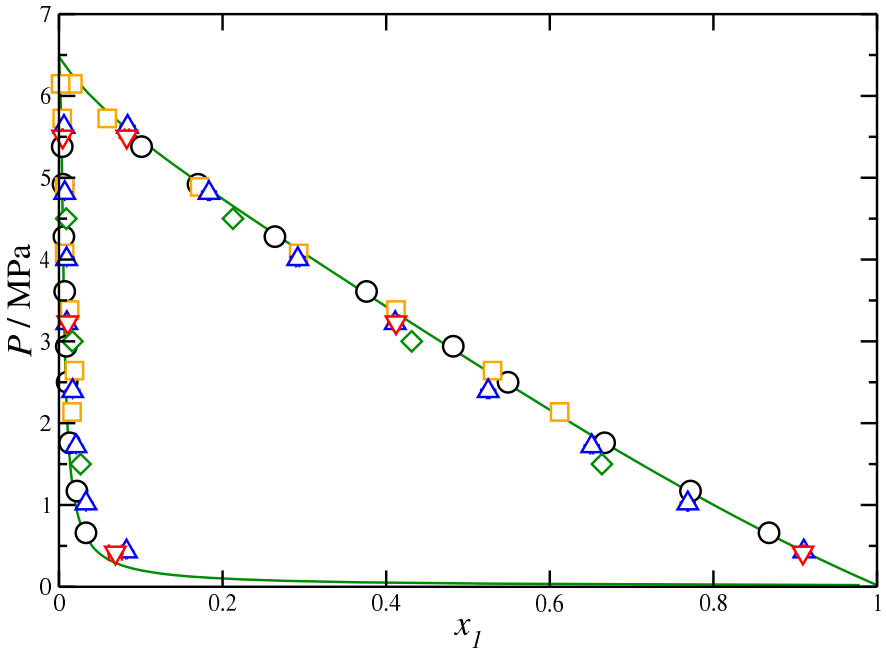

Figura 8.5: Pressure-composition slices of the phase diagram of the THF(1) +CO_2(2) binary mixture at $T = 298.15$ K as obtained from experiment and simulation. Black circles [25] and yellow squares [27] correspond to experimental data taken from literature. Blue up triangles and red down triangles correspond to predictions obtained from MD NVT simulations using the planar and rigid TraPPE-UA and the original (flexible) TraPPE-UA models, respectively. Green diamonds are the predictions obtained from the GEMC simulations for the original (flexible) TraPPE-UA model.

theoretical predictions obtained from the SAFT-VR approach obtained in our previous work [28], as well as the experimental data taken from the literature [29]. In the particular case of SAFT-VR, we have used the same set of molecular parameters for THF and CO_2 described in Table 1 (Optimized Square-Well Intermolecular Potential Parameters) and $\xi_{12} = 1.0$, from the work of Míguez *et al.* [28]

As we have mentioned previously in the Introduction, Míguez *et al.* [28] have predicted the high-pressure phase equilibria of mixtures of THF with CO_2, CH_4, and THF. In this work, the authors used the well-known extension of the Statistical Associating Fluid Theory (SAFT) for potentials of variable range, the SAFT-VR approach [50, 51], to predict the phase equilibria of THF(1) + CO_2(2) mixture. In particular, they determined the PT projection of the phase diagram of the system showing that the mixture exhibits type I phase behavior according to the van der Konynenburg and Scott classification [22, 23]. It is important to recall here that Míguez *et al.* [28] used rescaled molecular parameters to the critical points of pure components to obtain the best possible representation of the critical behavior of the system. However, this produces an accuracy loss in the calculated saturated liquid density of pure components, as it has been shown in previous works [52–55]. However, these sets of parameters provide a good description of the coexistence compositions and critical curves. A more satisfactory description of these systems could be obtained using the versions of SAFT-VR proposed by McCabe and Kiselev, using a crossover treatment [56, 57] or the more recent versions of Forte *et al.*, [58, 59] in combination with the renormalization group theory. Because of that, we only

present the predictions of SAFT-VR for the Px projections of the phase diagram. Agreement between experimental data taken from the literature and predictions from the theory is good in whole range of compositions, especially taking into account that SAFT-VR results are pure predictions. In addition to that, the theory is also able to predict very accurately the Px slices of the phase diagram in a wide range of temperatures varying from 298.15 to 353.15 K.

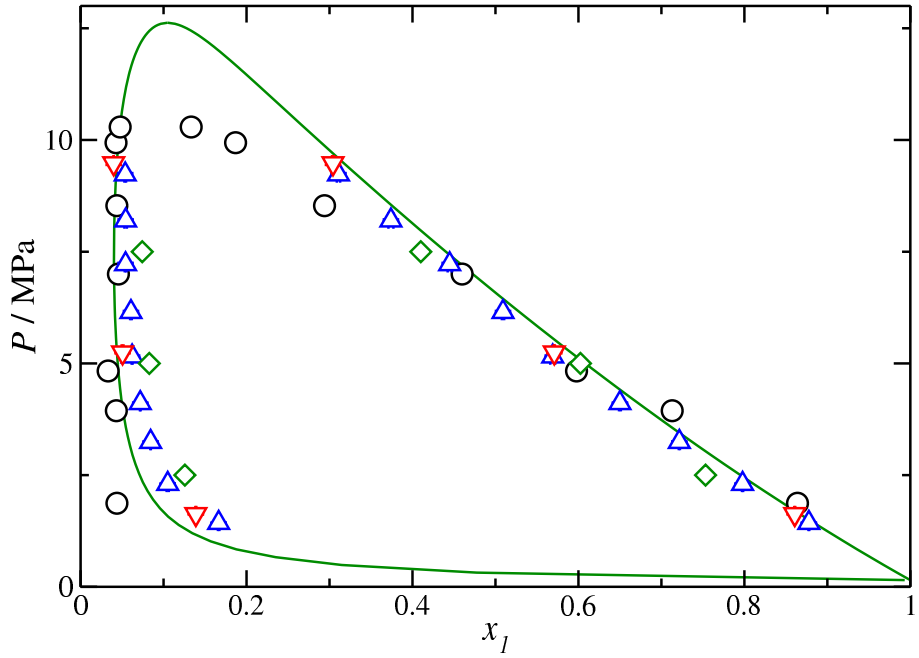

Figura 8.6: Pressure-composition slices of the phase diagram of the THF(1) +CO_2(2) binary mixture at $T = 353.15$ K as obtained from experiment and simulation. Black circles correspond to experimental data taken from literature [26]. Blue up triangles and red down triangles correspond to predictions obtained from MD NVT simulations using the planar and rigid TraPPE-UA and the original (flexible) TraPPE-UA models, respectively. Green diamonds are the predictions obtained from the GEMC simulations for the original (flexible) TraPPE-UA model.

We see clearly in Fig. 8.5 that at 298.15 K the vapor-liquid phase separation takes place at any composition of the mixture since both components are subcritical. As in the case of the $P\rho$ slice of the mixture, the Px diagram is very nicely predicted by simulation. Note that we have presented in the Figure not only the MD NVT computer simulation results for both models but also the Gibbs ensemble MC calculations corresponding to the original flexible model. Agreement between simulation, experiments, and theory is remarkable in the whole range of pressures considered. This is especially important if we taken into account that results from simulations are predictions from the values of the molecular parameters of pure components.

Fig. 8.6 shows the Px slice of the phase diagram at 353.15 K. Computer simulation results are in good agreement with experimental and theoretical predictions obtained from SAFT-VR. Unfortunately, simulation results for both models overestimate the composition of THF in the vapor phase at low pressures, as well as the molar fraction of THF in the liquid phase at high pressures. The deviations of

the molar composition of THF in the liquid phase is due probably to the proximity of the system to the critical pressure of the mixture. Near a critical point, density fluctuations in the system could be large compared with the characteristic correlation length of the system, and virtually, be larger than the size of the simulation box. Although it is possible to use special simulation methods to avoid such problems, including finite-size scaling techniques, this is beyond the scope of this work.

To recap, we have demonstrated that the TraPPE-UA simulation models for THF and CO_2 are able to predict accurately the phase behavior of the mixture. In particular, they account for the $P\rho$ and Px slices of the phase diagram in a wide range of pressures at two different temperatures. This is true when THF is modeled using the TraPPE-UA model proposed by Keasler *et al.*, that takes into account explicitly the internal degrees of freedom of THF (bending and torsional degrees of freedom). Even more important, the simplified version of the TraPPE-UA model, in which molecules are considered planar and rigid but with the same non-bonded interaction intermolecular parameters and partial charges, is also able to predict the phase behavior of the mixture with the same degree of accuracy. This is a key issue from a computational point of view since allows, *a priori*, to use a simpler model to simulate systems containing THF molecules, saving CPU time.

Finally, and once we have considered the phase equilibria of the system at several thermodynamic conditions, we analyze the interfacial behavior of both models. We have calculated the vapor-liquid interfacial tension of the mixture MD simulations in the NVT canonical ensemble. In particular, we have determined the surface tension using its mechanical definition that involves the difference between the tangential and normal macroscopic components of the pressure tensor, according to the Eq. (8.2). We compare the results obtained using the original TraPPE-UA model for THF and the simplified model. As we have mentioned previously, interfacial properties and particularly surface tension, are extremely sensitive to molecular details of the system. This comparison is, therefore, a crucial test to check the ability of the planar and rigid model in predicting the behavior of the mixture, which is one of the key goals of this work.

The pressure dependence of the surface tension is shown in Figs. 8.7 and 8.8. Predictions from simulations using both models for THF are in excellent agreement at low, intermediate, and high pressure conditions. Both models are able to account for the experimental data in the whole range of pressures at 353.15 K. At 298.15 K, agreement with experimental data at low and intermediate pressures ($\approx$ 3 MPa) is also excellent; however, computer simulation results for both models at high pressures ($\approx$ 3-6 MPa) slightly overestimate the experimental data. Note that one possible reason for this behavior is caused but the fact that the force field over predicts the critical pressure at these conditions, especially in the case of 298.15 K. Additionally, as the pressure increases, the interfacial tension decreases and deviations are more notorious.

In order to quantify adsorption, Fig. 8.9 display the relative Gibbs adsorption isotherms of CO_2 into the THF liquid phase calculated according Eq. (19) of our previous work [29]. The results illustrated in this figure have been calculated both from experimental interfacial tension data [29] as well as NVT-MD simulations. From Fig. 8.9, it is possible to observe that Γ_{12} is positive over the whole pressure range, thus implying that CO_2 is always adsorbed into the liquid phase. On the one hand, from the quoted figure it is possible to observe that, at fixed pressure, Γ_{12} decreases as the temperature increases. On the other hand, it is also possible to observe also that the experimental Γ_{12} values increase as the pressure increases, and they eventually reach an inflection point. One possible explanation for this behavior can be attributed to the fact that CO_2 reached at the limit of saturation al the liquid THF phase, as results for NVT-MD shown in Figs. 8.1 and 8.2 for density profiles.

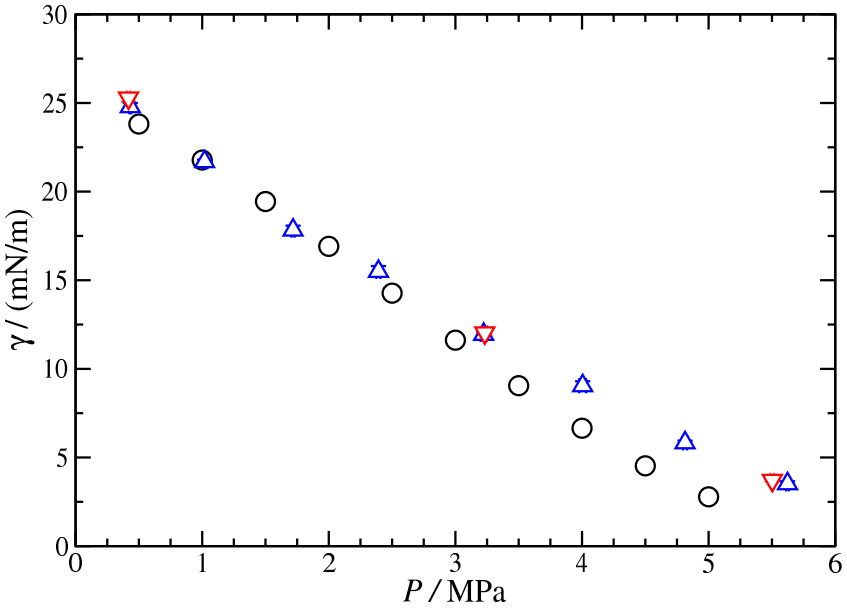

Figura 8.7: Interfacial tension as a function of pressure for the THF(1) +CO_2(2) binary mixture at $T = 298.15\,\mathrm{K}$ as obtained from experiment and simulation. Black circles correspond to experimental data taken from literature [29]. Blue up triangles and red down triangles correspond to predictions obtained from MD NVT simulations using the planar and rigid TraPPE-UA and the original (flexible) TraPPE-UA models, respectively.

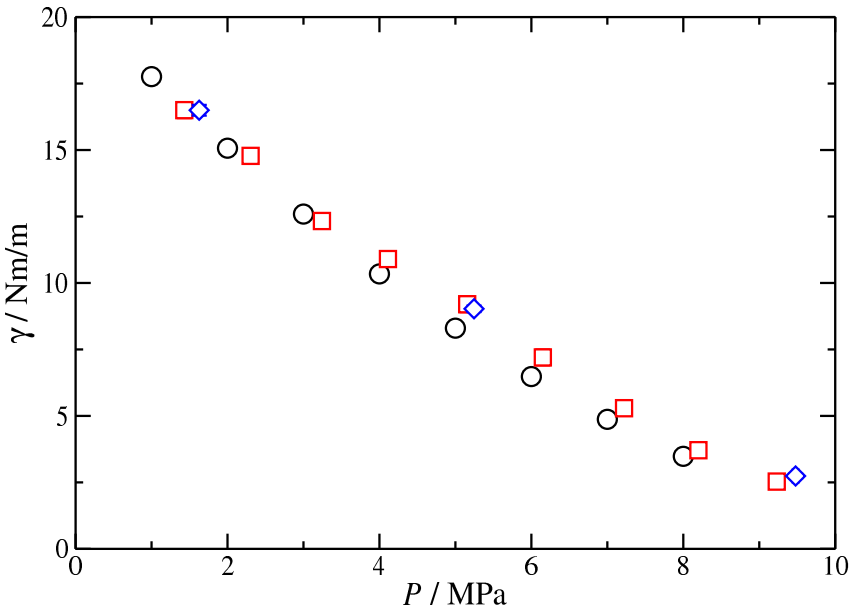

Figura 8.8: Interfacial tension as a function of pressure for the THF(1) +CO_2(2) binary mixture at $T = 353.15\,\mathrm{K}$ as obtained from experiment and simulation. Black circles correspond to experimental data taken from literature [29]. Red squares and blue diamonds correspond to predictions obtained from MD NVT simulations using the planar and rigid TraPPE-UA and the original (flexible) TraPPE-UA models, respectively.

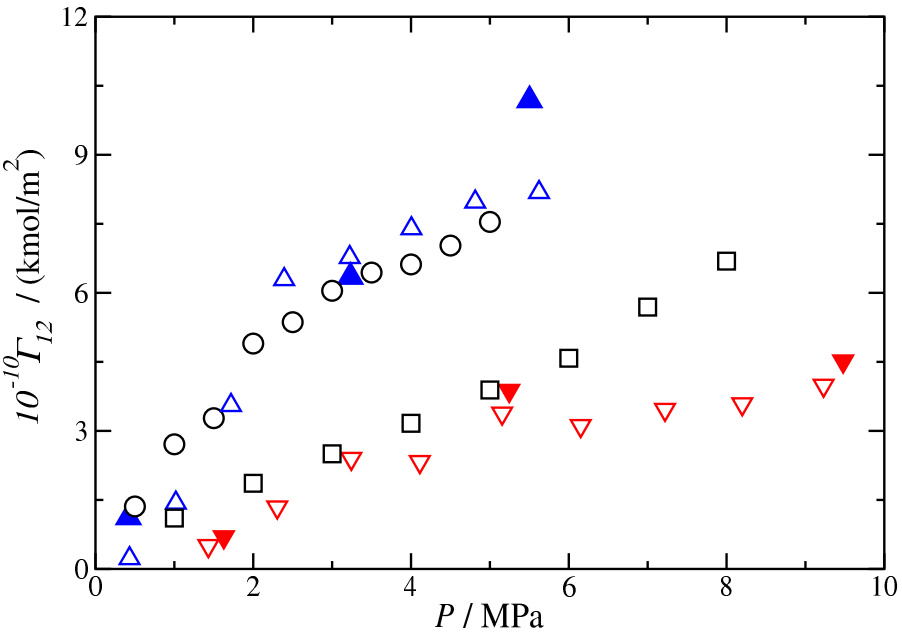

Figura 8.9: Relative Gibbs Absorption, Γ_{12}, as a function of pressure for the THF(1) +CO_2(2) as obtained from experiment and simulation. Black circles and squares correspond to experimental data taken from literature [29] at 298.15 K and 353.15 K, respectively. Open and filled up-triangles correspond to predictions obtained from MD NVT simulations using the planar and rigid TraPPE-UA and the original (flexible) TraPPE-UA models at 298.15 K, respectively. Open and filled down-triangles correspond to predictions obtained from MD NVT simulations using the planar and rigid TraPPE-UA and the original (flexible) TraPPE-UA models at 353.15 K, respectively.

As a final comment, we demonstrated in our previous work [21] that the planar and rigid simplified model of THF was able to describe accurately its vapor-liquid interfacial tension in the whole range of coexistence region. The results presented here confirm that the same model is also a good choice for predicting the mixture behavior with CO_2 and we believe that the same should be true for other binary mixtures containing THF. This conclusion is relevant if we take into account that MD simulations for this model are faster (up to twice those corresponding to the original flexible model), which is particular suited for computer simulations that involve large systems or complex mixtures containing THF.

8.4 Conclusion

We have determined the interfacial properties of the vapor-liquid interface of the THF(1) + CO_2(2) binary mixture at high pressure and temperatures of 298.15 and 353.15 K considering two different models of THF based on the TraPPE-UA approach. In the first model, we use the original (flexible) TraPPE-UA model. The second model is a planar and rigid approximated TraPPE-UA model.

We use MD NVT simulations of the inhomogeneous system containing two vapor-liquid interfaces. We also use the Gibbs ensemble MC technique for simulating the phase coexistence for the original

TraPPE-UA model. The surface tension is evaluated from the normal and tangential components of the pressure tensor using the virial route. In addition to that, we have calculated the pressure-density and pressure-composition slices of the phase diagram from an analysis of the density profiles of the components in a wide range of pressures. All properties have determined using the two models of THF. Predictions obtained from MD and Gibbs ensemble simulations are compared with experimental data taken from the literature.

Density profiles of THF exhibit a monotonic behavior when passing from the liquid to the vapor side of the interface, characterized by the standard hyperbolic tangent behavior. However, carbon dioxide is adsorbed at the interface region, showing that its surface activity (accumulation) decreases as pressure increases, and eventually reaching the saturation limit where both profiles show the classical hyperbolic tangent shape. This characteristic preferential adsorption of accumulation at the interface is probably related with the asymmetry in size and differences in vapor pressures of the components of the mixture.

The vapor-liquid phase envelopes of the mixture, including the pressure-density and pressure-composition slices, are predicted remarkably well by the two models of THF used here. In particular, computer simulation predictions for both models are equally accurate at 298.15 K. However, both models slightly underestimate the saturated liquid density and overestimate the THF composition in the vapor phase at low pressures. We have also used the two models to predict the vapor-liquid interfacial tension of the mixture. Both models are able to predict quantitatively the behavior of the interfacial tension, as a function of pressure, at the two temperatures considered. However, agreement between simulation results and experimental data is less accurate at 298.15 K and high pressures.

As a final conclusion, although both models seem to predict in general the phase behavior and interfacial tension with a high accuracy in a wide range of pressures, the planar and rigid model is faster for simulating since internal degrees of freedom are frozen (neither bending nor torsional intramolecular interactions need to be evaluated). This is an important and clear advantage, especially when interfacial properties need to be calculated and in the case of mixtures containing other chemical compounds. We are currently investigating the advantage of this model for simulating liquid-liquid interfaces of mixtures containing THF.

8.5 Acknowledgement

The authors thank helpful discussions with Manuel M. Piñeiro. We also acknowledge Centro de Supercomputación de Galicia (CESGA, Santiago de Compostela, Spain) and MCIA (Mésocentre de Calcul Intensif Aquitain) of the Universités de Bordeaux and Pau et Pays de l'Adour (France), for providing access to computing facilities and Ministerio de Economía, Industria y Competitividad through Grant with reference FIS2017-89361-C3-1-P co-finanded by EU FEDER funds. Further financial support from Junta de Andalucía and Universidad de Huelva is also acknowledged. J.A.F. acknowledges Contrato Predoctoral de Investigación from XIX Plan Propio de Investigación de la Universidad de Huelva nad a FPU Grant (Ref. FPU15/03754) from Ministerio de Educación, Cultura y Deporte. J.M.G thanks the partial financial support of FONDECYT, Chile (Project 11170111) A. M. also acknowledges the finnacial support of FONDECYT, Chile (Project 1150656).

Bibliography

[1] W. L. Mao, H. K. Mao, A. F. Goncharov, V. V. Struzhkin, Q. Guo, J. Hu, J. Shu, R. J. Hemley, M. Somayazulu, and Y. Zhao *Science*, vol. 297, pp. 2247–2249, 2002.

[2] W. L. Mao and H. K. Mao *Proc. Natl. Acad. Sci.*, vol. 101, pp. 708–710, 2004.

[3] L. J. Florusse, C. J. Peters, J. Schoonman, K. C. Hester, C. A. Koh, S. F. Dec, K. N. Marsh, and E. D. Sloan *Science*, vol. 306, pp. 469–471, 2004.

[4] H. Lee, J. W. Lee, D. Y. Kim, J. Park, Y. T. Seo, H. Zeng, I. L. Moudrakovski, C. I. Ratcliffe, and J. A. Ripmeester *Nature*, vol. 434, pp. 743–746, 2005.

[5] T. Uchida, M. Wakakura, A. Miyake, and T. Ogawa *J. Therm. Anal. Colorim.*, vol. 93, pp. 47–52, 2008.

[6] S.-P. Kang, H. Lee, C.-S. Lee, and W.-M. Sung *Fluid Phase Equil.*, vol. 185, pp. 101–109, 2001.

[7] A. Delahaye, L. Fournaison, S. Marinhas, and I. Chatti *Ind. Eng. Chem. Res.*, vol. 45, pp. 391–397, 2006.

[8] R. Anderson, A. Chapoy, and B. Tohidi *Langmuir*, vol. 23, pp. 3440–3444, 2007.

[9] Y.-J. Lee, T. Kawamura, Y. Yamamoto, and J.-H. Yoon *J. Chem. Eng. Data*, vol. 57, pp. 3543–3548, 2012.

[10] T. Makino, T. Sugahara, and K. Ohgaki *J. Chem. Eng. Data*, vol. 50, pp. 2058–2060, 2005.

[11] W. L. Jorgensen *J. Am. Chem. Soc.*, vol. 103, pp. 335–340, 1981.

[12] W. L. Jorgensen *J. Am. Chem. Soc.*, vol. 103, pp. 341–345, 1981.

[13] W. L. Jorgensen *J. Am. Chem. Soc.*, vol. 103, pp. 345–350, 1981.

[14] J. Chandrasekhar and W. L. Jorgensen *J. Chem. Phys.*, vol. 77, pp. 5073/1–10, 1982.

[15] J. Chandrasekhar and W. L. Jorgensen *J. Chem. Phys.*, vol. 77, pp. 5080/1–11, 1982.

[16] W. L. Jorgensen and J. Tirado-Rives *J. Am. Chem. Soc.*, vol. 110, pp. 1657–1666, 1988.

[17] W. L. Jorgensen, D. S. Maxwell, and J. Tirado-Rives *J. Am. Chem. Soc.*, vol. 118, pp. 11225–11236, 1996.

[18] J. Helfrich and R. Hentschke *Macromolecules*, vol. 28, pp. 3831–3841, 1995.

[19] S. Girard and F. Müller-Plathe *Mol. Phys.*, vol. 101, pp. 779–787, 2003.

[20] S. J. Keasler, S. M. Charan, C. D. Wick, I. G. Economou, and J. I. Siepmann *J. Phys. Chem. B*, vol. 116, pp. 11234–11246, 2012.

[21] J. M. Garrido, J. Algaba, J. M. Míguez, B. Mendiboure, A. I. Moreno-Ventas Bravo, M. M. Piñeiro, and F. J. Blas *J. Chem. Phys.*, vol. 144, pp. 144702/1–11, 2016.

[22] R. L. Scott and P. H. van Konynenburg *Discuss. Faraday Soc.*, vol. 49, pp. 87–97, 1970.

[23] P. H. van Konynenburg and R. L. Scott *Phil. Trans.*, vol. A298, pp. 495–540, 1980.

[24] J. Li, M. Rodrigues, A. Pavia, H. A. Matos, and E. G. de Azevedo *J. Supercrit. Fluids*, vol. 41, pp. 343–351, 2007.

[25] J. S. B. Michael J. Lazzaroni, David Bush and C. A. Eckert *J. Chem. Eng. Data*, vol. 50, pp. 60–65, 2005.

[26] Z. Knez, M. Škerget, L. Ilič, and C. Lütge *J. Supercrit. Fluids*, vol. 43, pp. 383–389, 2008.

[27] D. Kodama, T. Yagihashi, T. Hosoya, and M. Kato *Fluid Phase Equil.*, vol. 297, pp. 168–171, 2010.

[28] J. M. Míguez, M. M. Piñeiro, J. Algaba, B. Mendiboure, J. P. Torré, and F. J. Blas *J. Phys. Chem. B*, vol. 119, pp. 14288–14302, 2015.

[29] J. M. Garrido, M. Cartes, A. Mejía, J. Algaba, J. M. Míguez, F. J. Blas, A. I. Moreno-Ventas Bravo, and M. M. Piñeiro *J. Supercrit. Fluids*, vol. 128, pp. 359–369, 2017.

[30] J. J. Potoff and J. I. Siepmann *AIChE Journal.*, vol. 47, pp. 1676–1682, 2001.

[31] D. Frenkel and B. Smit, *Understanding Molecular Simulations.* 2nd ed. Academic, San Diego, 2002.

[32] M. P. Allen, *Computer Simulation of Liquids.* Claredon, Oxford, 1987.

[33] G. Galliero, M. M. Piñeiro, B. Mendiboure, C. Miqueu, T. Lafitte, and D. Bessieres *J. Chem. Phys.*, vol. 130, pp. 104704/1–10, 2009.

[34] G. Galliero *J. Chem. Phys.*, vol. 133, pp. 074705/1–7, 2010.

[35] J. M. Míguez, M. M. Piñeiro, and F. J. Blas *J. Chem. Phys.*, vol. 138, pp. 034707/1–11, 2013.

[36] D. Van Der Spoel, E. Lindahl, B. Hess, G. Groenhof, A. E. Mark, and H. J. Berendsen *J. Comput. Chem.*, vol. 26, no. 16, pp. 1701–1718, 2005.

[37] M. A. Cuendet and W. F. van Gunsteren *J. Chem. Phys.*, vol. 127, pp. 184102/1–9, 2007.

[38] S. Nosé *Mol. Phys.*, vol. 52, pp. 255–268, 1984.

[39] H. J. C. Berendsen, J. P. M. Postma, W. F. van Gunsteren, A. di Nola, and J. R. Haak *J. Chem. Phys.*, vol. 81, pp. 3684/1–8, 1984.

[40] H. Hulshof *Ann. Phys. (Berlin)*, vol. 4, pp. 165–186, 1901.

[41] J. S. Rowlinson and B. Widom, *Molecular Theory of Capillarity.* Claredon Press, 1982.

[42] E. de Miguel, F. J. Blas, and E. M. del Río *Mol. Phys.*, vol. 104, pp. 2919–2927, 2006.

[43] E. de Miguel and G. Jackson *J. Chem. Phys.*, vol. 125, pp. 164109/1–12, 2006.

[44] "Medea gibbs ® - materials design." http://www.materialsdesign.com/medea/gibbs.

[45] J. M. Garrido, M. Cartes, and A. Mejía *J. Sol. Chemistry*, vol. 129, pp. 83–90, 2017.

[46] J. M. Garrido, M. M. Piñeiro, A. Mejía, and F. J. Blas *Phys. Chem. Chem. Phys.*, vol. 18, pp. 1114–1124, 2016.

[47] A. Mejía, M. Cartes, H. Segura, and E. A. Müller *J. Chem. Eng. Data*, vol. 59, pp. 2928–2941, 2014.

[48] J. M. Garrido, L. Cifuentes, M. Cartes, H. Segura, and A. Mejía *J. Sol. Chemistry*, vol. 89, pp. 78–88, 2014.

[49] E. A. Müller and A. Mejía *Fluid Phase Equil.*, vol. 282, pp. 68–81, 2014.

[50] A. Gil-Villegas, A. Galindo, P. J. Whitehead, S. J. Mills, G. Jackson, and A. N. Burgess *J. Chem. Phys.*, vol. 106, pp. 4168–4186, 1997.

[51] A. Galindo, L. A. Davies, A. Gil-Villegas, and G. Jackson *Mol. Phys.*, vol. 93, pp. 241–252, 1998.

[52] F. J. Blas and A. Galindo *Fluid Phase Equil.*, vol. 194–197, p. 501, 2002.

[53] A. Galindo and F. J. Blas *J. Phys. Chem. B*, vol. 106, pp. 4503–4515, 2002.

[54] G. N. I. Clark, A. J. Haslam, A. Galindo, and G. Jackson *Mol. Phys.*, vol. 104, pp. 3561–3581, 2006.

[55] A. Galindo, P. J. Whitehead, G. Jackson, and A. N. Burgess *J. Phys. Chem.*, vol. 100, pp. 6781–6792, 1996.

[56] C. McCabe and S. B. Kiselev *Fluid Phase Equil.*, vol. 219, pp. 3–9, 2004.

[57] C. McCabe and S. B. Kiselev *Ind. Eng. Chem. Res.*, vol. 43, no. 1, pp. 2839–2851, 2004.

[58] E. Forte, F. Llovell, L. F. Vega, J. P. M. Trusler, and A. Galindo *J. Chem. Phys.*, vol. 134, pp. 154102/1–16, 2011.

[59] E. Forte, F. Llovell, J. P. M. Trusler, and A. Galindo *Fluid Phase Equil.*, vol. 337, pp. 274–287, 2013.

Capítulo 9

Phase Equilibria and Interfacial Properties of the Tetrahydrofuran + Methane Binary Mixture from Experiment and Computer Simulation

Abstract

We have determined the pressure-density diagram and the surface tension of the tetrahydrofuran + methane (THF + CH_4) binary mixture from experiments at 300.15 and 370.15K and over the pressure range (0.1 to 20) MPa. In addition to that, we have also obtained the phase equilibria and interfacial properties of the system from direct simulation of the vapor-liquid interface at the same thermodynamic conditions. THF is modeled as a rigid and planar approximated TraPPE-UA model proposed by us in a previous work [*J. Chem. Phys.* **144**, 144702 (2016)]. This model has been used recently to determine the vapour-liquid interfacial properties of the THF + carbon dioxide binary mixture [*J. Chem. Phys. C* **122**, 16142 (2018)] with high accuracy. The simulations are performed using the direct coexistence technique in the Molecular Dynamics (MD) NVT canonical ensemble. We have obtained the density profiles, pressure-density and pressure-composition phase equilibria diagrams and the surface tension. The vapor-liquid surface tension is evaluated from the normal and tangential components of the pressure tensor according to the mechanical virial route. The simulation results predict accurately the vapor-liquid phase equilibria of the system, in good agreement with experimental results. Predictions for surface tension obtained from simulation also have been compared with experimental results, being the agreement excellent in all cases. The surface relative Gibbs adsorption of the species along the interfacial region is reported; methane is adsorbed along the interfacial region, whereas tetrahydrofuran does not exhibit any special adsorption activity. The adsorption of methane increases with pressure and decreases with temperature.

9.1 Introduction

Tetrahydrofuran, c-$(CH_2)_4O$ or simply THF, is a cyclic ether usually used as a solvent in many chemical and industrial processes [1]. Among its diverse applications, THF is normally used to stabilize

clathrate hydrates from a thermodynamic point of view [2–5]. Gas hydrates are non−stoichiometric crystalline inclusion compounds consisting of a network of hydrogen-bonded molecules forming cages in which various types of low molecular weight compounds, such as methane (CH_4), carbon dioxide (CO_2), or hydrogen (H_2), among many others, can be enclathrated under appropriate thermodynamic conditions. Due to the characteristics properties of hydrates to selectively encage guest molecules within this solid hydrate crystalline structures, hydrates are nowadays considered strategic and key materials for the industry of gas storage/transportation and mixture separation applications [6, 7]. This includes CH_4, CO_2, and H_2 among the most relevant substances. Although storage, transportation, and mixture separation are key applications for industry, the view of gas hydrates as a possible future source of energy, and particularly CH_4, and the environmental use of hydrates for CO_2 sequestration make the understanding of these systems from kinetic, thermodynamic, and structural points of view even more attractive for the scientific community.

The thermodynamic conditions at which the clathrate hydrates structures are formed and become stable depend in a complex fashion on the shape, structure, and molecular interactions of the low molecular weight compounds or guests that are enclathrated in the cages of the water-like crystalline network formed, as well as on the intermolecular interactions between guest and water molecules. In many occasions, the temperatures and pressures at which different clathrate hydrates are stable are far from being considered as mild conditions. Due to that, THF is used as clathrate hydrates promoter since it allows mixed gas hydrates to form at significantly lower pressure and higher temperature than the hydrates formed without this promoter. This is particularly true in the case of CH_4, CO_2, and H_2 hydrates, among other examples [2–5].

During the last decades, there has been an increasing interest in the use and development of molecular modelling techniques for the prediction of the thermodynamic, interfacial, structural, and dynamical properties of clathrate hydrates. This is the particular case of hydrates of mixtures of THF with CH_4 and/or CO_2. A key point for the success of molecular modelling techniques in predicting this kind of properties is the availability of good molecular models able to describe accurately different properties. In particular, phase equilibria and interfacial properties are very sensitive to molecular details and are especially suited to be studied from computer simulation to check if molecular models, i.e., intermolecular potentials and chemical structures, could be used to study this kind of hydrates.

Although THF has been used in a relatively large amount of experiments, phase equilibria and interfacial properties of mixtures involving THF, such as THF + CO_2 and + CH_4 are really scarce, as noticed previously by Algaba *et al.* [8] In the particular case of the THF + CH_4 binary mixture, there is no experimental data in the literature for phase equilibria and interfacial properties at any temperature and pressure. From our knowledge, the same is true for studies using computer simulation techniques. The only exception, from our knowledge, is the work of Míguez *et al.* [9] devoted to the determination of the phase behavior of the mixture from a theoretical perspective. In that paper, the authors determined the global phase behavior of the THF + CH_4 binary mixture, among others, using the Statistical Associating Fluid Theory for potentials of Variable Range (SAFT-VR).

According to the study of the THF + CH_4 mixture using the SAFT-VR approach [9], this system exhibits a highly non-ideal phase behavior, and particularly, type III phase behavior according to the van Konynenburg and Scott classification [10, 11]. In terms of the topology of the PT projection of its phase diagram, the behavior of the system is dominated by a huge liquid-liquid immiscibility region located at temperatures below one of the branches of the fluid-fluid critical line of the mixture and high pressures. This branch of the fluid-fluid critical line, that runs from the critical point of the

heaviest component (THF), changes continuously its character from vapor-liquid (at low pressures and temperatures close to the critical point of THF) to liquid−liquid as the temperature decreases. The other branch of the gas-liquid critical line, which is usually very short and the case of this mixture is not an exception, starts at the critical point of the lightest component (CH_4), ending at an upper critical end-point (UCEP) and meeting a three-phase liquid-liquid-vapor (LLV) line coming from low temperatures and pressures. For further details, we recommend a detailed inspection of Figures 3, 4, and 5 of the work of Míguez *et al.* [9]

The molecular characteristics of THF make it a remarkably difficult target for molecular modeling, being the cyclic structure and the presence of the ether chemical group two of the most challenging molecular details to be modelled. The last ingredient produces a strong polarity and a marked spacial anisotropy, inducing complex molecular interactions. In addition to that, mixing THF and small molecules, such as CH_4, results in asymmetric interactions, not only due to different sizes of both compounds but also to very different unlike dispersive interactions. This produces a complex phase diagram difficult to predict from a molecular perspective, as it has been explained above. Consequently, good molecular models for THF are needed if an accurate description of the phase behavior and interfacial properties, including hydrate phases, are required.

Unfortunately, and in spite of the interest of use of THF as hydrate thermodynamic promoter during last years, THF molecular models are scarce in literature. For a review of the most important models existing in literature we recommend the papers of Garrido *et al.* [12] and Algaba *et al.* [8]. Here we use an approximated, planar, and rigid TraPPE-UA model in which non-bonded interaction intermolecular parameters and partial charges located at the different chemical groups are identical to those of the original TraPPE-UA model proposed by Keasler *et al.* [13] (see the works of Garrido *et al.* [12] and Algaba *et al.* [8] for further details). In addition to that, bending and torsional degrees of freedom are frozen, i.e., we consider that the equilibrium bond angles are fixed and the molecule has not torsional degrees of freedom. As an additional approximation, THF is considered in this case not only rigid but also planar. [12] This means that although the fixed bonded angles in this new model are the same than those of equilibrium in the flexible model, the bond lengths are slightly different [8].

Our previous works demonstrate that: (1) the rigid TraPPE-UA model is able to provide an excellent accuracy in the whole coexistence range for the vapor-liquid phase envelope and surface tension of THF [12]; (2) the same model for THF is also able to predict very accurately the vapor-liquid pressure-density and pressure-composition phase envelopes, as well as the vapor-liquid surface tension of the THF + CO_2 binary mixture [8]. The use of a rigid model instead of the original and flexible TraPPE-UA model of Keasler *et al.* [13] is an important and clear advantage since is faster for simulating since internal degrees of freedom are frozen, i.e., neither bending nor torsional intramolecular interactions need to be evaluated.

The research we are carrying out in these series of papers is devoted to the test and develop models of THF and mixtures with other substances to accurately predict the phase equilibrium and interfacial properties of these systems using computer simulation. The long-term goal of these works is to use the proposed molecular models to predict the phase equilibrium of THF hydrates and hydrates of mixtures of THF with CH_4 and/or CO_2. In this third paper we concentrate in the study of vapor-liquid phase equilibria and interfacial properties of the THF + CH_4 binary mixture.

Finally, to the best of our knowledge, do not exist works published in the literature dealing either the phase equilibria nor interfacial properties of the THF + CH_4 mixture from the experimental and/or molecular simulation perspective. As we have mentioned previously along this Introduction, since we

are considering the possibility of studying the phase behavior of clathrate hydrates of mixtures of CH_4 and THF, it is necessary to check if models available in the literature are capable to accurately predict the phase behavior and interfacial properties of the system. This may be considered as the continuation of our previous works [8, 12], as well as a step forward in the global study of phase equilibria and interfacial properties covering experiments, theoretical modelling, and computer simulation.

The two main goals of the work are the following: (1) to determine experimentally the pressure-density projection of the phase diagram and the interfacial properties of the THF + CH_4 binary mixture, with particular emphasis on the surface tension and the relative Gibbs adsorption, at different temperatures and high pressures; and (2) to determine the ability of the approximated rigid model of THF, based on the TraPPE-UA model, for predicting the vapor-liquid phase equilibria and interfacial properties of the THF + CH_4 mixture, with particular emphasis on the surface tension, using MD computer simulations.

The rest of the paper is organized as follows. In Section 2 we summarize the experimental details. Molecular models considered, as well as the simulation details are presented in Section 3. Results and discussion are presented in Section 4. Finally, in Section 5 we present the main conclusions.

9.2 Experimental Section

9.2.1 Purity of materials

Methane (CH_4) was purchased from Linde S.A. (Chile) with a certified purity greater than 99.9%, whereas tetrahydrofuran (THF) was purchased without stabilizers from Aldrich and used without further purification (0.999 mass fraction purity). The purity of the pure liquid was also verified by gas chromatography (0.999 mass fraction purity).

Additionally, the purity of THF was verified by report the refractive index (n_D), the liquid mass density (ρ) and the surface tension (γ) at 298.15 K and 0.1013 MPa. Table 9.1 summarizes the measure values of n_D, ρ, γ and those previously reported by NIST – REFPROP [14].

Tabla 9.1: Refractive index (n_D), liquid mass density (ρ) and surface tension (γ) at 298.15 K and 0.1013 MPa of pure Tetrahydrofuran (THF)[a,b]

n_D		ρ (kg/m^3)		γ (mN/m)	
Exp.	Lit.	Exp.	Lit.	Exp.	Lit.
1.4062	1.4069	881.93	881.95	26.30	26.87

[a] Standard uncertainties are $u(T) = 0.01$K, $u(P) = 0.03$kPa, $u(n_D) = 4 \times 10^{-4}$, $u(\rho) = 0.09$kg/m^3, $u(\gamma) = 0.06$mNm^{-1}. The combined expanded uncertainty (0.95 level of confidence, $k = 2$) for $U_c(n_D) = 10^{-3}$, $U_c(\rho) = 0.175$kg/m^3 and $U_c(\gamma) = 0.1$mNm^{-1}. [b] Experimental data have been taken from NIST – REFPROP data base [14].

9.2.2 Tensiometry

For the mixture considered in this work (THF + CH_4), the isothermal experimental conditions (300.15 and 370.15 K) and pressure range (0.1 to 20 MPa), the most appropriate device for the surface tension measurements is the pendant drop tensiometer. [15] Here, a drop of the denser component (THF), is allowed to hang from the tip of a needle in a high pressure visual cell filled with a gaseous CH_4. After equilibration, the surface tension, γ, is obtained by analyzing the drop silhouette and the mass densities of the coexisting liquid and gas phases. Mathematically, the geometry of the drop and densities are related by the expression:

$$\gamma = (\rho_L - \rho_V)\, g d_e^2 f\,(d_e, d_s) \tag{9.1}$$

In Eq. (9.1), ρ_L is the mass density of THF saturated with CH_4 and ρ_V is the mass density of CH_4 saturated with THF, both of which must be determined at the experimental temperature and pressure. g is the local gravitational constant ($\approx 9.81\,\mathrm{m/s^2}$), d_e is equatorial diameter of the drop, (the largest one), and d_s is the horizontal diameter, which is located at a distance d_e from the apex of the drop. $f(d_e, d_s)$ corresponds to a function related to the silhouette of the drop, whose value is determined from numerical tables [16].

In this work, γ and ρ_L and ρ_V are measured at the isothermal conditions of 300.15 and 370.15 K. In both cases, these measurements were carried out over the pressure range 0.1 to 20 MPa. The experimental procedure and technical description of the equipment are described below.

Complementarily to surface tension measurements, their values can be used to predict, as a first approximation, the magnitude of Γ_{ij} (i.e., relative Gibbs adsorption isotherm of a species i on species j). According to Masterton *et al.* [17] for a gas–liquid system in which the pressure is changing, Γ_{ij} can be calculated by the following expression:

$$\Gamma_{ij} \simeq -\rho_i^{\alpha} \left(\frac{\partial \gamma}{\partial P}\right)_T \tag{9.2}$$

where the slope $(\partial\gamma/\partial P)_T$ is obtained from experimental values of $\gamma - P$ projection. ρ_i^{α} is the mass density of the pure gas (here CH_4). ρ_i^{α} can be directly measured as a function of T and P or alternatively, it can be obtained from a data base [14].

9.2.3 Densimeter

The mass density (ρ) of the mixture in the liquid and gas phases are measured at the experimental temperature and pressure using a DMA HP densimeter (Anton Paar GmbH, Austria) with an accuracy of $5 \times 10^{-3}\mathrm{kg/m^3}$. The mass density determination is based on measuring the period of oscillation of a vibrating U-shaped tube filled with the fluid mixture sample. During the operation, the temperature of the apparatus is maintained constant to within ± 0.01 K, and the pressure is measured by means a Swagelok type S pressure transducer connected to the densimeter, and maintained constant to within ± 0.001 kPa by means of the high-pressure syringe pump (Teledyne Isco Pump. Model 100DM, USA). The density measurements are repeated 25 times for each condition and the average is reported.

9.2.4 Interfacial Tension Cell

A pendant drop tensiometer model IFT-10, manufactured by Temco Inc. (USA) is used for surface tension measurements. The pendant drop cell is a stainless steel cylindrical chamber (with an inner volume of ~ 42 cm^3), with two injection orifices one at the top and the other at the bottom of the chamber. On the top orifice, a stainless steel needle (1.4 mm i.d. and 2.45 mm o.d.) is placed for generating pendant drops. The bottom orifice is connected to the high-pressure syringe pump (Teledyne Isco Pump. Model 100DM, USA), which is used to compress CH_4 from a commercial ultra-high purity CH_4 with a certified purity greater than 99.9% (Linde S.A., Chile) and also maintained the experimental pressure constant within ± 0.001 kPa. The chamber is equipped with appropriately sealed borosilicate glass windows, which allow visualization of the inner space during operation. The light beam source, located at one side of the visualization axis, is a led fiber optic light source (20W LED Fiber Optic, AmScope, USA) covered by a white diffuser made of Teflon. The camera, located at opposite side of the visualization axis, is a monochrome video camera model CS8320Bi (Toshiba Teli, Corp., Japan) connected to a personal computer through a frame grabber card. The temperature of the cell is measured by means a K-type thermocouple, and maintained constant to within ± 0.1 K by means of electric band heaters operated by a Watlow temperature controller model TC-211-K- 989 (USA). The tensiometer, the light source and the camera are mounted on a free vibration table (Vibraplane, model 2210, USA) in order to avoid the effect of noisy measurements due to external vibrations. Surface tension measurements are made by analyzing images of liquid (THF) pendant drops generated at the tip of an injection needle, which are surrounded by CH_4. The images are then processed by using the DROPimage Advanced software version 1.5 (Ramé – Hart instruments, co. USA) [18].

The experimental procedure for determining surface tension is as follows. The cell is heated to the desired experimental temperature (300.15 or 370.15 K), and then it is slightly pressurized with CH_4. After degasification in an ultrasonic bath, THF is pumped through a stainless-steel tube to the needle tip. The pump is a positive displacement ELDEX HP Series Model B-100-S-2 CE (USA). Initially, a small portion of the liquid is pumped into the chamber in order to saturate the gas that fills the cell. Then, the cell is pressurized to the desired experimental pressure and a liquid drop is generated at the tip of the needle. The pressure in the IFT cell is maintained constant to within ± 0.10 kPa by means of the high-pressure syringe pump. Once the drop is formed and the desired experimental temperature and pressure are reached, it is necessary to wait, approximately, 10 to 20 min until the drop reaches an equilibrium state. This value is based on the experimental evidence of the time evolution of surface tension. After this equilibration step, the drop dimensions are recorded (at least during 6 h) in order to check the stability of its geometry. Once the shape and volume of the drop are deemed constant, the diameters of the drop (d_e, d_s) are recorded and, simultaneously, the liquid and the gas phases are transported to the high-pressure densimeter, through a heated stainless steel tube, in order to measure the mass density of the liquid THF saturated with CH_4 (ρ_L) and the mass density of CH_4 saturated with THF (ρ_V) both densities are measured at the experimental temperature and pressure. The geometry of the drop and the mass density of the liquid and gas phases are used in Eq. (9.1) to calculate the value of γ. For each image, γ is calculated 25 times in order to report a mean value.

It is also important to recall that γ in a pendant drop tensiometer is not measured directly; therefore it is important to establish that the uncertainties of γ values are affected by the value of temperature, pressure, density difference, experimental replicability of γ itself and its standard uncertainties. In order to quantify these effects the expanded or combined relative uncertainty of γ, u_c, the following relationship [19] has been considered:

$$u_c^2(\gamma) = \left[\frac{1}{\gamma}\left(\frac{\partial\gamma}{\partial P}\right)_T \delta P\right]^2 + \left[\frac{\delta\Delta\rho}{\Delta\rho}\right]^2 + \left[\frac{\sigma(\gamma)}{\gamma}\right]^2 \tag{9.3}$$

In Eq. (9.3) δP and $\delta\Delta\rho$ correspond to the standard uncertainties in pressure and density, respectively. $\sigma(\gamma)$ is the standard deviation of γ which, together with the maximum value of partial derivatives of γ in P, have directly been estimated from experimental data. For the binary system investigated here, the average $u_c(\gamma)$, value was found to be 0.71 %. Therefore, the expanded relative uncertainty of γ at 95 % confidence was 1.4 %. Finally, it is important to recall that the chamber cleaning plays a key role in the accuracy of the pendant drop technique, since negligible impurity concentrations strongly affect γ measurements. Consequently, appropriate precautions were taken when cleaning the chamber surfaces by replicating experimental γ values of the pure fluids at 298.15 K and 0.1 MPa (see Table 9.1).

For additional details concerning to the pendant drop technique and implementation, the reader is redirected to the following references: Andreas *et al.* [16], Rusanov and Prokhorov [20], Ambwani and Fort [21] and Evans [15].

9.3 Models and simulation details

9.3.1 Models

In this work, CH_4 has been modeled as an unique spherical interaction site following the force field proposed by Goodbody *et al.* [22]. THF has been modeled as an approximated, planar and rigid TraPPE-UA (Transferable Potentials for Phase Equilibria-United Atoms) model proposed by us in a previous work [12] and based on a flexible model introduced by Keasler *et al.* [13]. This model of THF has also been used by us in a recent work to study the interfacial properties of the THF + CO_2 binary mixture [8]. This simplified model is able to predict accurately the phase behavior of the mixture but also the most important interfacial properties including surface tension. THF is modeled using three different types of united-atom chemical groups: the ether group or oxygen atom, O, two α-methyl (α-CH_2) bonded directly to the ether group, and two β-methyl (β-CH_2) chemical groups bonded to the α-methyl groups and closing the ring of the cyclic ether.

Tabla 9.2: Lennard-Jones well depth, ε, and size, σ, partial charges, q, parameters for the chemical groups of the TraPPE-UA force field for non-bonded interactions of THF and CH_4.

atom	ε/k_B(K)	σ(Å)	q(e)
	THF		
O	190	2.20	-0.410
$CH_2(\alpha)$	56.3	3.88	0.160
$CH_2(\beta)$	56.3	3.88	0.045
	CH_4		
CH_4	147.95	3.730	0.000

Non-bonded interactions between different chemical groups have been described by the Lennard-Jones and Coulomb intermolecular potentials:

$$U(r_{ij}) = 4\epsilon_{ij}\left[\left(\frac{\sigma_{ij}}{r_{ij}}\right)^{12} - \left(\frac{\sigma_{ij}}{r_{ij}}\right)^{6}\right] + \frac{q_i q_j}{4\pi\epsilon_0 r_{ij}} \tag{9.4}$$

where r_{ij} is the distance between interaction sites i and j, σ_{ij} and ϵ_{ij} are the diameter and well depth associated to the LJ intermolecular potential, q_i and q_j are the partial charges on interaction sites i and j, and ϵ_0 is the permittivity of vacuum. The parameters for the potentials of each chemical group of each molecule are presented in Table 9.2. All the LJ parameters for unlike interactions are obtained always using the Lorentz-Berthelot combining rules and all the intramolecular interactions are excluded.

As we mentioned previously, the simplified model of THF used in this work is a planar and rigid version of the original TraPPE-UA model proposed by Keasler *et al.* [13] Here we use the same non-bonded LJ interaction parameters and partial charges located at the different chemical groups than those of the original model, as it is shown in Table 9.2. To be consistent with the rigidity of the model, bending and torsional degrees of freedom are frozen and we consider that the equilibrium bond angles are fixed. Since the model is planar, the bond length between different chemical groups are slightly different [12]. The numerical values used for bond and lengths in the rigid model for THF are summarized in Table 9.3.

Tabla 9.3: Bond angles and lengths for the rigid TraPPE-UA model of THF

angle	θ(deg)	bond	length(nm)
CH_2-CH_2-CH_2	105.5	α-CH_2-β-CH_2	0.1540
CH_2-CH_2-O	108.5	α-CH_2-O	0.1440
CH_2-O-CH_2	112.0	β-CH_2-β-CH_2	0.1565

9.3.2 Simulation details

The vapor-liquid phase equilibria and interfacial properties of the mixture are obtained from MD simulations using the direct coexistence technique in the NVT canonical ensemble. [23, 24] In order to prepare the vapor-liquid interface, homogeneous liquid and vapour systems, at a given temperature and pressure, are equilibrated independently using parallelepipedic simulation boxes of volumes $V = L_x \times L_y \times L_z$, where L_x, L_y, and L_z are the dimensions of the simulation boxes. The vapour and liquid boxes are prepared using as initial values for density and composition the predictions obtained from the SAFT-VR approach at the same temperature and pressure [25]. Both phases are equilibrated at the same temperature and pressure using an $NP_z\mathcal{A}T$ ensemble in which L_x and L_y are kept constant and only L_z is varied along the simulation. L_z lengths are chosen appropriately to ensure phase separation at the corresponding temperature and pressure. The final vapor-liquid-vapor simulation box is built linking up both equilibrated bulk boxes forming a vapor-liquid-vapor system. The total number of THF and CH_4 molecules is different since depends on the composition of the mixture. We use periodic boundary conditions in all three dimensions and a cut-off radius $r_c = 1.94$nm ($r_c = 5\sigma_{CH_2}$ where σ_{CH_2} is the large value of the size parameter of the LJ intermolecular potential). Long-range interactions are determined using three-dimensional Ewald technique with a convergence parameter of $1\,\mathrm{nm}^{-1}$ and a maximum value for the reciprocal lattice equal to 31 [23, 24].

All MD simulations are carried out using GROMACS (version4.6.1). [26] We have used a Verlet leapfrog algorithm [27] with a time step of 0.002 ps and a Nosé-Hoover thermostat [28] with a time constant equal to 1.0 ps. We use 10 ns for equilibration of the vapor-liquid-vapor system and 50 ns for averages. In order to estimated the errors, the sub-blocks average method of Berendsen *et al.* [29] is applied. The average period is divided into M independent blocks and the statistical error is obtained as the standard deviation of the average $\bar{\sigma}/\sqrt{M}$, where $\bar{\sigma}$ is the variance of the block averages and M has been fixed in this work to $M = 10$.

The equilibrium vapor pressure, P_v, and surface tension, γ, are obtained from the diagonal components of the pressure tensor. The vapor pressure corresponds to the normal component, $P_v = P_{zz}$, of the pressure tensor, while the surface tension is obtained using the mechanical route [30–33] as:

$$\gamma = \frac{L_z}{2}\left[P_{zz}(z) - \frac{P_{xx}(z) + P_{yy}(z)}{2}\right] \tag{9.5}$$

In Eq. (9.5), the additional factor 1/2 comes from having two interfaces in the system, and L_z is the size of the simulation box in the z direction, defined along the longitudinal dimension across the interface.

9.4 Results and discussion

In this section we present new experimental results for the bulk phase mass densities and surface tension for the THF + CH_4 binary mixture at 300.15 and 370.15 K, as well as the predictions obtained from the direct simulation of the vapor-liquid interface of the system using MD simulations in the NVT canonical ensemble. In addition to that, we have also included theoretical predictions for the pressure-density and pressure-composition projections of the phase diagram of the system as obtained from the well-known SAFT-VR equation of state (EOS) in a previous work. [9]

We have determined the equilibrium molecular density profiles for each component of the binary mixture corresponding to THF, $\rho_1(z)$, and to CH_4, $\rho_2(z)$, as well as for the total density of the system, $\rho(z) = \rho_1(z) + \rho_2(z)$, being z the direction perpendicular to the planar vapour-liquid interface of the system. Note that THF is arbitrarily chosen as component 1 and CH_4 as component 2. The profiles are obtained by dividing the system in 200 slabs along the z-axis direction and averaging the density of each slab over the production stage. We have fit the density profiles using hyperbolic tangent functions, following the approach from previous works [34, 35]. If the system is well equilibrated, it is expected to find the same bulk vapour density on both sides of the liquid film within statistical uncertainties. Similarly, it is expected that the $10-90$ interfacial thickness associated to both interfaces are the same within statistical uncertainties. This two proofs are used to check if the system under study is well equilibrated. In order to avoid repetitions, we only present one half of the profiles corresponding to one of the interfaces. In addition to that, all density profiles have been shifted along the z-axis to place z_0, the Gibbs dividing surface, at origin. Total densities in the liquid and vapor phases and surface tension corresponding to the experimental data obtained in this work are collected in Tables 9.4 and 9.5. We have included in Tables 9.6 and 9.7 the simulation results for the total densities in the liquid and vapor phases, molar fractions of THF in each phase, and the surface tension at different pressures and temperatures.

Tabla 9.4: Liquid density, ρ_L, vapor density, ρ_V, and surface tension, γ, at 300.15 K and different pressures as obtained from experiments.

P (MPa)	ρ_L (kg/m^3)	ρ_V (kg/m^3)	γ (mN/m)
0.1	892.87	1.52	26.4
2	877.57	13.98	21.64
4	864.45	28.73	18.86
6	853.49	44.81	16.26
8	843.80	61.88	13.13
10	834.49	79.59	10.45
12	824.65	97.60	8.63
14	813.38	115.56	6.83
16	799.79	133.14	5.30
18	782.98	149.98	3.94
20	762.06	165.75	2.84

Tabla 9.5: Liquid density, ρ_L, vapor density, ρ_V, and surface tension, γ, at 370.15 K and different pressures as obtained from experiments.

P (MPa)	ρ_L (kg/m^3)	ρ_V (kg/m^3)	γ (mN/m)
0.1	806.26	1.93	17.21
2	788.76	13.09	14.05
4	773.81	24.78	11.45
6	761.41	36.50	9.68
8	750.51	48.31	8.18
10	740.08	60.31	6.76
12	729.07	72.59	5.49
14	716.44	85.14	4.13
16	701.16	98.13	3.12
18	682.18	111.60	2.25
20	658.47	125.63	1.51

Tabla 9.6: Liquid density, ρ_L, vapor density, ρ_V, molar fraction of THF in the liquid phase, x_1^L, molar fraction of THF in the vapor phase, x_1^V and surface tension, γ, at 300.15 K and different pressures as obtained from MD NVT simulations. The errors are estimated as explained in the text.

P (MPa)	ρ_L (kg/m^3)	ρ_V (kg/m^3)	x_1^L	x_1^V	γ (mN/m)
4.62(2)	820.9(19)	36.1(5)	0.897(4)	0.020(3)	17.6(3)
8.94(3)	794.1(3)	71.6(3)	0.818(5)	0.017(20)	11.2(4)
13.50(5)	761.3(3)	119.9(18)	0.734(6)	0.028(7)	7.4(4)
18.43(6)	716.9(5)	176.0(13)	0.639(11)	0.040(3)	3.9(20)
18.97(5)	707.9(24)	180.6(13)	0.622(5)	0.041(4)	4.0(4)
22.55(12)	669.0(20)	220.5(13)	0.547(5)	0.056(4)	2.2(4)
25.43(14)	643.4(21)	264.0(3)	0.501(5)	0.081(9)	1.0(3)

Tabla 9.7: Liquid density, ρ_L, vapor density, ρ_V, molar fraction of THF in the liquid phase, x_1^L, molar fraction of THF in the vapor phase, x_1^V and surface tension, γ, at 370.15 K and different pressures as obtained from MD NVT simulations. The errors are estimated as explained in the text.

P (MPa)	ρ_L (kg/m^3)	ρ_V (kg/m^3)	x_1^L	x_1^V	γ (mN/m)
1.14(7)	769.2(3)	14.4(5)	0.981(6)	0.384(7)	15.13(15)
2.87(15)	757.9(17)	24.9(21)	0.949(23)	0.166(3)	13.54(16)
4.43(20)	746.9(7)	36.1(3)	0.918(21)	0.129(23)	11.73(12)
8.07(3)	718.0(7)	61.2(3)	0.844(4)	0.094(3)	8.46(14)
13.78(3)	671.8(3)	111.7(10)	0.733(5)	0.098(6)	4.95(16)
17.73(5)	619.7(22)	148.3(21)	0.633(10)	0.107(4)	3.23(17)

We show in Figure 9.1 the density profiles of THF, $\rho_1(z)$, and CH_4, $\rho_2(z)$, corresponding to the THF(1) + CH_4(2) binary mixture at 300.15 K and several pressures, from 4.6 up to 25.4 MPa, approximately. This temperature is below the critical temperature of THF ($T_c^{\mathrm{THF}} \approx 540$ K) but it is above the critical temperature of CH_4 ($T_c^{\mathrm{CH_4}} \approx 190.5$ K). This indicates that THF is subcritical and CH_4 is supercritical, and consequently, the mixture exhibits a critical point at 52.0 MPa, approximately. As can be seen, $\rho_1(z)$ in the liquid-like region phase decreases as the pressure is increased meanwhile in the vapor-like region increases as the pressure is increased. Contrary, $\rho_2(z)$ increases as the pressure is increased in both vapor- and liquid-like regions. As a consequence of this, the absolute value of the slope of the density profiles corresponding to THF at the interface decreases as the pressure is increased. This produces the expected increase of the interfacial thickness of the interface as the pressure is higher due to the proximity to the critical point.

An inspection of the density profiles of both components indicates a nearly monotonic increasing behavior when passing from the liquid side to the vapour side along the interface at high pressures in the case of methane density profiles. However, at pressure below 18.5 MPa, CH_4 is preferentially adsorbed at the interface. As can be seen, the preferential adsorption decreases as the pressure is increased. This behavior is usually seen in binary mixtures with significant differences in the values of the vapor pressure at a given temperature, as it was reported in several works. [8, 36–41]

We also consider the interfacial behavior of the system at a higher temperature, 370.15 K. As we have previously mentioned, this temperature is below the critical temperature of THF and above the critical temperature of CH_4. At these conditions, the mixture exhibits another critical point at 45.0 MPa, approximately. Figure 9.2 shows $\rho_1(z)$ and $\rho_2(z)$ of the system at 370.15 K and several pressures, from 1.1 up to 17.7 MPa, approximately. It is clearly seen that density profiles of THF and CH_4 exhibit qualitatively the same behavior as in the previous case. The only significant difference between the behavior of profiles of CH_4 at 300.15 and 370.15 K is that preferential adsorption of methane at the interface now occurs at all pressure studied.

From the density profiles obtained simulating the vapor-liquid interface using the direct coexistence technique it is possible to determine the liquid and vapor bulk densities as indicated previously. This allows to obtain the pressure-density or $P - \rho$ projection of the phase diagram of the mixture at 300.15 and 370.15 K, as it shown in Figures 9.3 and 9.4, respectively. Since we have measured the bulk mass densities of THF and CH_4 (see Tables 9.4 and 9.5), we have also included this information in the corresponding figures. In a previous work [9], some of us have determined the high-pressure phase behavior of the THF + CH_4 mixture using the well-known SAFT-VR EOS. We also present

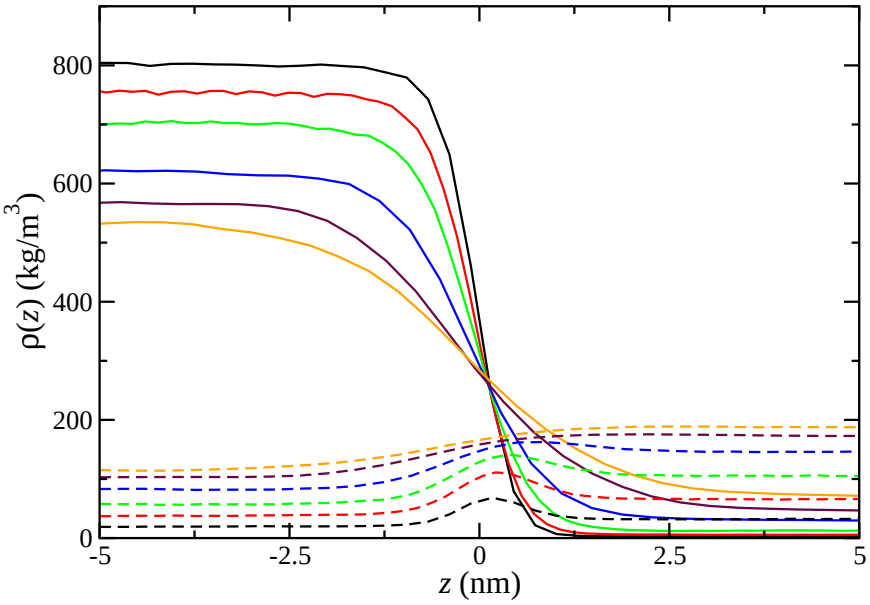

Figura 9.1: Simulated equilibrium density profiles of THF (continuous curves) and density profiles of CH_4 (dotted curves) obtained using MD NVT simulations across the vapor-liquid interface of the THF +CH_4 binary mixture at 300.15 K . From bottom to top: 4.62 MPa (black), 8.94 MPa (red), 13.50 MPa (green), 18.43 MPa (blue), 22.55 MPa (maroon) and 25.43 MPa (orange)

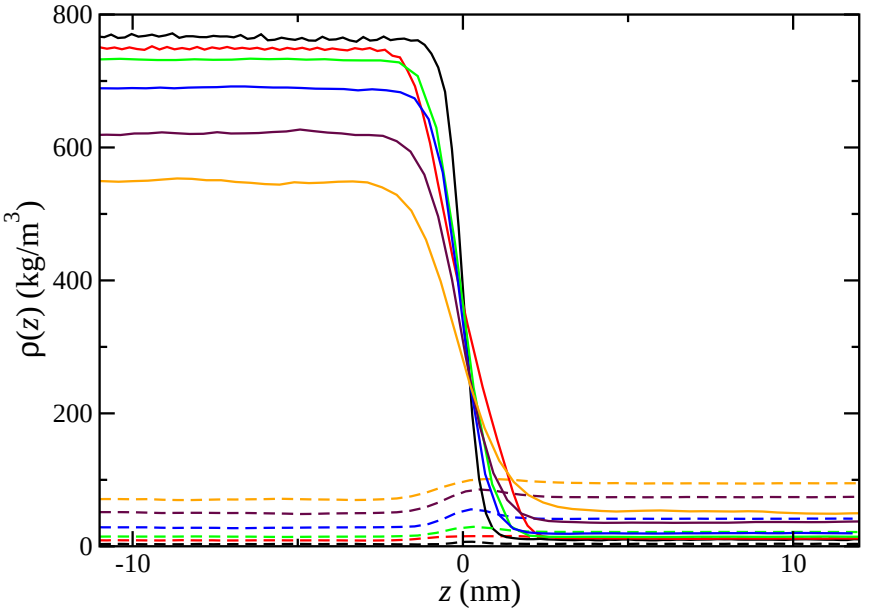

Figura 9.2: Simulated equilibrium density profiles of THF (continuous curves) and density profiles of CH_4 (dotted curves) obtained using MD NVT simulations across the vapor-liquid interface of the THF +CH_4 binary mixture at 370.15 K . From bottom to top: 1.14 MPa (black), 2.87 MPa (red), 4.43 MPa (green), 8.07 MPa (blue), 13.78 MPa (maroon) and 17.73 MPa (orange)

the predictions obtained from this theoretical formalism to check its ability in predicting the $P-\rho$ projection of the phase diagram of the system.

As can be seen in Figure 9.3, agreement between MD simulation results, theoretical predictions, and experimental data obtained in this work are in good agreement in the whole range of pressures, especially at low pressure and for the vapor coexistence densities, an expected result. However, MD simulation results systematically underestimate the liquid densities and slightly overestimate the vapor densities at high pressures. We believe this behavior is a consequence of the force field used to describe THF, but also could be due to a fail of the Berthelot combining rule for predicting the mixture behavior at these conditions of high pressures [9]. At this point is important to remark that MD simulation results are obtained from the Lorentz-Berthelot combining rules for the mixture, which means that predictions from simulations have been obtained without any further fitting.

We have also determined the $P-\rho$ projection of the phase diagram at 370.15 K, as it is shown in Figure 9.4. At this temperature, the phase diagram exhibits the same qualitative behavior that the corresponding at lower temperature (300.15K). As in the previous case, theoretical predictions and experimental data measured in the laboratory are in excellent agreement meanwhile the MD simulation results systematically underestimate liquid density and slightly overestimate the vapor density at a high pressures. The excellent agreement between all results corresponding to the vapor side of the phase envelope, in the whole pressure range obtained experimentally, is expected due to the ideal behavior of the system. However, the liquid phase is governed by strong molecular interactions between the components of the mixture. Since the number and strength of interactions at these conditions are more important than in a vapor-like phase, accuracy of molecular interactions between THF and CH_4 play a key role. Probably, the reason for the discrepancies between simulation and theory in the liquid size of the phase envelope of the system. It is important however to recall here that the phase behavior of the mixture is highly non-ideal. In particular, the mixture exhibits type III phase behavior according to the van Konynenburg and Scott classification [10, 11]. Nevertheless, theoretical predictions are able to provide a reasonable agreement with experimental data if we take into account that no further fitting has been done.

As it is happens with $P-\rho$ projection of the phase diagram, it is also possible to obtain the pressure-composition or $P-x$ projection at different temperatures from the analysis of the density profiles obtained from the simulation results of the vapor-liquid interface. Here we have also considered the comparison with the predictions obtained from SAFT-VR. Unfortunately, we have not measured the composition of the mixture in each phase because of lack of the corresponding equipment.

Figure 9.5 shows the $P-x$ diagram at 300.15 K. As can be seen, agreement between simulation results and theoretical predictions is excellent at low and mid pressures, below 15 MPa, approximately. At higher pressures, simulation results overestimate SAFT-VR predictions for the composition of THF in the vapor side of the phase envelope and underestimate its composition along the liquid side of the phase diagram. We have also obtained the $P-x$ phase envelope at 370.15 K. As in the previous case, simulations results overestimate the theoretical predictions corresponding to the composition of THF in the vapor phase for the whole range of pressures. In addition to that, SAFT underestimates the composition of THF in the liquid phase at low and mid pressures. Discrepancies between simulation and theory at high pressures should be due to the nonphysical behavior of the SAFT-VR EOS, as any classical formalism, close to the critical region.

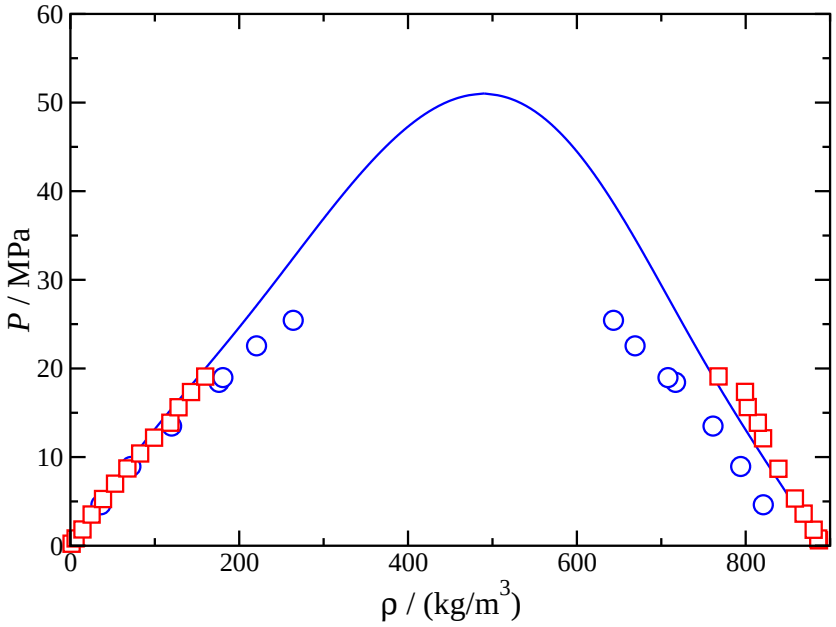

Figura 9.3: Pressure-density slices of the phase diagram of the THF $+CH_4$ binary mixture at 300.15 K. Red squares correspond to experimental data, blue circles and blue curve correspond to MD NVT simulation results and theoretical predictions obtained from the equation of state SAFT-VR [9] respectively.

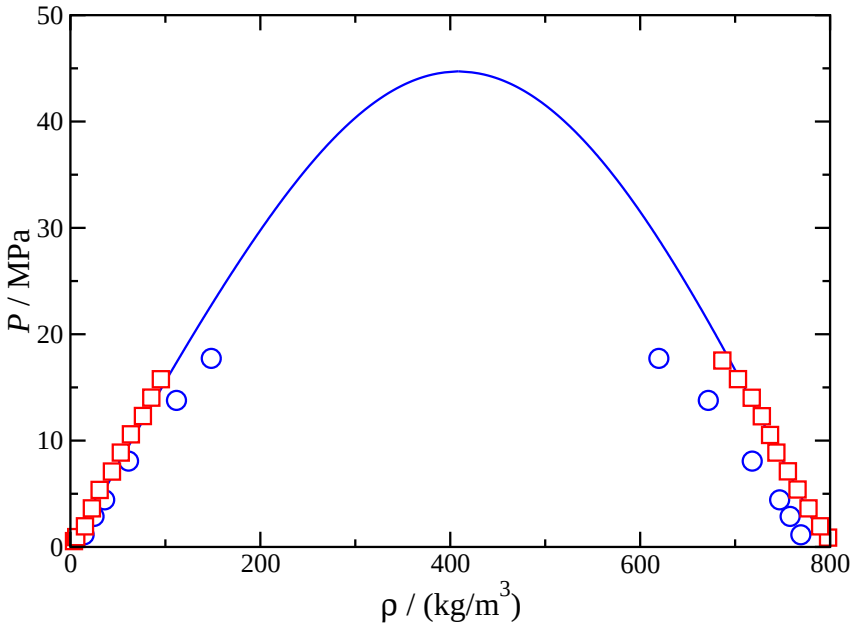

Figura 9.4: Pressure-density slices of the phase diagram of the THF $+CH_4$ binary mixture at 370.15 K. Red squares correspond to experimental data, blue circles and blue curve correspond to MD NVT simulation results and theoretical predictions obtained from the equation of state SAFT-VR [9] respectively.

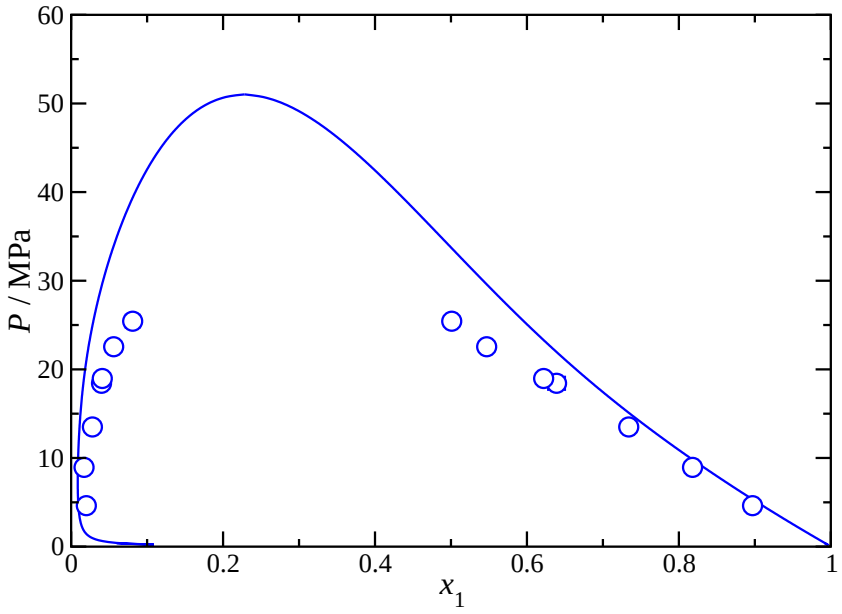

Figura 9.5: Pressure-composition slices of the phase diagram of the THF $+CH_4$ binary mixture at 300.15 K obtained from simulation (blue circles). Blue curve correspond to theoretical predictions obtained from the equation of state SAFT-VR [9].

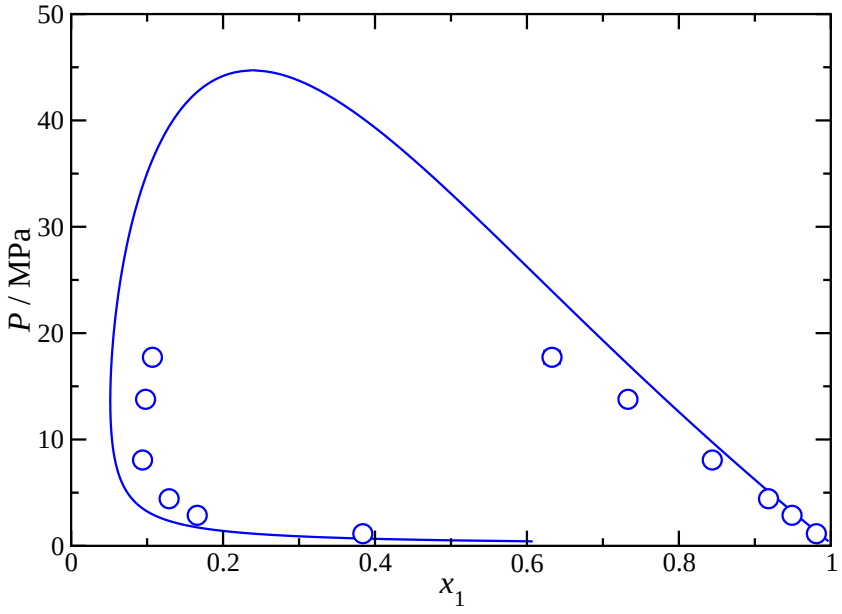

Figura 9.6: Pressure-composition slices of the phase diagram of the THF $+CH_4$ binary mixture at 370.15 K obtained from simulation (blue circles). Blue curve correspond to theoretical predictions obtained from the equation of state SAFT-VR [9].

Finally, we have determined the the vapor-liquid surface tension of the mixture from tensimetric measurements as indicated in the Experimental Section. In addition to that, we have also calculated the surface tension of the system from molecular simulation using its mechanical definition that involves the difference between the tangential and normal macroscopic components of the pressure tensor, according to the Eq. (9.5). The surface tension is probably one of the most sensitive properties to to molecular models in a system. For this reason, it can be used to check the ability of molecular models to predict a number of thermodynamic properties, including phase equilibria and interfacial properties. As can been seen in Figure 9.7, at 300.15 K, the surface tension is a monotonic decreasing function of the pressure. This is an expected behavior since the difference between the vapor and liquid densities in both phases decreases as the pressure is increased. Agreement between simulation and experimental results is excellent in the whole range of pressures considered.

We have also obtained the surface tension at 370.15 K (see Figure 9.8). Surface tension values obtained are lower than at 300.15 K. This behavior is expected since an increase of the temperature provokes lower molecular cohesion, and consequently the surface tension decreases. Agreement between experimental values and MD simulation is excellent in all cases. At higher pressures, MD simulation results seem to slightly overestimate the experimental data measured in this work. This is probably due to the proximity of the critical point.

The relative Gibbs adsorption isotherm of a species i relative to a species j (Γ_{ij}) can be expressed in terms of the concentration profiles along the interfacial region, $\rho_i(z)$, by the following integral equation [31]:

$$\Gamma_{ij} = \int_{-\infty}^{z_0^j} \left[\rho_i(z) - \rho_i^{\alpha}\right] dz + \int_{z_0^j}^{+\infty} \left[\rho_i(z) - \rho_i^{\beta}\right] dz \tag{9.6}$$

In Eq. (9.6), z_0^j denotes the location of the divide position relative to a species j, and $\rho_i^{\alpha,\beta}$ are the bulk densities in the α, β phases. $\rho_i(z)$ and $\rho_i^{\alpha,\beta}$ are obtained from MD simulations. z_0^j is calculated from Eq. (9.6), considering that species j does not have adsorption along the interfacial region (*i.e.*, Eq. (9.6) is solved for the case that $\Gamma = 0$). Mathematically:

$$z_0^j = \frac{\int_{-\infty}^{+\infty} \rho_j(z)\, dz}{\rho_j^{\alpha} - \rho_j^{\beta}} \tag{9.7}$$

The adsorption of CH_4 (component 2) in THF (component 1) can be approximately quantified by the relative Gibbs adsorption isotherm (Γ_{21}). Figures 9.9 and 9.10 depict Γ_{21} as a function of pressure at 300.15 and 370.15 K, respectively. These figures include the results from both experimental data (Eq. (9.2)) and molecular dynamics simulations (Eqs. (9.6) and (9.2)). From Figures 9.9 and 9.10, it is possible to observe that the results from Eqs. (9.6) and (9.2) differs to each other. The reason for this difference is attributed to the fact that Eq. (9.6) uses an explicit definition of the Gibbs dividing surface, whereas the evaluation of Eq. (9.2) is based on the isothermal variation of γ with P with an implicit theoretical definition of the divide position. It is important to remark that both definitions are equivalent to each other, but their values may differ due to the poor definition of the dividing plane. Physically, of course, such plane does not exist, as the interface region is a diffuse region. There is no preferred approach to calculate Γ_{ij}; however, the application of Eq. (9.6) is straightforward in MD simulations (i.e., from $\rho(z)$ profiles), whereas Eq. (9.2) is the usual route used to process experimental measurements. Indeed, Γ_{ij} is evaluated from tensiometry and densimetry measurements.

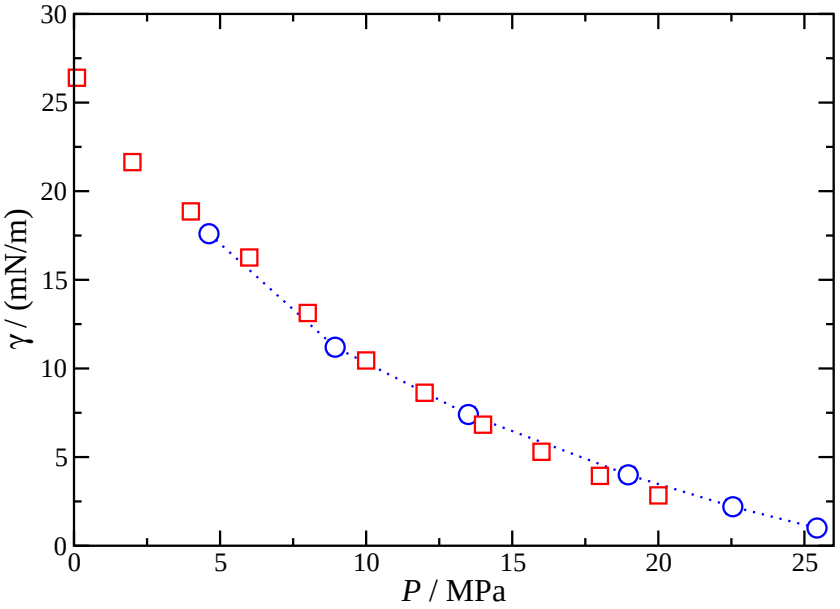

Figura 9.7: Surface tension of the THF + CH_4 binary system at 300.15 K as a function of pressure. Red square correspond to experimental data and blue circles correspond to predictions obtained from MD NVT simulations. The dotted curve is included as a guide to the eye.

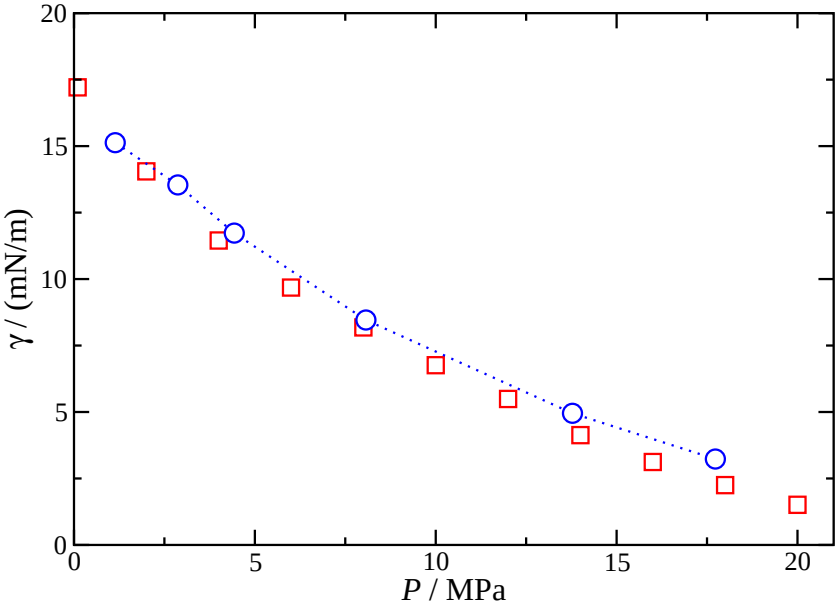

Figura 9.8: Surface tension of the THF + CH_4 binary system at 370.15 K as a function of pressure. Red square correspond to experimental data and blue circles correspond to predictions obtained from MD NVT simulations. The dotted curve is included as a guide to the eye.

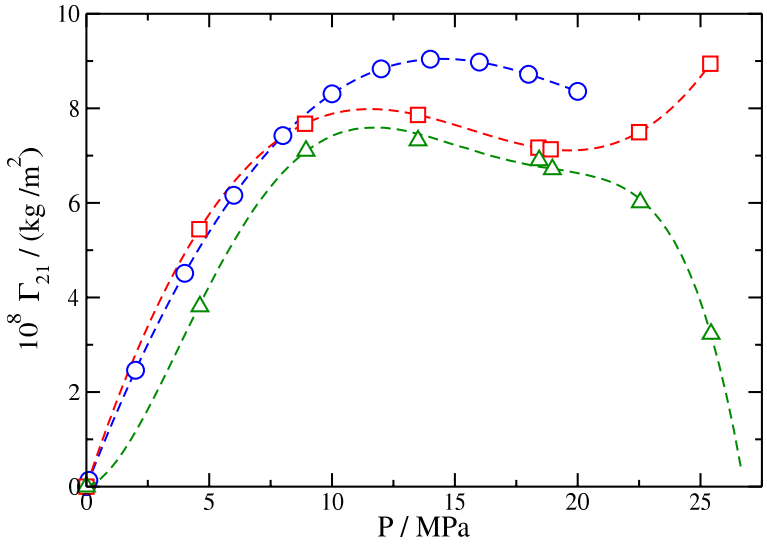

Figura 9.9: Relative Gibbs adsorption isotherm for THF + CH_4 mixture at 300.15 K as a function of pressure calculated from: Eq. (9.2) and experimental data of surface tension (blue circles); Eq. (9.2) and MD results of surface tension (red squares); and Eq. (9.6) and MD results of concentration profiles (green triangles). The dashed curves are included as guides to the eye.

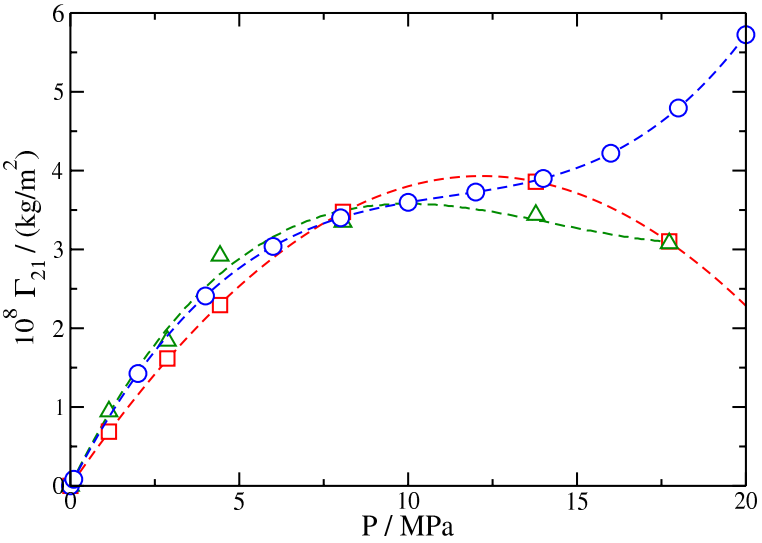

Figura 9.10: Relative Gibbs adsorption isotherm (Γ_{21}) for THF + CH_4 mixture at 370.15 K as a function of pressure calculated from: Eq. (9.2) and experimental data of surface tension (blue circles); Eq. (9.2) and MD results of surface tension (red squares); and Eq. (9.6) and MD results of concentration profiles (green triangles). The dashed curves are included as guides to the eye.

Focused on the results at 300.15 K (Figure 9.9), it is possible to observe that although Γ_{21} increases as the pressure increases, Γ_{21} reaches a maximum value. The maximum in Γ_{21} reflects an adsorption saturation limit, which occurs at approximately 14.44 MPa (from experimental results) and 11.35 MPa (from molecular dynamics simulations). Passed this maximum, Γ_{21} decreases as the pressure decreases. This behavior of Γ_{21} is also observed on CO_2 + n-alkanes, such as n-decane to n-eicosane (see Mejía *et al.* [42] and Cumicheo *et al.* [43]).

Figure 9.10 depicts the Γ_{21} as a function of P at 370.15 K. In this case, the results from experimental γ (see Eq. (9.2)) describe that Γ_{21} increases as the pressure increases without reaches a maximum value, and also Γ_{21} generates an inflection which can probably be attributed to the supersaturation of CH_4 on the interfacial zone. This behavior has also been observed in the THF + CO_2 binary mixture. [8] However, MD results from Eqs. (9.6) and (9.2) show a similar behavior than Γ_{21} at 300.15 K (*i.e.*, Γ_{21} increases as the pressure increases) then Γ_{21} reaches a maximum. Passed this maximum, Γ_{21} decreases as the pressure decreases, with a very good agreement each other. One possible reason for the difference between experimental and MD results can be attributed to the slop $(\partial\gamma/\partial P)_T$ at high pressure.

Comparing the Γ_{21} results at 300.15 K (Figure 9.9), and 370.15 K (Figure 9.10), it is possible to conclude that the adsorption of CH_4 in THF decreases with the increment of the isothermal condition.

9.5 Conclusion

We have determined the vapor-liquid phase equilibria and interfacial properties of the THF + CH_4 binary mixture at high pressures and temperatures of 300.15 and 370.15 K from experiments and computer simulation. In particular, experimental measurements have been performed using a densimeter and a pendant drop tensiometer for mass density and surface tension measurements, respectively. Simulation predictions are obtained using MD NVT simulations of the inhomogeneous system using the direct coexistence simulation technique and surface tension is evaluated from the normal and tangential components of the pressure tensor using the virial route. THF is described using an approximated rigid and planar model proposed by us in a previous work.

Density profiles of THF exhibit the standard monotonic behavior when passing from the liquid to the vapor side of the interface. However, methane is adsorbed at the interfacial region, showing surface activity (accumulation) as the pressure is increased. This is an expected behavior for binary mixtures formed by components with significant differences in the values of the vapor pressure and/or asymmetry in size or unlike dispersive energies.

The vapor-liquid phase envelopes of the mixture, including the pressure-density and pressure-composition slices, have been determined from experiments (in the case of the pressure-density diagram) and computer simulation. Both results are compared including theoretical predictions from the SAFT-VR approach at all thermodynamics conditions studied. Theory and simulation are able to provide a reasonable description of the phase envelopes at 300.15 and 370.15 K. We have also compared new experimental measurements carried out in this work with computer simulation results for the vapor-liquid surface tension of the mixture. Simulation predictions are able to quantitatively predict the behavior of the surface tension, as a function of pressure, at the two temperatures considered.

We have also studied explicitly the surface activity of methane at the interface. In particular, CH_4 is always adsorbed along the interfacial zone, showing a surface activity that increases with pressure.

The activity (adsorption) is also verified from the relative Gibbs adsorption isotherm. According to the results, the relative Gibbs adsorption increases with pressure and at fixed pressure, the adsorption decreases as the temperature increases.

We have demonstrated that the planar and rigid THF model is able to describe accurately the vapor-liquid surface tension of the mixture. Similar results were obtained in our previous work for describing pure THF and the THF + CO_2 system in the whole range of coexistence region studied. These results confirmed that the model is a good choice to predicting phase equilibria and interfacial properties of mixtures involving THF.

9.6 Acknowledgement

The authors thank discussions with Ángel Gijón. We also acknowledge Centro de Supercomputación de Galicia (CESGA, Santiago de Compostela, Spain) and MCIA (Mésocentre de Calcul Intensif Aquitain) of the Universités de Bordeaux and Pau et Pays de l'Adour (France), for providing access to computing facilities and Ministerio de Economía, Industria y Competitividad through Grant with reference FIS2017-89361-C3-1-P co-finanded by EU FEDER funds. Further financial support from Junta de Andalucía and Universidad de Huelva is also acknowledged. J.A.F. acknowledges Contrato Predoctoral de Investigación from XIX Plan Propio de Investigación de la Universidad de Huelva and a FPU Grant (Ref. FPU15/03754) from Ministerio de Educación, Cultura y Deporte. J. A., J. M. M., and F. J. B. thankfully acknowledge the computer resources at Magerit and the technical support provided by the Spanish Supercomputing Network (RES) (Project QCM-2018-2-0042) .A.M. and M.C. also acknowledges the finnancial support of FONDECYT, Chile (Project 1190107).

Bibliography

[1] T. Uchida, M. Wakakura, A. Miyake, and T. Ogawa *J. Therm. Anal. Colorim.*, vol. 93, pp. 47–52, 2008.

[2] S.-P. Kang, H. Lee, C.-S. Lee, and W.-M. Sung *Fluid Phase Equil.*, vol. 185, pp. 101–109, 2001.

[3] A. Delahaye, L. Fournaison, S. Marinhas, and I. Chatti *Ind. Eng. Chem. Res.*, vol. 45, pp. 391–397, 2006.

[4] R. Anderson, A. Chapoy, and B. Tohidi *Langmuir*, vol. 23, pp. 3440–3444, 2007.

[5] Y.-J. Lee, T. Kawamura, Y. Yamamoto, and J.-H. Yoon *J. Chem. Eng. Data*, vol. 57, pp. 3543–3548, 2012.

[6] E. D. Sloan and C. Koh, *Clathrate Hydrates of Natural Gases.* New York: CRC PRess, 3 ed., 2008.

[7] S. Sarupria and P. G. Debenedetti *J. Phys. Chem. A*, vol. 115, pp. 6102–6111, 2011.

[8] J. Algaba, J. M. Garrido, J. M. Míguez, A. Mejía, A. I. M.-V. Bravo, and F. J. Blas *J. Phys. Chem. C*, vol. 122, pp. 16142–16153, 2018.

[9] J. M. Míguez, M. M. Conde, J.-P. Torré, F. J. Blas, M. M. Piñeiro, and C. Vega *J. Chem. Phys.*, vol. 142, p. 124505, 2015.

[10] R. L. Scott and P. H. V. Konynenburg *Discuss. Faraday Soc.*, vol. 49, pp. 87–97, 1970.

[11] P. H. V. Konynenburg and R. L. Scott *Phil. Trans.*, vol. A298, pp. 495–540, 1980.

[12] J. M. Garrido, J. Algaba, J. M. Míguez, B. Mendiboure, A. I. Moreno-Ventas Bravo, M. M. Piñeiro, and F. J. Blas *J. Chem. Phys.*, vol. 144, pp. 144702/1–11, 2016.

[13] S. J. Keasler, S. M. Charan, C. D. Wick, I. G. Economou, and J. I. Siepmann *J. Phys. Chem. B*, vol. 116, pp. 11234–11246, 2012.

[14] M. H. E.W. Lemmon and M. McLinden, "Nist chemistry webbook, nist standard reference database 23: Reference fluid thermodynamic and transport properties-refprop, version 9.1; 2013."

[15] M. J. B. Evans, *Measurement of Surface and Interfacial Tension, in Measurement of the Thermodynamic Properties of Multiple Phases*, vol. VII. Elsevier, 2006.

[16] J. Andreas, E. Hauser, and W. Tucker *J. Phys. Chem.*, vol. 42, no. 8, pp. 1001–1019, 1938.

[17] W. Masterton, J. Bianchi, and E. Slowinski Jr *J. Phys. Chem.*, vol. 67, no. 3, pp. 615–618, 1963.

[18] F. K. Hansen. Ramé-Hart Instrument Co., USA, advanced edition ed., 2005.

[19] B. N. Taylor and C. E. Kuyatt 1994.

[20] A. I. Rusanov and V. A. Prokhorov, *Interfacial Tensiometry*. Elsevier, Amsterdam, 1996.

[21] D. S. A. Jr and T. Fort in *Surface and Colloid Science* (R. Good and R. Stromberg, eds.), vol. 11, New York: Plenum Press, 1979.

[22] S. J. Goodbody, K. Watanabe, D. MacGowan, J. P. Walton, and N. Quirke *J. Chem. Soc.*, vol. 87, no. 13, pp. 1951–1958, 1991.

[23] D. Frenkel and B. Smit, *Understanding Molecular Simulations*. 2nd Ed. Academic, San Diego, 2002.

[24] M. P. Allen and D. J. Tildesley, *Computer Simulation of Liquids*. Claredon, Oxford, 1987.

[25] J. M. Míguez, M. M. Piñeiro, J. Algaba, B. Mendiboure, J. P. Torré, and F. J. Blas *J. Phys. Chem. B*, vol. 119, pp. 14288–14302, 2015.

[26] D. van der Spoel, E. Lindahl, B. Hess, G. Groenhof, A. E. Mark, and H. J. Berendsen *J. Comput. Chem.*, vol. 26, no. 16, pp. 1701–1718, 2005.

[27] M. A. Cuendet and W. F. V. Gunsteren *J. Chem. Phys.*, vol. 127, pp. 184102/1–9, 2007.

[28] S. Nosé *Mol. Phys.*, vol. 52, pp. 255–268, 1984.

[29] H. J. C. Berendsen, J. P. M. Postma, W. F. V. Gunsteren, A. D. Nola, and J. R. Haak *J. Chem. Phys.*, vol. 81, pp. 3684/1–8, 1984.

[30] H. Hulshof *Ann. Phys. (Berlin)*, vol. 4, pp. 165–186, 1901.

[31] J. S. Rowlinson and B. Widom, *Molecular Theory of Capillarity*. Claredon Press, 1982.

[32] E. D. Miguel, F. J. Blas, and E. M. D. Río *Mol. Phys.*, vol. 104, pp. 2919–2927, 2006.

[33] E. D. Miguel and G. Jackson *J. Chem. Phys.*, vol. 125, pp. 164109/1–12, 2006.

[34] F. J. Martínez-Ruiz and F. J. Blas *Mol. Phys.*, vol. 113, no. 9-10, pp. 1217–1227, 2015.

[35] F. J. Martínez-Ruiz, A. I. Moreno-Ventas Bravo, and F. J. Blas *J. Chem. Phys.*, vol. 143, p. 104706, 2015.

[36] J. M. Garrido, M. Cartes, A. Mejía, J. Algaba, J. M. Míguez, F. J. Blas, A. I. Moreno-Ventas Bravo, and M. M. Piñeiro *J. Supercrit. Fluids*, vol. 128, pp. 359–369, 2017.

[37] J. M. Garrido, M. Cartes, and A. Mejía *J. Supercrit. Fluids*, vol. 129, pp. 83–90, 2017.

[38] J. M. Garrido, M. M. Piñeiro, A. Mejía, and F. J. Blas *Phys. Chem. Chem. Phys.*, vol. 18, pp. 1114–1124, 2016.

[39] A. Mejía, M. Cartes, H. Segura, and E. A. Müller *J. Chem. Eng. Data*, vol. 59, pp. 2928–2941, 2014.

[40] J. M. Garrido, L. Cifuentes, M. Cartes, H. Segura, and A. Mejía *J. Supercrit. Fluids*, vol. 89, pp. 78–88, 2014.

[41] E. A. Müller and A. Mejía *Fluid Phase Equil.*, vol. 282, pp. 68–81, 2014.

[42] A. Mejía, M. Cartes, H. Segura, and E. A. Müller *J. Chem. Eng. Data*, vol. 50, no. 10, pp. 2928–2941, 2014.

[43] C. Cumicheo, M. Cartes, E. A. Müller, and A. Mejía *Fluid Phase Equilib.*, vol. 380, pp. 82–92, 2014.

Capítulo 10

Interfacial properties of 1-alkanol (1-butanol to 1-heptanol)+water binary mixtures by Molecular Dynamics Simulation

Abstract

The liquid-liquid equilibrium and interfacial properties of aqueous solutions of alcohols is of great interest in fundamental and applied research. In this work, we used molecular simulations and the direct coexistence technique to comprehensively study interfacial properties of 1-$C_nH_{2n}OH$ + H_2O binary mixtures, with $n = 4 - 7$, as well as to provide insights into the underlying microscopic behaviour. For the considered thermodynamic conditions, atmospheric pressure and temperatures ranged from 280 to 380 K, our simulations predict the coexistence of two phases: An aqueous phase and an organic phase. The considerable difference between the equilibrium coexistenting densities denotes highly immiscible phases. The temperature is found to hardly affect the aqueous phase and to slightly favor miscibility in the organic phase. The increase of the alkyl chain leads to a lower miscibility of the mixture components and to a consequent higher consistency with experimental data, since we approach to thermodynamic equilibrium of two single-component phases. The density profiles show two peaks between the interface and the equilibrated density in the organic phase related to a preferred orientational order of the alcohol molecules at the interface. The interfacial tension is a challenging property to quantify for inhomogeneous systems. Although our obtained data is non-negligibly overestimated, we reproduce for these systems the parabolic dependence of this property with temperature, which is related to the maximum tie line in the liquid-liquid equilibria. As well, we predict and rationalize the increase of interfacial tension with increasing the chain length of the alcohols. Overall, the satisfactory agreement of our results with available experimental data points to the reliability of the methods for further predictions.

10.1 Introduction

Interfacial properties of liquid-liquid equilibria (LLE) are essential in numerous chemical processes in the petroleum industry and environmental engineering. The presence of coexisting phases gives rise to inhomogeneities, increasing the richness of the structure and phase behavior, with an additional surface tension contribution to the thermodynamics of the system associated with the corresponding interfaces. Overall, surface tension is a challenging property to be measured in inhomogeneous systems, and the interpretation of experimental data is subject to the underlying physical models. There have been significant efforts in developing molecular-based theories of Statistical Mechanics to describe the behavior of coexisting phases. Among them, Density Functional Theory (DFT) [1–6] is likely the most powerful approach. In recent years, with the ever-increasing computational power, molecular simulation techniques [7, 8] have emerged as alternative route, providing likewise fundamental understanding of the underlying microscopic behavior. However, molecular simulation for liquid-liquid systems are time consuming due to the diffusional processes. This issue implies that simulations of L-L systems need to run for longer than L-V simulations to appropriately explore the accessible microscopic states. As a consequence, research concerning the characterization of interfacial properties of liquid-liquid systems is very limited compared to the extensive work on liquid-vapor systems [9–12]

Some particular cases of LLE in the environment engineering field are those involving contaminates removal from water, like hydrocarbons or alkanols produced in the petroleum industry. Liquid alkanols, as also occurs for the hydrocarbons, have very low solubility in water and they float in water because of their lower densities. Consequently, the alkanols transport or mobility are controlled by the interfacial properties of the system, among others. Besides, these aqueous solutions are of great fundamental interest. In this context, obtaining an accurate description of the LLE and interfacial behavior is a crucial step toward a better understanding of the process. Computer simulations [13–15]and experiments [16] of alkane-water interfaces for different length alkanes has been addressed, contributing in understanding liquid-liquid interfaces and interactions of alkyl chains with water. Here, we go one step further and report for the first time computational data of LLE of aqueous solutions of primary alkanols, for chain lengths from 4 to 7 carbon atoms and at various thermodynamic conditions. As it is well-known, water is a highly structured liquid with a local tetrahedral structure, and alcohol molecules contain two distinct parts: the alkyl group, which is hydrophobic, and the hydroxide group, which is hydrophilic and is able to form hydrogen bonds. The self- and cross- association of these polar molecules in the binary mixture lead to complex networks with significant impact on physical and chemical properties, especially phase equilibrium behavior and hence interfacial properties [17–19].

We conducted Molecular Dynamics simulations of the 1-alkanol+water binary mixtures from 1-butanol to 1-heptanol at atmospheric pressure and temperatures ranged between 280 and 380 K. We used the direct coexistence method [20, 21], which allowed us to obtain an explicit interface in the mixture, providing simultaneously coexistent densities and interfacial tension. Details of this methodology can be found in section 2 and elsewhere [7, 8]. Microscopic properties, namely the density profiles across the interface and the molecular ordering near and within the interface, were assessed and related to the above-mentioned macroscopic properties.

The remainder of this article is arranged as follows. The molecular models for water and 1-alkanols, the interaction potentials, and the details of the simulations are outlined in the next section. Thereafter, we present simulation results and discussions in section 3. Finally, main results are summarized in section 4.

10.2 Molecular Simulation Details

To describe the systems under study, we used models and force fields available in the literature. The 1-alkanols were represented by united-atom flexible models with CH_n group as a single-interaction site with potential parameters from the TraPPE force field [22]. Bond lenghts are fixed and intramolecular interactions include bond-bending and torsion potentials. The bond bending between three neighboring beads is modeled by a harmonic potential, and changes in the torsional angle are controlled by TraPPE cosine series potential. The beads in a chain separated by more than three bonds interact with each other through a Lennard-Jones potential. Concerning water, we have selected the TIP4P-2005 model [23], which has been shown to provide accurate estimates of water bulk properties, if compared with other similar versions, but also is remarkably proficient in the estimation of interfacial properties [10, 24]. It is a non-polarizable model that considers four interacting sites placed on the three atom positions and an additional site placed in the bisector of the angle formed by the molecule bonds. The characteristic parameters of both UA-TraPPE and TIP4P/2005 can be found in the original papers [22, 23].

The non-bonded energy potential consists of Lennard-Jones (L-J) and electrostatic interactions, which were truncated at 2 nm. The minimum length of the axes of the simulation box is larger than twice this cutoff distance. Periodic boundary conditions were exerted in the three dimensions. Long-range electrostatic interactions were evaluated using Ewald summation [7, 8, 25], with a relative precision of 10^6. To account for the interactions between 1-alkanols and water molecules, we consider cross-interacting parameters obtained from Lorentz-Berthelot mixing rules.

Using the above-described models and force fields, we conducted Molecular Dynamics simulations to analyze the coexisting and interfacial properties for the 1-alkanol+water binary mixtures using GROMACS software package (version 4.6.1) [26]. To simulate the equilibrium and interface between these hardly miscible compounds, we used the direct coexistence technique [20, 21], which we describe as follows. The first step entails the construction of a single inhomogeneous biphasic simulation box from the equilibration of two independent simulation boxes: A water-rich box and an 1-alkanol-rich box. Both boxes were equilibrated in the NP_zT ensemble at the estimated coexistence conditions. This step should be carefully performed since is crucial for a proper evolution of the system. If the initial values of the involved variables were far from the coexisting conditions predicted by the molecular models, the boxes would not develop a stabilized interface after they have been put into contact. It is chosen in the way that *i)* it fulfils at each temperature the experimental density and composition of each liquid phase [27], and *ii)* a good compromise between accurately enough predicting the LLE and the computational costs. They are detailed in Table 10.1. The simulations were arranged in cycles of N moves including translation moves, rotation moves, with the same probability. The acceptance ratio was set to 0.33. The box dimensions were adjusted to facilitate the subsequent assembly of a biphasic box.

Once both boxes were equilibrated, we assemble in the $z-$direction a slab of the rich-water phase in the middle (in order to optimize CPU time since it is the denser phase) and two replicas of the organic phase at both ends, by simply displacing the appropriate value of the z coordinate for both organic boxes. The setup yields an inhomogeneous simulation box containing two explicit interfaces between both liquid phases. For the sake of clarity, it is illustrated in Figure 10.1 for the specific mixture of 1-butanol+water. In order to avoid molecular overlapping and assure an adequate formation of the interface, the liquid phases are located slightly separated from each other in the assembly. From the initial configuration, the biphasic simulation box is allowed to evolve by conducting MD

Tabla 10.1: Density values of 1-alkanol (ρ_{COH}) and water (ρ_{H2O}) for aqueous (water-rich) and organic (alkanol-rich) phases at a at atmospheric pressure and at temperatures 280, 300, 320, 340, 360 and 380 K. The values of interfacial tension (γ) at the same conditions of pressure and temperature are exposed in the last two columns. The results obtained by molecular simulation are compared with experimental results take from literature.The errors are estimated as explained in the text.

T/K	ρ_{H2O} (kg/m^3)	ρ^{exp}_{H2O} (kg/m^3)	ρ_{COH} (kg/m^3)	ρ^{exp}_{COH} (kg/m^3)	ρ_{H2O} (kg/m^3)	ρ^{exp}_{H2O} (kg/m^3)	ρ_{COH} (kg/m^3)	ρ^{exp}_{COH} (kg/m^3)	γ (mN/m)	γ^{exp} (mN/m)
			aqueous phase				organic phase			
280	948(4)	889	46.2(2.1)	99	141(3)	168	707(3)	690	3.0(4)	1.49
300	952.3(2.3)	917	39.0(1.6)	69	133(4)	156	691(3)	688	3.1(5)	1.68
320	951(3)	883	33.3(2.2)	71	143(3)	162	660.2(2.3)	669	3.3(4)	1.63
340	936.1(1.4)	909	36.1(0.9)	60	152(3)	182	646(3)	639	3.6(4)	1.39
360	925.8(2.4)	883	35.8(2.0)	71	145(3)	216	630(3)	594	3.1(3)	1.04
380	906.0(1.9)		37.0(1.4)		165(4)		596.0(1.2)		2.60(23)	
280	978.0(1.1)	967	18.2(1.0)	29.1	75(4)	81.7	754(3)	761	6.2(8)	3.96
300	983.0(1.3)	972	12.6(1.1)	21.4	75(4)	81.8	738(3)	747	5.8(4)	4.35
320	981.0(1.0)	969	9.7(8)	18.3	80(3)	87.0	722(4)	728	6.6(3)	4.51
340	971.1(5)	959	9.0(5)	17.7	85.0(2)	96.6	697(3)	705	6.2(3)	4.37
360	958.0(1.2)	947	10.6(8)	19.2	97(3)	110	668(3)	677	6.11(20)	3.94
380	939.7(8)		10.3(7)		99.1(1.7)		645(3)		6.20(21)	
280	992.3(9)	992	5.8(6)	7.57	54(2)	55	775(5)	786	7.8(9)	5.77
300	994.1(1.3)	990	3.0(5)	5.92	56(2)	58	757(3)	769	7.5(7)	6.29
320	990.0(8)	984	2.9(5)	5.41	57(2)	63	743(4)	757	9.1(4)	6.18
340	982.0(8)	974	2.1(3)	5.63	62(2)	68	721.0(2.2)	737	9.6(3)	6.14
360	970.7(6)		2.8(3)		66(3)		704(4)		8.5(4)	
380	954.5(1.1)		4.7(6)		73.0(1.7)		670(2)		8.0(3)	
280	995.2(1.1)	998	2.8(5)	1.97	42.3(2.1)	37.5	788(3)	804	10.3(8)	6.61
300	996.9(1.5)	995	1.3(3)	1.72	40.4(2.2)	41.0	773(3)	787	10.1(8)	7.40
320	992.5(5)	988	1.26(14)	1.70	38.0(2.0)	45.4	759(3)	768	11.8(8)	7.73
340	984.3(8)	978	1.4(3)	1.86	47(3)	50.6	735(3)	748	10.4(6)	7.90
360	974.9(7)	967	1.2(3)	2.22	47.0(2.0)	56.6	714(3)	725	10.1(6)	7.74
380	961.0(6)		1.44(17)		65.3(2.5)		682(4)		9.9(5)	

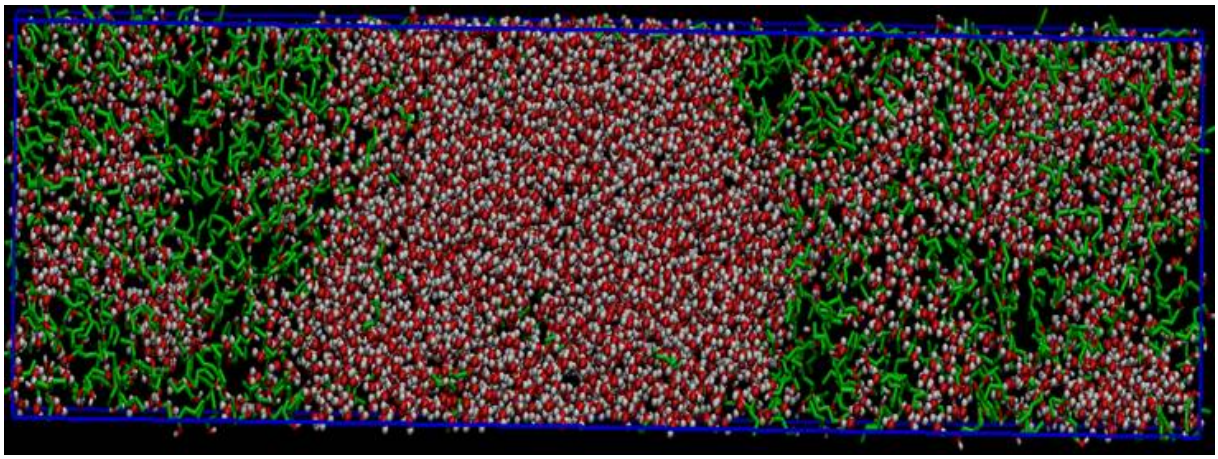

Figura 10.1: Projection $z - x$ of the initial biphasic simulation box. This initial configuration is composed by 3600 H_2O (O-red and H-white) molecules and 1400 1-butanol (CH_3-green, CH_2-green, O-red and H-white) molecules.

molecular simulations in the $NPzT$ ensemble [7, 8]. Volume variations of the simulation box were hence performed by variations in the L_z distance. The L_x and L_y dimensions were kept constant at 40 A. The simulations were arranged in cycles of N moves including translation moves, rotation moves, and volume changes (by varying L_z). The probability of a volume change was set at $1/N$, and that for molecular translation and rotation moves at $(N-1)/(2N)$. The acceptance ratio was set to 0.33. For each binary mixture, we explore at 1 bar the isotherms of 280, 300, 320, 340, 360 and 380 K. Temperature and pressure were kept constant using Nosé-Hoover thermostat [28, 29] and Parrinello-Rahman barostat [30, 31] with a relaxation time of 2 ps. The time step was set to 1 fs, and runs of 10^7 time steps (10 ns) were used for equilibrating the system and of $5\Delta 10^7$ steps (50 ns) to sample the data.

10.3 Results and discussion

This simulation technique has the advantage of providing direct access to the structure of the interface, allowing the simultaneous determination of coexistence densities, interfacial properties, and microscopic structural properties, as the case of density profiles, across the interface. These properties were obtained through the usual block averaging method [32]. In particular, we divided the production stage into 10 data blocks of 5 ns. The error bars indicate the standard deviation over the blocks.

The simulation box was divided in $n = 100$ identical slabs parallel to xy plane of width $\Delta z = L_z/n$, and the density in each of them was computed as the ratio between the number of molecules in the slab $N(z)$ and its volume $V_s = L_x L_y \Delta_z$. The coexisting densities are obtained by averaging this quantity over the slabs belonging to each liquid phase and far enough from the interface, to assure stable and reliable values. The equilibrium density profiles across the interfaces vary along the z coordinate $\rho{=}\rho(z)$ and were computed from averages of the density histogram along this direction over the production stage.

For each binary mixture, we also analyzed the composition of both phases in terms of the 1-alkanols molar fractions (denoted with subscript 1), which were computed from the coexisting densities according to following expressions:

$$X_1^O = \frac{\rho_{COH}^O}{\rho_{COH}^O + \rho H_2O^O} \tag{10.1}$$

$$X_1^W = \frac{\rho_{COH}^W}{\rho_{COH}^W + \rho H_2O^W} \tag{10.2}$$

where superscripts O and W refer the organic and aqueous phase, respectively.

The interfacial tension, γ, is the surface free energy associated with creating new surface area (the interface). To determine this property, we used the mechanical virial route [33–36], which consists on the evaluation of the microscopic components of the pressure tensor in the inhomogeneous system from the virial. Since the simulated liquid-liquid interfaces are planar and perpendicular to z direction, only two components of the pressure tensor are needed: Tangential and normal components relative to the interface, $P_T(z) = P_{xx}(z) = P_{yy}(z)$ and $P_N(z) = P_{zz}(z)$.

Figure 10.2 shows the molecular density profiles along the interface-normal z axis of the coexisting liquid phases for 1-butanol+water and 1-pentanol+water binary mixtures at the various considered

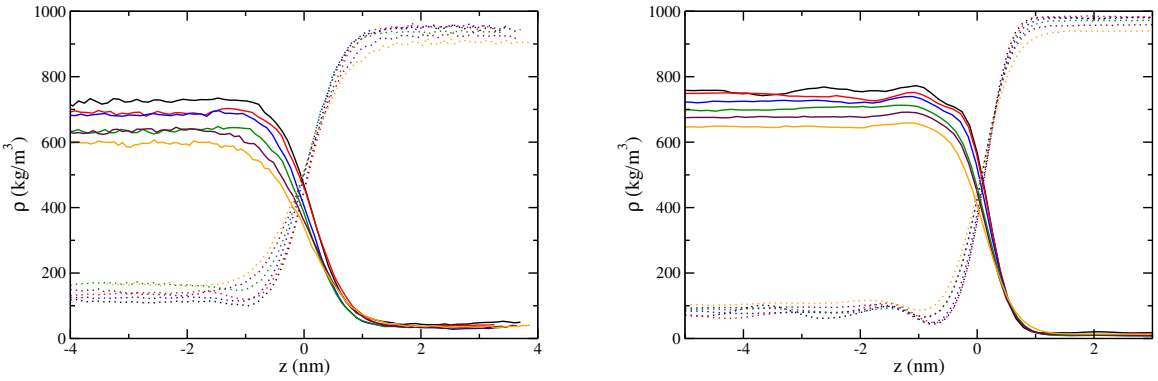

Figura 10.2: Simulated density profiles $\rho(z)$ of 1-butanol+water (a) and 1-pentanol+water (b) binary mixtures at 280 K(black), 300 K (red), 320 K (blue), 340 K (green), 360 K (violet) and 380 K (orange). Continuous and dashed lines refer results for 1-alkanol and water, respectively

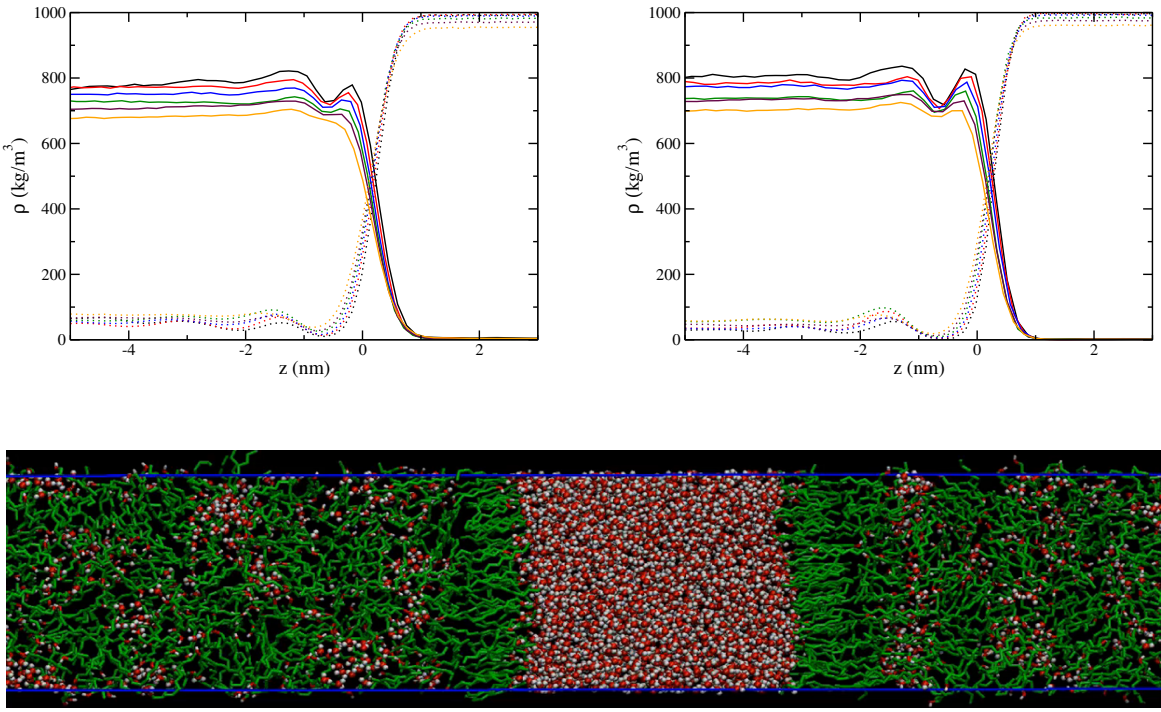

Figura 10.3: Simulated density profiles $\rho(z)$ of 1-hexanol+water (a) and 1-heptanol+water (b) binary mixtures at 280 K (black), 300 K (red), 320 K (blue), 340 K (green), 360 K (violet) and 380 K (orange). Continuous and dashed lines refer results for 1-alkanol and water, respectively. The snapshot shows the preferred orientational order of the alkanol molecules at the interface, mainly pointing its polar heads (OH groups) into the aqueous phase.

temperatures. Although the simulated systems correspond to alcohol+water+alcohol, as commented in *Molecular Simulation Details* section, density profiles are depicted for only one of the interfaces for the sake of clarity. The presence of two distinct liquid phases, namely water-rich (on the left) and organic-rich (right) phases, is clearly apparent for all the temperatures. They are separated by a 2 nm interfacial region, approximately, which slightly increases with temperature. Results are in good agreement with experimental data taken from Cardenas et al. [27]. The density profiles for these both mixtures are found almost the same. Only note the relatively lower presence of the minor component (or higher presence of the major component) in each phase for the mixture involving 1-pentanol. This evidences a lower miscibility at the same thermodynamic conditions, which is a consequence of stronger hydrophobic interactions as the alkyl chain increases. The density profiles for 1-hexanol+water and 1-heptanol+water systems are depicted in Figure 10.3. Unlike for 1-butanol and 1-pentanol, they show evident anomalies near the interface. There exist two clear peaks between the interface and the equilibrated density in the organic phase. This fact suggests a strong tendency of alkanols molecules to concentrate at the interface. As it is apparent from the snapshot (Figure 10.1), there is a preferred orientational order of the alkanol molecules at the interface pointing its polar heads (OH groups) into the aqueous phase, leading to the formation of layers. As it can be observed, the hydrophobic alkyl chain being rejected from the water-rich phase of the system results in an alkanol molecular orientation nearly paralled to z axis, ie, perpendicular to the interface. Far enough from the interface, a stable value of density is found since interaction with water molecules is almost negligible. Finally, it is worth noting that the interfacial thickness is observed to slightly decrease with increasing the alkyl chain of the alkanol.

To gain insigths into comments above, we analyze the molecular orientations of the alakanol molecules with respect to the interface. To this end, we computed for each slab Δz the average (minimun) angle formed by the line connecting the end carbon atoms of the alkyl chain (directed from that bonded with the hydroxide group) and the z axis (directed perpendicularly and outwards the interface). The average values are computed over all the alkanol molecules contained in each slab each cycle, and over the simulation run. Obviously, the angle between the two defined vectors ranges between 0^o and 180^o. Results are depicted along the z axis for each considered mixture at 280 K in Figure 10.4. The average angle of about 90^o obtained enoughly far from the interface means a totally random orientation of the alcohol molecules in the bulk organic phase. Oppositely, the angle values obtained near the interface indicate a preferential orientation of the alkanol molecules in this case, in consistency with the snapshot of the molecular system. Interestingly, we found two peaks of about 40^o above and below 90^o, repectively. This fact, which becomes more remarkable as the alkyl chain increases, evidences the formation of a alkanol bilayer in the interface, with the hydroxide groups in each layer pointing to the closer phase (organic and aqueous from left to right). Finally, it is worth noting that the fluctuating angle values in the aqueous phase are reasonable due to the small amount of alkanol molecules.

Figure 10.5 provides information on the molecular configurations of the alkanol molecules. We plot along the z axis the average end-to-end distance of the alkyl chain. Analogously to Figure 10.4, the average values in each Δz are computed over all the alkanol molecules contained in the slab each cycle, and over the simulation run. Also, the depicted results correspond to each binary mixture at 280 K. On the one hand, we obtained stable values along the bulk organic phase, which obviously increase as the alkyl chain increases, from 0.4 nm for 1-butanol to 0.69 nm for 1-heptanol, approximately. On the other hand, the low statistics in the aqueous phase lead to considerable dispersion, as in Figure 10.4. What is of special relevance is the peak formed in the interface, especially for 1-heptanol, indicating a

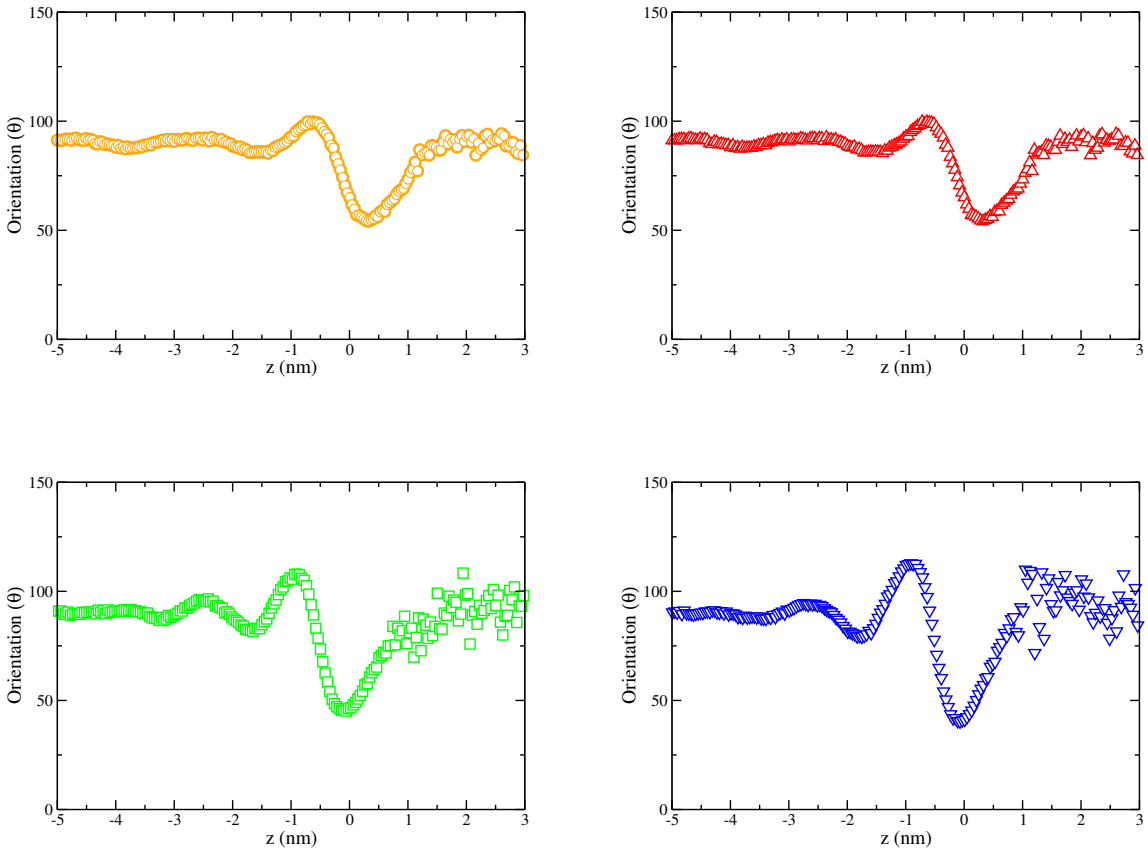

Figura 10.4: Molecular orientations of the 1-alkanol molecules with respect to the interface at 280 K for each binary mixture: Orange circles (1-butanol), red up triangles (1-pentanol), green squares (1-hexanol) and blue down triangles (1-heptanol). Average angle formed by the line connecting the end carbon atoms of the alkyl chain (directed from that bonded with the hydroxide group) and the z axis (directed perpendicularly and outwards the interface), along the z axis. The average angle values in each slab Δz are computed over all the alkanol molecules contained in the slab, and over the simulation run.

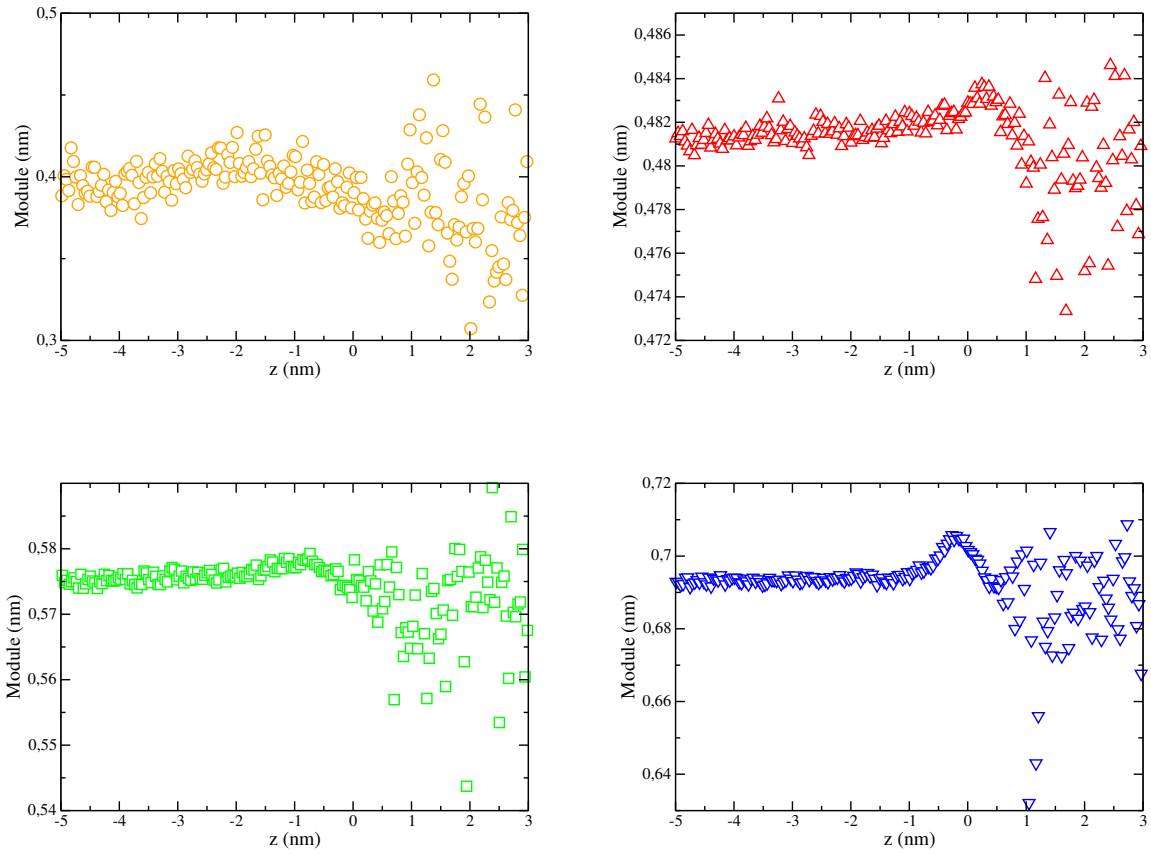

Figura 10.5: Molecular configurations of the 1-alkanol molecules at 280 K for each binary mixture: Orange circles (1-butanol), red up triangles (1-pentanol), green squares (1-hexanol) and blue down triangles (1-heptanol). Average distance between the alkyl chain ends along the z axis. The average distance values in each slab Δz are computed over all the 1-alkanol molecules contained in the slab, and over the simulation run.

more stretched configuration than in the bulk organic phase. This can be visualized in the snapshot of Figure 10.3, and is rationalized in the basis of the hydrophobic interactions of the alkyl chains with water molecules.

To address the effect of temperature, we plot in Figure 10.6 the results on both molecular orientation with respect to the interface and molecular configurations at all the considered temperatures, for the particular case of 1-heptanol+water mixture. As it can be seen, there is no qualitative changes induced by the temperature, but non-negligible quatitative differences are apparent. The commented peaks obtained for both properties in the interface, denoting preferential orientation and molecular stretching respectively, become less notable as the temperature increases. In the bulk of the organic phase, while the molecular orientation is kept random regardless of the temperature, the end-to-end distance of the alkyl chain decreases (molecular contraction) with increasing temperature.

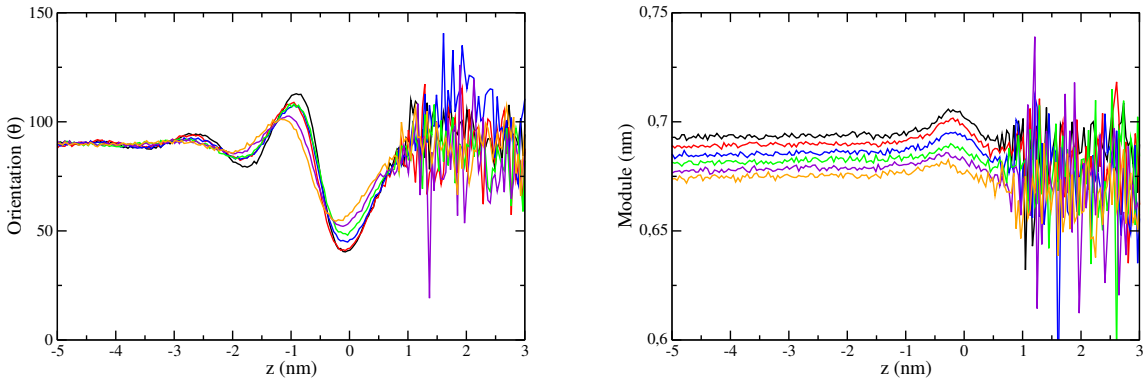

Figura 10.6: Molecular orientations with respect to the interface (a) and molecular configurations (b) of the alkanol molecules along the z axis for specific 1-heptanol+water binary mixture at the various considered temperatures: 280 K (black), 300 K (red), 320 K (blue), 340 K (green), 360 K (violet) and 380 K (orange).

The coexisting mass densities of the 1-alkanol and water are displayed in Figures 10.7 and 10.8, respectively, in both organic and aqueous phases for all the targeted mixtures. We plot the simulated results at the various temperatures together with the experimental values [27] for comparison. Densities of 1-butanol and water are about 100 kg/m^3 and 950 kg/m3, respectively, in the aqueous phase, and 700 kg/m^3 and 150 kg/m^3 in the organic phase. The considerable difference between the equilibrium coexisting densities denotes highly immiscible phases. Overall, there is a good agreement between computational and experimental data, especially for the organic phase. For the aqueous phase, we slightly underestimated (overestimated) the density of the alkanol (water). As the alkyl chain increases, the density values of both phases evidence lower miscibility of the mixture components. Indeed, for the largest alcohols, the coexisting densities show that water-rich phase is basically single-component, and these density values are the highest consistent with experimental data. These more accurate predictions result since we approach to thermodynamic equilibrium of two single-component phases, where cross interactions are roughly negligible. The effect of temperature on the coexisting densities is found slight regardless of the mixture. It basically affects the organic phase; in particular, an increase of temperature leads to a decrease of the density of the major component (alkanol), and to a consequent increase of the density of the minor component (water), favouring hence the miscibility. This is likely due to the enhancement of molecular thermal agitation, which induces a volume increase. The fact that low temperatures hinder the miscibility of the components explains that our simulated data at these

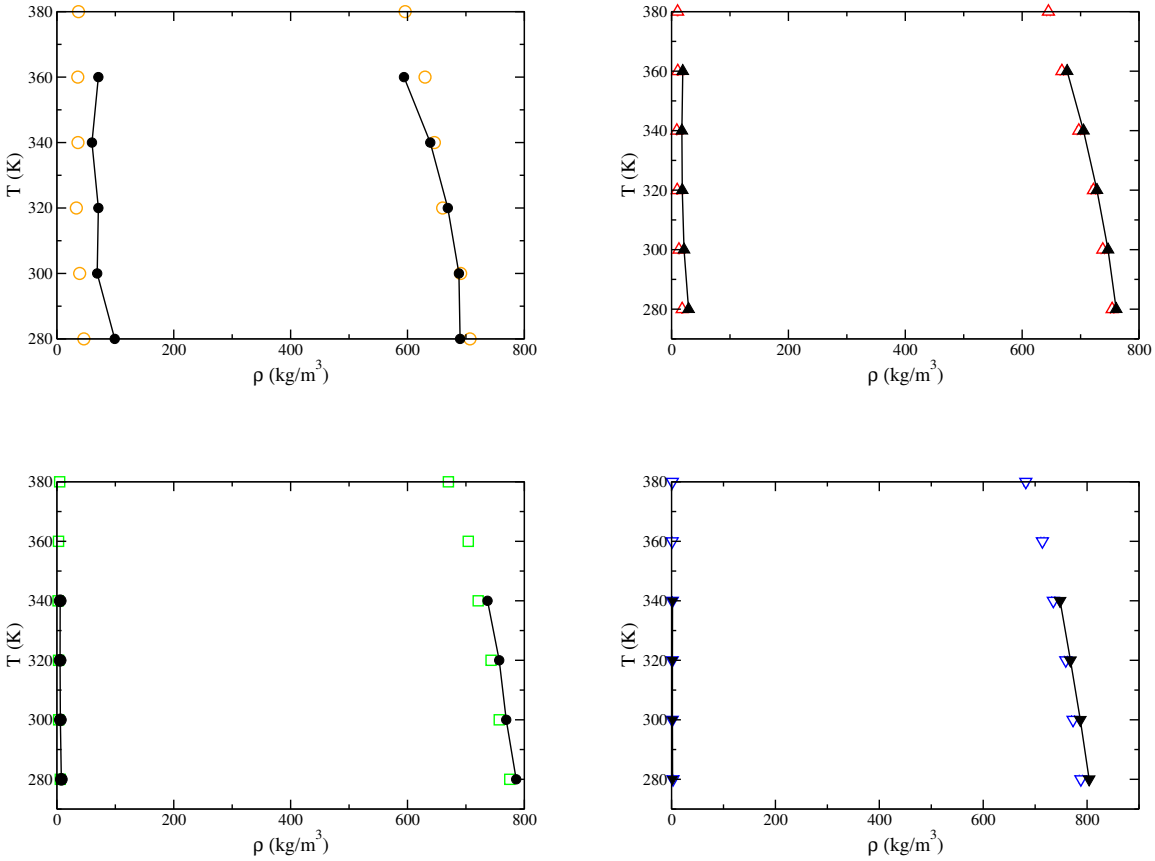

Figura 10.7: Simulated and experimental coexisting densities of the 1-alkanols in the coexisting organic and aqueous phases for each 1-alkanol+water binary mixture at atmospheric pressure and as a function of temperature. Orange circles (1-butanol+water), red up triangles (1-pentanol+water), green squares (1-hexanol+water) and blue down triangles (1-heptanol+water) correspond to MD simulation results. Black lines represent experimental data taken from Cardenas et al. [27]

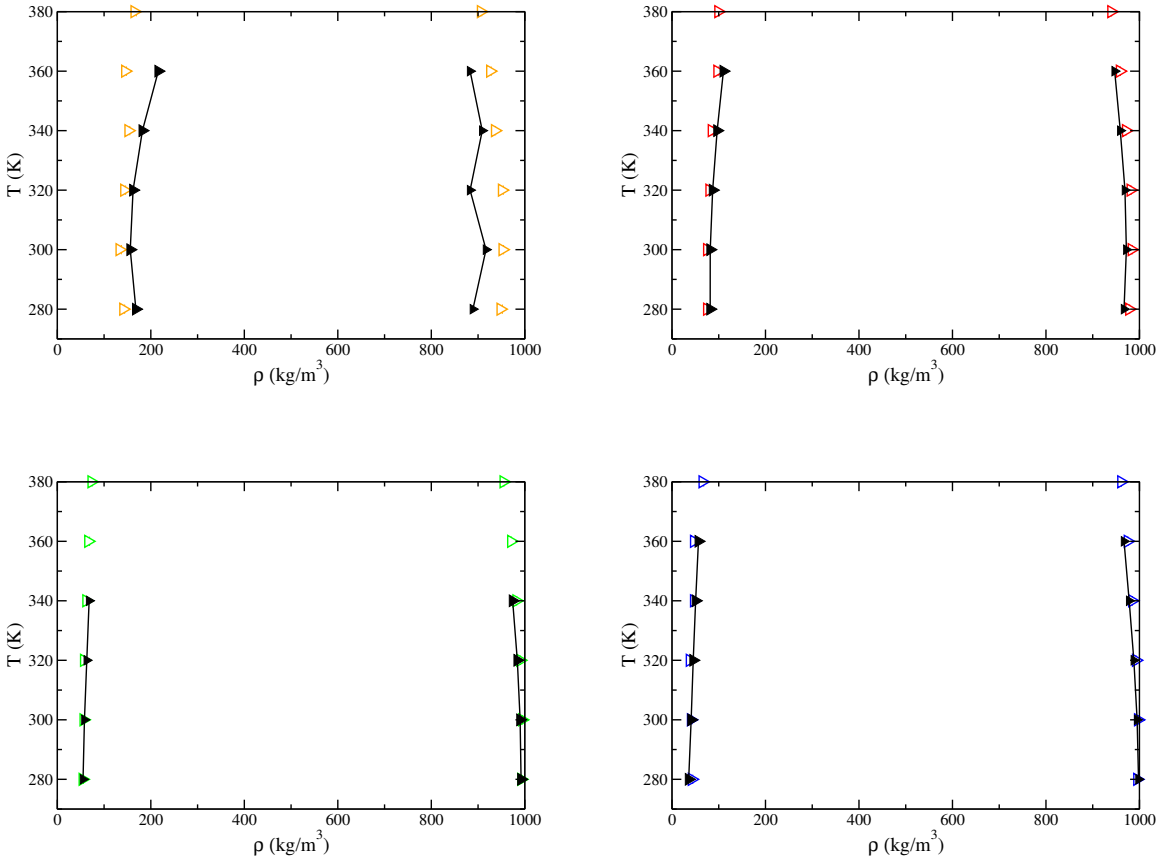

Figura 10.8: Simulated and experimental coexisting densities of H_2O in the coexisting organic and aqueous phases for each 1-alkanol+water binary mixture at atmospheric pressure and as a function of temperature.Orange (1-butanol+water), red (1-pentanol+water), green (1-hexanol+water) and blue (1-heptanol+water) triangles correspond to MD simulation results. Black symbols and lines represent experimental data taken from Cardenas et al. [27]

conditions are the most consistent with experiments due to the almost absence of cross interactions, as reasoned above.

The composition of each coexisting phase is studied in terms of the alkanol molar fractions. The results at the various temperatures are depicted in Figure 10.9 along with the experimental data. On the one hand, the presence of alkanol in the aqueous phase is insignificant regardless of the considered alkanol. On the other hand, the organic phase shows a molar fraction of alkanol (X_1^O) of about 0.55 at the lowest temperature for the 1-butanol+water mixture, and it increases with the chain length of the alkanol component up to 0.75 for 1-heptanol, approximately. These values slightly decrease with increasing the temperature. This behavior confirms that the miscibility of the 1-alkanols and water of the organic phase is favored by the temperature and decreases with the alkyl chain. The molar fractions from molecular simulations and experiments are found reasonably consistent except for the 1-butanol+water mixture, in which the concentration of 1-butanol in the organic phase is non-negligibly overestimated.

Finally, the results for the liquid-liquid interfacial tension at the different temperatures for each binary mixture are summarized in Figure 10.10. Typically, the interfacial tension decreases with increasing temperature. However, the obtained curves exhibit a parabolic shape: The interfacial tension in 1-alkanol +water mixtures increases with the temperature up to a maximum value, which is related to the maximum value in the LLE line [37–39], from which the interfacial tension starts to decreases with temperature. This dependence of the interfacial tension on the temperature agrees well with the reported experimental trend [ref], as well as with other experimental and theoretical work [40, 41]. This rare trend is computationally reproduced more successfully for the shortest alcohol components, oppositely to that found for the coexisting densities. Also, molecular simulations satisfactorily predict higher values of interfacial tension when the alkyl chain increases. This can be rationalized as follows. As it is well-known, water is a highly structured liquid with a three-dimensional tetrahedral hydrogen bond network, resulting in a relative strong surface tension. In contrast, alkanols are associated liquids in which molecules form winding chains. The addition of alkanols in water breaks its hydrogen bond network, to form water-alkanol and alkanol-alkanol hydrogen bonds. Since water-water is the strongest interaction, this results in a loss of energy. Alkanols with larger chains have a more marked hydrophobic nature and are in minor presence in the aqueous phase; consequently, water-water hydrogen bonding and the associated high surface tension is less affected.

Despite the overall qualitative agreement between computational and experimental results in predicting interfacial tension for our systems, quantitative differences are evident. The computed values are overestimated in about 10-30 % percent. In this sense, it is worthwhile remarking that to accurately predict L-L interfacial tension is computationally challenging. It is extremely sensitive to the considered models and force fields and to other simulation details such as the cutoff radius, box size, number of particles, among others. Besides, it is important to recall that the molecular parameters of the models used in this work describe pure fluid data, and we used the Lorentz-Berthelot mixing rules for cross interactions, without any type of model tuning to simultaneously predict the complex mixture phase behaviour and hence interfacial properties.

10.4 Conclusions

By using classical MD simulation techniques, we have explored the liquid-liquid equilibrium and interfaces of aqueous solutions of primary alkanols at various temperatures, and provided information on the underlying behavior at the molecular scale. Our simulations predict the coexistence of two clear

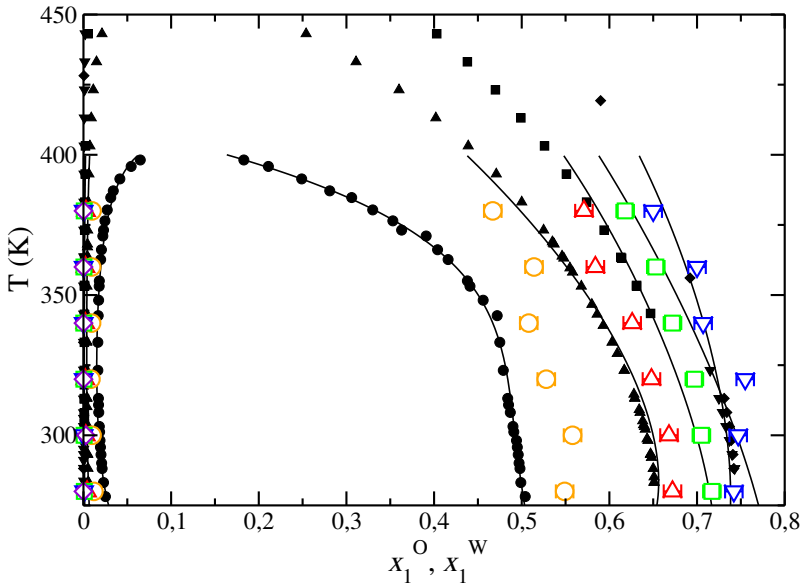

Figura 10.9: Alkanol molar fraction in the coexisting organic (X_1^O) and aqueous (X_1^W) phases for each 1-alkanol+water binary mixture at atmospheric pressure and as a function of temperature. Orange circles (1-butanol+water), red up triangles (1-pentanol+water), green squares (1-hexanol+water) and blue down triangles (1-heptanol+water) correspond to MD simulation results. Black symbols and lines represent experimental data taken from Cardenas et al. [27]

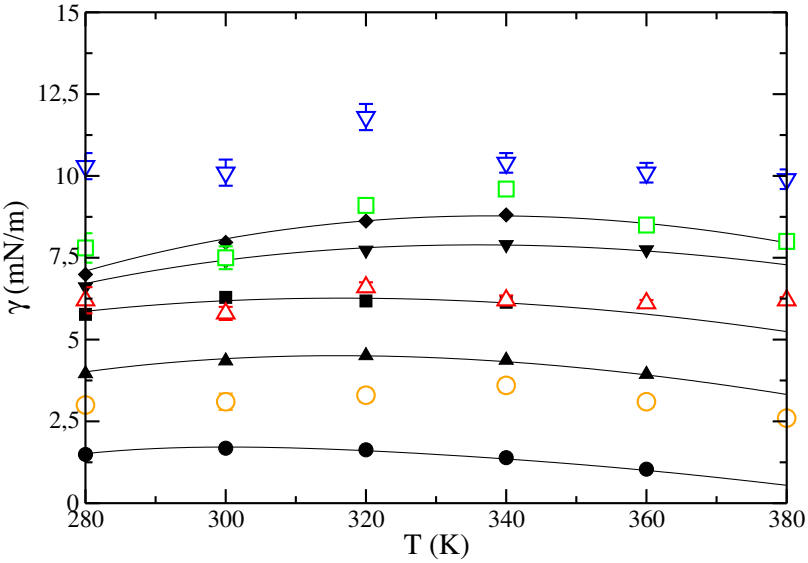

Figura 10.10: Liquid-liquid interfacial tension γ for each 1-alkanol+water binary mixture at atmospheric pressure and as a function of temperature. Orange circles (1-butanol+water), red up triangles (1-pentanol+water), green squares (1-hexanol+water) and blue down triangles (1-heptanol+water) correspond to MD simulation results. Black symbols and lines represent experimental data taken from Cardenas et al. [27]

phases: An aqueous phase and an organic phase. We found singular peaks in the density profiles for the 1-hexanol+water and 1-heptanol+water mixtures due to the preferred molecular ordering near the interface, pointing the alkyl chains to the organic phase nearly perpendicularly to the interface. Snapshots of the molecular system and calculations of structural properties corroborated this orientation and even the formation of layers. This effect is apparent for large 1-alkanols due to the higher degree of hydrophobicity. The obtained coexisting densities of both phases are in satisfactory agreement with experimental data. The effect of the temperature is slight, mainly noted for the organic phase of the 1-butanol+water mixture. Results on the composition of each phase indicate lower miscibility as the alkyl chain of the alcohols increases in the way that the thermodynamic equilibrium approach to two single-component phases for large 1-alkanols components. This results in a high consistency with experimental data, since our models are based on pure fluids, without artificial parameters taking into accor peaks in the density profiles for the 1-account the deviations from ideality of these mixtures. Likely because of this, interfacial tension is overpredicted. This is a challenging property to quantify for inhomogeneous systems; even so, we qualitatively reproduce its behavior. In particular, we suitably predict the parabolic dependence of this property with temperature for these systems as well as its increase with the alkyl chain. Overall, our computational methodology has been proved to satisfactorily predict the liquid-liquid equilibrium and interfacial properties of these fundamental binary mixtures. Further work is however needed to minimize quantitative discrepancies, especially for the interfacial tension.

Acknowledgment

We acknowledge Centro de Supercomputación de Galicia (CESGA, Santiago de Compostela, Spain) and MCIA (Mésocentre de Calcul Intensif Aquitain) of the Universités de Bordeaux and Pau et Pays de l'Adour (France), for providing access to computing facilities and Ministerio de Economía, Industria y Competitividad through Grant with reference FIS2017-89361-C3-1-P co-finanded by EU FEDER funds. Further financial support from Junta de Andalucía and Universidad de Huelva is also acknowledged. J.A.F. acknowledges Contrato Predoctoral de Investigación from XIX Plan Propio de Investigación de la Universidad de Huelva and a FPU Grant (Ref. FPU15/03754) from Ministerio de Educación, Cultura y Deporte. J. A., J. M. M., and F. J. B. thankfully acknowledge the computer resources at Magerit and the technical support provided by the Spanish Supercomputing Network (RES) (Project QCM-2018-2-0042) .A.M. and M.C. also acknowledges the finnancial support of FONDECYT, Chile (Project 1190107).

Bibliography

[1] H. T. Davis, *Statistical Mechanics of Phases, Interfaces and Thin Films.* Weinhem: VCH, 1996.

[2] R. Evans, *Density Functionals in the Theory of Nonuniform Fluids. In Fundamentals of Inhomogeneous Fluids.* New York: Dekker, 1992.

[3] J. Wu *AIChE Journal.*, vol. 52, pp. 1169–1193, 2006.

[4] J. Wu and Z. Li *Annu. Rev. Phys. Chem.*, vol. 58, pp. 85–112, 2007.

[5] H. Löwen *J. Phys. Condens. Matter*, vol. 14, pp. 11987–11905, 2002.

[6] B. M. J. Algaba, J. M. Míguez and F. J. Blas *Phys. Chem. Chem. Phys.*, vol. 21, pp. 11937–11948, 2019.

[7] D. Frenkel and B. Smit, *Understanding Molecular Simulations.* 2nd ed. Academic, San Diego, 2002.

[8] M. P. Allen, *Computer Simulation of Liquids.* Claredon, Oxford, 1987.

[9] J. M. Míguez, J. M. Garrido, F. J. Blas, H. Segura, A. Mejía, and M. M. Piñeiro *J. Phys. Chem. C*, vol. 118, p. 24504, 2014.

[10] J. M. Míguez, D. González-Salgado, J. L. Legido, and M. M. Piñeiro *J. Chem. Phys.*, vol. 132, p. 184102, 2010.

[11] C. Miqueu, J. M. Míguez, M. M. Piñeiro, T. Lafitte, and B. Mendiboure *J. Phys. Chem. B*, vol. 115, no. 31, p. 9618, 2011.

[12] J. M. Míguez, M. M. Piñeiro, and F. J. Blas *J. Chem. Phys.*, vol. 138, p. 034707, 2013.

[13] J. L. Rivera, C. McCabe, and P. T. Cummings *Phys. Rev. E*, vol. 67, p. 011603, 2003.

[14] T. R. Underwood and H. C. Greenwel *Sci. Rep.*, vol. 8, pp. 352–362, 2018.

[15] H. Xiao, Z. Zhen, H. Sun, X. Cao, Z. Li, X. Song, X. Cui, and X. Liu *Sci. China Chem.*, vol. 53, pp. 945–949, 2010.

[16] S. Zeppieri, J. Rodríguez, and A. López de Ramos *J. Chem. Eng. Data*, vol. 46, pp. 1086–1088, 2001.

[17] J. M. Míguez, M. M. Conde, J.-P. Torré, F. J. Blas, M. M. Piñeiro, and C. Vega *J. Chem. Phys.*, vol. 142, p. 124505, 2015.

[18] M. M. Conde and C. Vega *J. Chem. Phys.*, vol. 133, p. 064507, 2010.

[19] M. M. Conde and C. Vega *J. Chem. Phys.*, vol. 138, p. 056101, 2013.

[20] J. M. Míguez, M. C. dos Ramos, M. M. Piñeiro, and F. J. Blas *J. Phys. Chem. B*, vol. 115, p. 9604, 2011.

[21] J. Algaba, J. M. Garrido, J. M. Míguez, A. Mejía, A. I. M.-V. Bravo, and F. J. Blas *J. Chem. Phys.*, vol. 122, pp. 16142–16153, 2018.

[22] B. Chen, J. J. Potoff, and J. I. Siepmann *J. Phys. Chem. B*, vol. 105, pp. 3093–3104, 2001.

[23] J. L. F. Abascal and C. Vega *J. Chem. Phys.*, vol. 123, no. 234505, 2005.

[24] C. Vega and E. de Miguel *J. Chem. Phys.*, vol. 126, p. 154707, 2007.

[25] U. Essmann, L. Perera, M. L. Berkowitz, T. Darden, H. Lee, and L. G. Pedersen *J. Chem. Phys.*, vol. 103, p. 8577, 1995.

[26] D. V. D. Spoel, E. Lindahl, B. Hess, G. Groenhof, A. E. Mark, and H. J. Berendsen *J. Comput. Chem.*, vol. 26, no. 16, p. 1701, 2005.

[27] H. Cárdenas, M. Cartes, and A. Mejía *Fluid Phase Equil.*, vol. 396, pp. 88–97, 2015.

[28] S. Nosé *Mol. Phys.*, vol. 52, p. 255, 1984.

[29] W. G. Hoover *Phys. Rev. A*, vol. 31, p. 1695, 1985.

[30] M. Parrinello and A. Rahman *J. Appl. Phys.*, vol. 52, p. 7182, 1981.

[31] Nosé and M. L. Klein *mol. Phys.*, vol. 50, p. 1055, 1983.

[32] H. J. C. Berendsen, J. P. M. Postma, W. F. van Gunsteren, A. di Nola, and J. R. Haak *J. Chem. Phys.*, vol. 81, p. 3684, 1984.

[33] H. Hulshof *Ann. Phys. (Berlin)*, vol. 4, p. 165, 1901.

[34] J. S. Rowlinson and B. Widom, *Molecular Theory of Capillarity.* Claredon Press, 1982.

[35] E. de Miguel, F. J. Blas, and E. M. del Río *Mol. Phys.*, vol. 104, p. 2919, 2006.

[36] E. de Miguel and G. Jackson *J. Chem. Phys.*, vol. 125, p. 164109, 2006.

[37] H. M. Backes *Fortschr. Ber. VDI Z. Reihe*, vol. 3, pp. 506–3108, 1984.

[38] J. J. Bikerman, *Physical Surfaces.* Academic Press, 1970.

[39] D. Villers and J. K. Platten *J. Chem. Phys.*, vol. 92, pp. 4023–4024, 1988.

[40] M. L. Schlossman *J. Chem. Phys.*, vol. 7, pp. 235–243, 2002.

[41] S. Enders and H. Kahl *Fluid Phase Equil.*, vol. 263, pp. 160–167, 2008.

Capítulo 11

Resumen y Conclusiones

El objetivo principal de esta tesis doctoral es el estudio y determinación de las propiedades interfaciales y de los equilibrios de fases de promotores/inhibidores de hidratos y sus mezclas. En particular, nos hemos centrado en el THF, como promotor de hidratos, y en la familia de los 1−alcanoles, como inhibidores de hidratos. Esta investigación ha sido llevada a cabo utilizando una combinación de técnicas de simulación molecular y del formalismo teórico SAFT-VR. Como resultado, los descubrimientos obtenidos en este trabajo han sido publicados en revistas internacionales de prestigio. Los resultados mas relevantes y las principales conclusiones de este trabajo son las siguientes:

- En el trabajo desarrollado en el **Capítulo 5**, los diagramas de fases a altas presiones de las mezclas binarias de THF(1) + CO_2(2), + CH_4(2), y + H_2O(2) fueron obtenidos utilizando la ecuación de estado SAFT-VR. Este trabajo fue una primera aproximación teórica para obtener una visión global del comportamiento termodinámico de las mezclas binarias del promotor de hidratos THF con H_2O (que conforma la estructura cristalina del hidrato), y con CO_2 y CH_4 (dos moléculas huésped del hidrato de gran interés).

  Para la mezcla binaria de THF(1) + CO_2(2) (comportamiento de fase tipo I), se obtuvieron proyecciones presión-temperatura y cortes presión-composición, a varias temperaturas, del diagrama de fases utilizando dos parámetros diferentes para describir las interacciones cruzadas (ver **Capítulo 5**). En ambos casos, el acuerdo entre predicciones teóricas y datos experimentales tomados de la literatura fue excelente.

  Se obtuvo, además, el comportamiento de las fases de la mezcla binaria de THF(1) + CH_4(2). En concreto, la teoría fue capaz de predecir que la mezcla exhibe un comportamieno de fase tipo III. También se obtuvieron cortes Px del diagrama de fases a varias temperaturas y cortes Tx del diagrama de fases a varias presiones. En un trabajo posterior (**Capítulo 9**), se obtuvieron nuevos datos experimentales para esta mezcla (en colaboración con Mejía y su equipo) y predicciones obtenidas mediante simulación en dinámica molecular. El acuerdo entre predicciones teóricas, resultados de simulación y datos experimentales fue excelente en todos los casos. En este punto, es importante remarcar que antes del trabajo desarrollado en el **Capítulo 9** no existían datos experimentales ni resultados de simulación para este sistema.

  Adicionalmente, se determinó el comportamiento de fase a altas presiones de la mezcla binaria

THF(1) + H_2O(2). Dos sets diferentes de parámetros moleculares fueron usados para describir las interacciones asociantes entre las moléculas de THF y las moléculas H_2O (ver **Capítulo 5**). La teoría es capaz de predecir un comportamiento de fase tipo VI para esta mezcla, en buen acuerdo con los datos experimentales. En general, las predicciones utilizando ambos sets de parámetros moleculares están en buen acuerdo con los valores experimentales tomados de la literatura.

La ecuación de estado SAFT-VR ha demostrado ser capaz de describir el comportamiento de las fases de las mezclas binarias de THF(1) + CO_2(2), + CH_4(2), y + H_2O(2). A pesar de la complejidad de las mezclas estudiadas en este trabajo, los resultados obtenidos con SAFT-VR están en buen acuerdo con los datos experimentales. Este formalismo demostró ser capaz de predecir las características más importantes de los sistemas estudiados. Estos resultados teóricas fueron el primer paso en la determinación de las propiedades interfaciales de las mezclas binarias de THF. La información obtenida en este trabajo fue utilizada como punto de partida en trabajos posteriores (**Capítulos 6-9**).

- En el trabajo desarrollado en el **Capítulo 6**, las propiedades interfaciales de seis modelos diferentes de THF fueron determinadas mediante simulación directa de la interfase líquido-vapor. Los resultados de las simulaciones fueron comparados con datos experimentales. El objetivo principal fue examinar la habilidad de diferentes modelos de THF, tomados de la literatura, para proporcionar una descripción precisa de las propiedades interfaciales y del equilibrio líquido-vapor del sistema. Este trabajo puede considerarse como un paso previo antes de estudiar, mediante simulación molecular, las mezclas binarias de THF(1) + CO_2(2) y + CH_4(2).

  Tres de los modelos de THF utilizados estaban basados en la aproximación de CG. En este caso, el THF fue modelado como una esfera, una molécula diatómica y una cadena en forma de anillo compuesta por tres monómeros Mie. Los parámetros para cada uno de estos modelos fueron obtenidos utilizando la ecuación de estado SAFT-γ Mie. Los otros tres modelos de THF fueron modelados según la aproximación de UA usando la parametrización de los campos de fuerzas TIPS y TraPPE. En particular, se usaron dos modelos TraPPE-UA de THF. El primero fue el modelo TraPPE-UA original de THF propuesto por Siepmann y colaboradores, y el segundo fue una versión rígida y plana aproximada de este modelo propuesta por nosotros. El modelo TIPS-UA no fue capaz de proporcionar una buena descripción del comportamiento del sistema, por lo que este modelo no va a ser tenido en cuenta en estas conclusiones finales.

  En este trabajo se estudiaron las propiedades interfaciales de la interfase líquido-vapor del THF. En concreto, se obtuvieron los perfiles de la densidad, la anchura interfacial y la tensión interfacial en función de la temperatura. Las densidades de coexistencia líquido-vapor fueron predichas excelentemente por los tres modelos CG y los dos modelos TraPPE-UA. Las predicciones obtenidas con el modelo TraPPE-UA original de THF fueron ligeramente mejores para la densidad de la fase líquida a bajas temperaturas. La presión de vapor, en función de la temperatura, fue predicha remarcablemente bien por los tres modelos CG y por el modelo TraPPE-UA rígido. El modelo TraPPE-UA original reproduce la presión de vapor experimental del sistema con gran precisión para todas las temperaturas estudiadas.

  Finalmente, se examinó la tensión interfacial líquido-vapor del sistema de THF. La tensión interfacial es una propiedades extremadamente sensible a los detalles moleculares del sistemas. A pesar de que los modelos de CG fueron capaces de predecir cualitativamente el comportamiento de la tensión interfacial, solo los modelos TraPPE-UA proporcionaron una descripción precisa de la tensión interfacial líquido-vapor del THF. El modelo TraPPE-UA orinal predijo la tensión

interfacial ligeramente mejor que el modelo rígido y plano aproximado de TraPPE-UA.

En resumen, solo los modelos TraPPE-UA fueron capaces de predecir las propiedades interfaciales del sistema de THF. El modelo TraPPE-UA original proporciona una descripción más precisa de las propiedades interfaciales. Sin embargo, el modelo TraPPE-UA rígido y plano proporciona simulaciones más rápidas y una excelente descripción de las propiedades interfaciales.

- En los **Capítulos 7** y **8** se examinaron las propiedades interfaciales y el equilibrio de fases líquido-vapor de la mezcla binaria THF + CO_2. En este estudio se combinaron medidas experimentales, modelos teóricos y simulaciones en MD y MC. El sistema fue estudiado a dos temperaturas, 298.15 y 353.15 K, y a varias presiones.

  En el trabajo presentado en el **Capítulo 7**, las densidades de las fases bulk y las tensiones interfaciales líquido-vapor del sistema THF + CO_2 fueron medidas experimentalmente y modeladas teóricamente. El comportamiento interfacial fue modelado usado la Teoría del Gradiente Cuadrado basada en la ecuación de estado de Peng-Robindson. La isoterma de adsorción relativa de Gibbs del CO_2 en la región interfacial fue predicha a partir de los valores experimentales de las tensiones interfaciales y de las densidades.

  Además, se determinaron las propiedades interfaciales de la mezcla binaria de THF + CO_2 mediante simulación en dinámica molecular de la interfase líquido-vapor (**Capítulo 8**). En este trabajo fueron utilizados los dos modelos TraPPE-UA de THF estudiados en el **Capítulo 6**, y las simulaciones fueron realizadas a las mismas condiciones estudiadas en el **Capítulo 7**. También se usó la técnica de simulación *Gibss ensemble* Monte Carlo para comparar los resultados obtenidos mediante las dos metodologías.

  Las densidades experimentales de coexistencia obtenidas (**Capítulo 7**) estaban en buen acuerdo con los datos experimentales de la literatura. También se compararon valores experimentales, predicciones teóricas (**Capítulos 5** y **7**) y resultados de simulación (**Capítulo 8**). A pesar de que el acuerdo entre todos los resultados fue bueno, los resultados obtenidos mediante simulación (MD y MC) con ambos modelos de THF subestimaron sistemáticamente las densidades de la fase líquida. También se compararon las composiciones de coexistencia obtenidas con la ecuación de estado SAFT-VR (**Capítulo 5**) y mediante simulación (**Capítulo 8**) con datos experimentales tomados de la literatura. El acuerdo entre ambos modelos fue excelente, sin embargo, ambos subestimaron ligeramente las densidades de la fase vapor a bajas presiones. Además, el acuerdo entre los resultados experimentales y de simulación para la absorción relativa de Gibbs fue bueno.

  Finalmente, también se examinó la tensión interfacial de la mezcla. El acuerdo entre resultados experimentales y de simulación fue excelente en todos los casos. Los resultados mostraron que el modelo TraPPE-UA rígido y plano fue capaz, no solo de proporcionar una descripción precisa del sistema líquido-vapor puro de THF, sino que también es capaz de predecir el comportamiento de la mezcla binaria de THF+CO_2. Es importante señalar este hecho porque las simulaciones en dinámica molecular con el modelo rígido y plano son del orden de 10 veces más rápidas que con el modelo original.

- Ambos modelos TraPPE-UA de THF han demostrado ser capaces de predecir la tensión interfacial y el comportamiento de las fases del sistema puro de THF y de la mezcla binaria de THF + CO_2. Sin embargo, las simulaciones en dinámica molecular utilizando el modelo rígido y plano son más rápidas dado que los grados internos de libertad de la molécula están congelados. Por esta razón, en el estudio de la mezcla binaria de THF+CH_4 (**Capítulo 9**) solo se ha usado el modelo

rígido y plano. Para este sistema, se han obtenido los perfiles de la densidad, los diagramas $P\rho$ y Px y la tensión interfacial mediante simulación en dinámica molecular a 300 y 370 K y a varias presiones.

Las densidades de coexistencia y las tensiones interfaciales fueron también medidas experimentalmente. Es importante recordar aquí que no existen datos experimentales de equilibrios de fase y tensión interfacial en la literatura para este sistema. La habilidad del modelo rígido y plano de THF para proporcionar una descripción precisa de las propiedades interfaciales y del comportamiento de las fases fue examinada comparando resultados experimentales y de simulación. También se incluyeron predicciones teóricas obtenidas mediante la ecuación de estado SAFT-VR (**Capítulo 5**).

El acuerdo entre las densidades de coexistencia experimentales y las predicciones teóricas fue excelente en todo el rango de condiciones termodinámicas medidas. Los resultados obtenidos mediante simulación sobrestimaron ligeramente las densidades del vapor a elevadas presiones y subestimaron ligeramente las densidades del líquido. También se obtuvieron los diagramas Px utilizando simulación molecular y SAFT-VR. El acuerdo fue excelente a bajas y medias presiones, sin embargo, a altas presiones los resultados de simulación sobrestiman la composición del THF en la fase vapor y subestiman la composición del THF en la fase líquida.

Para comprobar la habilidad del modelo TraPPE-UA rígido y plano para predecir el comportamiento del sistema, se comparó los valores de la tensión interfacial obtenidos mediante experimentos con los resultados de simulación. El acuerdo fue excelente en todo el rango de condiciones termodinámicas estudiadas. En este trabajo, se demostró que el modelo TraPPE-UA rígido es una buena elección para estudiar las propiedades interfaciales de la mezcla binaria THF+CH_4.

- La familia lineal delos 1-alcanoles puede modificar drásticamente los equilibrios de fases y las propiedades interfaciales de los hidratos. Como primer paso para estudiar los sistemas hidrato + 1-alcanol, se realizaron simulaciones en MD de las mezclas binarias de agua + 1-alcanol (desde 1-butanol hasta 1-heptanol, ver **Capítulo 10**). Estos sistemas se estudiaron a presión atmosférica y varias temperaturas (desde 280 hasta 380 K). Para estas mezclas, obtuvimos los perfiles de densidad, los diagramas $P\rho$ y Px y la tensión superficial. También se estudió la orientación de las moléculas de 1-alcanol cerca de la interfase.

  El acuerdo entre las densidades de coexistencia experimental y los resultados de simulación fue bueno para todos los casos, especialmente para la fase rica en 1-alcanol. Para la fase rica en agua, las densidades del 1-alcanol (agua) fueron ligeramente subestimadas (sobrestimadas). La miscibilidad de los 1-alcanoles y el agua en la fase orgánica se ve favorecida por la temperatura, sin embargo, disminuye con el tamaño de la cadena alquílica. El acuerdo entre los datos experimentales y los resultados de simulación es razonablemente bueno, excepto por la concentración de 1-butanol en la fase rica en 1-alcanol, que se sobrestima.

  Finalmente, se obtuvo la tensión interfacial líquido-líquido a diferentes temperaturas y para cada mezcla binaria. A pesar de que los resultados de las simulaciones en dinámica molecular sobreestimaron la tensión interfacial experimental, fueron capaces de predecir cualitativamente el máximo de la tensión interfacial.

  En las condiciones termodinámicas estudiadas, el sistema presenta dos fases líquidas en coexistencia (una fase rica en agua y una fase rica en 1-alcanol). Las moléculas de 1-hexanol y 1-heptanol

están orientadas apuntando las cadenas alquílicas a la fase orgánica debido al mayor grado de hidrofobicidad de las grandes cadenas alquílicas.

Capítulo 12

Summary and Conclusions

The main goal of this Thesis is the study and determination of the interfacial properties and phase equilibria of hydrate promoters/inhibitors and its mixtures. In particular, we focus on THF, as hydrate promoter, and on the 1−alkanols family, such as hydrate inhibitors. The research has been carried out using a combination of molecular simulation and SAFT-VR approach. As a result, several findings have been published in international peer-reviewed journals. The most relevant results and the principal conclusions are the following:

- In the work developed in **Chapter 5**, the high-pressure phase diagrams of the THF(1) + CO_2(2), + CH_4(2), and + H_2O(2) binary mixtures were obtained using the SAFT-VR equation of state. This work was a first theoretical approximation in order to understand the phase behaviour of the hydrate promoter THF with H_2O (which conforms the crystalline hydrate structure), and with CO_2 and CH_4 (which are two hydrate guest molecules of enormous interest).

  For the THF(1) + CO_2(2) binary mixture (type I phase behaviour), pressure-temperature projections and pressure-composition slices, at several temperatures, of the phase diagram were obtained using two different mixture parameters (see **Chapter 5**). In both cases, agreement between theoretical predictions and experimental data taken from the literature was excellent.

  We also obtained the phase behaviour of the THF(1) + CH_4(2) binary mixture. Particularly, in this work the theory was able to predict that the mixture exhibit type III phase behaviour. We also obtained the Px slices of the phase diagram at several temperatures and the Tx slices of the phase diagram at several pressures. In a later work (**Chapter 9**), we obtained new experimental data for this mixture (in collaboration with Meía and coworkers) and molecular dynamics predictions. Agreement between theoretical predictions, simulation results and experimental data was excellent in all cases. At this point, it is important to remark that before the work developed in **Chapter 9** there were neither experimental data nor simulation results for this system.

  In addition to that, we determined the high-pressure phase behaviour of the THF(1) + H_2O(2) binary mixture. We used two different sets of molecular parameter to account for the association interactions between THF and H_2O molecules (see **Chapter 5**). Theory is able to predict type VI phase behaviour for the mixture, in agreement with experimental data. In general, the predictions using both sets of molecular parameters were in good agreement with experimental

values taken from the literature.

The SAFT-VR formalism demonstrated to be able to describe the phase behaviour of the THF(1) + CO_2(2), + CH_4(2), and + H_2O(2) binary mixtures. In spite of the complexity of the mixtures studied in this work, the SAFT-VR predictions were in good agreement with experimental data. This formalism proved to be able to predict the most important features of the systems studied. These theoretical findings were the first step in the determination of the interfacial properties of the THF binary mixtures. The information obtained in this work was used as starty point for later works (**Chapters 6-9**).

- In the work developed in **Chapter 6**, the interfacial properties of six different models of THF were determined from direct MD simulation of the vapour-liquid interface. The simulation results were compared with experimental data. The main objective was to examine the ability of different THF models, taken from the literature, to provide an accurate description of the interfacial properties and phase behaviour of the vapour-liquid interfacial system. This work can be considered as a necessary previous step before studying, using molecular simulation, the THF(1) + CO_2(2) and + CH_4(2) binary mixtures.

  Three of the THF models used were based on a CG approach. In this case, THF was modelled as a single sphere, a diatomic molecule, and a ring-like chain formed from three Mie monomers according to the SAFT-γ Mie top-down approach. The other three THF models were modelled according to the UA approach using the TIPS and TraPPE force field parametrizations. In particular, we used two TraPPE-UA THF models. The first one was the original TraPPE-UA THF model proposed by Siepmann and coworkers, and the second one was an approximate rigid and planar version of this model proposed by us. The TIPS-UA model was not able to provide a good description of the phase behaviour, so this model is not going to be included in these final conclusions.

  In this work, we studied the interfacial properties of the vapour-liquid interface of THF. We focused on the determination of the density profiles, the interfacial thickness and the surface tensions as function of the temperature. The vapour-liquid phase envelope of THF was predicted in excellent agreement by the three CG models and by the two TraPPE-UA models. Predictions obtained by the original TraPPE-UA THF model were slightly better for the saturated liquid density at low temperatures. The vapour pressure, as a function of temperature, was predicted remarkably well by the three CG models and by the approximated rigid TraPPE-UA model. The original TraPPE model reproduces the experimental vapour pressure of the system at all temperatures very accurately.

  Finally, we examined the behaviour of the vapour-liquid surface tension of THF. Surface tension is extremely sensitive to molecular details of the system. Although the CG models were able to predict qualitatively the behaviour of the surface tension, only the TraPPE-UA models provided an accurate prediction of the THF vapour-liquid interfacial tension. The original TraPPE-UA model predicted slightly better the surface tension than the approximated rigid and planar TraPPE-UA model.

  In summary, only the TraPPE-UA models were able to predict the interfacial properties of the THF pure system. The original TraPPE-UA model provided a more accurate description of the interfacial properties. However, the approximate planar and rigid TraPPE-UA model is faster to simulate and is able to provide and excellent description of the interfacial properties.

- In **Chapters 7** and **8** we examined the interfacial properties and phase equilibria of the THF + CO_2 binary mixture. In this study, we combined experimental measurements, theoretical modelling, and MD and MC simulations. The system was studied at two temperatures, 298.15 and 353.15 K, and several pressures.

  In the work presented in **Chapter 7**, bulk phase mass densities and interfacial tensions at vapour-liquid equilibrium for THF + CO_2 were experimental measured and theoretically modelled. The interfacial behaviour was modelled using the Square Gradient Theory based on a Peng-Robinson equation of state. The relative Gibbs adsorption isotherm of CO_2 in the interfacial region was also predicted from the experimental values of surface tension - density representation.

  Also, we determined the interfacial properties of the THF + CO_2 binary mixture from direct molecular dynamics simulation of the vapour-liquid interface (**Chapter 8**). In this work, we used the two TraPPE-UA models studied in **Chapter 6**, and the simulations were performed at the same conditions studied in **Chapter 7**. We also used the *Gibbs ensemble* MC simulation technique to compare results from both methodologies.

  The experimental coexistence densities obtained (**Chapter 7**) were in good agreement with experimental data taken from the literature. We also compared experimental values, theoretical predictions (**Chapters 5** and **7**) and simulation results (**Chapter 8**). Although agreement between all results was good, molecular simulations (MC and MD) of both models systematically underestimate liquid densities. We also compared the coexistence composition obtained from SAFT-VR equation of state (**Chapter 5**) and simulation (**Chapter 8**) with experimental data taken from the literature. Agreement between both results was excellent, although, both models slightly overestimated the THF composition in the vapour phase at low pressures. In addition, agreement between simulation and experimental results of the relative Gibbs adsorption was good in the whole range of measures.

  Finally, we also examined the interfacial tension of the mixture. Agreement between simulation and experimental results was excellent in all cases. These results showed that the approximate rigid and planar TraPPE-UA model was not only able to provide an accurate description of the vapour-liquid pure THF system but also was able to predict the behaviour of the THF+CO_2 binary mixture. This is important to remark that the MD simulations for the rigid and planar model are 10 times faster than with the original one.

- Both THF TraPPE-UA models have shown to be equally able to predict the interfacial tension and the phase behaviour of the THF pure system and THF + CO_2 binary mixture. However, MD simulations using the rigid and planar model are faster since internal degrees of freedom are frozen. For this reason, in the study of the THF+CH_4 binary mixture (**Chapter 9**), we only used the rigid and planar model. For the THF+CH_4 binary mixture, we obtained density profiles, $P\rho$ and Px diagrams, and surface tension from MD simulation at 300 and 370 K, and at several pressures.

  The coexistence densities and surface tension were also measured experimentally. It is important to recall here that no experimental data for phase equilibria and interfacial tension existing in the literature for this system. In order to check the ability of the rigid and planar model to provide an accurate description of the interfacial properties and of the phase behaviour, we compared experimental and simulation results. We also included the theoretical predictions obtained using the equation of state SAFT-VR (**Chapter 5**).

Agreement between experimental coexistence densities and theoretical predictions was excellent in the whole range of thermodynamic conditions measured. The MD simulation results slightly overestimated the vapour densities at high pressures and slightly underestimated the liquid densities. We also obtained the Px phase envelope using SAFT-VR and MD simulations. Agreement was excellent at low and mid pressures. However, at higher pressures simulation results overestimate the composition of THF in the vapour phase and underestimated the composition of THF in the liquid phase.

To check the ability of the rigid and planar THF TraPPE-UA model to predict the phase behaviour of the system, we compared the surface tension values obtained by experiments and MD simulations. Agreement was excellent in the whole range of thermodynamic conditions studied. In this work, it showed that the rigid and planar THF TraPPE-UA model is a good choice to study the interfacial properties of the THF+CH_4 binary mixture.

- Linear family of 1-alkanols are able to modify drastically the phase equilibria and interfacial properties of hydrates. As a first step to study the hydrate + alkanol systems, we performed MD simulations of the water + 1-alkanol binary mixtures (from 1-butanol to 1-heptanol, see **Chapter 10**). These systems were studied at atmospheric pressure and different temperatures (from 280 to 380 K). For these mixtures, we obtained the density profiles, $P\rho$ and Px diagrams, and surface tension as a function of temperature. We also considered the orientation of 1-alkanols near the liquid-liquid interface.

  Agreement between experimental coexistence densities and simulation results was good for all the cases, especially for the organic rich phase. For the aqueous rich phase, predictions obtained from simulation underestimated (overestimated) the density of the alkanol (water). The miscibility of the 1-alkanols and water in the organic phase is favoured by the temperature, however, it decreases with the size of the alkyl chain. Agreement between experimental data and simulation results is reasonably good except for the concentration of 1-butanol in the organic rich phase, which is overestimated.

  Finally, we obtained the liquid-liquid interfacial tension at different temperatures and for each binary mixture. Although, the MD simulations results overestimated the experimental interfacial tension, it was able to predict qualitatively the maximum of the interfacial tension.

  At the thermodynamic conditions studied, the system exhibit two liquid phases in coexistence (an aqueous rich phase and an organic rich phase). The 1-hexanol and the 1-heptanol molecules are oriented pointing the alkyl chains to the organic phase due to the higher degree of hydrophobicity of the large alkyl chains.

Parte IV

Anexo: Trabajos Publicados Derivados de la Tesis Doctoral

Understanding the phase behaviour of tetrahydrofuran + carbon dioxide, + methane, and + water binary mixtures from the SAFT-VR approach

Autores/as: J. M. Míguez, M. M. Piñeiro, J. Algaba, B. Mendiboure, J.-P. Torré y F. J. Blas.

Publicado en: Journal of Physical Chemistry B, 119, 14288-14302 (2005).

DOI: 10.1021/acs.jpcb.5b07845

Factor de impacto de la revista en el año de publicación: 3.187

Rank 48/144 en Chemistry/Physical Q2

THE JOURNAL OF PHYSICAL CHEMISTRY B

Article

pubs.acs.org/JPCB

Understanding the Phase Behavior of Tetrahydrofuran + Carbon Dioxide, + Methane, and + Water Binary Mixtures from the SAFT-VR Approach

J. M. Míguez,[†] M. M. Piñeiro,[‡] J. Algaba,[§] B. Mendiboure,[†] J. P. Torré,[†] and F. J. Blas*[,§]

[†]Laboratoire des Fluides Complexes et Leurs Reservoirs, Université de Pau et des Pays de l'Adour, CNRS, TOTAL - UMR 5150, Avenue de l'Université, B.P. 1155 - PAU, F-64013 Pau, France

[‡]Departamento de Física Aplicada, Universidade de Vigo, E36310 Vigo, Spain

[§]Laboratorio de Simulación Molecular y Química Computacional, CIQSO-Centro de Investigación en Química Sostenible and Departamento de Física Aplicada, Universidad de Huelva, 21007 Huelva, Spain

ABSTRACT: The high-pressure phase diagrams of the tetrahydrofuran(1) + carbon dioxide(2), + methane(2), and + water(2) mixtures are examined using the SAFT-VR approach. Carbon dioxide molecule is modeled as two spherical segments tangentially bonded, water is modeled as a spherical segment with four associating sites to represent the hydrogen bonding, methane is represented as an isolated sphere, and tetrahydrofuran is represented as a chain of *m* tangentially bonded spherical segments. Dispersive interactions are modeled using the square-well intermolecular potential. In addition, two different molecular model mixtures are developed to take into account the subtle balance between water−tetrahydrofuran hydrogen-bonding interactions. The polar and quadrupolar interactions present in water, tetrahydrofuran, and carbon dioxide are treated in an effective way via square-well potentials of variable range. The optimized intermolecular parameters are taken from the works of Giner et al. (*Fluid Phase Equil.* **2007**, *255*, 200), Galindo and Blas (*J. Phys. Chem. B* **2002**, *106*, 4503), Patel et al. (*Ind. Eng. Chem. Res.* **2003**, *42*, 3809), and Clark et al. (*Mol. Phys.* **2006**, *104*, 3561) for tetrahydrofuran, carbon dioxide, methane, and water, respectively. The phase diagrams of the binary mixtures exhibit different types of phase behavior according to the classification of van Konynenburg and Scott, ranging from types I, III, and VI phase behavior for the tetrahydrofuran(1) + carbon dioxide(2), + methane(2), and + water(2) binary mixtures, respectively. This last type is characterized by the presence of a Bancroft point, positive azeotropy, and the so-called closed-loop curves that represent regions of liquid−liquid immiscibility in the phase diagram. The system exhibits lower critical solution temperatures (LCSTs), which denote the lower limit of immiscibility together with upper critical solution temperatures (UCSTs). This behavior is explained in terms of competition between the incompatibility with the alkyl parts of the tetrahydrofuran ring chain and the hydrogen bonding between water and the ether group. A minimum number of unlike interaction parameters are fitted to give the optimal representation of the most representative features of the binary phase diagrams. In the particular case of tetrahydrofuran(1) + water(2), two sets of intermolecular potential model parameters are proposed to describe accurately either the hypercritical point associated with the closed-loop liquid−liquid immiscibility region or the location of the mixture lower- and upper-critical end-points. The theory is not only able to predict the type of phase behavior of each mixture, but also provides a reasonably good description of the global phase behavior whenever experimental data are available.

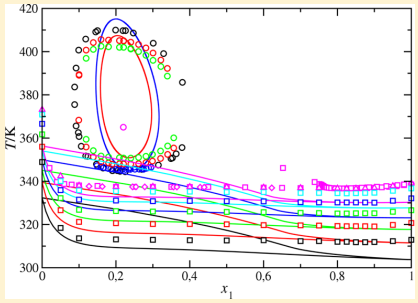

INTRODUCTION

Tetrahydrofuran (c-$(CH_2)_4O$, denoted hereafter as THF for brevity) is a cyclic ether widely used as solvent in many industrial processes. Among its diverse applications, it is used as thermodynamic clathrate hydrate promoter,[1,2] and that represents a particular motivation for the present study. Clathrate hydrates are nonstoichiometric crystalline inclusion compounds consisting of a network of hydrogen-bonded molecules forming cages in which various types of low molecular weight compounds (e.g., methane, carbon dioxide, hydrogen sulfide, THF, etc.) can be encapsulated under appropriate thermodynamic conditions. A mixture of THF and water forms the so-called "THF hydrate" (17 H_2O molecules per THF molecule), in which THF molecules occupy only the large cages of the structure II (sII).[1,2] This hydrate can be formed easily and dissociates around 277 K at atmospheric pressure. For this reason, it is used as a model system in many fundamental and practical applications. THF

Received: August 12, 2015
Revised: October 2, 2015
Published: October 14, 2015

DOI: 10.1021/acs.jpcb.5b07845
J. Phys. Chem. B 2015, 119, 14288−14302

Understanding the phase behaviour of tetrahydrofuran + carbon dioxide, + methane, and + water binary mixtures from the SAFT-VR approach

Autores/as: J. M. Garrido, J. Algaba, J. M. Míguez, B. Mendiboure, A. I. Moreno-Ventas Bravo, M. M. Piñeiro y F. J. Blas

Publicado en: Journal of Chemical Physics, 144, 144702-10 (2016)

DOI: 10.1063/1.4945385.

Factor de impacto de la revista en el año de publicación: 2.965

Rank 57/146 en Chemistry/Physical Q2

THE JOURNAL OF CHEMICAL PHYSICS **144**, 144702 (2016)

On interfacial properties of tetrahydrofuran: Atomistic and coarse-grained models from molecular dynamics simulation

J. M. Garrido,[1] J. Algaba,[2] J. M. Míguez,[3,4] B. Mendiboure,[3] A. I. Moreno-Ventas Bravo,[5] M. M. Piñeiro,[4] and F. J. Blas[2,a)]

[1]*Departamento de Ingeniería Química, Universidad de Concepción, POB 160-C Concepción, Chile*
[2]*Laboratorio de Simulación Molecular y Química Computacional, CIQSO-Centro de Investigación en Química Sostenible and Departamento de Física Aplicada, Universidad de Huelva, 21007 Huelva, Spain*
[3]*Laboratoire des Fluides Complexes et Leurs Reservoirs, Université de Pau et des Pays de l'Adour, CNRS, TOTAL–UMR 5150, Avenue de l'Université, B.P. 1155, Pau F-64013, France*
[4]*Departamento de Física Aplicada, Universidade de Vigo, E36310 Vigo, Spain*
[5]*Laboratorio de Simulación Molecular y Química Computacional, CIQSO-Centro de Investigación en Química Sostenible and Departamento de Geología, Universidad de Huelva, 21007 Huelva, Spain*

(Received 16 October 2015; accepted 22 March 2016; published online 11 April 2016)

We have determined the interfacial properties of tetrahydrofuran (THF) from direct simulation of the vapor-liquid interface. The molecules are modeled using six different molecular models, three of them based on the united-atom approach and the other three based on a coarse-grained (CG) approach. In the first case, THF is modeled using the transferable parameters potential functions approach proposed by Chandrasekhar and Jorgensen [J. Chem. Phys. **77**, 5073 (1982)] and a new parametrization of the TraPPE force fields for cyclic alkanes and ethers [S. J. Keasler *et al.*, J. Phys. Chem. B **115**, 11234 (2012)]. In both cases, dispersive and coulombic intermolecular interactions are explicitly taken into account. In the second case, THF is modeled as a single sphere, a diatomic molecule, and a ring formed from three Mie monomers according to the SAFT-γ Mie top-down approach [V. Papaioannou *et al.*, J. Chem. Phys. **140**, 054107 (2014)]. Simulations were performed in the molecular dynamics canonical ensemble and the vapor-liquid surface tension is evaluated from the normal and tangential components of the pressure tensor along the simulation box. In addition to the surface tension, we have also obtained density profiles, coexistence densities, critical temperature, density, and pressure, and interfacial thickness as functions of temperature, paying special attention to the comparison between the estimations obtained from different models and literature experimental data. The simulation results obtained from the three CG models as described by the SAFT-γ Mie approach are able to predict accurately the vapor-liquid phase envelope of THF, in excellent agreement with estimations obtained from TraPPE model and experimental data in the whole range of coexistence. However, Chandrasekhar and Jorgensen model presents significant deviations from experimental results. We also compare the predictions for surface tension as obtained from simulation results for all the models with experimental data. The three CG models predict reasonably well (but only qualitatively) the surface tension of THF, as a function of temperature, from the triple point to the critical temperature. On the other hand, only the TraPPE united-atoms models are able to predict accurately the experimental surface tension of the system in the whole temperature range. © *2016 AIP Publishing LLC.* [http://dx.doi.org/10.1063/1.4945385]

I. INTRODUCTION

Tetrahydrofuran, c-$(CH_2)_4O$ or simply THF, is a cyclic ether widely used as solvent in many industrial processes. One of its various applications is the use as thermodynamic hydrate promoter.[1,2] This molecule is able to form structure II (sII) hydrates[1] when mixed in stoichiometric ratio with water (17 H_2O molecules per THF molecule), at 277.15 K and atmospheric pressure. From an applied point of view, its effect on systems exhibiting hydrate phases is very important, because it produces a pronounced shift on the hydrates coexistence curves when used as an additive. This ability has been widely exploited to produce hydrates in appropriated temperature and pressure ranges depending on the application envisaged. As an example, several authors[3–5] used THF for applications as the reduction of the equilibrium pressure of H_2 clathrate hydrates, considering its application in H_2 storage cells,[6,7] and of carbon dioxide (CO_2) hydrates for environmental concerns related with greenhouse gas emission control and effects on global climate change.[8–11]

During the last decades, remarkable progresses have been made on the development and application of the so-called molecular modeling techniques for the prediction of thermodynamic properties (i.e., phase equilibrium and interfacial properties) of an important number of complex mixtures of industrial interest. Examples of these methods

a)Electronic mail: felipe@uhu.es

Understanding the phase behaviour of tetrahydrofuran + carbon dioxide, + methane, and + water binary mixtures from the SAFT-VR approach

Autores/as: J. Matías Garrido, M. Cartes, A. Mejía, J. Algaba, J. M. Míguez, F. J. Blas, I. Moreno-Ventas Bravo y M. M. Piñeiro.

Publicado en: Journal of Supercritical Fluids, 128, 359-369 (2017)

DOI: 10.1016/j.supflu.2017.04.008

Factor de impacto de la revista en el año de publicación: 3.122

Rank 60/147 en Chemistry/Physical Q2 y **Rank** 34/137 en Engineering/Chemical Q1

The Journal of Supercritical Fluids 128 (2017) 359–369

Contents lists available at ScienceDirect

The Journal of Supercritical Fluids

journal homepage: www.elsevier.com/locate/supflu

Measurement and modeling of high pressure density and interfacial tension of carbon dioxide + tetrahydrofuran mixture

José Matías Garrido[a,*], Marcela Cartes[a], Andrés Mejía[a], Jesús Algaba[b], José Manuel Míguez[b], Felipe J. Blas[b], Ignacio Moreno-Ventas Bravo[c], Manuel M. Piñeiro[d]

[a] Departamento de Ingeniería Química, Univ. de Concepción, POB 160-C Concepción, Chile
[b] Laboratorio de Simulación Molecular y Química Computacional, CIQSO-Centro de Investigación en Química Sostenible and Departamento de Ciencias Aplicadas, Universidad de Huelva, 21007 Huelva, Spain
[c] Laboratorio de Simulación Molecular y Química Computacional, CIQSO-Centro de Investigación en Química Sostenible and Departamento de Ciencias de la Tierra, Universidad de Huelva, 21007 Huelva, Spain
[d] Departamento de Física Aplicada, Univ. de Vigo, E36310 Vigo, Spain

ABSTRACT

We report experimental interfacial tension, coexisting densities and relative Gibbs adsorption measurements for carbon dioxide + tetrahydrofuran mixture in the vapor-liquid equilibrium at 298.15 K and 353.15 K and pressure up to 12.0 MPa. Measurements are based on the use of a high-pressure pendant drop tensiometer coupled to a high-pressure densimeter. The results were compared to literature values where possible. In order to complement experimental measurements, theoretical modeling on the interfacial behavior was carried out using the Square Gradient Theory based on a Peng-Robinson equation of state. Investigating the applicability of the model to describe interfacial behavior in the mixture revealed very good agreement between calculated and experimental data, where the interfacial tension decreases as the pressure increases. In order to examine accumulation of compounds at the interface the model was applied. Thereby, peculiar adsorption effects of carbon dioxide in the liquid interface of tetrahydrofuran were observed.

1. Introduction

In the last years, the precise theoretical description of the interfacial properties of inhomogeneous fluid systems, including greenhouse gases (CH_4, CO_2, N_2, N_2O, etc.) has received much attention due to their environmental implications. Particularly, CO_2 emissions from the combustion of fossil fuels for power generation has been identified as the main source to global warming, according to the Intergovernmental Panel on Climate Change (IPCC) [1]. This report states clearly that efforts in all scientific and technical fields to reduce the emissions of antropogenic CO_2, and to capture and safely store it [2,3] must be significantly enhanced. Nowadays, CO_2 capture is perhaps the first and crucial step, and although several useful technologies have been proposed, amine solvents are mostly used for its capture after combustion in fossil fuel power plants [4]. However, this effective method presents issues as high corrosion and remarkable energy consumption [5,6]. Consequently, new environmentally friendly and efficient technologies must be explored to expand conventional approaches [7–9]. In this context, capture through hydrate crystallization is a promising method, due to not only to its high and safe gas storage capacity [10–13] but also to the reduced energy consumption involved in hydrate formation/dissociation processes [3,14–16].

Gas hydrates are non-stoichiometric inclusion solid compounds, consisting of a crystalline structure formed by a network of water molecules which, under certain thermodynamic conditions, can enclathrate individual small guest molecules of suitable size and shape [17]. Several hydrate structures are known [18,17], and the most common ones encountered in nature are *sI* [19], *sII* [20], and *sH* structures [21]. The nature of guest molecule determines the type of gas hydrate structure. Normally, these crystals are stable under high pressures and low temperatures. The empty hydrate water lattice itself is a thermodynamically unstable structure in these conditions, and it is the interaction between water and guest molecules that stabilize the lattice structure [22]. Many details and properties of these compounds can be found elsewhere in literature [18].

The concept of CO_2 capture by forming hydrates was first proposed by Spencer in 1997 [23,24]. Many investigations were carried out to improve the method concerning thermodynamic, kinetic, economic and process design aspects [25–28]. Tajima et al. [29] presented an estimation of energy consumption of CO_2 separation from flue gases

* Corresponding author.
E-mail addresses: josemagarrido@udec.cl (J.M. Garrido), amejia@udec.cl (A. Mejía).

http://dx.doi.org/10.1016/j.supflu.2017.04.008
Received 15 February 2017; Received in revised form 13 April 2017; Accepted 14 April 2017
Available online 21 April 2017

Understanding the phase behaviour of tetrahydrofuran + carbon dioxide, + methane, and + water binary mixtures from the SAFT-VR approach

Autores/as: J. Algaba, J. Matías Garrido, J. M. Míguez, A. Mejía, A. I. Moreno-Ventas Bravo y F. J. Blas

Publicado en: Journal of Physical Chemistry C, 122, 16142-16153 (2018)

DOI: 10.1021/acs.jpcc.8b04154

Factor de impacto de la revista en el año de publicación: 4.484 (La base de datos está actualizada hasta 2017, el factor de impacto indicado se corresponde con ese año y no con 2018 que fue el año de publicación del artículo)

Rank 38/147 en Chemistry/Physical Q2, **Rank** 33/92 en Nanoscience/Nanotechnology Q2 y **Rank** 54/285 Materials Science/Multidisciplinary Q1

THE JOURNAL OF PHYSICAL CHEMISTRY C

Article

Cite This: J. Phys. Chem. C 2018, 122, 16142−16153

pubs.acs.org/JPCC

Interfacial Properties of Tetrahydrofuran and Carbon Dioxide Mixture from Computer Simulation

Jesús Algaba,[†] José Matías Garrido,[‡] José Manuel Míguez,[†] Andrés Mejía,[‡] A. Ignacio Moreno-Ventas Bravo,[†] and Felipe J. Blas*[,†]

[†]Laboratorio de Simulación Molecular y Química Computacional, CIQSO-Centro de Investigación en Química Sostenible and Departamento de Ciencias Integradas, Universidad de Huelva, 21006 Huelva, Spain

[‡]Departamento de Ingeniería Química, Universidad de Concepción, POB 160-C Concepción, Chile

ABSTRACT: We determined the interfacial properties of the tetrahydrofuran + carbon dioxide (THF + CO_2) binary mixture from direct simulation of the vapor−liquid interface. We consider two different models of THF based on the transferable parameters for phase equilibria-united atom (TraPPE-UA) version approach. In the first case, we use the original (flexible) TraPPE-UA model force field for the ether [*J. Phys. Chem. B* **2012,** *115,* 11234]. The second model is a planar, rigid, and approximated TraPPE-UA model recently proposed by us [*J. Chem. Phys.* **2016,** *144,* 144702]. It is demonstrated that the sophisticated flexible model does not have an overall advantage in comparison with the simplified planar model. Indeed, both models are able to predict the phase behavior and interfacial tension of pure THF with high accuracy in a wide range of temperatures and pressures. It is noticed that the planar model is faster for simulation because the internal degrees of freedom are frozen (neither bending nor torsional intramolecular interactions need to be evaluated). Most of the simulations were performed in the molecular dynamics canonical ensemble, and the vapor−liquid interfacial tension is evaluated from the normal and tangential components of the pressure tensor according to the mechanical virial route. We also used the Gibbs ensemble Monte Carlo simulation technique to determine the phase behavior of the mixture under selected conditions to compare the results from both methodologies. In addition to the interfacial tension, we also obtained density profiles and pressure−density and pressure−composition slices of the phase diagram of the mixture at different temperatures and pressures. Simulation results obtained from both models are able to accurately predict the vapor−liquid phase envelope of the system, which is in good agreement with the experimental results. We also compare the predictions for interfacial tension, as obtained from simulation results for the two models, with the experimental data. Agreement between computer simulation predictions and experiments for the interfacial tension of THF + CO_2 mixtures, as a function of pressure, is excellent in nearly all cases. In addition to that, the density profiles associated with carbon dioxide exhibit a relative maximum related to preferential adsorption at the liquid interface of THF. This accumulation in the interface is probably related to the asymmetry in the size of the components of the mixture.

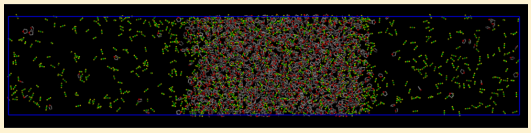

1. INTRODUCTION

Gas hydrates are nonstoichiometric crystalline inclusion compounds consisting of a network of hydrogen-bonded molecules forming cages in which various types of low-molecular-weight compounds, such as methane (CH_4), carbon dioxide (CO_2), hydrogen sulfide (H_2S), or hydrogen (H_2), among many others, can be enclathrated under appropriate thermodynamic conditions. Because of the characteristic properties of hydrates to selectively encage guest molecules within this solid hydrate crystalline structures, hydrates are nowadays considered strategic and key materials in the gas storage/transportation industry and in mixture separation applications. This includes CH_4, CO_2, and H_2 among the most relevant substances. Although storage, transportation, and mixture separation are key applications for industry, the view of gas hydrates as a possible future source of energy and the environmental use of hydrates for CO_2 sequestration make the understanding of these systems from kinetic, thermodynamic, and structural points of view even more attractive for the scientific community.

The thermodynamic conditions at which the clathrate hydrate structures are formed and become stable depend, in a complex fashion, on the shape, structure, and molecular interactions of the low-molecular-weight compounds or guests that are enclathrated in the cages of the waterlike crystalline network formed as well as on the intermolecular interactions between the guest and water molecules. In many occasions, the temperatures and pressures at which different clathrate hydrates are stable are far from being considered as mild conditions. As an example, H_2 can be stabilized in clathrate hydrates at extremely high pressures, typically 220 MPa at 249 K.[1,2] To avoid these extreme conditions, it is normal to add some chemical additives, called hydrate thermodynamic

Received: May 2, 2018
Revised: June 19, 2018
Published: June 26, 2018

DOI: 10.1021/acs.jpcc.8b04154
J. Phys. Chem. C 2018, 122, 16142−16153